Experimental Characterization of the Photocathode Laser System for Advanced 3D Pulse Shaping at PITZ

Dissertation
zur Erlangung des Doktorgrades
an der Fakultät für Mathematik, Informatik
und Naturwissenschaften
Fachbereich Physik
Der Universität Hamburg

vorgelegt von
James Good

Hamburg
2019

Gutachter des Dissertation	Prof. Dr Florian Grüner Dr. Mikhail Krasilnikov
Zusammensetzun der Prüfungskomission:	Dr. Mikhail Krasilnikov Prof. Dr Florian Grüner Prof. Dr Joerg Rossbach Prof. Dr Wolfgang Hillert
Vorsitzender der Prüfungskomission:	Prof. Dr. Olaf-Svan Moch
Datum der Disputation:	19.05.2020
Vorsitzender Fach-Promotionsausschusses PHYSIK:	Prof. Dr. Günter H. W. Sigl
Leiter des Fachbereichs PHYSIK:	Prof. Dr. Wolfgang Hansen
Dekan der Fakultat MIN:	Prof. Dr. Heinrich Graener

Abstract

Light is one of the most versatile tools in an experimenter's toolbox and has been used to investigate the natural world since the invention of the lens and as new techniques, sources, and materials have been developed. One of the biggest turning points was the development of a brilliant, coherent, light source: the laser. This simple device revealed predicted but hitherto unprovable science before the availability of such an intense light source. Since then this versatile tool has enabled and opened up numerous avenues of research and development of communication networks, computer processors, medical manufacturing and treatments, drug research, basic commerce, and much more.

However, despite its flexibility a conventional laser system is limited by its material constraints. The crystals, glasses, and optical elements used in modern, ultrafast, high power lasers can only endure a finite amount of energy flux before damage sets in. Furthermore, the spectral range is limited by the most fundamental of material properties: absorption. Extending the operational range further and further into the ultraviolet (UV) wavelengths and beyond is difficult with the increasing number of exotic technical requirements.

Modern Free Electron Lasers (FEL) circumvent these constraints on the generation and propagation of extreme light pulses by simply not having any material. Instead coherent, ultrashort light pulses are generated by exploiting relativistic electron bunches generated in an accelerator. By utilizing periodically alternating magnetic fields and spontaneous light generation Self Amplifcation by Stimulated Emision (SASE) can be induced and a brilliant, coherent laser pulse in the deep UV, soft X-ray, and beyond can be produced. In effect a laser system without an optical cavity- without materials. This approach permits unparalleled tunability and flexibility of the laser pulse properties as the repetition rate, duty cycle, duration, wavelength, intensity and coherence can all be dynamically modified.

For modern, linear, electron accelerators and light sources such as the Free Electron Laser in Hamburg (FLASH) and the European XFEL the entire foundation of this process is the photoinjector and the conventional laser system used to drive photoelectron production within it. Fundamentally, the properties of the electron bunches determine the quality of lasing. The size, charge, duration, distribution and subsequently the emittance (the volume the bunches take in phasespace) all play a role and are determined by the photoinjector and primarily by the laser pulse properties.

The Photo Injector Test Facility at DESY, Zeuthen (PITZ) was founded to pioneer new technologies and concepts to improve and characterize photoinjectors and subsequently help push the limits and capabilities of FELs. As such it is uniquely situated to test and develop new photocathode drive lasers.

In this work the feasibility and application of a new method to produce volumetrically shaped photocathode laser pulses, and subsequently shaped electron bunches, at PITZ is detailed and demonstrated. First, the basic theory, and numerical simulations of laser pulses shaped by directly accessing their spectral domain and modifying it with Spatial Light Modulators, and the potential advantages of the shaped electron bunches are shown.

Furthermore, shaped electron bunches arising from shaped photocathode laser pulses are demonstrated and utilized to improve photoelectron bunch properties. Finally, lessons, designs, and preliminary results of an improved laser system are shown.

Zusammenfassung

Seit Erfindung der optischen Linse und vorangetrieben durch die kontinuierliche Entwicklung neuer Methoden, Quellen und Materialien ist Licht eines der mächtigsten Werkzeuge der experimentellen Physik. Einer der größten Meilensteine dieser Entwicklung war die Erfindung des Lasers, einer kohärenten und brillianten Lichtquelle. Der Laser hat die Erforschung von vorhergesagten Phänomenen ermöglicht, die Experimenten vor seiner Entdeckung unzugänglich waren. Seitdem hat dieses vielseitige Werkzeug der Forschung und Entwicklung vielfältige Wege eröffnet: Kommunikationsnetzwerke, Mikroprozessoren, Medizinprodukte, medizinische Behandlungen, Pharmazie, kommerzieller Handel sowie viele weitere Aspekte unseres Lebens verlassen sich heute auf Lasertechnik.

Nichtsdestotrotz sind die Möglichkeiten konventioneller Laser durch die Eigenschaften der verwendeten Materialien eingeschränkt. Kristalle, Gläser und andere optische Elemente, die in modernen Kurzpuls- und Hochleistungslasern Anwendung finden, können nur endliche Energieflüsse transportieren, bevor sie Schaden erleiden. Weiterhin wird der Spektralbereich des erzeugten Lichts durch Absorption der Materialien vor allem zu niedrigen Wellenlängen hin begrenzt. Tiefer und tiefer in den ultravioletten (UV) Bereich der Laserwellenlängen vorzustoßen hat so durch die Summe der komplexen technischen Ansprüche und Hürden die Grenzen der physikalischen Machbarkeit erreicht.

Moderne Freie Elektronen Laser (FEL) umgehen diese Einschränkungen indem sie ohne die Verwendung von Materialien zur Lichterzeugung auskommt. Als Medium für die Erzeugung von kohärenten und ultrakurzen Lichtpulsen dienen stattdessen Pakete relativistischer Elektronen, die von Teilchenbeschleunigern bereitgestellt werden. Durch die Ablenkung dieser Pakete in periodisch wechselnden magnetischen Feldern wird anstelle reiner spontaner Emission von Synchrotronstrahlung sogenannte Selbstverstärkung durch stimulierte Emission (engl. Self Amplification by Stimulated Emission, SASE) hervorgerufen. Dies ermöglicht die Bereitstellung von Lichtpulsen mit Lasereigenschaften im kurzwelligen UV- und weichen Röntgen-Bereich bis hin zu noch kleineren Wellenlängen ohne die Verwendung eines optischen Resonators und damit ohne Materialeinschränkungen. Da Pulswiederholrate, Betriebszyklus, Pulsdauer, Wellenlänge und Kohärenz der erzeugten Lichtpulse vom verwendeten Elektronenstrahl abhängen bietet der FEL einzigartige Flexibilität in der Lichterzeugung.

Die Grundlage zur Bereitstellung dieser Elektronenstrahlen in Lichtquellen wie dem Freie Elektronen Laser in Hamburg (FLASH) und dem europäischen Röntgenlaser (European XFEL) ist der Photoinjektor und das konventionelle Lasersystem, das darin zur Freisetzung der Elektronenpakete aus einer Photokathode mittels des Photoelektrischen Effekts dient. Eigenschaften wie Größe, Ladung, Dauer und das Volumen, das die Elektronenpakete im Phasenraum einnehmen – die sogenannte Emittanz – sind maßgeblich für die Lichterzeugung im FEL und hängen direkt von den Eigenschaften des Photoinjektors und insbesondere von den Photokathodenlaserpulsen ab.

Der Photoinjektor Teststand am DESY in Zeuthen (PITZ) wurde errichtet um neue Technologien und Methoden zur Verbesserung von Photoinjektoren zu erfoschen und damit die Leistungsfähigkeit und Möglichkeiten von FELs zu erweitern. Die Anlage bietet daher einmalige Voraussetzungen für die Entwicklung und experimentelle Erprobung von neuen Photokathodenlasersystemen.

Im Rahmen dieser Arbeit wird die Machbarkeit und experimentelle Umsetzung eines neuartigen Konzepts zur dreidimensionalen Formung von Photokathodenlaserpulsen – und folglich der damit erzeugten Elektronenpakete – bei PITZ beschrieben und demonstriert. Dazu werden zunächst die Vorteile von ellipsoidförmigen Elektronenpaketen und die theoretischen Grundlagen und numerische Simulationen der Erzeugung dreidimensional geformter Laserpulse durch direkte Manipulation ihrer Spektralverteilung mit sogenannten räumlichen Lichtmodulatoren (engl. Spatial Light Modulators, SLMs) beschrieben. Weiterhin werden die Erzeugung von dreidimensional geformten Elektronenpaketen mit Hilfe dieser Laserpulse und die dadurch erreichte Optimierung der Eigenschaften des Elektronenstrahls experimentell gezeigt. Schließlich werden Lehren aus den experimentellen Ergebnissen mit dem verwendeten Lasersystem gezogen und der Aufbau und vorläufige Ergebnisse eines neuen, verbesserten Lasersystems vorgestellt.

Contents

Chapter 1 Introduction 1
Chapter 2 Theory 10
2.1 Beam Dynamics 10
2.2 Photoinjectors 12
2.3 Uniformly filled ellipsoidal distributions 14
2.4 Space charge forces 16
2.5 Optical theory 18
2.6 Spatial Light Modulators (SLMs) 23
2.7 Imaging scheme 26
2.8 Frequency conversion 29
2.9 Diagnostics 34
2.9.1 Autocorrelation 35
2.9.2 Cross-correlation 35
2.9.3 Spectrograph 35
Chapter 3 PITZ accelerator 40
3.1 General layout 40
3.2 Primary photocathode system 42
3.3 RF photoelectron gun 45
3.4 Solenoid magnets 46
3.5 CDS booster 47
3.6 Diagnostics 48
3.7 Transverse phase-space measurements 49
Chapter 4 Laser pulse shaping and electron beam dynamics simulations 51
4.1 Optical simulations 51
4.1.1 Zemax studies 51
4.1.2 Matlab numerical simulations 56
4.1.3 Efficiency 64
4.1.4 Non-linear conversion 68
4.1.5 Laser transport beamline 72
4.2 Electron beam dynamics simulations 74
4.2.1 Multi-charge bunches 76
4.2.2 Simulations of startup experiments at PITZ 81
Chapter 5 The Ellipsoidal Laser (ELLA) system 88
5.1 Generalized scheme 88
5.2 Actual layout 89
5.3 The Er-Yb sscillator-preamplifier 91

5.4 The Yb:KGW thin-disc multipass amplifier 92
5.5 The shaping scheme 94
5.6 Infrared diagnostics 97
5.7 Self-characterization 98
5.8 Spectral diagnostics 101
5.8.1 Spectrometer 101
5.8.2 Spectrograph 101
5.9 Temporal characterization 103
5.10 Harmonic conversion 106
5.11 Laser beam transport 108
5.12 Synchronization 110
Chapter 6 Electron beam results 113
6.1 Comissioning 113
6.2 Electron beam shaping 117
Chapter 7 Redesign 122
7.1 Pharos laser 123
7.2 Zemax studies 126
7.3 ELLA2 construction and outlook 128
Chapter 8 Summary 132
Appendix 135
A. Auxiliary tables 135
B. Gaussian relation 136
C. Flattop fit of a Gaussian envelope 137
D. Rectangular fit of elliptical envelope 138
E. Circular fit of a Gaussian envelope 141
F. Elliptical fit of a Gaussian envelope 142
Bibliography 143

Chapter 1 Introduction

For many particle accelerators beam quality is one of the properties of utmost importance and is a constant avenue of research and development. Over the last century many improvements have been implemented depending on circumstance and requirement. From the alternating gradient FODO lattice first introduced to the Brookhaven's Cosmotron synchrotron in 1952 [1] and in the same year the first undulator was demonstrated at Standford [2], with photoinjectors introduced in 1985 [3], all these concepts are still utilized in high-gain Free Electron Lasers (FELs). The demands of which have been pushing boundaries ever since, including the more recent seeded FELs and high gain harmonic generation (HGHG) FELs.

FELs are widely-tuneable, coherent radiation sources that provide ultra-short, highly brilliant laser pulses for scientific and industrial use. The radiation originates from the synchrotron radiation emitted by the undulation of accelerated charged particle bunches passing through a series of alternating magnetic fields, an undulator. As the radiation field strength grows it can self-interact with the charged bunch forcing the particles to further emit radiation in phase, thereby producing coherent radiation.

As each particle is a source of electromagnetic radiation multiple times throughout the process it is self-evident that the greater the number of particles, the greater the bunch charge, then the better the possibility for radiation production. Furthermore, it is preferable to have the bunch as small as possible and the charges to be travelling as parallel to one another as possible to further increase the interaction and superimpose the radiation for even higher brilliance.

Brilliance is defined by the number of photons per second within the cross-sectional area of the beam and the angular divergence of the beam for a given bandwidth of the central wavelength or frequency. This is expressed in units of photons/s/mm^2/mrad^2/0.1% bandwidth [4] and modern FELs such as FLASH, the European XFEL, and LCLS can reach peak magnitudes on the order of 10^{33} [5]. This is approximately nine orders of magnitude higher than that of conventional, 3rd generation synchrotron sources such as PETRA III and Spring-8.

In the case of a low-gain FEL setup (Figure 1.1) two mirrors are placed on either side of a short undulator to form an optical cavity in which only the desired wavelength may constructively form a standing wave. In this manner the radiation may be stored and amplified by repeated passes of the beam through the undulator [6].

As mirrors for wavelengths shorter than 100 nm are difficult to produce to form an optical resonator, to reach smaller wavelengths a separate single-pass high-gain method is required. By using a significantly longer undulator the bunch can self-interfere with the produced electromagnetic field and produce micro-bunching within itself. These micro-bunches can then radiate coherently producing optical power proportional to the number of charges squared. This process is called Self Amplified Spontaneous Emission (SASE) [7].

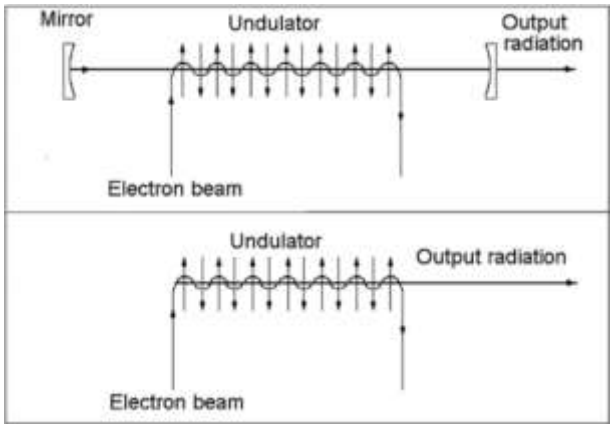


Figure 1.1: Free-Electron Laser setups: low gain FEL optical cavity (top), and Self Amplified Spontaneous Emission high gain FEL (bottom) [4].

For this high-gain regime strict requirements are placed on the quality of the electron bunch at the undulator aperture. A large amount of charge must be contained within a short bunch to produce a high peak current, the emittance (a loose definition being a measure of the product of beam size and divergence of the bunch at a beam focus point) and the momentum spread must also be small. Since emittance cannot be reduced in-flight the electron bunch must have good properties from the very start of the accelerator, at the injector.

A photoinjector uses laser pulses to generate electron bunches at a photocathode in a high electric field to produce low emittance beams. This is achieved by placing a Cs_2Te semiconductor photocathode in a RF cavity, to avoid material breakdown in a static field, and then utilizing ultraviolet laser pulses on the cathode to produce electrons through photoemission. The short wavelength of the photocathode laser pulses is necessary to overcome the bandgap of the semiconductor material and to take advantage of its high Quantum Efficiency (QE) in comparison to metal cathodes. The strong electric field then accelerates the particles downstream for injection into further accelerator modules.

The technical requirements for a photoinjector are often very stringent: requiring high RF power, high bunch charge, low emittance, a high bunch repetition rate, and as large RF duty cycle as possible. For example, see the nominal European XFEL photoinjector design specifications [4] in the following table:

Table 1.1: European XFEL photoinjector design parameters [4].

Charge [nC]	1
Laser wavelength [nm]	257
Laser flat-top pulse length [ps]	20
Laser pulse rise/fall time [ps]	2
Laser spot radius [mm]	1.1
Laser repetition (microbunch) rate [MHz]	4.5
Peak electric field at cathode [MV/m]	60
Macrobunch length [μs]	600
Macrobunch repition rate [Hz]	10
Electron beam energy [MeV]	6.6
Electron beam normalized projected emittance [mm.mrad]	<0.9

Typically the emittance of a charged particle bunch arises from intrinsic contributions from the emission process at the cathode (thermal emittance), the temporal variation of the accelerating electromagnetic field (RF induced emittance), focusing variance due to the energy spread of the bunch, and internally through space charge effects of the bunch (space charge induced emittance growth). The latter effect can be reduced by increasing beam energy, and as the beam energy after exiting the gun is still relatively low and therefore still experiences significant space charge forces, the beam is quickly accelerated in further accelerating cavities.

A number of photoinjector "knobs" may be tuned to reduce the various contributions and to counteract the non-linear space charge forces. Gun gradient, accelerating cavity (booster) gradient, solenoid field strength, RF phase, beam steering through the injector, laser spotsize at the photocathode, bunch charge, all play a role in reducing or compensating various emittance contributions. As the beam energy after the gun is still quite low, and space charge forces are reduced with increasing beam energy, the space charge forces within the bunch are still significant and further acceleration is needed. As such the booster is one of the primary tuning factors for minimization of the space charge forces and the emittance.

In the case of photoinjectors for FELs the space charge contribution is of significant interest since minimum emittance is required. The distribution of electrons within the bunch volume and with this the internal space charge forces can be modulated through manipulation of the photonic distribution of the photocathode laser pulse used to generate the electrons.

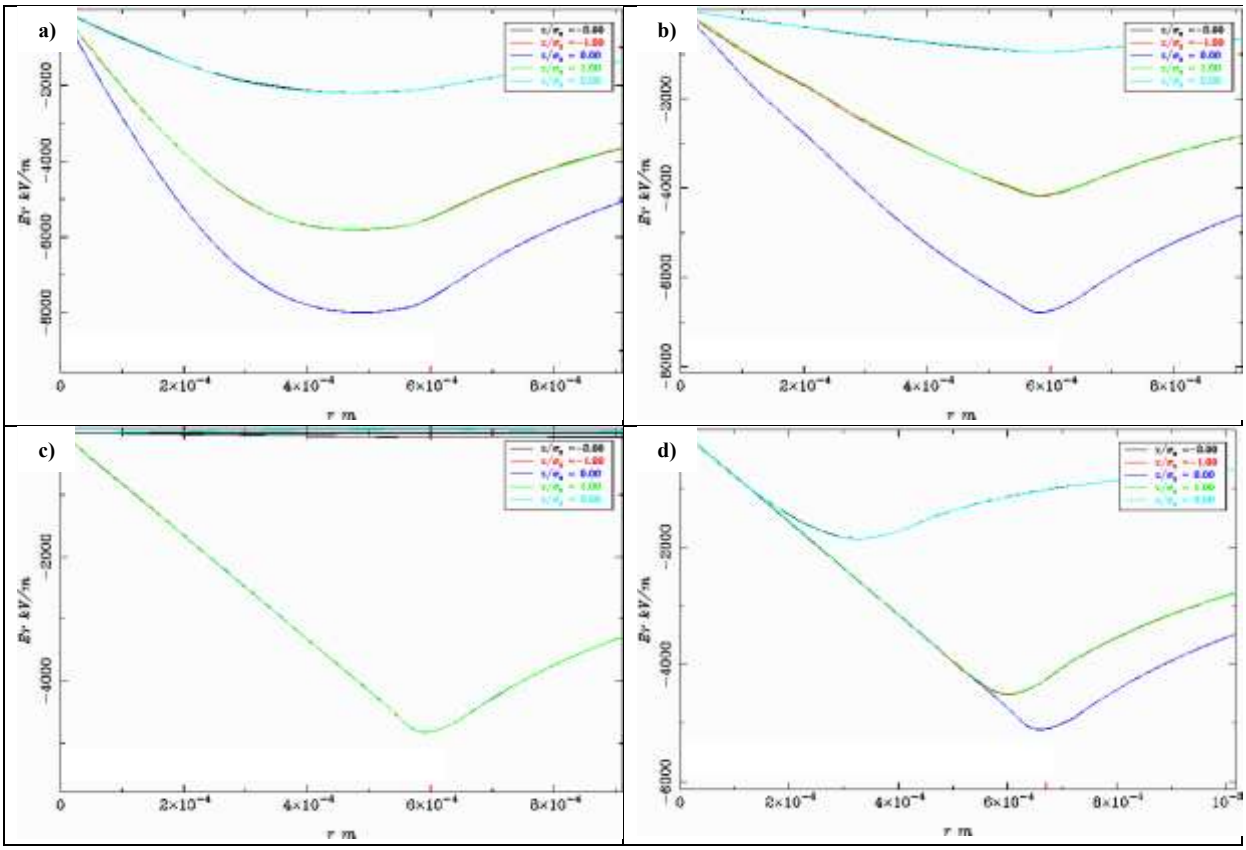


Figure 1.2: Non-linear and linear radial Lorentz forces for 6.5 MeV/c, 1 nC electron bunches with equivalent RMS bunch lengths (σ_z = 1.73 mm) and various topographies. a) 3D Gaussian distribution (σ_r = 0.3 mm) truncated at r=0.6 mm, b) Gaussian temporal envelope and 2D transverse Gaussian distribution truncation at σ_r = 0.6, c) fully cylindrical distribution, and d) ellipsoidal distribution.

An examination of the transversal Lorentz forces within various electron bunch distributions (Figure 1.2) shows increasing linearization for increasingly homogenous distributions. Linearization of the transverse force can already be seen by homogenization of the transverse profile (a & b) where transverse cropping of a Gaussian distribution at its rms value reduces the amount of transverse charge variation and therefore improves beam quality of the photoinjector. Cylindrical pulses show a marked improvement over fully Gaussian pulses and maintain a constant field gradient for a majority of the bunch. However, the bunches still suffer from non-linear space charge forces at the heads and tails owing to the finite bunch length, this is especially pronounced during emission where these forces can distort the bunch distribution before significant energy has been imparted. This is minimized by ellipsoidal charge distributions.

In simulation it can be seen that the bunch distribution at the cathode has a noticeable effect on intrinsic bunch properties such as bunch current and thermal emittance (Figure 1.3), as well as on projected emittance formation along the bunch during photoemission.

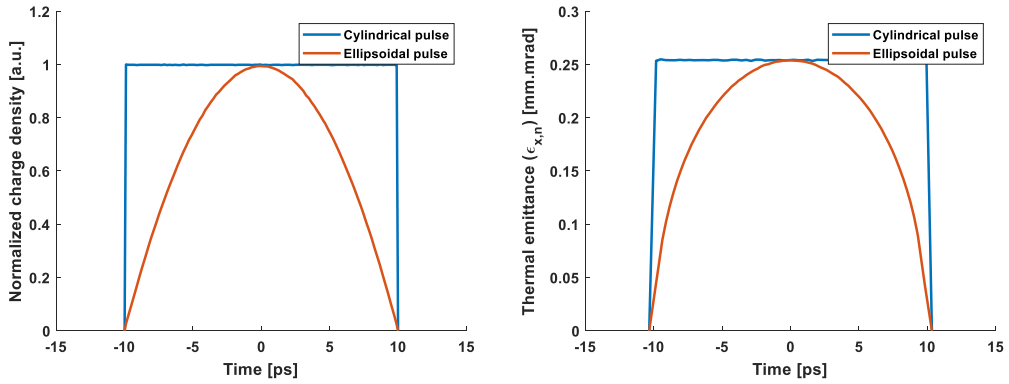


Figure 1.3: Current profiles (left) and estimated thermal slice emittances (right) for idealized cylindrical (blue) and ellipsoidal (orange) electron bunches.

By comparing an ellipsoidal pulse of comparable transverse and longitudinal RMS size to that of a cylindrical pulse of nominal parameters (t_{FWHM}=20 ps, r=0.6 mm), and of equal charge, significant differences can be seen. Owing to linearization of the space-charge forces a significant reduction in slice emittance along the bunch during emission can be seen, as well as a smoother profile, see Figure 1.4.

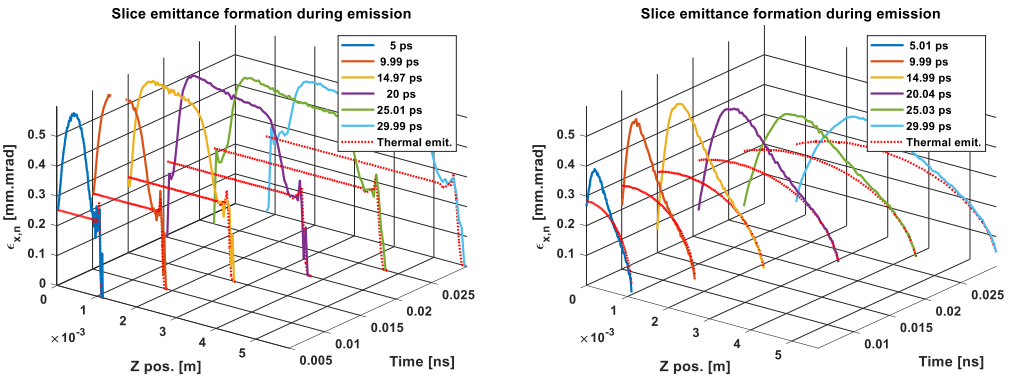


Figure 1.4: Slice emittance formation during emission for 500 pC cylindrical (left) and ellipsoidal (right) pulses with comparable transverse and longitudinal RMS distributions (σ_r=0.3 mm, σ_t=5.77 ps).

From these simple considerations of the beam dynamics the advantage of electron bunch shaping is evident, in particular with regard to ellipsoidal bunches. This is still a major motivation for photocathode laser pulse shaping today and the main driver behind this work.

Historically, the original photocathode lasers used in the first generation of FELs typically had Gaussian temporal and transverse profiles [8] which generated, by first order approximation, correspondingly Gaussian particle beams. Even without simulation it can easily be imagined how the non-linear distribution of charge and the resulting induced space charges forces within a concentrated volume of the bunch results in an undesirably large contribution to the emittance budget from space charge induced expansion.

This naturally leads to manipulations of the transverse laser beam profile (Figure 1.5) by masking with pinholes [9] or variable irises in order to produce a more constant photon density over the photoemission area. Similarly, techniques to manage the temporal profile have also been developed typically utilizing birefringent materials to produce pulse stacking in a Solc fan configuration [10], bandwidth suppression by Lyot filters, or Fourier masking of the spectrum [11].

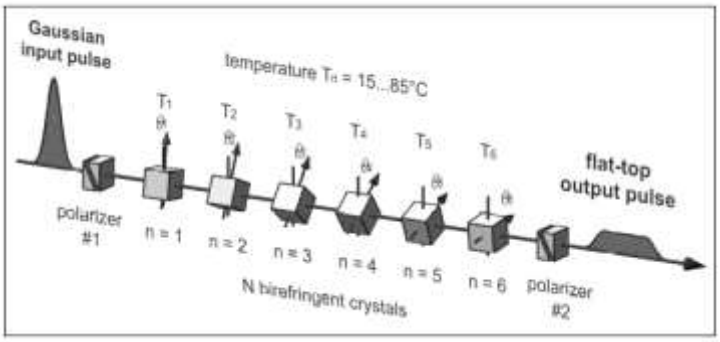


Figure 1.5: A Solc fan longitudinal shaper [10].

Furthermore, there are any number of exotic beam manipulation techniques for as many specialized requirements over the diverse fields of applied photonics. Axicons are used to produce Bessel beams and ring focuses for electron plasma generation through field ionization [12], corneal surgery, laser machining and various other applications. Cylindrical lenses or amorphic prism pairs can be utilized to produce line focusses, and π-shapers [13] can produce transversal flattops.

At the Photo Injector Test Facility at DESY, location Zeuthen (PITZ), photocathode laser shaping techniques are under development for FLASH, and the European XFEL [14]. Cylindrical pulses, together with beam dynamics simulations, have been used to show the effects and demonstrated a distinct improvement in transverse emittance (Figure 1.6). The results for the 12 ps FWHM “long Gaussian” laser pulse were obtained by experimentally optimizing the gun parameters (RF phase, main solenoid strength, laser spotsize, etc.) and performing simulations for the obtained parameters [14].Contrariwise, the results for 21 ps FWHM “flattop” laser were obtained by optimization in simulation of the gun parameters (gun gradient, RF phase, main solenoid strength, laser spotsize) and performing the same optimization procedure experimentally in parallel [15] to compare the outcomes.

Finally, the simulations of electron beams produced from ellipsoidal laser pulses were produced [16] by optimization of the gun parameters to produce minimized emittance at the equivalent point of the emittance measurement station in the PITZ beamline.

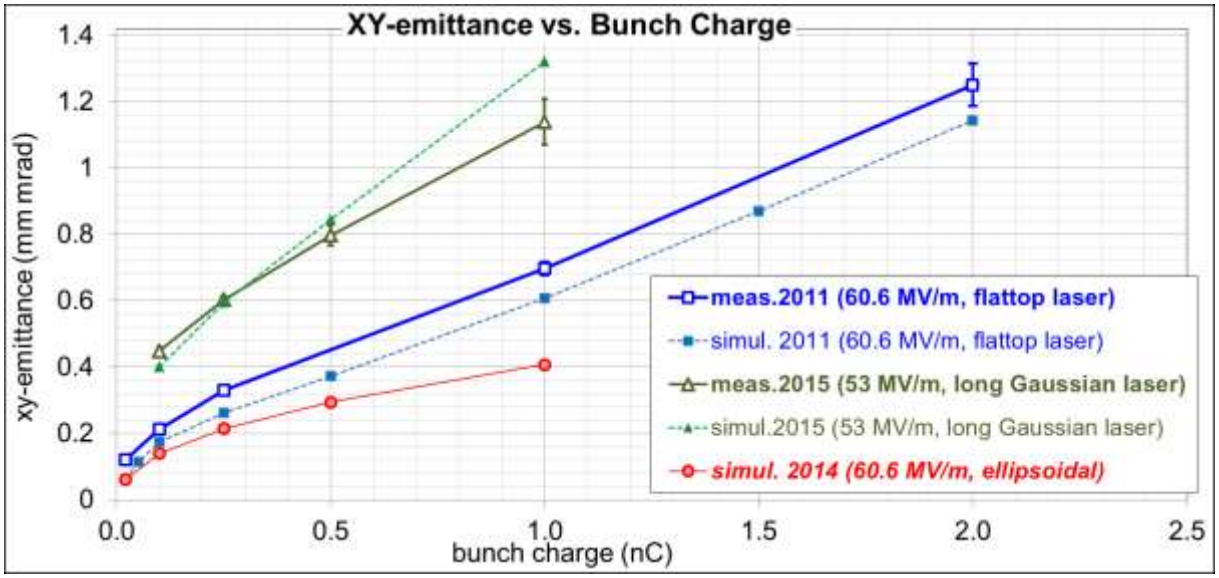


Figure 1.6: A comparison of simulated and measured emittance for electron bunches produced with transversal flattop distributions and flat-top and Gaussian temporal envelopes at various charges at PITZ. Simulations for ellipsoidal pulses are shown also.

Historically, the idealized volumetric distribution for the minimization of the space charge forces was found in the ellipsoid. The form was first introduced [17] for use in proton LINACs and used as the idealized composition ever since in simulations for photoinjectors such as LCLS and the originally envisioned TESLA facility [18].

Soon after in theoretical astrophysics it was realized that an elongated spheroid of uniform density would collapse by gravitational force into a pancake [19]. This collapse is the time-reversal equivalent of Coulombic expansion of a charged bunch. Therefore an approach to produce ellipsoidal particle bunches via longitudinal beam expansion was modelled [20] and in this 'blow-out regime', where the transverse dimension is far greater than the temporal, the formation of an ellipsoid bunch is achieved by a parabolic the transverse intensity profile of an ultra-short laser pulse. This concept was experimentally tested at the PITZ photoinjector with 750 pC bunch charge generated by a photocathode laser with a Gaussian temporal RMS duration of 1 ps. [21], however, the generated pulses were distorted by image charge forces and incomplete emittance compensation due to low accelerating gradients.

In the interim a few proposals and experimental systems have been put forth to produce ellipsoidal laser pulses using chromatic aberration [22], Dazzlers, and MEMS-coupled fiber bundes [23]. However, these methods were single pulse measurements and are of limited use for pulse train operation as required for photoinjectors driving superconducting linac-based light sources like FLASH and the European XFEL.

However, with the continuous advancement of lithographic microstructuring in the last decades Liquid Crystal Display (LCD) technology has seen an explosion in consumer uptake, research, and development. Owing to this advancement recent techniques to generate ellipsoidal pulses have focused on schemes involving Spatial Light Modulators (SLMs), a

type of referable liquid-crystal matrix much like an LCD panel, in either a zero-dispersion compressor layout [24] [25] (and the focus of this work) or as a spectral modulator coupled with volume Bragg gratings [26].

For a photoinjector, such as PITZ, these techniques to produce (quasi-)ellipsoidal laser pulses have been shown in simulation to drastically reduce the space charge related emittance contribution in comparison to nominal aforementioned laser pulse structures [27]. Therefore, based on the promising simulations of enhanced electron beam quality a collaboration between the Institute of Applied Physics of the Russian Academy of Sciences (IAP RAS, Nizhny Novgorod) and PITZ was formed and a conceptual prototype photocathode laser system was developed and first constructed in Nizhny Novgorod. The primary goal was to develop a system capable of producing trains of quasi-ellipsoidal UV laser pulses with sufficient energy to produce 1 nC bunches in the photoinjector at the nominal PITZ and XFEL timing requirements. An ultra-short (~0.2 ps), broadband IR laser system capable of laser pulse shaping, conversion, and characterization was then installed at PITZ and entered the commissioning phase in December 2014. This was in preparation for experimental review to demonstrate the pulse shaping technique as a proof-of-principle and to observe improvements in beam quality as a result of pulse shaping.

The laser systems are invariably located outside the accelerator tunnel to enable access and to protect them from radiation damage. Therefore, the laser pulses must be *transported* from the laser system to the photocathode while maintaining their shape. Furthermore, the laser pulses must arrive at the correct time; the laser oscillator must be synchronous with the RF and any temporal offsets compensated for.

Even more crucially, there exist no laser systems that directly operate in the UV at the necessary pulse parameters. Excimer gas lasers operate primarily within the UV range but cannot reach the required MHz repetition rate. More to the fact, there exist few methods for pulse shaping directly in the UV because of high losses due to material absorption, stronger dispersion, and numerous other material constraints.

Fortunately, infrared lasers have a long and industrious R&D history with many alternatives possible for ultra-short, high power laser generation techniques. In fact, the first laser ever demonstrated in 1960 [28] was a red, visible laser at 694.3 nm. The telecoms industry also has a long illustrious history since the 1970s utilizing pulsed near-IR and IR semiconductor lasers for long-haul, high-bandwidth fibre optic communications. There has been a significant amount of development in the preceding decades on solid-state IR lasers and optical materials within this spectrum which make it ideal for laser pulse shaping.

There are numerous design benefits and trade-offs with this approach. A large optical bandwidth is vital for the production of ultra-short laser pulses; the shorter a pulse is then the greater the bandwidth required to produce it. Ultra-short pulses also permit the self-characterization of chirped (stretched) laser pulses and ease constraints in the pulse shaping scheme.

Conversely, the greater the optical bandwidth then the greater the difficulty in non-linear frequency conversion as the bandwidths diverges from the phase-matching condition in standard conversion schemes. This increases the difficulty of shape preservation throughout the conversion process and, by extension, reduces the efficiency and effectively increasing the

required laser pulse energy. As non-linear conversion is an intensity-dependent process it is desirable to focus the laser beam on the crystal, however in the pulse shaping scheme utilized this focal point would coincide with the Fourier plane containing the spatial information. As the intensity is not constant across all spatial frequencies the frequencies would be converted at different rates and the spatial information imparted onto the pulse would be modified. The crystal would act as a low-pass frequency filter.

Finally, the desired pulse shape must actually be generated. This requires knowledge of the input distribution, accurate calibration of the adaptive optics, and iterative modification of the pulse in conjunction with characterization of the produced pulse.

This thesis aims to evaluate the prototype laser system developed by IAP in the framework of charged ellipsoidal bunch production in a photoinjector and the subsequent impact this novel pulse shaping technique has on the beam properties.

A number of key issues must be considered in order to demonstrate the feasibility of ellipsoidal bunches with respect to photocathode laser pulses:

- Infrared shape generation and characterization
- Shape preservation through non-linear frequency conversion from IR through green to UV
- Sufficient UV pulse energy for nC bunch production
- Laser beam transport to the photocathode
- Synchronization with the RF field in the gun
- Electron bunch characterization
- Stability (jitter and drift)

This thesis is structured as follows:

The following chapter, Chapter 2, details the fundamentals of charged particle beam dynamics in the context of photoinjectors and FELs; the basics of bunch acceleration, steering, characterization and desirable beam qualities and their impact on the FEL lasing process. It then goes into detail on the aspects of optics and photonics relevant to the production of shaped laser pulses from photocathode lasers for the generation of electron bunches in photoinjectors.

Chapter 3 then outlines and describes the layout and functions of the PITZ accelerator and its components. The fundamental components, the accelerating cavities, magnetic optics, diagnostics, primary photocathode laser and measurement devices are briefly described. This puts into context the primary method of emittance measurement utilized at PITZ, and its applicability as a testbed for prototyping photoinjector and FEL related projects.

From this perspective an understanding and applicability of shaped laser pulses and their correspondingly shaped electron bunches can be taken from simulations. This is found in Chapter 4 where geometric and numerical simulations of the laser system are undertaken of the various aspects of the laser pulse shaping scheme and the impact of shaped electron bunches on electron beam properties and dynamics is presented.The unintuitive implementation of the spatio-spectral laser pulse shaper is simulated and explained, and the effect this planar device has on a volumetric distribution is calculated. This leads then to pulse shaping and conversion efficiency calculations as an indicator of available bunch charge in

the accelerator. Of course, knowing the impact these shaped electron bunches is desirable, and so electron beam dynamics simulations for various bunch charges and bunch imperfections are shown.

Chapter 5 contains the description, operating principles, and characterization of the prototype laser system used in the experiments. The technicalities of the innovative polarization-exploiting reciprocal design and the consequences of the implementation on the spatial, spectral, and temporal qualities of the pulses are described.

Commissioning and operation of the system as a photocathode laser is then detailed in Chapter 6, where a comparison of the bunches produced by the two available photocathode lasers is made.

In response to the results, Chapter 7 outlines and discusses critiques of the original prototype and introduces a new optical layout and redesign of the pulse shaping scheme based around a single frontend laser system.

Finally, the outcome is summarized in Chapter 8, with closing remarks and an outlook for future experiments and results.

Chapter 2 Theory

Of course, it is instructive to have a basic theoretical understanding of the physics at work and therefore the motivations and consequences arising out of them. First, it is worthwhile to consider the dynamics of charged particle acceleration and the impact of charged bunch properties on the generation of radiation with an undulator.

From these properties it becomes clear that the generation of electrons by photoemission and subsequent acceleration is preferable, the basic principles of a photoinjector are explored, and the advantages of various bunch distributions from a beam dynamics perspective.

This then motivates shaping of the photocathode laser to produce said bunch distributions and the physics of laser pulses, laser pulse shaping, frequency conversion, and characterization are analysed.

2.1 BEAM DYNAMICS

The basic function of an accelerator is to impart kinetic energy onto a charged particle such as an electron. The only mechanism available to do this is the Lorentz force:

$$\vec{F} = q\left(\vec{E} + \vec{v} \times \vec{B}\right) \tag{2.1}$$

and the energy gain (or change in kinetic energy) of a particle under acceleration by Lorentz force is given by:

$$\Delta W = \int \vec{F}.d\vec{s} = q \int \vec{E}.d\vec{s} + q \int (\vec{v} \times \vec{B}) d\vec{s}, \tag{2.2}$$

where $\vec{F}$ is the force, q is the charge on the particle, $\vec{v}$ is the velocity, $\vec{E}$ is the electric field, $\vec{B}$ is the magnetic field, and s is the direction of motion of the charged particle.

From these equations it clear that the electric field in the direction of motion of a particle can only increase its energy while the magnetic field perpendicular to that direction can only deflect it. Therefore, generally only electric fields are used to accelerate particles.

When the energy of a charged particle becomes higher than its rest mass energy (m_0c^2), where m_0 is the rest mass of the particle, and c is the velocity of light) it is considered relativistic and its energy is defined in terms of particle moment as:

$$\mathrm{E} = \sqrt{p^2c^2 + (m_0c^2)^2}. \tag{2.3}$$

This ratio of total energy to rest mass energy is defined as the Lorentz factor:

$$\gamma = \frac{1}{\sqrt{1-\beta^2}} = \frac{1}{\sqrt{1-\frac{v^2}{c}}} = \frac{E}{m_0c^2}. \tag{2.4}$$

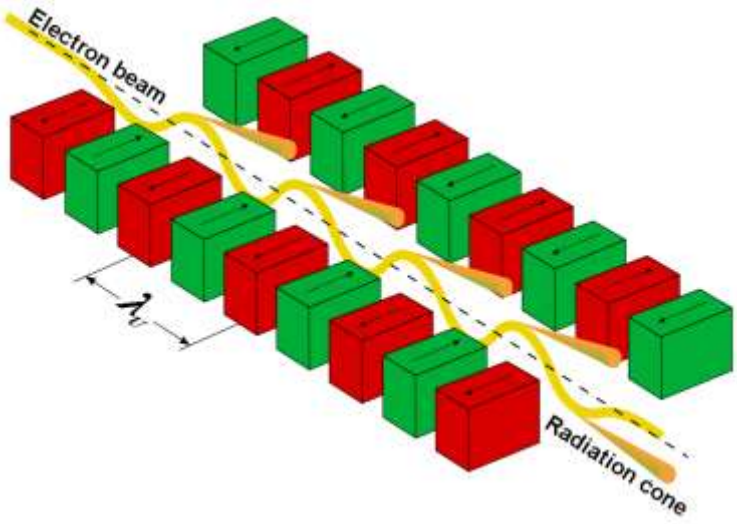


Figure 2.1: An undulator with period λ_u producing undulator radiation. [29]

When a relativistic electron passes through an undulator, in which alternating magnets are arranged to produce a sinusoidal magnetic field, it produces electromagnetic radiation of wavelength [6]:

$$\lambda_r = \frac{\lambda_u}{2\gamma^2}\left(1 + \frac{K^2}{2}\right), \tag{2.5}$$

where λ_u is the undulator period (Figure 2.1) and K is the undulator parameter. This is defined as:

$$K = \frac{\lambda_u e B_0}{2\pi m_e c} \tag{2.6}$$

with e being the electron charge, m_e is the electron rest mass, and B_0 is the amplitude of magnetic field.

As can be seen from the equation (2.5) the wavelength of undulator radiation is reliant upon the electron momentum, and the undulator period and can be tuned by varying any of these quantities.

For the high-gain FEL lasing process the requirement of beam quality parameters is very stringent. The minimum achievable wavelength is dependent on the bunch normalized transverse emittance ε_n, energy spread ΔE, peak current I_p, and the undulator parameter K [30]:

$$\lambda_{min} \propto \varepsilon_n \Delta E \sqrt{\frac{(1+\frac{K^2}{2})}{2\gamma I_P K^2}}. \tag{2.7}$$

The wavelength of the radiation has an interdependence on the electron bunch energy and its spread, the normalized emittance, and the peak current; the higher the peak current the shorter the wavelength.

Peak current is often defined as either the total charge over the FWHM of the bunch length, or as the fractional ratio which for ultrashort pulses can be similar:

$$I_p = \frac{Q}{\Delta\tau_{FWHM}}, \text{ or } I_p = \frac{dQ}{dt}. \tag{2.8}$$

However this dependence of the undulator radiation on peak current can impact the space charge forces and be detrimental to emittance. It is a trade-off of various contradictory electron bunch properties.

Furthermore, the power gain length of an undulator, the minimum undulator length in which to achieve saturation in FEL power, is given by [30]:

$$L_g \propto \frac{\varepsilon_n \gamma^{3/2}}{K\sqrt{2\mathrm{I}_p\left(1+\frac{K^2}{2}\right)}} \tag{2.9}$$

Similarly, the dependence on peak current, emittance, and bunch energy is seen and is influential in keeping undulators sufficiently short.

2.2 PHOTOINJECTORS

From the previous formulas it can be seen that high momentum, low emittance, low kinetic spread, and high peak current are all desirable factors to produce FEL radiation. To achieve these high quality factors photoinjectors are utilized.

At its most simplest a photoinjector can be modelled as a pillbox accelerating cavity in which photoelectrons are produced at the cathode via photoemission and focussed using a solenoid magnet.

Assuming a three-step Spicer photoemission model [31] in Cs_2Te (Figure 2.2) in which an electron is excited from the valance band by an absorbed UV photon at 257 nm (4.8 eV), migrates across the band gap (3.3 eV) to the cathode surface, and emits across the surface potential barrier (0.2 eV) to a final energy of 4.05 eV. This produces photoelectrons with a kinetic energy E_{kin} = 0.55 eV.

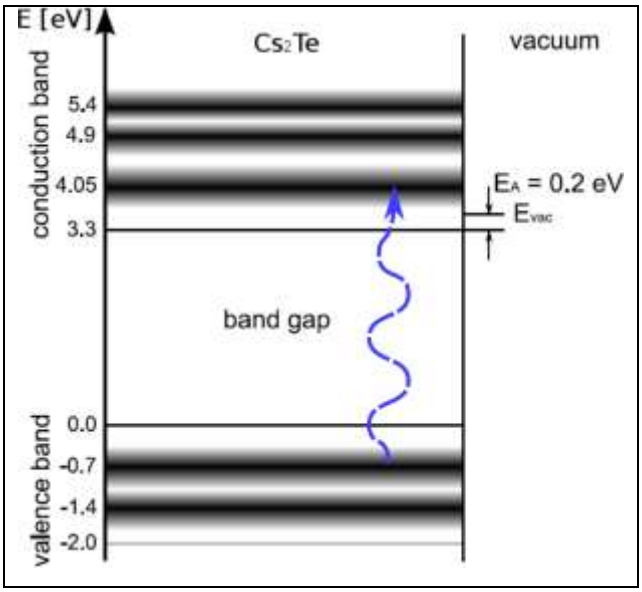


Figure 2.2: Cs_2Te band structure as determined by Powell [31].

The photocathode material is deposited onto a Molybdenum plug and is typically a layer 10s of nanometers thick [32]. This means the time required by the generated photoelectrons to migrate to the surface is very short and can be expected to produce a desirably short photocathode response time, as measured to be <0.5 ps [33]. The quantum efficiency (QE) of

such cathodes is the number of electrons generated per photon and is typically in the 5%-10% range for semiconductor materials. Contrariwise, the QE of pure metal cathodes, e.g. Cu, is typically an order of magnitude (or more) lower.

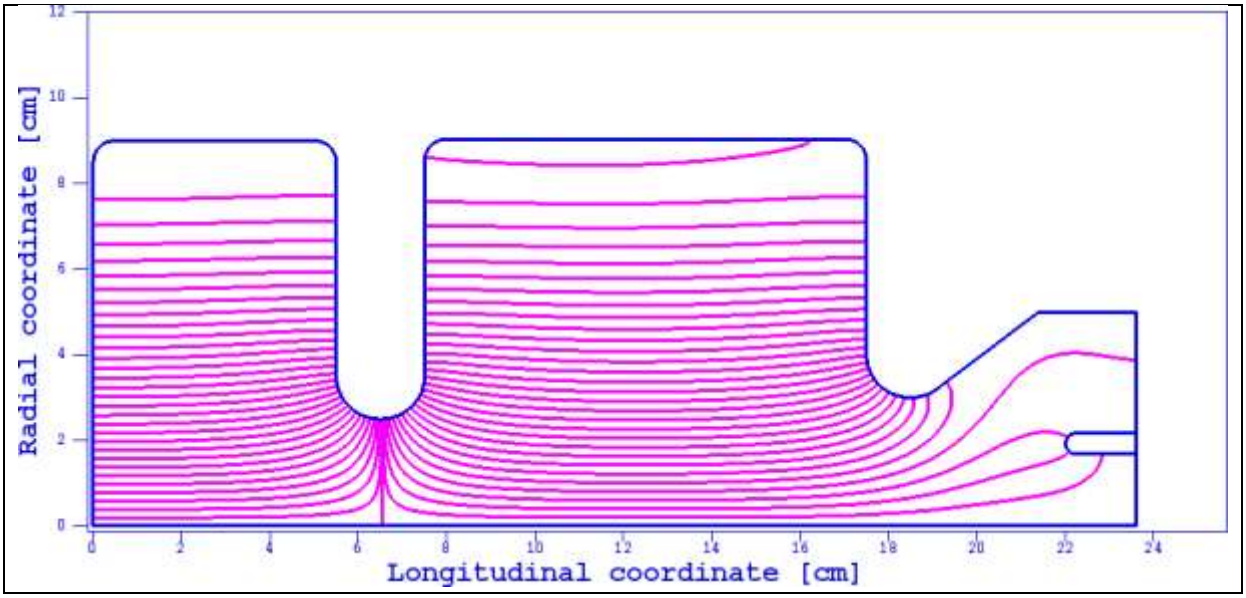


Figure 2.3: PITZ L-band 1.6 cell photocathode gun 4.6 with coaxial coupler (F = 1.3 GHz)

Although in reality the field mode of a cavity typically has a radial component and multiple cells (Figure 2.3) it is sufficient for a fundamental understanding to approximate it as the simpler, single cell pillbox resonator model without a radial dependence. A pillbox cavity operates in a standing TM010 mode with the components [34]:

$$\mathrm{E_r} = 0, \tag{2.10}$$

$$\mathrm{E_z} = E_0 J_0(k_r r)\cos(\omega t + \Phi_0), \tag{2.11}$$

$$\mathrm{H_\varphi} = -\frac{E_0}{Z_0} J_1(k_r r)\sin(\omega t + \Phi_0). \tag{2.12}$$

The lowest resonant frequency f of the cavity is one of the zeros of the Bessel function J_0 and confined by the cavity radius [35]:

$$\frac{2\pi f}{c} R = 2.4048. \tag{2.13}$$

The on-axis energy gain then becomes [36]:

$$\frac{d\gamma}{dz} = \frac{qE_0}{mc^2}\sin(\omega t + \Phi_0) \tag{2.14}$$

The electron beam is typically characterized by the 6D phase space formed by the electrons' position and angle, but for simplicity a Cartesian coordinate system {x, y, z, x', y', z'} in a right-handed orientation is adopted. The angles are given by the ratio of Cartesian component of the momentum and the total momentum. {x', y', z'} = $p_{x,y,z}/p$.

Often, they are decomposed into their respective longitudinal and transverse components and projected into their 2D trace spaces {xx'}, {yy'}, {zz'} as often only projections can be measured in experiment.

This leads to a number of important measures of beam quality as the normalized RMS emittance can then be calculated:

$$\varepsilon_{n,u} = \beta\gamma\sqrt{\langle u\rangle\langle u'^2\rangle - \langle uu'\rangle^2}, \tag{2.15}$$

where u = {x,y,z}.

This has a fundamental impact on the brightness of a single particle bunch [37] which is highly dependent on emittance (assuming no inter-dimensional coupling) and charge:

$$\mathrm{B} = \frac{Q}{\epsilon_{n,x}\epsilon_{n,y}\epsilon_{n,z}}. \tag{2.16}$$

However, the total transverse emittance arises from multiple contributions [37] from thermal emittance, spacecharge forces, and RF forces:

$$\varepsilon = \sqrt{\varepsilon_{thermal}{}^2 + \varepsilon_{spacecharge}{}^2 + \varepsilon_{RF}{}^2}, \tag{2.17}$$

where the initial thermal emittance contribution arises from the difference between the work-function of the photocathode material and the laser photon energy which produces a starting kinetic energy of the photoelectron during emission and a corresponding momentum spread and variation in emission angle.

The thermal emittance can be simply modelled with the correlation [38]:

$$\varepsilon_{thermal} \sim \sigma_{x,y}\sqrt{\langle E_k\rangle}, \tag{2.18}$$

where $\sigma_{x,y}$ is the transverse RMS beam size on the cathode and $\langle E_k\rangle$ is the average kinetic energy of the electrons emitted from the cathode.

The space-charge contribution arises from internal Coulombic forces within the bunch, while the RF contribution arises from the time-varying radial component of the accelerating electric field. The dependence on σ_z as RMS bunch length can be simply estimated by [37]:

$$\varepsilon_{RF} \sim \sigma_{x,y}^2\sigma_z^2. \tag{2.19}$$

This implies balancing the bunch length and charge between RF-induced emittance and longitudinal space-charge force components. Too long and the kinetic energy spread might be too large for a high FEL gain and the emittance is dominated by RF contributions. Too short and the bunch is space-charge dominated and blows out before it is significantly accelerated. Even shorter and you risk photonic ablation of the photocathode!

Ultimately, the space-charge contribution is dependent on the full, complex volumetric Coulombic forces within the bunch and must be numerically modelled and optimized. Fortunately, however, due to laser pulse shaping it is possible to directly access this component.

2.3 UNIFORMLY FILLED ELLIPSOIDAL DISTRIBUTIONS

For a homogenous ellipsoidal charge distributions the internal Columbic forces are linearly dependent on the internal coordinate and can be calculated analytically [39] with Poisson's equation:

$$\vec{\nabla}^2\varphi(\vec{r}) = \frac{\rho(\vec{r})}{\varepsilon_0}, \tag{2.20}$$

where $\varphi(\vec{r})$ is the electric field potential, ε_0 is the vacuum permittivity and ρ is the charge density.

For homogenous ellipsoidal distributions it is defined as:

$$\rho(\vec{r}) = \rho_0 \Theta\left\{1 - \left(\frac{x}{a}\right)^2 - \left(\frac{y}{b}\right)^2 - \left(\frac{z}{c}\right)^2\right\}, \tag{2.21}$$

where $\rho_0 = \frac{3Q}{4\pi abc}$ is the volume charge density, a, b, c being the semi-axes of the ellipsoid (Figure 2.4), and $\Theta(x) = \begin{cases} 0, if\ x < 0 \\ 1, if\ x \geq 0 \end{cases}$ is the Heaviside step function.



Figure 2.4: Ellipsoid in Cartesian coordinates with semi-axes a, b and c.

Inside the ellipsoid the electric field $\vec{E} = -\vec{\nabla}\varphi$ is a linear function of position $\vec{r} = (x, y, z)$ and given by:

$$\vec{E} = \left(E_x, E_y, E_z\right) = \frac{\rho_0}{\varepsilon_0}\left(M_x x, M_y y, M_z z\right). \tag{2.22}$$

M_x, M_y, M_z from above are the bunch form factors [40], defined as:

$$M_z = \frac{1+\Gamma}{\Gamma^3}(\Gamma - \tan^{-1}\Gamma), \tag{2.23}$$

$$M_x = M_y = \frac{1}{2}(1 - M_z), \tag{2.24}$$

$$\left(M_x + M_y + M_z = 1\right), \tag{2.25}$$

with $\Gamma \equiv \sqrt{\frac{a^2}{c^2} - 1}$ being the eccentricity of the ellipsoid.

A homogenous ellipsoid under its own field will proportionally change its dimensions but maintain its linear internal fields ($E_x \propto x, E_y \propto y, E_z \propto z$). Consequently, the velocities (momenta) of electrons remain linear functions of positon. Integrating the equation along its longitudinal axis obtains the surface charge density profile:

$$\sigma(x, y) = 2\rho_0 c\sqrt{1 - \left(\frac{x}{a}\right)^2 - \left(\frac{y}{b}\right)^2}. \tag{2.26}$$

Integrating along a coordinate produces a parabolic line density profile(s):

$$\Lambda(x) = \rho_0 \pi bc\left(1 - \frac{x^2}{a^2}\right), \tag{2.27}$$

$$\Lambda(y) = \rho_0 \pi ac\left(1 - \frac{y}{b^2}\right), \tag{2.28}$$

$$\Lambda(z) = \rho_0 \pi ab\left(1 - \frac{z}{c^2}\right). \tag{2.29}$$

The linear charge density in all dimensions is an inverted parabola for the ellipsoid profile with final integration of the line profile returns the charge of the ellipsoid which is the charge density multiplied by the volume of the ellipsoid:

$$Q = \rho_0 \frac{4}{3} \pi abc. \tag{2.30}$$

2.4 SPACE CHARGE FORCES

The electrostatic field of a charged relativistic bunch moving at a constant velocity, and therefore no energy spread, a "cold" beam, undergoes lateral field confinement due to Lorentz contraction. The modified field equations are [41]:

$$E_r(\mathrm{z}=0) = \frac{\mathrm{q}}{4\pi\varepsilon_0}\frac{\gamma}{r^2}, \tag{2.31}$$

$$B_\Phi(\mathrm{z}=0) = \frac{\mathrm{q}\beta}{4\pi\varepsilon_0 c}\frac{\gamma}{r^2}, \tag{2.32}$$

$$E_z(\mathrm{r}=0) = \frac{\mathrm{q}}{4\pi\varepsilon_0}\frac{1}{\gamma^2 z^2}. \tag{2.33}$$

It can be seen from the latter equation that the longitudinal electric field disappears as $1/\gamma^2$. However the transverse fields produce a Lorentz force on a transverse test charge:

$$F_r = \mathrm{q}(E_r - \beta c B_\Phi) = \frac{\mathrm{q}^2}{4\pi\varepsilon_0\gamma}\frac{1}{r^2}, \tag{2.34}$$

which again vanishes, albeit at a slower rate of $1/\gamma$.

Presupposing a relativistic homogenous cylinder of charge with a radius a, and a longitudinal charge distribution of λ_0, it can be found that the internal space charge forces are given by [41]:

$$F_r(\mathrm{r}) = \mathrm{q}(E_r - \beta c B_\Phi) = \frac{q}{\gamma^2}\frac{\lambda_0}{2\pi\varepsilon_0}\frac{r}{a^2}. \tag{2.35}$$

The transversal space charge force for a cylindrical bunch becomes linear and disappears as $1/\gamma^2$. Furthermore, considering an ellipsoidal bunch as a series of short, radially varying cylindrical bunches the same conclusion can be drawn.

Contrariwise, the internal space charge forces of a Gaussian bunch of charge Q is non-linear and (quasi-)continuous and given as [41]:

$$F_r(\mathrm{r},\mathrm{z}) = \mathrm{q}(1-\beta^2)E_r = \frac{q}{2\pi\varepsilon_0\gamma^2}\frac{Q}{\sqrt{2\pi}\sigma_z} e^{-\frac{z^2}{2\sigma_z{}^2}} \left(\frac{1 - e^{-\frac{r^2}{2\sigma_r{}^2}}}{r} \right). \tag{2.36}$$

It can be seen from these equations (plotted in Figure 2.5) that the conventional Gaussian distribution is non-linear, and that cylindrical and ellipsoidal distributions are linear (in the static case without energy spread).

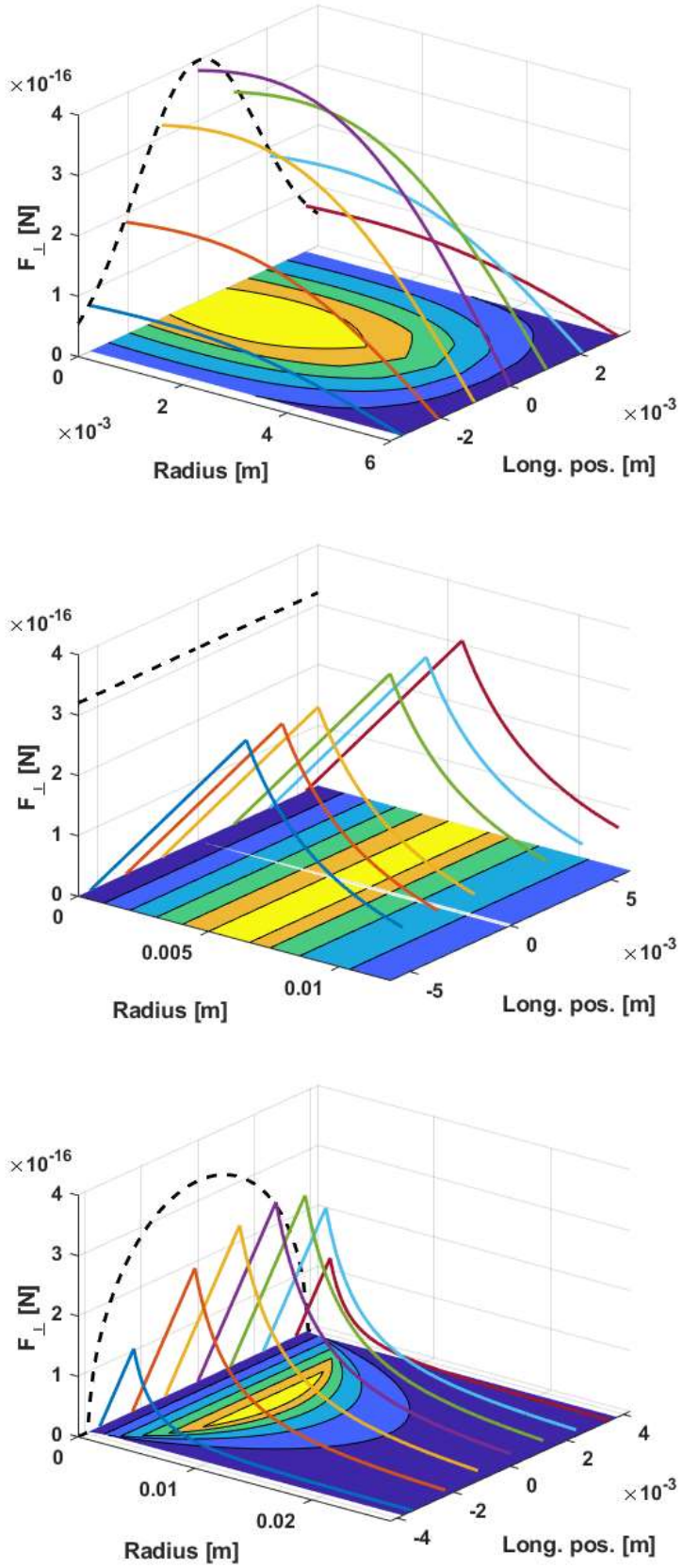


Figure 2.5: Transversal space-charge forces for Gaussian (top), cylindrical (middle), ellipsoidal (bottom) bunches with 1 nC charge and σ_r=3 mm, σ_l = 1.7 mm.

In conclusion, it can be summarized that the parameters of FEL production are highly dependent on bunch properties, particularly momentum, charge, and emittance. Furthermore, it can be seen how homogenization of the space charge density within the bunch linearizes the space charge forces, with an ellipsoid completely linearizing the forces in all dimensions.

Owing to the linear energy response of typical photocathode materials it can be expected, by first approximation, that an ellipsoidal laser pulse would produce a quasi-ellipsoidal electron bunch and that with further feedback and refinement of the laser pulse that the desirable electron bunch properties of an ellipsoidal can be taken advantage of. This then drives a demand for flexible volumetric laser pulse shaping.

2.5 OPTICAL THEORY

The field of direct optical pulse shaping in the frequency domain is not a new one. It was demonstrated by Colombeau, Vampouille and Froehly in 1976 [42] in which they demonstrated Fourier filtering with physical masks, and later repeated in a 4f-line for ps-pulses [11]. Their work was later explored by Weiner utilizing photolithographic masks (1993) [43] and expounded upon by Wefers and Nelson utilizing SLM-based masks [44] and introducing the general mathematical formalism in 1995 [45].

As this work is based upon the same techniques much of the mathematical theory can be borrowed from literature.

The Fourier transform (FT) is a mathematical tool that decomposes a signal (temporal, spatial) into its frequency components. This permits spectral analysis and manipulation of a function which can often be mathematically trivial in comparison to its real complement. For example, the notes (and harmonics) in a melody such as Twinkle Twinkle Little Star can be easily visualized (Figure 2.6).

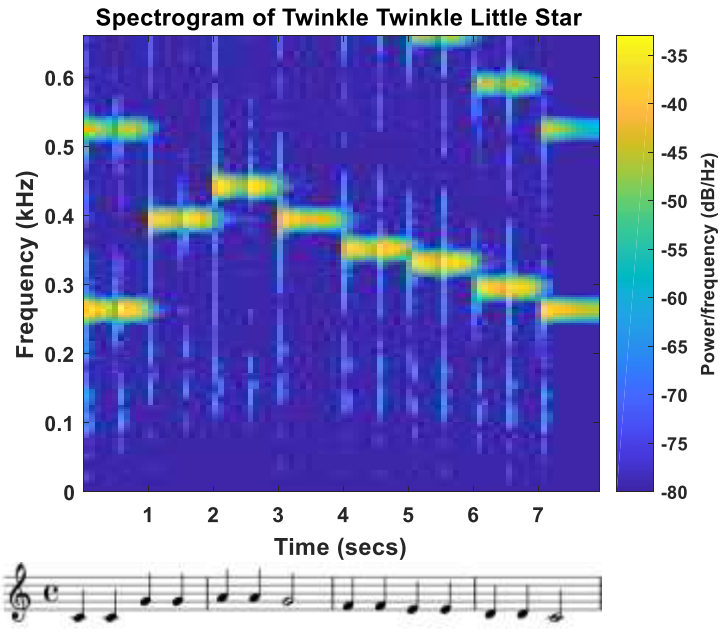


Figure 2.6: The first four bars and spectrogram (with harmonics) of Twinkle Twinkle Little Star [46].

Given that the electromagnetic properties of light; frequency (f), angular frequency (ω), and wavelength (λ), are fundamentally interconnected by very simple relations:

$$2\pi \frac{c}{\lambda}\Big|_{1030\ nm} = 2\pi f = \omega = 1.83\ PHz, \tag{2.37}$$

it can be seen that Fourier transform is an applicable tool for analysis and characterization of light at a fundamental level. Conveniently enough the Fourier transform of a Gaussian distribution is itself another Gaussian distribution:

$$f(t) = e^{-at^2}, \tag{2.38}$$

$$f(\omega) = \sqrt{\frac{1}{2a}} e^{-\frac{\omega^2}{4a}}. \tag{2.39}$$

This leads to the *transform limited pulse* and the (FWHM) *Time-Bandwidth product* (TBP) of the intensity [47]:

$$\Delta t \Delta\omega \geq 4 \ln 2, \tag{2.40}$$

which describes the fundamental relationship between, and limitations of, a pulse's spectrum and duration.

Therefore, it is very convenient to consider a laser pulse in the Fourier domain as all of its temporal characteristics arise from the complex spectral components of its electric field, where S(ω) is the spectral amplitude and φ(ω) is the spectral phase:

$$\tilde{\varepsilon}(\omega) = S(\omega) e^{-j\varphi(\omega)}. \tag{2.41}$$

The Fourier transform of the complex spectrum into the temporal domain of the electric field is given by:

$$\varepsilon(t) = \frac{1}{2\pi} \int \tilde{\varepsilon}(\omega) e^{j\omega t} d\omega, \tag{2.42}$$

Which is then linked to the optical intensity I(t) by:

$$I(t) = \varepsilon(t)\varepsilon^*(t) = |\varepsilon(t)|^2. \tag{2.43}$$

As a simple example (Figure 2.7) the spectrum of a Gaussian laser pulse can be constructed from the TBP and used to generate the Fourier transform-limited pulse with all the components in phase (φ(ω) = 0).

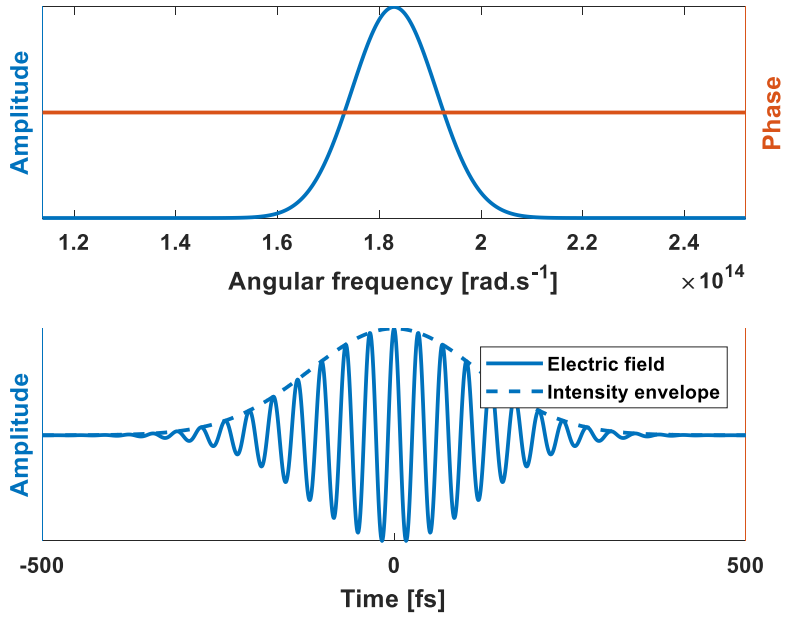


Figure 2.7: A Fourier transform-limited 200 fs FWHM 10 μm pulse of uniform spectral phase.

It is then quite intuitive that it is simpler to modify an ultrashort laser pulse by considering and manipulating its complex spectrum by some arbitrary function $\tilde{N}(\omega)$ rather than by attempting to directly modulate the pulse temporally:

$$\tilde{\varepsilon}_{out}(\omega) = \tilde{N}(\omega)\tilde{\varepsilon}_{in}(\omega). \tag{2.44}$$

This approach also simplifies modelling of higher-order dispersion effects in bulk material such as Group Velocity Dispersion (GVD) and Third Order Dispersion (TOD). These effects arise out of the higher order terms of the Taylor expansion of the phase term $\varphi(\omega)$:

$$\varphi(\omega) = \varphi_0 + \varphi_1(\omega - \omega_0) + \varphi_2\frac{(\omega-\omega_0)^2}{2} + \varphi_3\frac{(\omega-\omega_0)^3}{6} + \cdots \varphi_n\frac{(\omega-\omega_0)^n}{n!}, \tag{2.45}$$

- φ_0 describes of absolute phase, or Carrier Envelope Phase (CEP), and is significant for few-cycle ultrashort pulses.
- φ_1 is the relative delay of the pulse with respect to some arbitrary point in time, typically given in fs.
- φ_2 is the most significant term as it describes GVD or 'chirp'. This can account for spectral broadening of a pulse owing to the difference in refractive index for the various components where it is typically given in $fs^2.mm^{-1}$ [48].
- φ_3 is TOD, Typically given in $fs^3.mm^{-1}$ [48].

Therefore, GVD-induced chirp and the respective pulse length for an arbitrary pulse can be determined by setting $\tilde{N}(\omega)$:

$$\tilde{N}(\omega) = e^{-j\varphi_2\frac{(\omega-\omega_0)^2}{2}}. \tag{2.46}$$

For a Gaussian pulse of spectral amplitude A_ω and FWHM spectral width $\Delta\omega$ this results in a quadratic phase chirp:

$$\tilde{\varepsilon}_{out}(\omega) = A_\omega e^{-\ln(2)\left(\frac{2(\omega-\omega_0)}{\Delta\omega}\right)^2} e^{-j\varphi_2\frac{(\omega-\omega_0)^2}{2}}. \tag{2.47}$$

By taking the Fourier transform of the chirped Gaussian spectrum and equating the resulting optical intensity to the general form of a Gaussian pulse the dependency of the resulting pulse length on GVD can be determined:

$$\Delta t_{out}(\varphi_2) = \Delta t_{in}\sqrt{1+\left(\frac{4\ln(2)\varphi_2}{{\Delta t_{in}}^2}\right)^2}. \tag{2.48}$$

This can be rearranged to produce the required chirp for a given stretch factor:

$$\varphi_2 = \frac{1}{4\ln(2)}\sqrt{{\Delta t_{in}}^2{\Delta t_{out}}^2 - {\Delta t_{in}}^4}. \tag{2.49}$$

This has relevance for the actual implementation of a pulse shaped laser as ultrashort laser pulses are used to self-characterize the longer chirped pulses used to generate photoelectrons.

It should also be considered that the arbitrary function $\tilde{N}(\omega)$ can also be a *spectral amplitude mask*. So, with this knowledge in mind how can the spectral (Fourier) plane of the laser pulses be manipulated? The solution is a simple 4f-line (Figure 2.8) with gratings, lenses, and a Spatial Light Modulator (SLM) acting as a potential amplitude-phase mask at the Fourier plane.

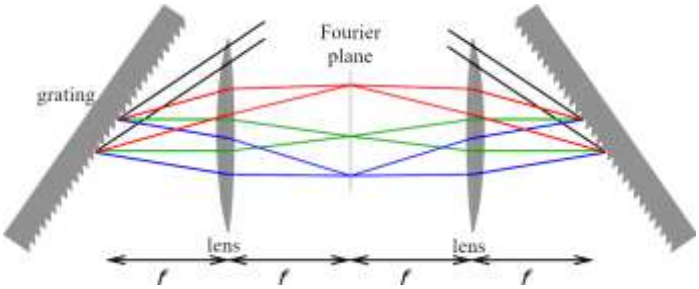


Figure 2.8: A basic 4f-line utilizing identical grating-lens pairs at equal focal length separations.

For a 4f-line with lenses of focal length f, gratings with periodicity ν (or groove separation d), and wavelength λ, the standard formulas are as follows.

The diffracted order from a grating is given by the formula:

$$\sin\theta_i - \sin\theta_d = \frac{m\lambda}{d} = m\lambda\nu. \tag{2.50}$$

where $\theta_i$is the incident angle on the grating, θ_d is the diffracted angle, and m is diffraction order. With this simple formula, and some basic geometry, the physical offset of each component from the central wavelength on the SLM can be determined by:

$$x(\lambda) = f\tan\left(\frac{\Delta\lambda}{d\cos\theta_d}\right). \tag{2.51}$$

Or in terms of angular frequency [45]:

$$x(\omega) = \frac{-2\pi cf}{{\omega_0}^2 d\cos[\theta_d(\omega_0)]}(\omega-\omega_0) \equiv \alpha(\omega-\omega_0). \tag{2.52}$$

Of course, as the SLM is a discrete device, and each spectral component has a diffraction-limited spot size, it can be instructive to know the finite size of each component. This is derived from Gaussian beam propagation to be [25]:

$$\Delta x_0 = 2\ln(2)\frac{\cos\theta_i}{\cos\theta_d}\frac{f\lambda_0}{\pi W_0\sqrt{2\ln(2)}}, \tag{2.53}$$

with W_0 being the waist of the input beam at the entrance of the 4f-line.

With these formulas it is easy to model the effects of spectral masking on a laser pulse envelope and to design a 4f-line of any spectral field width. However, it becomes apparent that a broadband laser source has many advantages; the 4f-line setup is smaller, and in practical implementation has reduced losses at the gratings. For a chirped pulse this offers greater flexibility with regards with spectral shaping due to the reduction of interdependence of the spectral components.

Furthermore, the short laser pulses can be sampled prior to stretching and used for self-characterization of a stretched pulse. Of course, these benefits do not come for free as the broadband pulse complicates the harmonic conversion process.

With this in mind the effects of spectral masking on chirped and unchirped pulses becomes trivial to model, and the advantages and disadvantages can be explored.

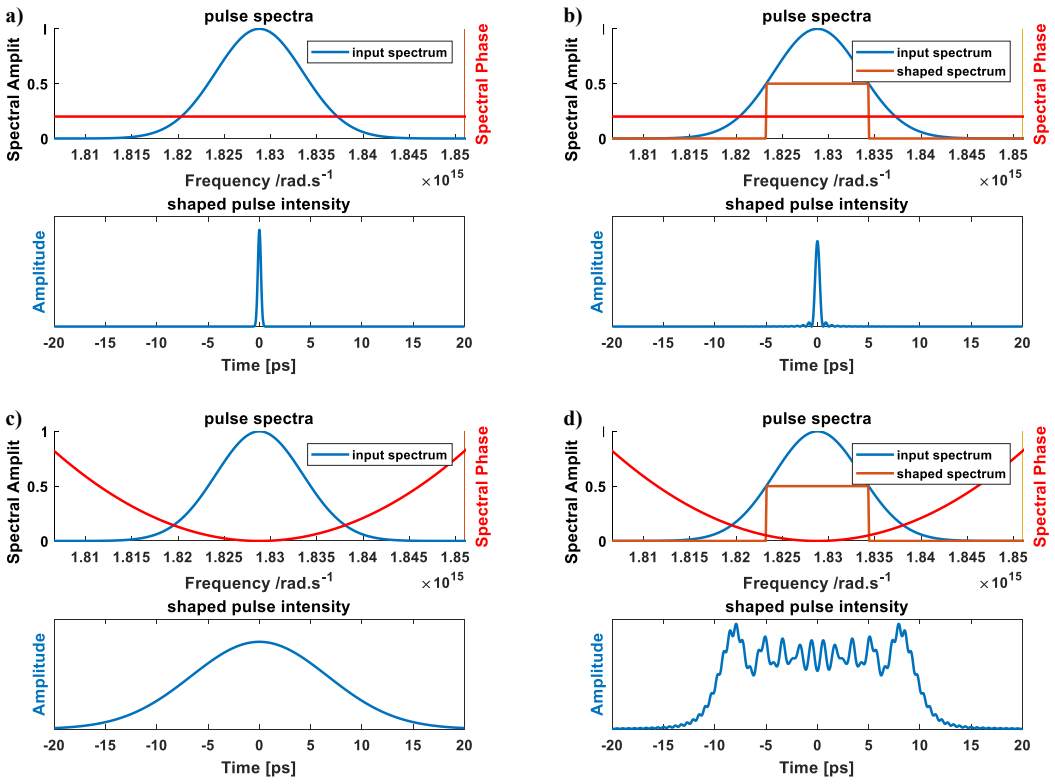


Figure 2.9: Output pulse profiles utilizing spectral amplitude masking. a) unshaped, unchirped pulse. b) unchirped pulse with flattop spectral amplitude mask. c) unshaped, chirped pulse. d) chirped pulse with flattop spectral amplitude mask.

As can be seen from basic masking on the Fourier plane (Figure 2.9), a flat-top spectral distribution produces a sinc response in the temporal domain (2.9b) for an unchirped pulse; as is expected from the Fourier transform. However, even a basic flat-top amplitude mask when applied to a chirped pulse (2.9c) approximates a flat-top laser pulse envelope(2.9d). This is the basis of a 4f-line with an SLM at the Fourier plane. However, in practical implementation an SLM can only control either phase or amplitude, so an SLM and complementary Fourier plane is required for each amplitude and phase mask.

2.6 SPATIAL LIGHT MODULATORS (SLMS)

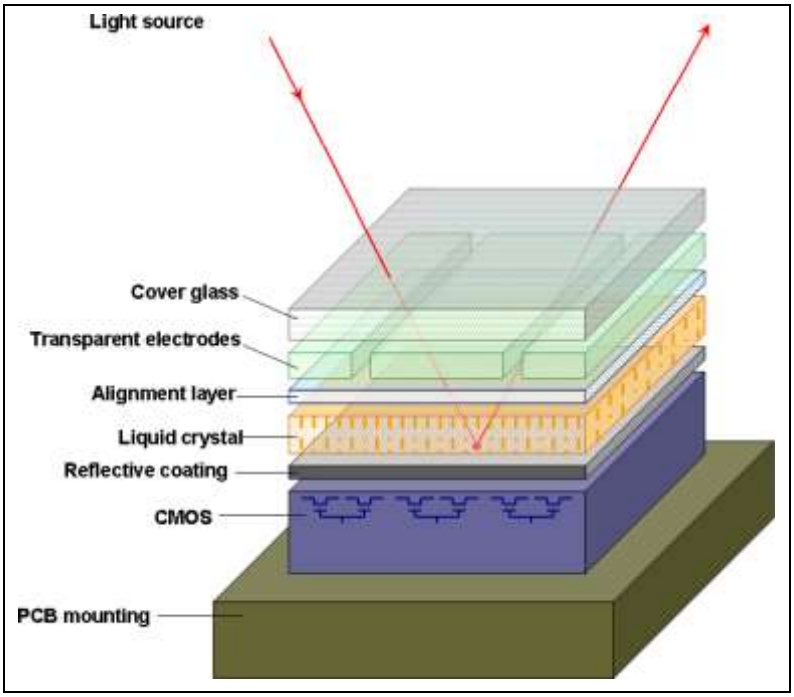


Figure 2.10: A cross-section of an SLM chip [49].

Spatial Light Modulators are based on liquid crystal technology and have progressed in leaps and bounds in parallel with advances in consumer lithographic and display technology [50].

An SLM is, in practicality, an individually programmable matrix of phase retarders. Specifically, the Holoeye Pluto NIR [51] and Hamamatsu LCOS x10468 SLMs [52] utilized in this work are based on nematic liquid-crystal-on-silicon (LCOS) technology. A layer of nematic liquid crystal is deposited on an addressable silicon substrate, with a transmissive electrode (Indium tin oxide) and glass layer covering (Figure 2.10). An electric field is then applied to re-orientate the crystals along the electric field direction and induce a refractive index change, and by extension a phase shift based on the standard phase retardation formula [53]:

$$\Gamma = 2\pi\Delta n \frac{l}{\lambda}, \tag{2.54}$$

where Δn is the induced refractive index change and l is the optical path length.

Practically, the wavelength-dependent phase range realized in these devices is typically $>2\pi$ across the designed wavelength range with an 8-bit addressable element space. This reduces the phase resolution but leaves provision for a full cycle phase shift across the spectrum.

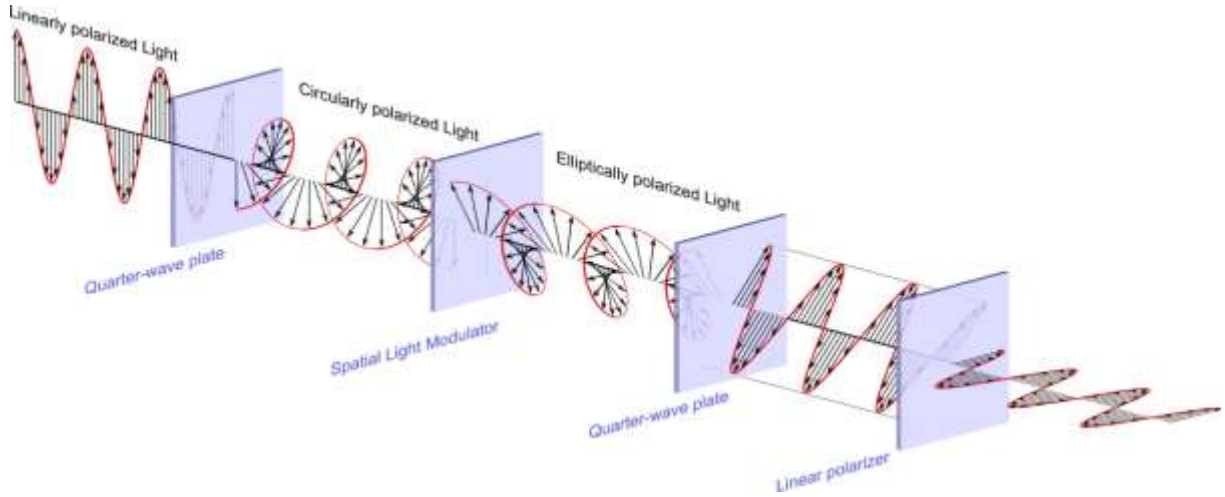


Figure 2.11: The principle of phase modulation used as amplitude modulation.

An intuitive method to produce an amplitude mask out of a phase retarding SLM is to create circularly polarized light by passing linearly polarized light through a λ/4 waveplate and modulate its ellipticity with the SLM. Then restore the linear polarization by means of another λ/4 waveplate. This effectively converts the SLM into a polarization rotator. When coupled with a linear polarizer the SLM becomes an amplitude mask (Figure 2.11). This is easily demonstrated with Jones formalism [53]. For polarized light rotated by β from some arbitrary angle θ the polarization rotation matrix is then:

$$M(\beta)\begin{bmatrix}\cos\theta\\ \sin\theta\end{bmatrix}=\begin{bmatrix}\cos(\theta+\beta)\\ \sin(\theta+\beta)\end{bmatrix}. \tag{2.55}$$

From the trigometric identities:

$$\cos(\alpha+\beta)=\cos\alpha\cos\beta-\sin\alpha\sin\beta, \tag{2.56}$$

$$\sin(\alpha+\beta)=\sin\alpha\cos\beta+\cos\alpha\sin\beta, \tag{2.57}$$

M is then the polarization rotation matrix:

$$M(\beta)=\begin{bmatrix}\cos\beta & -\sin\beta\\ \sin\beta & \cos\beta\end{bmatrix}. \tag{2.58}$$

Similarly, the Jones matrices for the optical layout should also simplify to this result. The matrix for a λ/4 waveplate at some angle θ is:

$$M_{\frac{\lambda}{4}}(\theta)=e^{-i\pi/4}\begin{bmatrix}\cos^2\theta+i\sin^2\theta & (1-i)\sin\theta\cos\theta\\ (1-i)\sin\theta\cos\theta & \sin^2\theta+i\cos^2\theta\end{bmatrix}. \tag{2.59}$$

And the matrix for an arbitrary birefringent linear phase retarder Γ of 2π range (SLM):

$$M_{SLM}(\theta)=e^{-i\Gamma/2}\begin{bmatrix}\cos^2\theta+e^{i\Gamma}\sin^2\theta & \left(1-e^{i\Gamma}\right)\cos\theta\sin\theta\\ \left(1-e^{i\Gamma}\right)\cos\theta\sin\theta & \sin^2\theta+e^{i\Gamma}\cos^2\theta\end{bmatrix}. \tag{2.60}$$

Simplifying the sequential matrices of the optical system:

$$M_{\frac{\lambda}{4}}(\theta\mp\pi/4)\cdot M_{SLM}(\theta\pm n)\cdot M_{\frac{\lambda}{4}}(\theta\pm\pi/4), where\ n=\left\{0,\frac{\pi}{2},\pi,\dots\right\}, \tag{2.61}$$

returns the polarization rotation matrix as a function of phase retardation of the SLM:

$$M(\beta)=M(\Gamma)=\begin{bmatrix}\cos\frac{\Gamma}{2} & -\sin\frac{\Gamma}{2}\\ \sin\frac{\Gamma}{2} & \cos\frac{\Gamma}{2}\end{bmatrix}. \tag{2.62}$$

Assuming a polarized input beam and polarizer it is rudimentary to find the expected intensity function and to plot it (Figure 2.12):

$$I(\Gamma) = \cos^2 \frac{\Gamma}{2}. \tag{2.63}$$

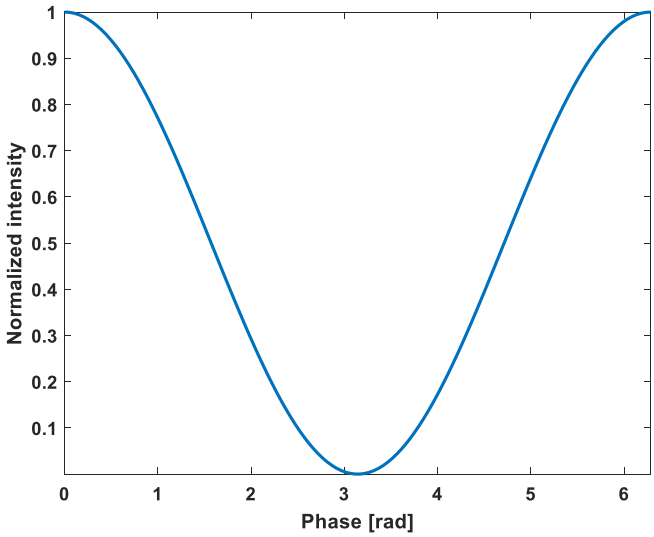


Figure 2.12: SLM transmission plot for linearly polarized light over a 2π phase range.

So, by chaining two 4f-lines in series, or by using a 4f relay within the 4f-line (Figure 2.13), both the amplitude and the phase of the spectral components of a laser pulse can be manipulated.

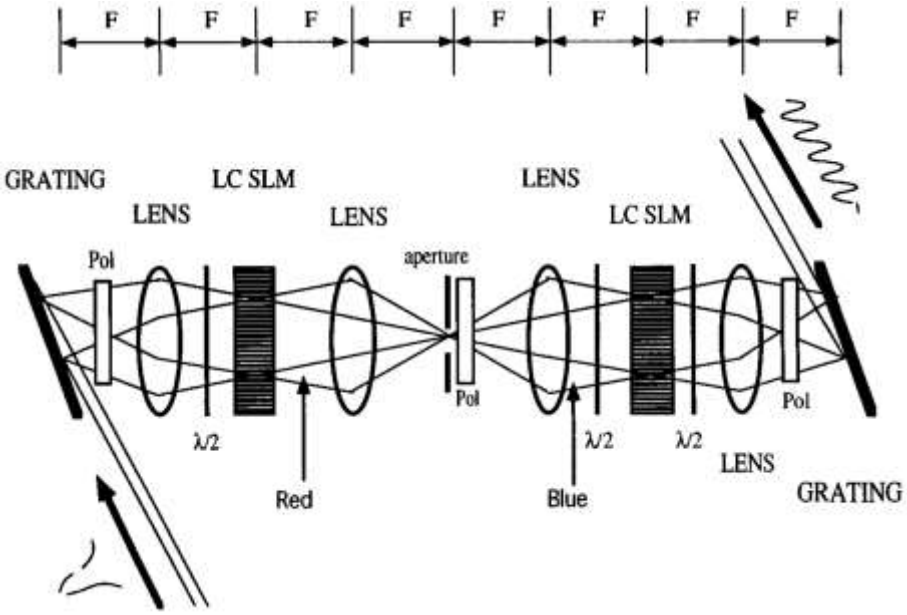


Figure 2.13: Two SLMs in a 8-F configuration [45]. The first SLM acts as an amplitude mask, and the second SLM acts as a phase mask.

2.7 IMAGING SCHEME

The base shaping scheme is, at its heart, based upon an imaging system. This permits generation, and conservation, of spatial information through the system- the fundamental premise of spatio-temporal shaping. The generalized 2x2 ABCD ray matrix for the optical system (Figure 2.14) is given by:

$$\begin{bmatrix} x_{out} \\ \theta_{out} \end{bmatrix} = \begin{bmatrix} A & B \\ C & D \end{bmatrix} \begin{bmatrix} x_{in} \\ \theta_{in} \end{bmatrix}, \tag{2.64}$$

$$X_{out} = Ax_{in} + B\theta_{in}, \tag{2.65}$$

$$\theta_{out} = Cx_{in} + D\theta_{in},$$

which must meet the criteria where the angular and spatial optical properties are conserved:

$$A = \frac{x_{out}}{x_{in}}\Big|_{B=0}, \tag{2.66}$$

$$D = \frac{\theta_{out}}{\theta_{in}}\Big|_{C=0}. \tag{2.67}$$

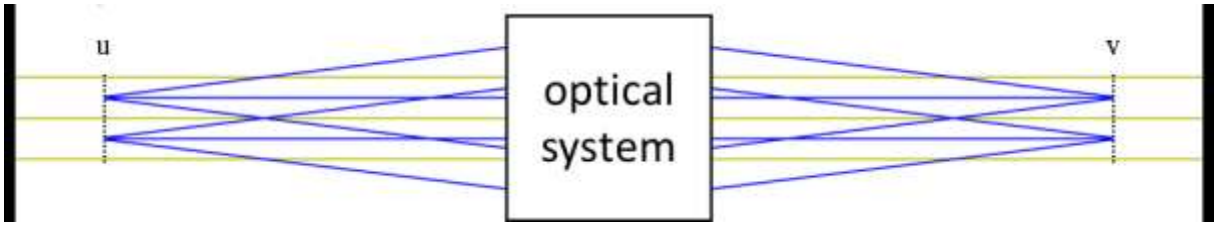


Figure 2.14: A generalized "blackbox" optical system meeting the ABCD imaging criteria with image u, and object v, planes.

This condition can be met for an n-element telescopic system, the simplest of which is the 2-element Keplerian 4f system (Figure 2.15) in which two convex lenses are separated by the sum of their focal lengths.

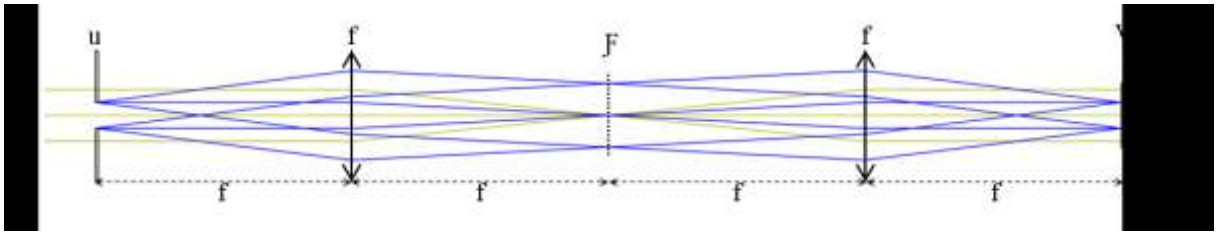


Figure 2.15: A basic 4f Keplerian imaging telescope where u and v are the object and image planes, and Ƒ is the intermediate Fourier plane.

The collimated rays are conserved and the point emitters at the entrance focal plane are retransmitted to an equivalent focal plane at the exit of the system. In this manner a number of imaging systems may be daisy-chained to maintain and relay the modified beam structure from start to finish.

By cropping a Gaussian distribution with a pinhole a reference object plane is created at the beginning of the optical system and and a pseudo-flattop distribution (Figure 2.16) is produced in the far-field by Fraunhofer diffraction [54]. This is owing to the finite bandwidth of the optical system limiting transport of the diffraction pattern.

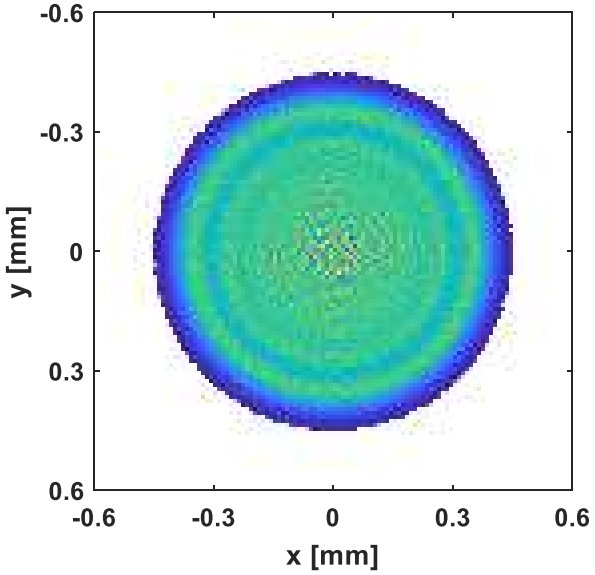


Figure 2.16: A pseudo-flattop transverse distribution produced by diffraction of an aperture.

To illustrate, by 1st order approximation the previous spectral mask (Figure 2.9d) could be passed through an aperture to produce a very basic quasi-cylindrical pulse (Figure 2.17).

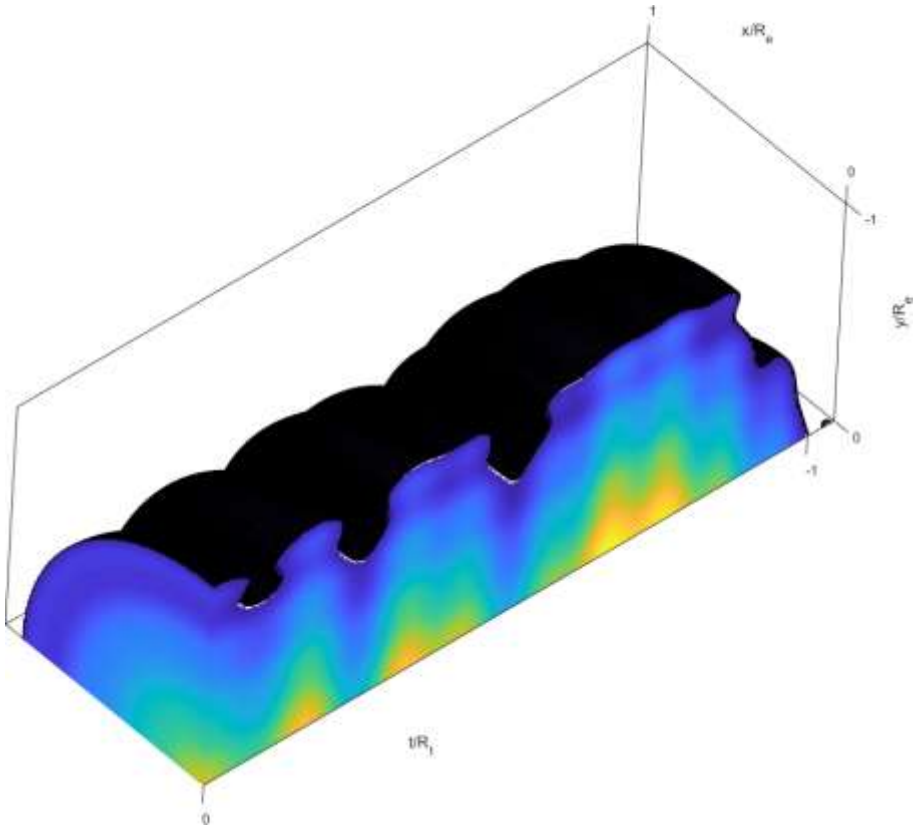


Figure 2.17: A quadrant cut of a chirped Gaussian beam that has been spectrally modulated and cropped by an aperture to produce a quasi-cylindrical pulse.

Although, this is far from ideal as the basic 8f-line design with spherical lenses only accounts for temporal shaping in the spectral domain. In order to achieve full volumetric shaping at the Fourier plane a more elaborate scheme must be considered. By merging the dispersive 8f scheme of the spectral shaper (Figure 2.13) with the image relay scheme of a

reference object plane (Figure 2.15) a spatio-temporal shaper that shapes across the transverse projection of the laser pulse can be produced. This involves replacing the first and last lens in the 8f-line with cylindrical lenses.

The first set of cylindrical lenses introduces asymmetry into the system by offsetting the transversal image planes, however this image plane is confined within the line focus of the beam which in turn is spatially modulated along the other transversal axis. By repeating the operation in the orthogonal plane with another set of cylindrical lenses in another 8f line the second transverse axis can be accessed and the decoupled image planes can be reconsolidated. Practically, this can be achieved by optically rotating the beam 90°around its propagation axis rather than construct an 8f-line in the orthogonal direction.

This allows the SLMs in a single 8f-line to access both the spectral components of the input laser distribution and one of the transverse components simultaneously. Then, by either passing it through two 8f-lines, or with rotation and passing the pulse back through the same shaper, can 3D shaping be achieved. As a double-pass, or double 8f-line, is required in orthogonal directions to prevent decoupling of the transverse image planes each setup affects a rectangular transverse profile. In order to achieve a rotationally symmetric transverse profile more and more setups are required to bring the profile from a square, to an octagon, to a dodecagon, and so forth. The number of sides increases as a function of 4^n setups. This of course comes at a cost of additional laser intensity and complexity.

However, this is for the IR Gaussian pulse, and the photoemission process of Cs_2Te requires UV pulses. Therefore, non-linear frequency conversion must also be considered.

2.8 FREQUENCY CONVERSION

Finally, the conversion of the pulse into its fourth harmonic via double harmonic conversion is to be discussed, the details of which are well known of in literature [48] [55]. Non-linear frequency conversion arises out of the relation between dielectric polarization (**P**) and an electric field (**E**):

$$P = \epsilon_0 \chi E, \tag{2.68}$$

where ϵ_0 is the vacuum permittivity, and χ is the susceptibility.

It is instructive is expand P into a power series as it is the 2nd term that is of interest:

$$P = \epsilon_0 \left[\chi^{(1)} E + \chi^{(2)} E^2 + \chi^{(3)} E^3 + \cdots \right]. \tag{2.69}$$

Here it can be seen that all second-order $\chi^{(2)}$, non-linear effects are dependent on E^2 or more-commonly the intensity [48]:

$$I = \frac{c\epsilon_0 n}{2} |E^2| \rightarrow \mathrm{I} \propto |E^2|. \tag{2.70}$$

where c is the speed of light, and n is the refractive index.

Of the mechanisms that arise out of this term the one primarily of interest is Sum Frequency Generation (SFG) where two photons combine to produce the sum:

$$\omega_3 = \omega_1 + \omega_2, \tag{2.71}$$

which in this case of Sum Harmonic Generation (SHG) or harmonic cross-correlation:

$$\omega_1 = \omega_2 \rightarrow \omega_3 = 2\omega_1, \tag{2.72}$$

The counterpoint to this is Difference Frequency Generation (DFG) which is significant for non-harmonic cross-correlation, where the result is the difference of the waves:

$$\omega_3 = \omega_1 - \omega_2. \tag{2.73}$$

For any non-linear effect there are two principle criteria that must be met to satisfy phase matching: the electric fields of the fundamental and harmonic laser pulses stay in phase and sum of the wave vectors (Figure 2.18) must match:

$$\vec{k}_3 = \vec{k}_1 + \vec{k}_2, \tag{2.74}$$

or, more simply for scalar collinear matching:

$$\omega_3 n_3 = \omega_1 n_1 + \omega_2 n_2, \tag{2.75}$$

where n_i is the respective refractive index of the wave.

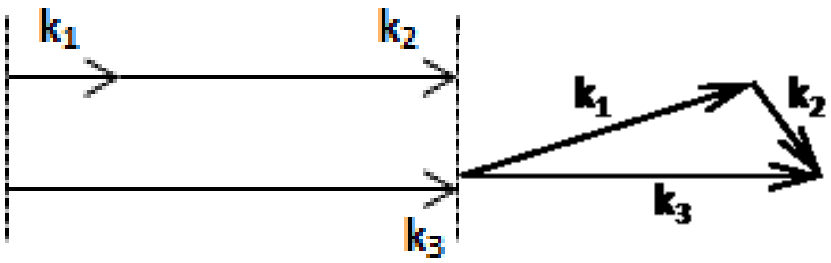


Figure 2.18: Collinear (scalar) phase matching (left) and vector phase matching (right).

Therefore, for SHG the refractive indices of the fundamental and harmonic pulses must be the same:

$$n(2\omega_1) = n(\omega_1). \tag{2.76}$$

To achieve this a non-isotropic optical material with a polarization-dependent refractive index and a large $\chi^{(2)}$ coefficient is utilized, either with a single optical axis (uniaxial) or two different optical axes (biaxial). By naming convention, the polarization perpendicular to the optical axis (O.A.) is coined "ordinary" with a refractive index of n_o, while the light parallel to the axis is "extraordinary" with a refractive index of n_e.

In the case of non-critical phase matching where the fundamental components have the same ordinary polarization combine to produce the harmonic with an extraordinary polarization in a negative-uniaxial crystal where $n_e(\omega) < n_o(\omega)$:

$$n_e(2\omega_1) = n_o(\omega_1), \ [oo \rightarrow e]. \tag{2.77}$$

A simple example of this is Lithium Niobate ($LiNbO_3$), a manmade negative uniaxial crystal whose refractive indices can meet the phase-matching conditions for SHG of 1064 nm [56] when the wave vector is normal ($\theta = 90°$) to the crystal axis (Figure 2.19).

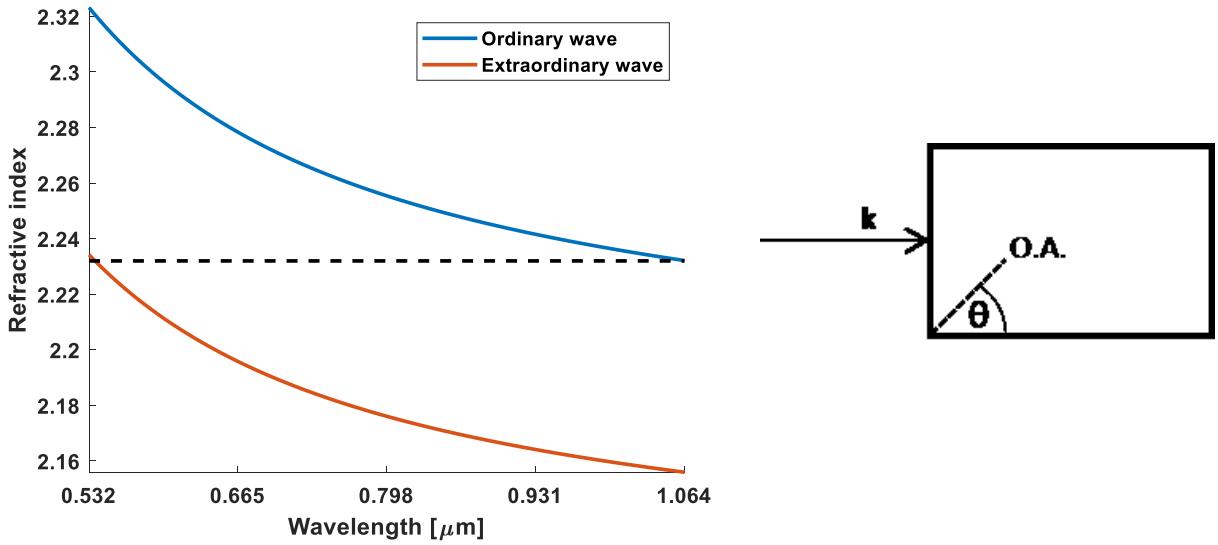


Figure 2.19: Refractive indices of $LiNb0_3$ for non-critical phase-matching of 1.064 μm for SHG at room temperature (left), where $\Delta n = 0.002 \rightarrow \Delta k = \sim 4(2\pi)/mm$. Wavevector normal to the crystal face (right).

For broadband, ultrashort pulses a number of issues arise in the non-linear conversion process. Phase matching is particularly arduous due to potential phase velocity mismatch and group velocity mismatch owing to the different refractive indices of all of the spectral components. This effectively limits the conversion bandwidth and efficiency in a standard collinear setup. For a chirped pulse this results in inconsistent conversion efficiency along the pulse duration leading to attenuation of the head and tail of the generated harmonic pulse.

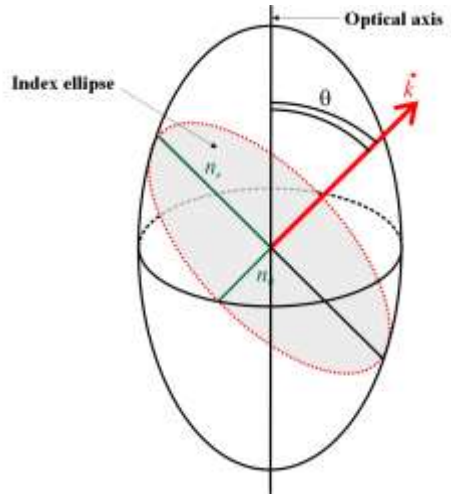


Figure 2.20: Index ellipsoid for a positive uniaxial crystal ($n_z > n_x = n_y$)

Furthermore, as conversion is an intensity-sensitive process a number of tradeoffs must be made. The pulse size should be minimized to maximize intensity but not sufficiently so to induce thermal changes or damage to the crystal. The crystal, and its optical axis, must be chosen (Figure 2.20) to maximize the effective non-linear coefficient (d_{eff}), the coefficient used for quantifying the strength of the nonlinear interaction, while maintaining the phase matching conditions which typically results in a non-orthogonal axis. This results in birefringent walk-off and lateral smearing (spatial chirp) of the pulse as it propagates through the crystal.

Due to its low thermal sensitivity, high effective non-linear coefficient, and small walkoff (Table 2.1) Lithium Triborate (LBO) was chosen for the first SHG stage of 1030 nm → 515 nm. By comparison, $LiNb0_3$ has no phase matching condition at room temperature for 1030 nm and is highly temperature sensitive, while beta Barium borate (BBO) although having a non-linear coefficient ~2.5x larger than that of LBO its birefingent walkoff is 7x larger.

Table 2.1: Lithium Triborate (LBO) biaxial crystal properties [55].

LBO [oo→e]	Fundamental (1030 nm)	Harmonic (515 nm)
Walkoff [mrad]	0	8.22
Phase velocity	c/1.606	c/1.606
Group velocity	c/1.626	c/1.642
Group delay dispersion [fs^2/mm]	20.5	91.2
Optical axis	θ = 90°,φ=13.6°	
d_{eff} [pm/V]	0.828	

Of course, this optical axis, and therefore phase-matching condition, is only perfectly valid for the specific fundamental and harmonic wavelengths and therefore has a very narrow conversion (acceptance) bandwidth where the phase mismatch is:

$$\Delta k = 4\pi \frac{\Delta\lambda}{\lambda}\left(\left.\frac{dn}{d\lambda}\right|_{2\omega} - \left.\frac{dn}{d\lambda}\right|_{\omega}\right). \tag{2.78}$$

From the phase-matching curves (Figure 2.21) it is obvious that for a broadband ultrashort (~200 fs ↔ 8 nm) laser pulse at 1030 nm that the condition won't be met for all spectral components; they require an angular spread or **angular chirp**.

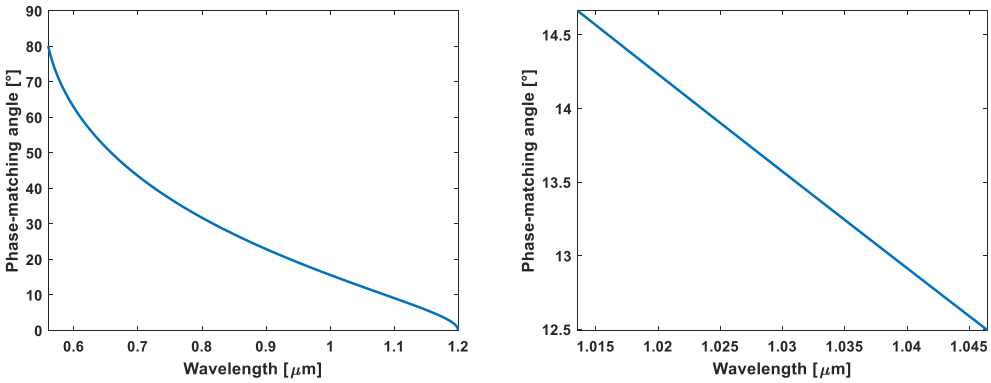


Figure 2.21: Phase-matching curve of LBO in the NIR-VIS (left). Phase-matching curve localized about 1030 nm fundamental (right) ($d\theta/d\lambda \approx -0.066$ deg/nm) [57].

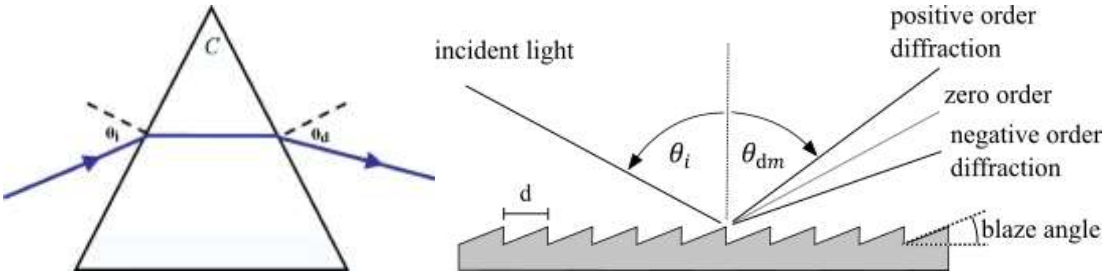


Figure 2.22: A schematic of prism angles (left), and of a diffraction grating (right).

This can be achieved with any spectrally dispersive element (Figure 2.22) such as a *prism* (2.79) or a diffraction grating (2.80), given by: [58]

$$\left.\frac{d\theta}{d\lambda}\right|_{\lambda_0} = \frac{\sin C}{\cos\theta_d \cos\left(asin\left[\frac{sin\theta_i}{n_0}\right]\right)} \cdot \left.\frac{dn}{d\lambda}\right|_{\lambda_0}, \tag{2.79}$$

$$\left.\frac{d\theta}{d\lambda}\right|_{\lambda_0} = \frac{m}{d\cos\theta_d}, \tag{2.80}$$

where C is the apex angle of the prism, θ_i and θ_d are the incident and diffraction angles, n_0 is the refractive index at the fundamental, m is the diffraction order, and d is the groove spacing.

The concepts are similarly extended to the 2nd harmonic stage (515 nm → 257 nm) with the inclusion of BBO. It has a number of advantages (Table 2.2), such as a simpler crystal structure, improved efficiency, and even a minimum in the phase matching curve (Figure 2.23) at ~1.47 μm.

Table 2.2: β-Barium Borate (BBO) uniaxial crystal properties [55].

LBO [oo→e]	Fundamental (515 nm)	Harmonic (257.5 nm)
Walkoff [mrad]	0	85.14
Phase velocity	c/1.676	c/1.676
Group velocity	c/1.727	c/1.916
Group delay dispersion [fs^2/mm]	142.8	464.8
Optical axis	θ = 50°	
d_{eff}(515 nm) [pm/V]	1.7	

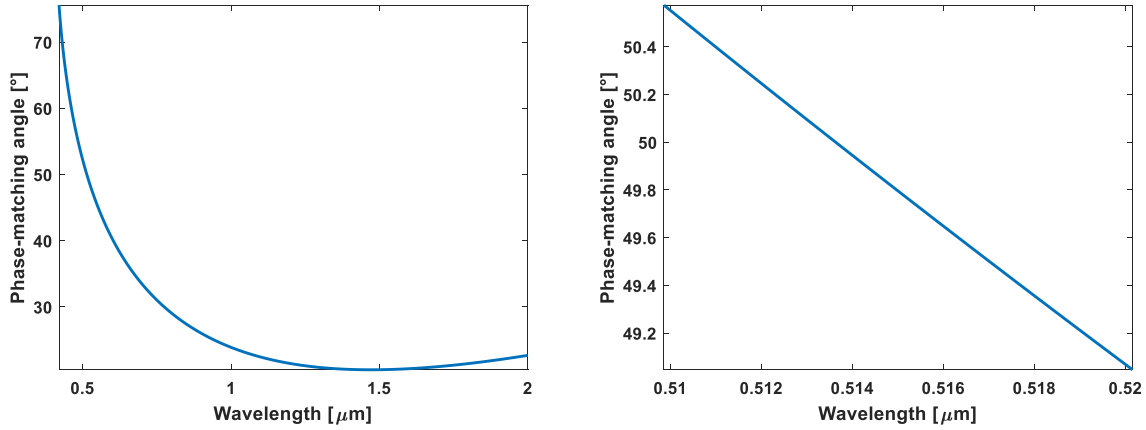


Figure 2.23: Broad phase-matching curve for BBO (left). Phase-matching curve localized about 515 nm (right) ($d\theta/d\lambda \approx -0.149$ deg/nm) [57].

However, the largest drawback of BBO is its very large walkoff which can laterally smear even a 1 mm beam by 8.5% in a 1 mm crystal. So, to maintain the pulse shape very thin crystals are desirable, however, as a trade-off against conversion efficiency and harmonic pulse energy.

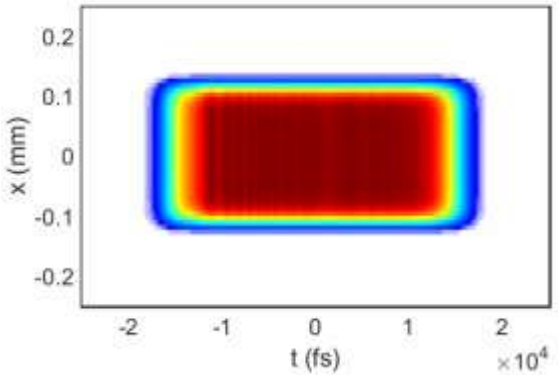


Figure 2.24: A longitudinal slice of a chirped, homogenous cylindrical pulse.

From these technicalities it is apparent that significant considerations must be taken into account, and that even if a perfect, homogenous cylindrical pulse is assumed (Figure 2.24), that one-to-one shape preservation is not perfectly possible. This is particularly true without angular chirp to compensate the phase-matching criteria (Figure 2.25), as borne out by simulations [59]. For these simulations BBO was used for second harmonic generation in order to emphasize the walkoff-induced lateral smearing induced in both pulses.

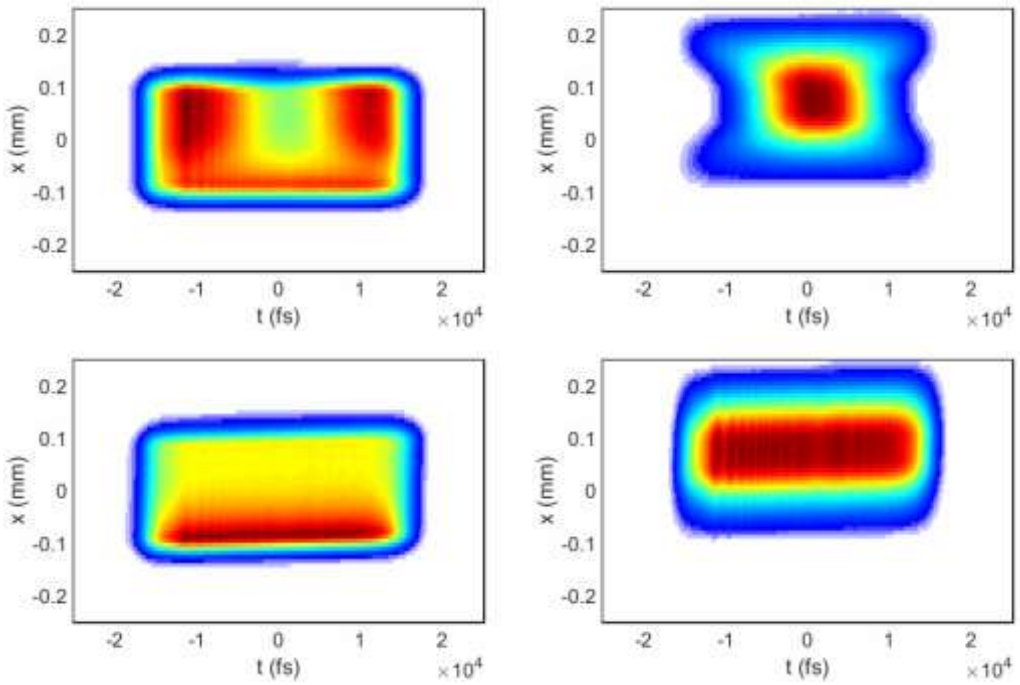


Figure 2.25: Non-linear conversion of an IR cylindrical pulse (left) through 2.5 mm of BBO without (top) and with (bottom) angular chirp to produce its harmonic (right).

The usage of these ultraviolet pulses also invalidates normal complex diagnostic techniques used for characterisation of the pulses such as FROG or SPIDER as the SHG processes required are non-functional in the vacuum ultraviolet. Although, one alternative is cross-correlated DFG FROG (DFG XFROG) [60].

2.9 DIAGNOSTICS

Naturally, it is vital to diagnose and characterize both the input and shaped laser pulses to achieve proper pulse shaping. To this end a number of diagnostic tools were used to characterize the pulses. Primarily, two techniques were used: correlative and spectrographic.

Exploiting the non-linear process from earlier in a non-collinear arrangement a short pulse can be used to characterize a longer pulse by scanning a delay stage and using a cross-correlation technique. The resolution of this method is typically limited by the duration of the shorter pulse, the step-size of the delay stage, and the available time.

Basic spectral information can be obtained by a simple spectrometer which can be used to infer basic pulse and experimental properties such as pulse duration, and SLM calibration. However, it returns no spatial information, or real temporal or phase information.

This was overcome by utilizing a spectrograph, what is essentially a Czerny-Turner spectrometer [61] modified with a scanable input slit, to produce a full volumetric spectral distribution thereby returning both the spatial information and the spectral information of the full pulse.

Of course, ideally a single measurement technique that produced the full complex-spectrum (such as FROG [62] or SPIDER [63]) over the full volume would be ideal. But in this work only the cross-correlation and spectrograph were used to characterize and cross-calibrate one-another.

2.9.1 Autocorrelation

Autocorrelation is a well-established process [64] based on self-characterization used to estimate the duration of a short pulse for an assumed pulse envelope. The pulse is split into two in a Michselon interferometer with a relative delay on one arm and then collinearly focused and overlapped in a non-linear χ^2 crystal (Figure 2.26). The angular wave vector phase matching applies here.

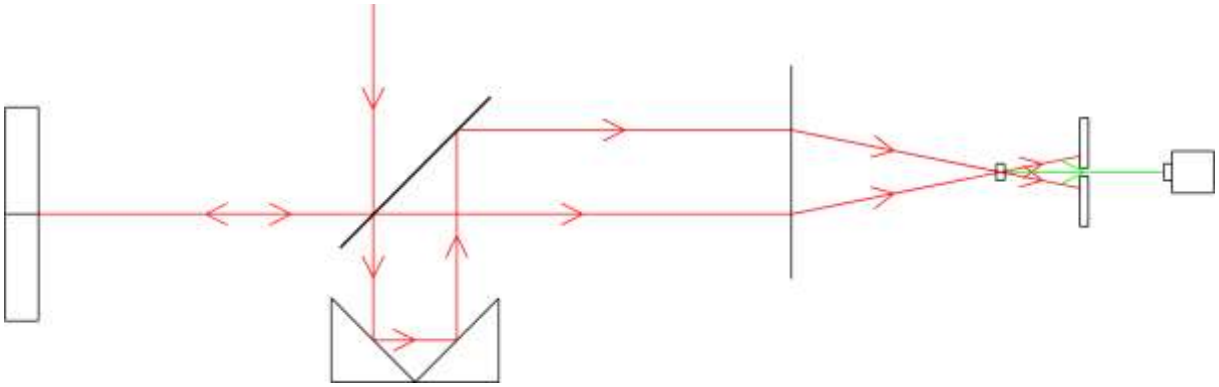


Figure 2.26: A basic autocorrelator setup for self-characterization of short laser pulses.

Owing to momentum conservation rules three second harmonic signals are generated. The individual conversions of the two pulses and the mixing signal in-between. A spatial filter (aperture) is used to pass the latter signal to a slow photodiode and the delay between the inputs pulse is varied. The autocorrelation signal given by the delay is:

$$I_{ac}(\tau) = \int I(t)I(t+\tau).dt \tag{2.81}$$

Where the typical analytical solutions for a Gaussian pulse are [64]:

$$I_{ac}(\tau) = e^{-\ln(2)\left(\frac{2\tau}{\Delta\tau}\right)^2}, \tag{2.82}$$

$$I(t) = e^{-\ln(2)\left(\frac{2t}{\Delta t}\right)^2}, \tag{2.83}$$

$$\frac{\Delta\tau}{\Delta t} = 1.41. \tag{2.84}$$

2.9.2 Cross-correlation

Cross-correlation follows the same basic principle of auto-correlation in that it is the temporal overlap of two laser pulses in a non-linear medium however in this case the pulses are independent. A shorter, known, typically transform limited, reference pulse $I_r(t)$ is used to "probe" a longer signal pulse $I_s(t)$:

$$I_{cc}(\tau) = \int I_s(t)I_r(t+\tau)dt. \tag{2.85}$$

2.9.3 Spectrograph

Finally, a spectrograph, essentially a slit-scanning imaging spectrometer, was designed and constructed. In essence, by placing an image plane of the shaped pulse at the slit, it is used to reconstruct the full volumetric distribution of the laser pulse by spectral imaging and slicing in the transverse plane along the axis of dispersion of the grating.

The spectrograph is based on the quintessential Czerny-Turner design [61] in which a slit is imaged onto a photodetector (Figure 2.27), or filtered by another slit at the image plane to form a monochromator.

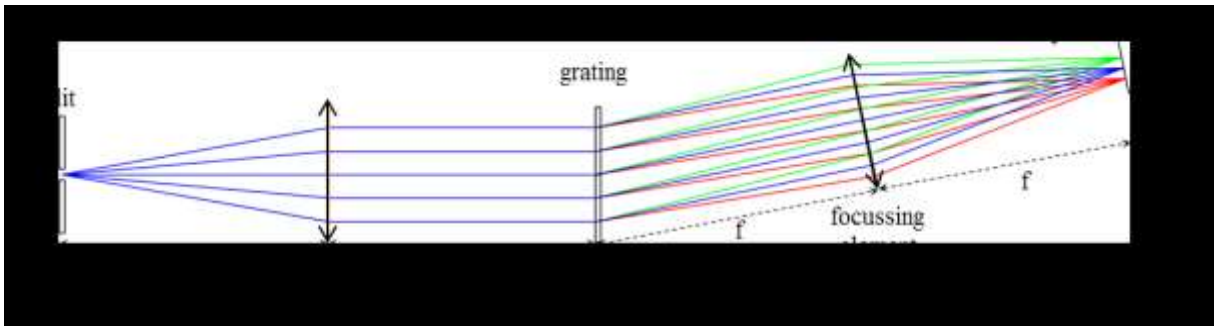


Figure 2.27: The basic 4f design of a Czerny-Turner spectrometer.

The design of which follows the standard formulas [65] for spectrometer design but with a tolerance added to the detector width to include the displacement of the slit on the detector. Consideration for optical component spacing in a reflective Z-fold configuration (Figure 2.28) must also be taken into account.

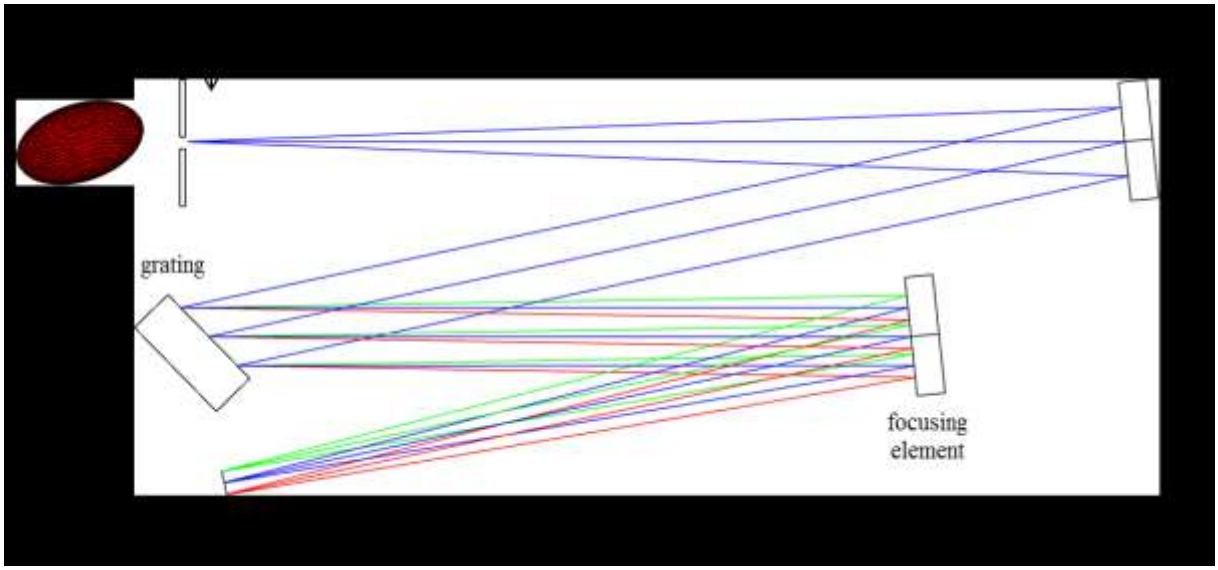


Figure 2.28: A slit scanning spectrograph in a reflective Z-fold configuration.

The focal length of the focusing element is determined by:

$$L_f = \frac{(L_d - \Delta_d)\cos(\beta)}{G \cdot \Delta\lambda}, \tag{2.86}$$

where (L_d - Δ_d) is the width of the camera chip minus a margin for scanning of the imaged beam spot from the slit, which is itself approximately defined by the slit width and the desired scan resolution. Here β is the diffraction angle, G is the grove frequency, and $\Delta\lambda = \lambda_{max} - \lambda_{min}$ is the wavelength range. The diffraction angle is to be chosen in a compromise between minimizing optical aberrations and practical considerations of optical component placement. Typically the lens diameters and focal lengths should be chosen to match the acceptance angles of the preceding optical system.

Letting L_d = 6.4 mm, Δ_d =1.4 mm, β = 44°, G = 1200 l.mm^{-1}, and Δλ = 20 nm the focal length of the focussing element is found:

$$L_f \rightarrow \frac{(6.4\ mm - 1.4\ mm)\cos(44°)}{1200\ \text{l}.mm^{-1} \cdot 20\ nm} \approx 150\ mm. \tag{2.87}$$

The focal length of the incoming collimating element is then defined by the magnification M and the ratio of the incident and diffraction angles:

$$L_c = L_f \frac{\cos(\alpha)}{M\cos(\beta)}. \tag{2.88}$$

Given a desired diffraction angle β of 10°, α is therefore 34°, and with a magnification factor of ~1 the collimating element is determined to be:

$$L_c \rightarrow 150\ mm \frac{\cos(34°)}{\sim 1\cos(44°)} \approx 175\ mm. \tag{2.89}$$

Finally, this results in a slit width being defined by:

$$w_{slit} = \frac{G \cdot \Delta\lambda \cdot L_c}{\cos(\alpha)} = \frac{G \cdot \Delta\lambda}{\cos(\alpha)} \frac{L_f \cos(\alpha)}{M\cos(\beta)}, \tag{2.90}$$

which for a given a pixel width of 4.65 µm [66] the above exposed detector width of 5 mm is ~1000 px, giving a maximum resolution limit of 0.02 nm/px and defining the slit width:

$$w_{slit} = \frac{1200\ l.mm^{-1} \cdot 0.02\ nm \cdot 175\ mm}{\cos(34°)} \approx 5\mu m. \tag{2.91}$$

Therefore, given the presumed margins above for a ~Ø1.0mm spotsize on the slit results in a scan resolution of 200 points. Of course, this may be too time-consuming so a "coarse" scan can be done, or the resolution may be reduced by increasing the slit width.

Taking these design parameters results in the following configurations:

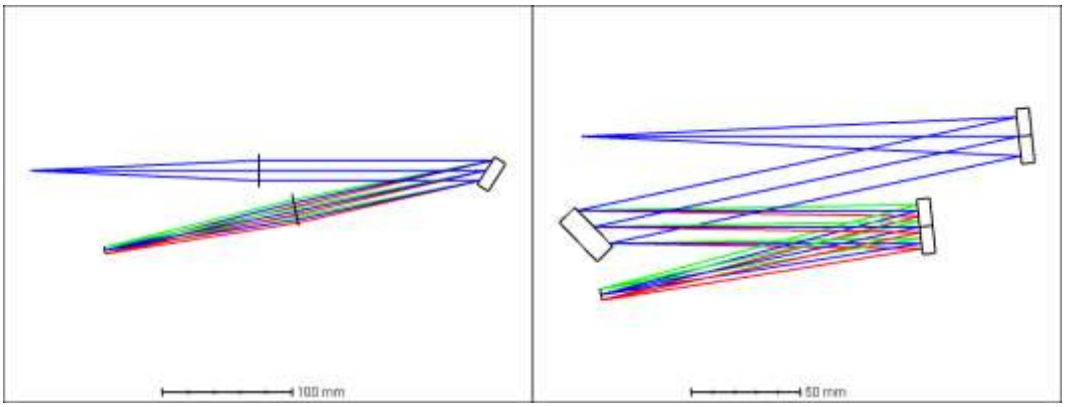


Figure 2.29: The spectrograph design with transmissive focusing elements (left), and folded with reflective focusing elements (right).

Historically speaking, the reflective scheme (Figure 2.29b) is the preferred configuration for broadband spectrometers as the reflective focusing elements are free of chromatic aberration, and the folded "Z" design minimizes the spatial footprint. Conversely, the scheme with transmissive optics simplifies alignment, and the extremely narrow bandwidth requirements of the device make chromatic aberration a negligible consideration.

The spectrograph effectively "slices" the input laser pulse spectrally across one transverse plane producing longitudinal slices. The width of the slit, and the size of the beam on the slit,

determines the spatial resolution. As the slit is of a finite width this also means that each "slice" is a transverse integral of a portion of the pulse.

This process can be visualized by taking a volumetric distribution and down-sampling, effectively binning, one of the transverse axes and plotting the longitudinal slices.

For example, taking the previous quasi-cylindrical pulse volume (see Figure 2.17) and scanning along the vertical axis produces λ-X longitudinal slices (Figure 2.30).

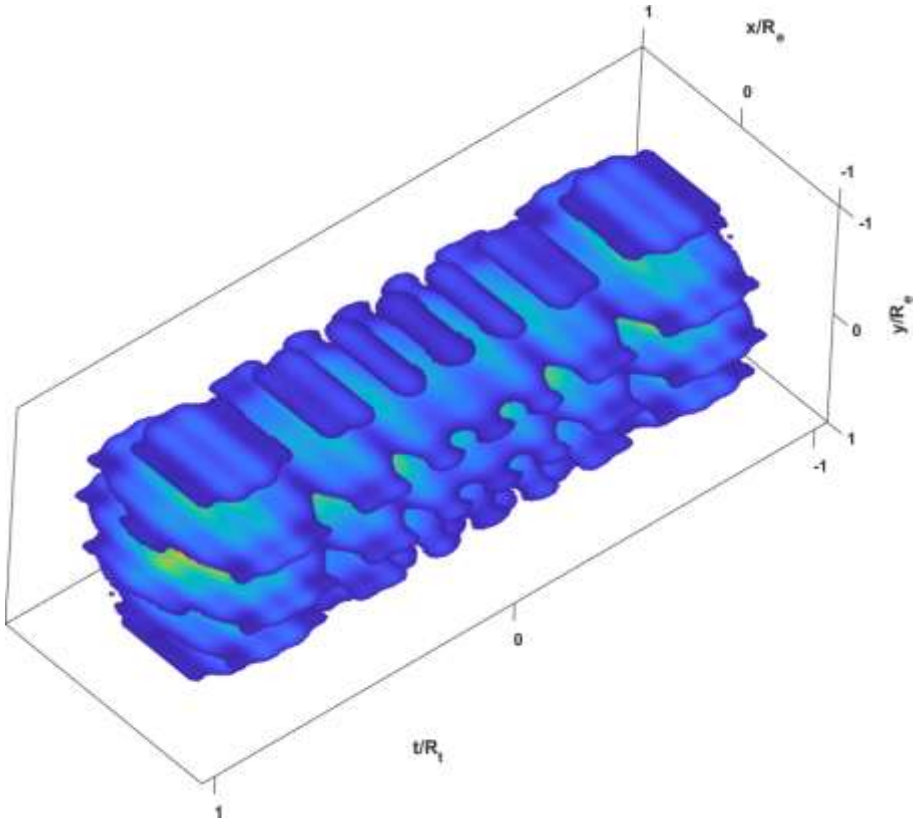


Figure 2.30: An equivalent spectrograph scan of the quasi-cylindrical pulse with a horizontal slit scanned vertically

Of course, there are a number of limitations to the technique. It does not return information on the complex electric field of the laser pulse or any temporal information. Therefore any spectro-temporal correlation must be either measured or assumed. Furthermore, any change in wavelength with transverse position (spatial chirp) can be convoluted with the inherent spectral "walking" of the spectrogram as the slit moves. Finally, as with any stepwise measurement technique, it can be quite time consuming for high-resolution scans.

In conclusion, particle accelerators permit access to new avenues of scientific research through the FEL lasing process that would be otherwise impossible through conventional optical radiation generation techniques. Furthermore, the FEL process is highly sensitive to the properties of the particle bunch; in particular the emittance which is primarily affected during photoemission.

To-date, many practical emittance minimization techniques have already been applied (some of which were tested at PITZ) and as such photocathode laser pulse shaping remains one of the avenues of research as even for cylindrical pulses space charge forces contribute an equal proportion to the total emittance as that of thermal emittance.

As the capacity to directly shape photocathode laser pulses directly in the UV is limited (primarily owing to material constraints) the pulses must be shaped in either the fundamental optical frequency of the laser or its first harmonic. SLMs in a 4f-line arrangement provide a dynamic method to manipulate both the spectral components of the laser pulse and the spatial components. This permits an incredibly flexible method capable of producing almost any arbitrary distribution, albeit with a quadratic symmetry, but with a particular interest in the ellipsoidal distribution which has long been held as the mathematical ideal.

Of course, this must be done in consideration of the harmonic conversion process and the trade-off of competing diagnostic requirements for (self-)characterization. As a test facility PITZ is ideally suited for developing and characterizing this new method of laser pulse shaping and applying it to emittance minimization.

Chapter 3 PITZ accelerator

3.1 GENERAL LAYOUT

The Photo Injector Test Facility at DESY in Zeuthen (PITZ) is a facility dedicated to the research, development, and characterization of RF photoinjectors and related technologies. It was built to demonstrate the electron source requirements (Table 1.1) for the Free electron LASer in Hamburg (FLASH), and the European XFEL.

An overall schematic layout of the facility is shown split across two lines in Figure 3.1. The components relevant to this work are the photocathode laser systems (shown in later figures), the electron gun with the primary focussing solenoid magnet and compensating bucking magnet, the Low-Energy Dispersive Arm (LEDA), the Cut-Disk Structure (CDS) booster [67], Emittance Measurement System (EMSY) stations, the High-Energy Dispersive Arm (HEDA1) and the transverse deflecting structure (TDS). There is also a multitude of magnets (dipoles, quadrupoles) and screen stations throughout the facility for steering, focussing, and imaging of the bunch.

For bunch shaping experiments the facility was only utilized up to the first screen in the Phase Space Tomography section, 12.3 m downstream from the cathode, which is used to view the TDS temporal streak. The plasma cell was also removed for all experiments relevant for this thesis and was replaced by a straight beam pipe.

UV laser pulses are imaged onto the photocathode in the gun section to produce electron bunches via the photoelectric effect. RF pulses are then used to drive the cavities and accelerate the bunches downstream to a nominal momentum of 6.5 MeV/c after the gun, and 25 MeV/c after the booster. A solenoid magnet, and various steerer correctors and quadrupoles are used to focus and transport the bunch throughout. Momentum measurements are obtained from the energy spectrometers LEDA and HEDA1, while the CDS booster demarcates the accelerator into low-energy and high-energy sections. The TDS deflecting cavity can be used to give the bunch a longitudinally dependent vertical kick and streak the bunch temporally. This can then be imaged across a screen or coupled with the final dispersive arm (HEDA2) to acquire the longitudinal phase space. Finally, the EMSY stations, utilizing the slit-scan technique, in conjunction with screen stations are used to measure the transverse phase space.

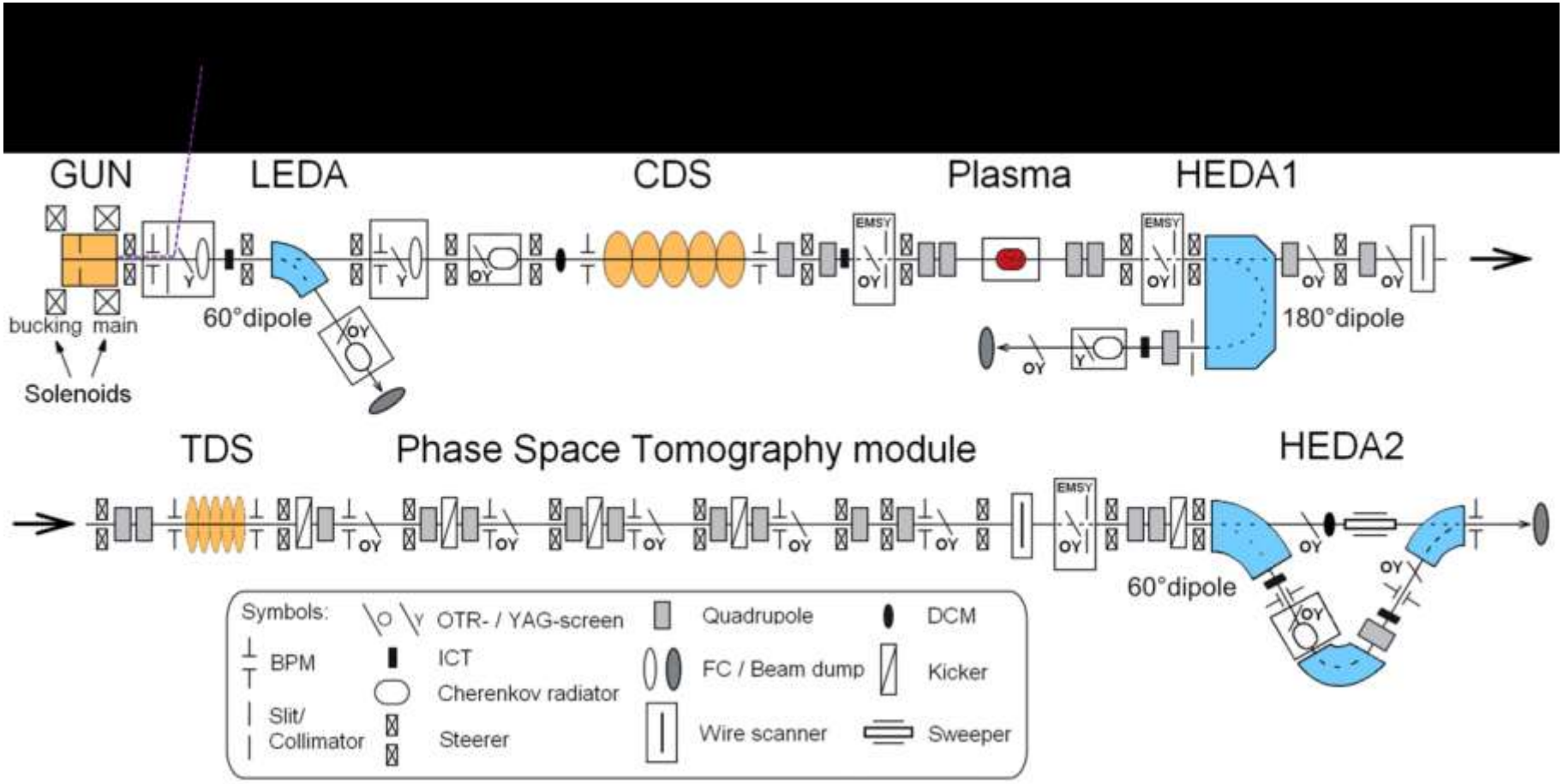


Figure 3.1: The overall layout of the PITZ facility.

3.2 PRIMARY PHOTOCATHODE SYSTEM

Here a description of the original photocathode laser system primarily used at PITZ is presented, with the new prototype described in Chapter 5, and the updated prototype in Chapter 7.

Laser pulses with a wavelength of 257 nm are utilized to produce electron bunches at PITZ. These ultrashort (several ps) UV pulses hit the photocathode with an active layer of Cs_2Te under ultra-high vacuum and with a strong longitudinal electric field at the cathode surface produce correspondingly short electron bunches. The high QE of Cs_2Te, typically ~5-10%, coupled with the high energy laser pulses, mean that bunches of many nC can be produced. The laser oscillator is fundamentally an Yb:YAG IR laser with a 54 MHz oscillator operating at 1030 nm wavelength with a pulse length of 2 ps. These pulses are split and used for cross-correlation or sent to the pulse shaper. After shaping further amplification produces 20 µJ pulses prior to UV conversion via a pair of second-order non-liner conversion crystals, LBO and BBO respectively.

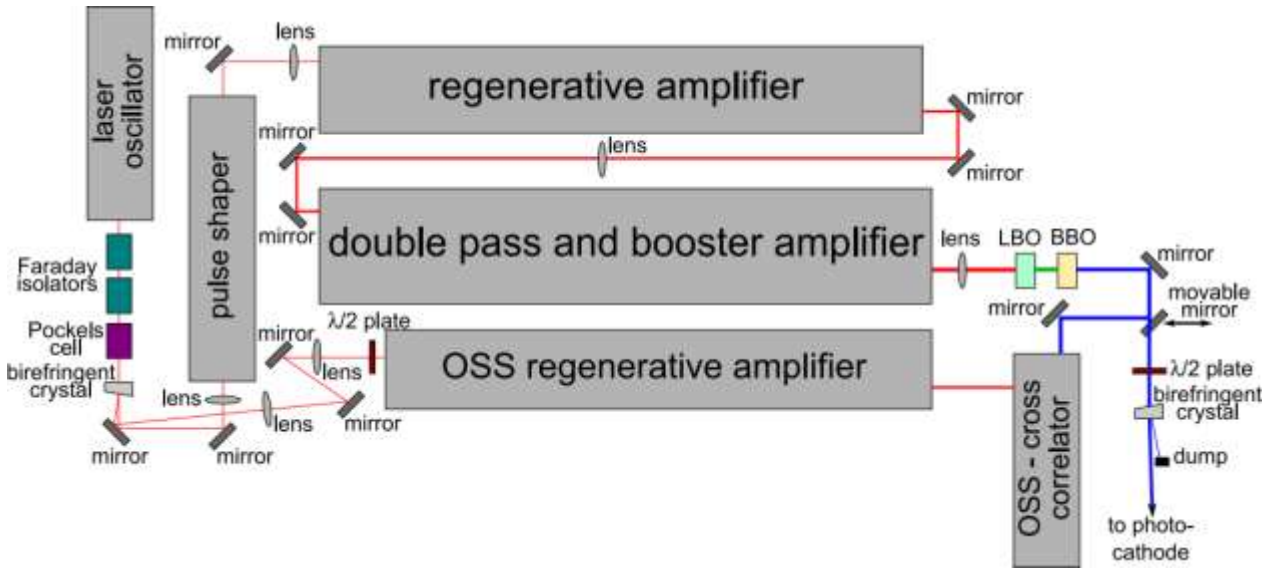


Figure 3.2: Layout of the photocathode laser developed by the Max Born Institute [68].

The laser (Figure 3.2), developed by the Max Born Institute (MBI, Berlin), can produce UV laser pulses of up to 1 µJ in trains of up to 800 pulses at a pulse repetition rate of 1 MHz and a train repetition rate of 10 Hz (Figure 3.4). The system can provide either ~12 ps (FWHM) Gaussian laser pulses or flattop pulses with a duration of up to ~22 ps FWHM with a rise/fall time of 2 ps. This is achieved by a series of birefringent crystals in a Solc-fan design to split, delay, and stack oscillator pulses into a temporal flattop in the IR regime [10]. Typical temporal profiles are shown below (Figure 3.3):

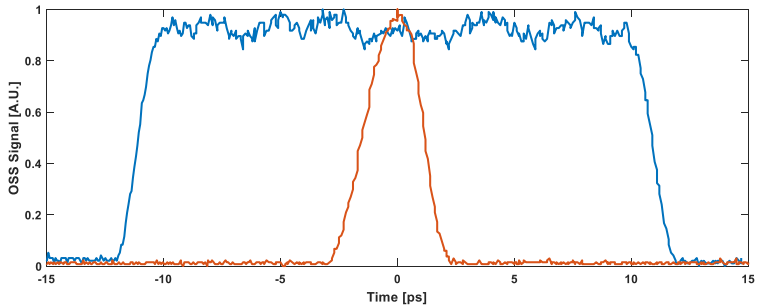


Figure 3.3: Optical Sampling System (DFG cross-correlation) trace of the 22 ps flattop pulse (blue) and the 2 ps Gaussian oscillator (red) laser pulses.

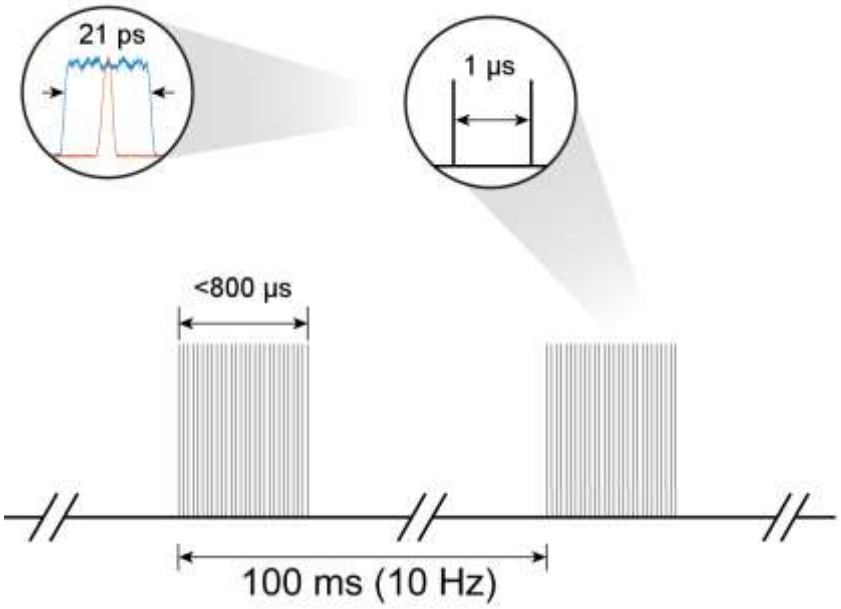


Figure 3.4: Time structure of the MBI laser system.

The UV flattop temporal pulse is transported to the tunnel from the laser hutch through a magnifying telescope onto a variable aperture called the Beam Shaping Aperture (BSA) [68]. The diameter of the aperture is much smaller than the σ of the transverse Gaussian distribution and crops the laser to produce a quasi-flattop radial transverse profile and combined with the temporal flattop shaper to produce a so-called “cylindrical” pulse. The pulse is then imaged from the aperture to the photocathode surface.

Prior to the BSA exists a mechanical shutter and a number of laser diagnostics along the tunnel section of the transport beamline [68]. There are two UV sensitive JAI cameras placed at optically equivalent pathlengths of the BSA and the cathode surface, called respectively virtual BSA (vBSA) and Virtual Cathode 2 (VC2). Typical transverse distributions with their Fraunhoffer diffraction rings are shown below (Figure 3.5):

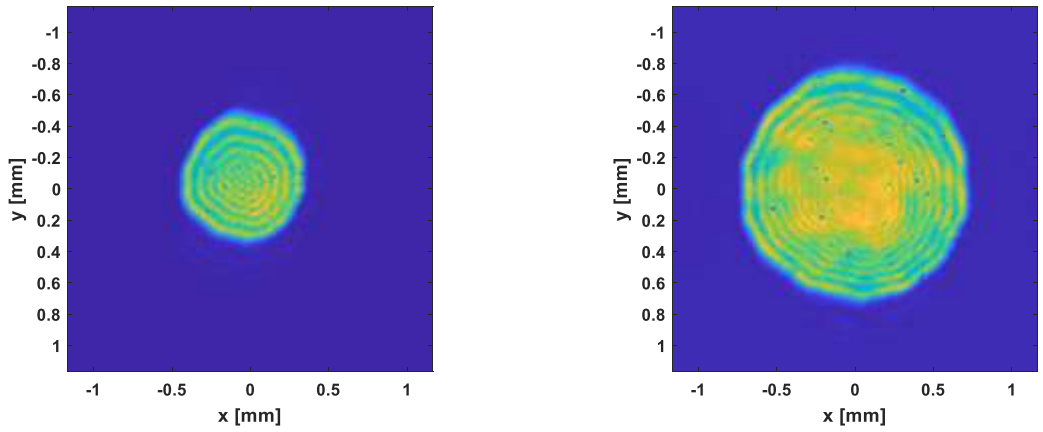


Figure 3.5: a) A BSA of 0.8 mm imaged on VC2. b) A BSA of 1.4 mm imaged on VC2.

The ring structure of the transverse distribution arises due to aforementioned diffraction (Sec. 2.7). The number and energy (Table 3.1) of the UV laser pulses, and therefore the amount of charge generated at the photochatode, is controllable (Figure 3.6). Controlling the number of pulses is achieved by switching the final Pockel cell timing, and the intensity is varied by a ½λ waveplate and birefringent beamsplitter combination wherein the waveplate is rotated to vary the laser pulse energy transmitted to the cathode.

Furthermore, there is an energy meter, photodiode, and quadrant diode located within the laser beamline next to the gun cavity for determining QE, pulse train uniformity, and alignment.

Table 3.1: Nominal on-table MBI laser pulse properties.

Wavelength	257nm	
Pulse-train length	<800 μs (600 pulses)	
Repetition rate	1 MHz	
Pulse energy	<10 μJ	
Temporal envelope	Gaussian	Flattop
FWHM duration	2-12 ps	~22 ps
Rise/fall times	-	~2 ps
Transverse shape	Gaussian	
Transverse RMS spotsize	1.27 mm	
Beam Shaping Aperture range	0.2 – 4.0 mm	

As can be seen, the pre-existing photocathode laser allows for flexible laser pulse shapes and the parameters are easily made easily accessible to the facility operators (Figure 3.6). This allows for emittance optimization for various bunch charges and for some variation of the space charge effects in the photoinjector by changing the volumetric space-charge density at the cathode.

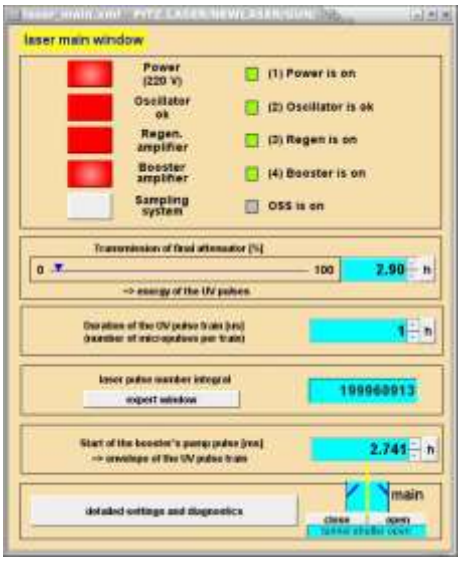


Figure 3.6: A typical example of the MBI laser control GUI used at PITZ. It presents basic status of the laser, the laser transmission control in percent, the length of the laser pulse train, and control of the shutter.

3.3 RF PHOTOELECTRON GUN

The electron gun cavity is the most critical component, and it is here where the electron bunch qualities are predominantly determined.

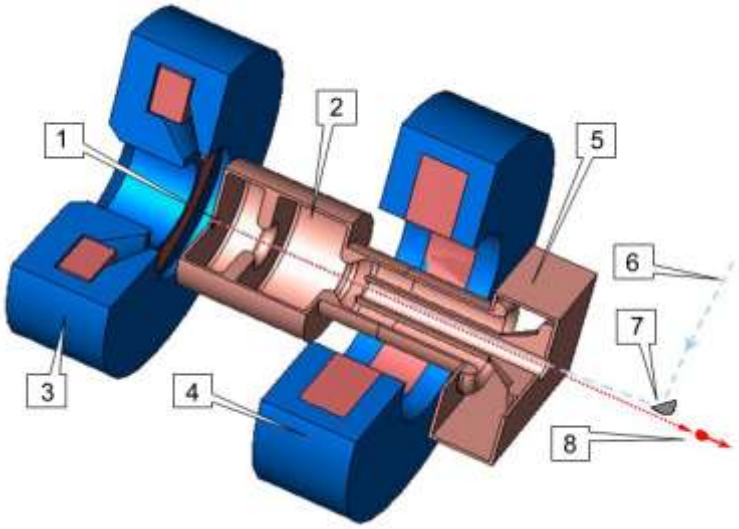


Figure 3.7: PITZ RF gun layout. 1) Cathode plane 2) Cavity 3) Bucking solenoid 4) Main solenoid, 5) RF coupler, 6) UV photocathode laser, 7) Laser vacuum mirror, 8) Photoelectron beam.

It consists of a 1.6-cell, L-band, normal conducting, standing wave radio-frequency copper cavity (Figure 3.7) operated in pulsed mode at 10 Hz. It is driven by a 10 MW klystron with power transmits via two RF waveguides towards the gun. The design gradient of 60 MV/m (Figure 3.8) routinely yields a photoelectron momentum of up to 6.5 MeV/c, which together with the flexible photocathode laser, and the changeable main solenoid current, is one of the main tools for emittance

optimization in the photoinjector. Naturally, the quality of the produced electron bunches by the RF gun strongly depends on the RF source. During the period of this thesis the Low Level RF (LLRF) had a phase stability of ~0.1°, and an amplitude stability of ~0.03% [69].

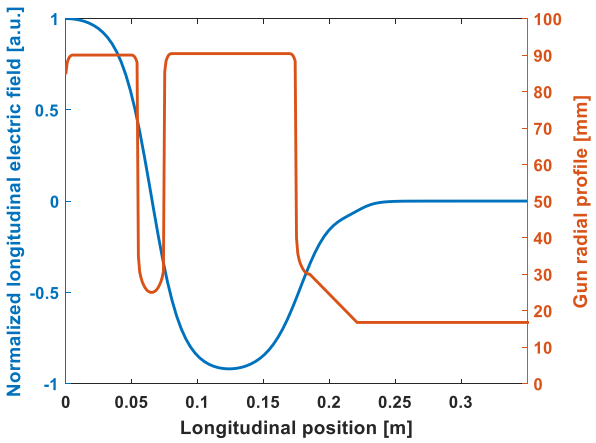


Figure 3.8: The normalized longitudinal component of the gun's electric field (blue) along with the radial profile of the cavity (red).

Two solenoid magnets, the larger of which is located downstream of the cavity, are used for focussing and emittance compensation [70] [71].

3.4 SOLENOID AND OTHER MAGNETS

The two solenoid magnets are situated before and after of the cavity along the longitudinal z-axis. The main solenoid magnet brings the photoelectrons to a transversal focus downstream of the gun. It has a peak longitudinal magnetic field of up to 0.29 T (500 A current) and is centered 0.276 m downstream of the cathode plane.

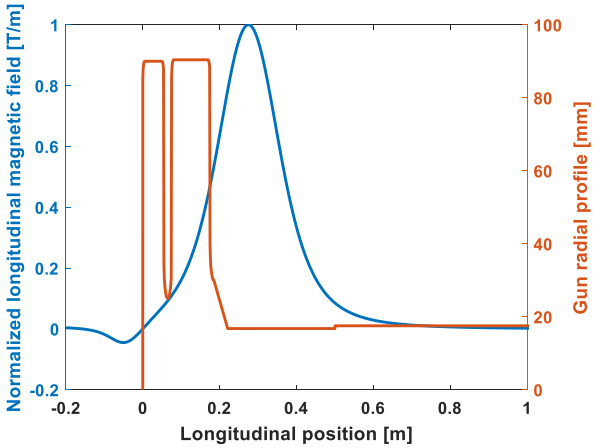


Figure 3.9: Combined normalized on-axis magnetic field component of the main solenoid and bucking solenoid (blue).

The bucking solenoid is located behind the cathode plane and is used to compensate any residual field of the main solenoid at the cathode surface (Figure 3.9) [71].

Outside of the gun section there exist multiple dipoles and quadrupoles, these act as bi-directional steerers and astigmatic focussing elements in either a horizontal or vertical configuration. All of the quadrupoles are identical and provide a maximum gradient of up to 7 T/m.

These are vital to beam transport throughout the accelerator as a range of diverse causes such as field asymmetries, mechanical tolerances, and local magnetic variation can cause deviations from the intended design. For example, the field axes of the main solenoid or of the booster cavity may not necessarily align to the mechanical axis of the devices. Solutions to these two example issues are 5D (x, y, z, pitch, yaw) reorientation of the solenoid at the cavity aperture to realign the solenoid axis to the electrical axis of the gun, and as the gun is not perfectly in-line with the accelerating cavity utilization of at least two bending elements in both transverse axes to correct for position and angle into the booster cavity, and quadrupoles at the exit of the gun cavity [72] to correct for electric field asymmetries arising out of the asymmetric RF coupler design [69].

Furthermore, there are three high-current dipoles in the dispersive sections which are utilized as energy spectrometers so that the momentum and momentum spread may be measured. However, only the first two are used to determine the beam momentum for projected emittance measurements.

The first energy spectrometer (LEDA) is situated ~1.1 m downstream of the gun, while the second (HEDA1) is a 180° dipole centred ~8 m downstream [73] in a vertical orientation with a designed trajectory radius of 300 mm.

3.5 CDS BOOSTER

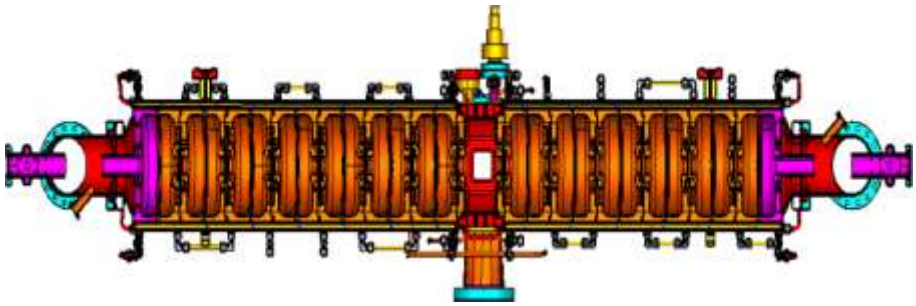


Figure 3.10: The PITZ CDS Booster cavity.

The CDS booster (Figure 3.10) was designed by the Institute for Nuclear Research (INR, Russia) for a maximum 900 μs long, 8 MW RF pulse to produce an accelerating gradient of up to 14 MV/m [74] and was installed at PITZ in 2012. It is also a 1.3 GHz L-band normal conducting copper cavity of 14 cells with time-varying longitudinal electric field (Figure 3.11) driven by a separate RF system. It can further accelerate the beam up to 27 MeV/c. It is a vital tool in the conservation of minimized emittance beams coming from the gun. This requires careful balancing of the booster gradient, phase, and main solenoid focussing to match the beam into the cavity and maintain an equilibrium between the transverse RF and space charge forces [75].

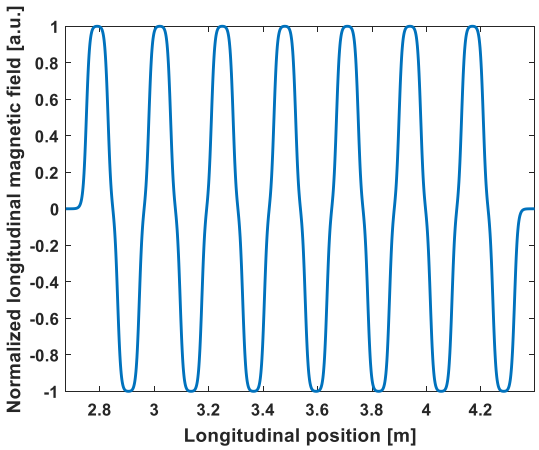


Figure 3.11: The normalized longitudinal electric field component in the CDS booster cavity.

3.6 DIAGNOSTICS

Finally, there exist a number of diagnostic stations throughout, with three located in the low energy section and further screens situated in the high energy section (Table 3.2). These contain various tools for beam measurement and characterization. Every station has a phosphorescent YAG screen and a Proscillica GC1350 camera for viewing the electron beam and its position, with a few stations also supporting LYSO screens for low charge bunches. Faraday cups are used to collect and measure charge of up to 500 pC and Integrated Current Transformers (ICTs) are used to passively measure greater charges [76].

Table 3.2: Screen stations, read out lenses, and resolution data.

Location	Position, [m]	Lens focal length, [mm]	Scale factor, [μm/px]	Notes
High1.Scr1	5.277	f160	28.2	EMSY1 slit position
		f200	15.9	
High1.Scr3	7.125	f160	40.5	EMSY2 slit position
		f250	14.9	
High1.Scr4	8.410	f100	72.4	EMSY1 observation station
		f160	38.2	
		f250	13.1	
High1.Scr5	8.920	f100	72.8	HEDA1 reference screen, EMSY2 observation station
		f160	39.1	
		f250	13.1	
Pst.Scr1	12.278	f140	76.1	TDS observation screen
		f200	44.4	
Disp1.Scr1		-	59.2	LEDA observation screen
Disp2.Scr2	Optical equiv. High1.Scr5	f50	116.7	HEDA1 observation screen
		f120	35.3	

3.7 TRANSVERSE PHASE-SPACE MEASUREMENTS

The primary method for measuring the transverse phase space at PITZ is the slit scan technique [77]. This takes place at three possible positions within the beamline, two of which are 5.3, and 7.1 m downstream from the cathode plane (see Table 3.2).

Rectangular apertures, known as slit masks, with a width of either 10 µm or 50 µm are installed at these locations and are scanned transversely across the beam and crop the beam into 'beamlets'. Each low-charge beamlet then propagates a known distance with negligible space charge forces downstream to a YAG screen which results in a measured local divergence of the beam and permits calculation from the intensity and spread on the screen. The full transversal phase-space may then be reconstructed from the combined dataset of all the beamlets (Figure 3.12) by scanning the respective slit for either orthogonal component.

As the Tungesten slits have a thickness depth of 1 mm they have limited acceptance angles of 10 mrad and 50 mrad for the 10 µm and 50 µm slits, respectively. Therefore, the slits are also mounted to rotation and goniometric stages [78] to re-angle them with respect to the electron beam direction.

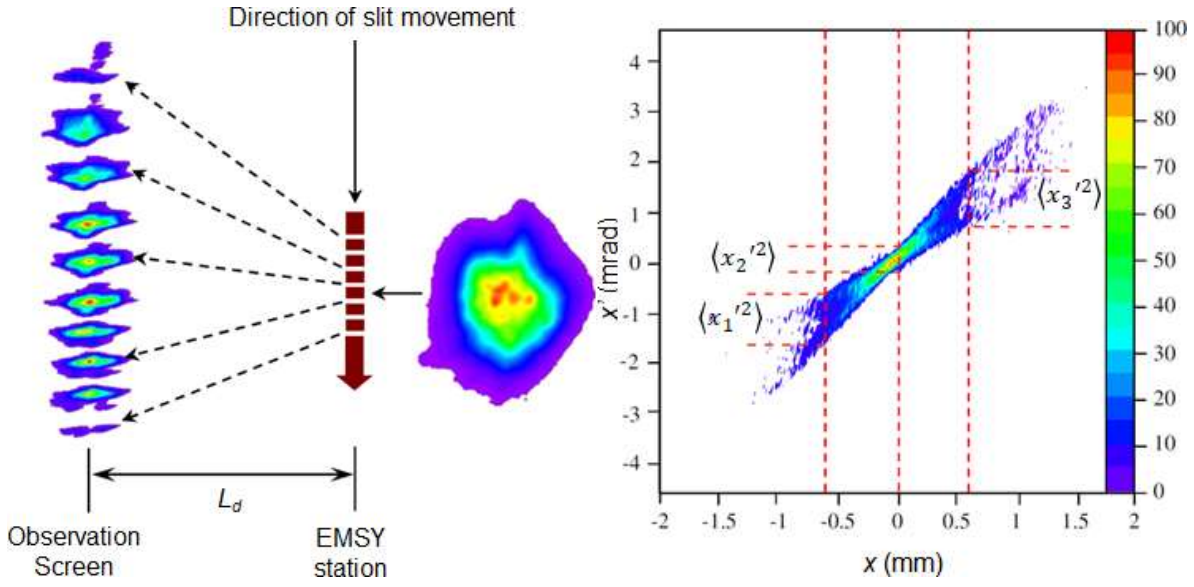


Figure 3.12: Principles of the slit-scan transverse emittance measurement technique. A slit is scanned transversely across the beam to crop it into beamlets (left) which is used to reconstruct the transverse phase space (right) [79].

There are a number of benefits and disadvantages to this technique. While it is not susceptible to space charge it requires repetitive measurements with different slit positions, can be time consuming, and very dependent on the short-term stability of the accelerator for measurements with low-charge bunches as the lower the bunch charge the longer bunch trains are required to obtain a sufficient signal-to-noise ratio.

It also requires multiple supportive measurements prior to beginning, and a lot of man-hours and machine time to perform. Although a measurement and reconstruction of a single phase space takes ~2-3 minutes a consistant measurement at the beam parameters to allow corresponding beam dynamics simulations requires multiple supplementary measurements: beam momentum in both the low energy and high energy sections, the transverse laser spotsize on the cathode, bunch charge, and

beamsizes at the slit station and measurement station.

A full transverse phase-space optimized as a function of the main solenoid current with basic statistics typically requires approximately 4 hours. This has obvious implications on long-term machine stability. Any interruption of operation mandates a complete restart of the measurement procedure, and any long-term drifts of key components add error onto the measurement.

Owing to limited sensitivity of the observation screens a correction factor $\sigma_x/\sqrt{<x^2>}$ containing the beam size at the slit station measured with a YAG screen σ_x, and the beamsize estimated from the slit scan x^2 is introduced to the normalized emittance to account for this:

$$\varepsilon_{n,x} = \beta\gamma \frac{\sigma_x}{\sqrt{\langle x^2 \rangle}} \sqrt{\langle x^2 \rangle \langle x'^2 \rangle - \langle x x' \rangle^2}. \quad (3.1)$$

This is to take into account a large fraction of the low intensity tails of the beam distribution and to perform a conservative measurement..

In conclusion, from the various technical aspects and features of the PITZ facility it is clear that it is a prime location for the prototyping and testing of novel FEL and photoinjector technologies. As such, it is instructive to estimate the impact these technologies might have and how they might be implemented. Before doing experimental tests this is best achieved by simulations.

Chapter 4 Laser pulse shaping and electron beam dynamics simulations

A modern photoinjector is a complex system involving the synchronous operation of various components and sub-systems in parallel: laser, RF, water, control, electronic, etc. It is a multivariate system and it is ideal to understand it as an overall whole and each substantial part in detail.

Simulations exist to provide insight, intuition and prediction of a system that might not be obvious or available experimentally or analytically. They are almost always cheaper and faster than experiment and offer the advantage that it is possible to effectively "tune a knob" on effects or variables that may be unphysical or impractical in reality and quantify them in locations that might be inaccessible. For example, a test particle can be "dropped" anywhere within an accelerator and the various forces acting upon it modelled.

In the first part of this chapter geometric modelling and numerical simulations were undertaken to develop an understanding of the pulse shaping scheme and its parameters, and to produce initial spatio-temporal SLM masks, and produce transmission efficiency estimates.

In order to access a transverse dimensions with a SLM inserted at the Fourier plane of a 4f-line the lenses are replaced with cylindrical lenses. However this introduces transverse asymmetries into the scheme which must be overcome in the orthogonal plane with a second shaper or a dual-pass layout. It is therefore instructive to evaluate two shapers in series and consider both orthogonal transverse dimensions simultaneously. This can also be considered as two back-and-forth passes of a single shaper decomposed into each pass.

In the second part of this chapter the effect of various charged bunch distributions on the electron beam properties are simulated within the framework of the PITZ facility. The desirability of idealized bunches is demonstrated, and the achievable bunches are evaluated to reflect practical experimental conditions.

4.1 OPTICAL SIMULATIONS

4.1.1 Zemax studies

Zemax OpticStudio [80] is a ray-tracing optical design suite and a useful tool for first order simulation of optical systems. It has provisions for sequential/non-sequential surface modelling, wavelength, and aberration analysis, polarization tracking, and more. In this case, simulation of a simplified optical layout equivalent to that of the proposed pulse shaping scheme can be validated. It must be noted that OpticStudio provides primarily a geometric analysis and cannot model temporal effects such as dispersion, chirp, harmonic generation, etc. and subsequently such modelling of spectral masks makes little sense in that context. Therefore the SLMs are initially modelled as simple reflective surfaces.

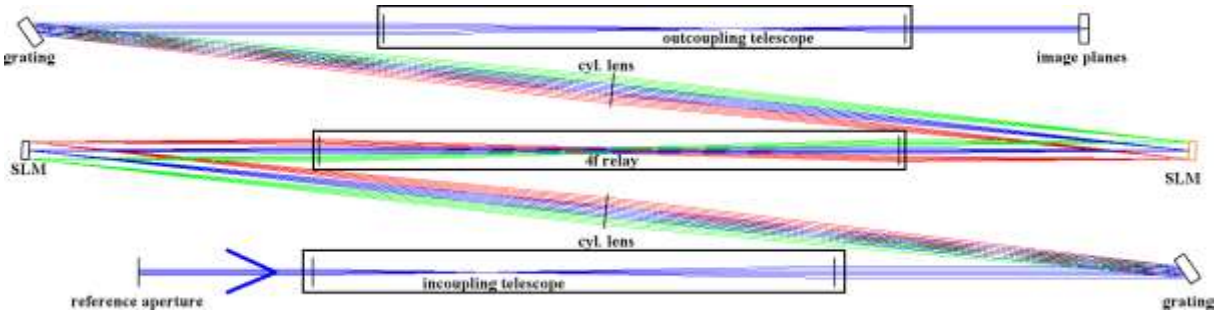


Figure 4.1: A basic spatio-temporal 4-f line shaper with amplitude/phase masking.

Any transverse shaping scheme, even as simple as an aperture, imparts spatial information onto a laser beam. However, this spatial information must be conserved by an optical system otherwise it would be lost due to diffraction.

Therefore, in geometric optical analysis two cases need to be considered as that must be conserved. A broadband collimated laser system with its equivalent object at infinity (Figure 4.1:), and the modulation and transfer of spatial information by the pulse shaping scheme is treated with a reference aperture as a near-field object. Owing to the radially asymmetric components the latter case is best considered decomposed into its orthogonal horizontal and vertical transversal components (Figure 4.2).

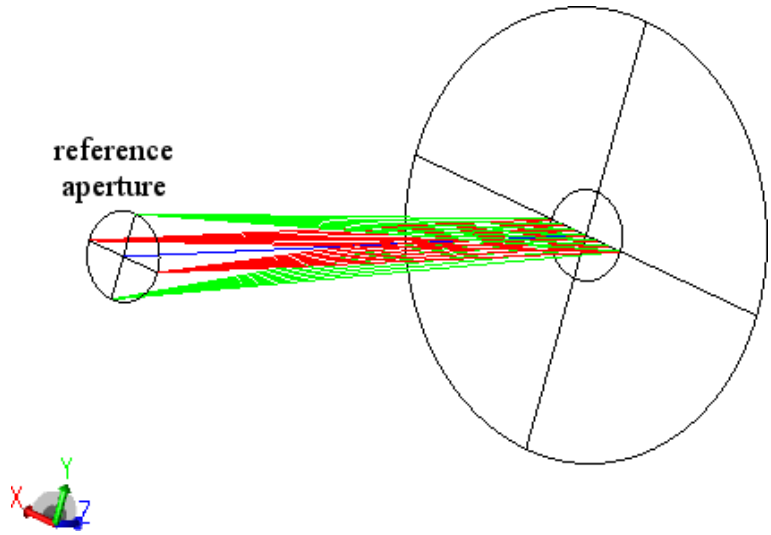


Figure 4.2: Colour coordinated Cartesian coordinate system and reference points, horizontal (red) and vertical (green) from a reference aperture.

For consideration of the pulse shaping scheme a reference plane is a useful mental construct. By considering point sources lying on the transverse axes of a reference aperture (Figure 4.2) the relay imaging onto, and between, the SLMs the transfer of spatial information via ray paths can be understood. This requires that the image distance of the incoupling telescope to be greater than the separation between the grating and SLM for projection of the spatial information onto the SLM.

Since the pulse shaping scheme is intended to provide both spectral shaping *and* spatial shaping the standard spherical lens in the 4f line (Figure 2.8) is replaced by a cylindrical lens. This allows access to the spectral component along one axis and *one* of the transverse spatial

information components along the other. It shall be seen that this introduces a longitudinal shift of the orthogonal transverse components, and as it is a shaping *plane* an interdependence is also introduced.

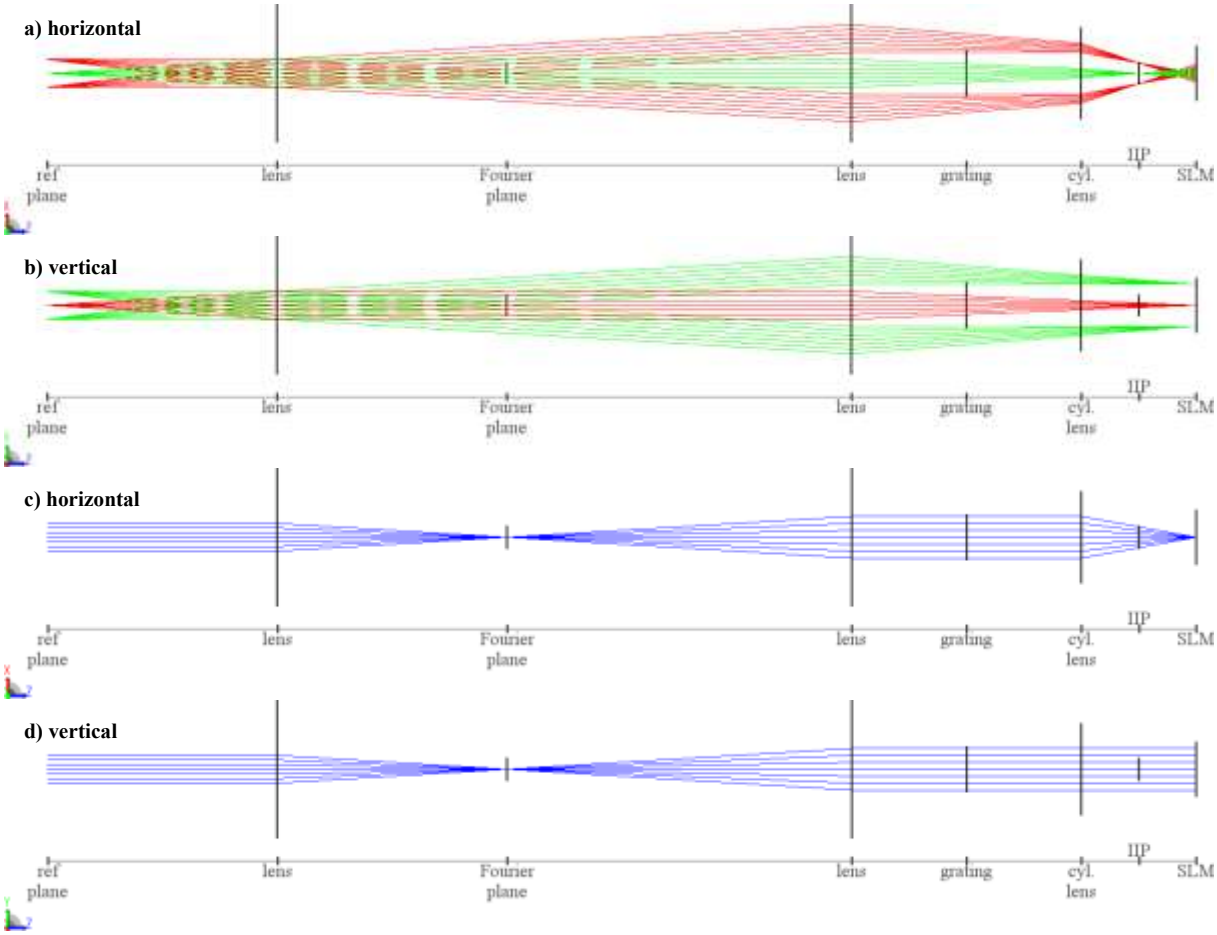


Figure 4.3: The first section of optical layout until the first SLM. a) & b) the relaying of spatial information of the uncoupled planes in the orthogonal directions, c) & d) the collimated laser beam at the central wavelength in both planes.

It can clearly be seen from ray tracing points in Figure 4.3 that the image planes (a&b) of the spatial information imparted by the reference aperture become orthogonally decoupled and longitudinally shifted in relation to one another as a result of the cylindrical lenses. An Intermediate Image Plane (IIP) is formed in the horizontal direction by the cylindrical lenses just before the SLM. Consequently, this needs to be matched further downstream by a second shaper in the opposite plane.

However, the entire horizontal spatial information is contained within the collimated laser beam which is horizontally focussed to a vertical line by the cylindrical lens and the spatial information is therefore constrained within the line focus in that plane.

Due to this, any modulation of information from the relayed reference plane performed by the first SLM along the line focus on the vertical plane is inherently applied across the entire horizontal plane.

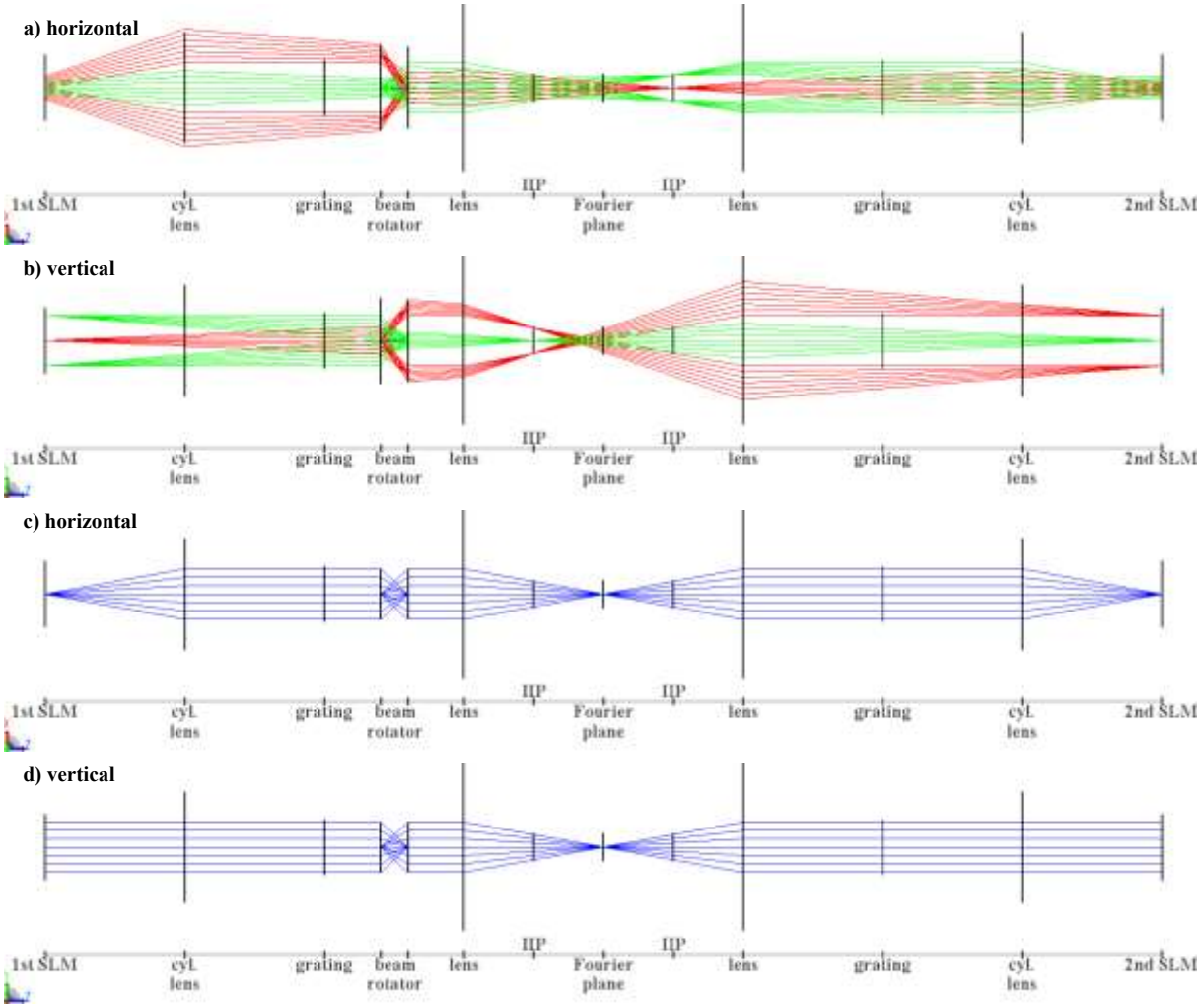


Figure 4.4: The 4f bridge and optical elements between the SLMs, with separated intermediate image planes (IIPs) either side of the Fourier plane.

In order to perform the operation in the orthogonal transverse direction the beam must be transported into a second shapter by a 4f bridge. The decoupling of the image planes is particularly evident here (Figure 4.4). Here the separate second cylindrical lens in the horizontal plane pushes the IIP even further downstream past the vertical image plane of the first SLM and the Fourier plane of the 4f bridge.

In practicality, it is easier (and safer) to axially rotate the beam 90 degrees around its longitudinal coordinate than to implement a vertical 4f line. To perform this axial rotation in the simulation of the linear system a coordinate break is used as a substitute to exchange the transverse axes. This results in the vertical axis of both SLM planes (Figure 4.4 b) acting as the spatial modulator for both transverse axes of the laser beam (as it would be in reality), and the horizontal axes maintains its application as the spectral shaper.

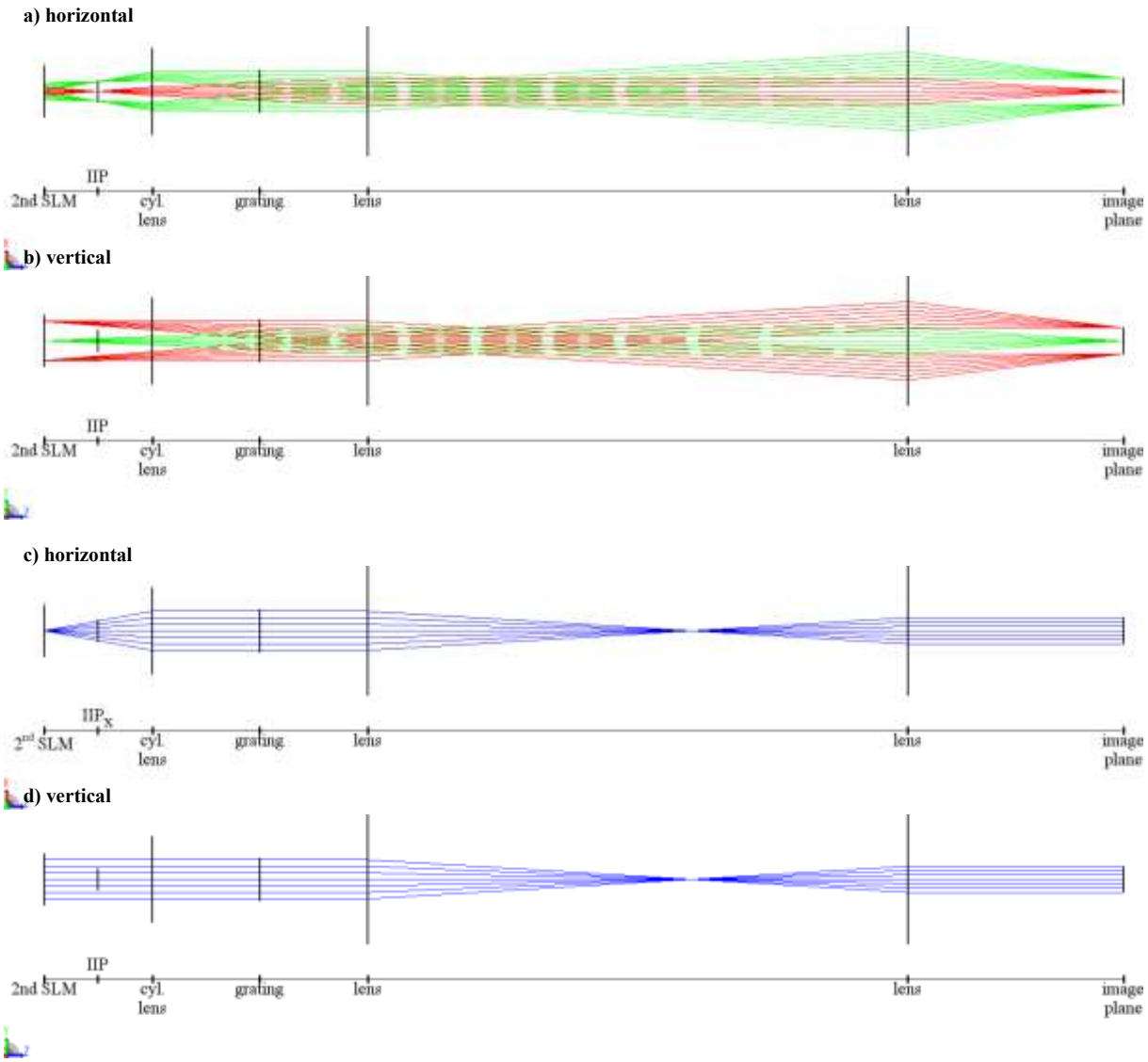


Figure 4.5: The final section after the 2nd SLM showing the restoration of axial symmetry and simultaneous imaging.

Finally, it can be seen that this axial rotation enables the second shaper to replicate the action of the first and push the orthagonal plane. The results in recomposition of the separated planes and symmetry in both planes is restored (Figure 4.5). The beam can then be re-collimated and brought to a final image plane for evaluation.

The transverse imaging of the system can now be evaluated with a test image at the reference plane (Figure 4.6). Although Zemax does support polarization analysis it is a non-trivial task to reproduce the SLM structure as a non-uniform, asymmetric matrix of phase retarders. It is much simpler to approximate amplitude masking of the SLMs with either a "slide" surface or by inserting an obscuration at the SLM surface.

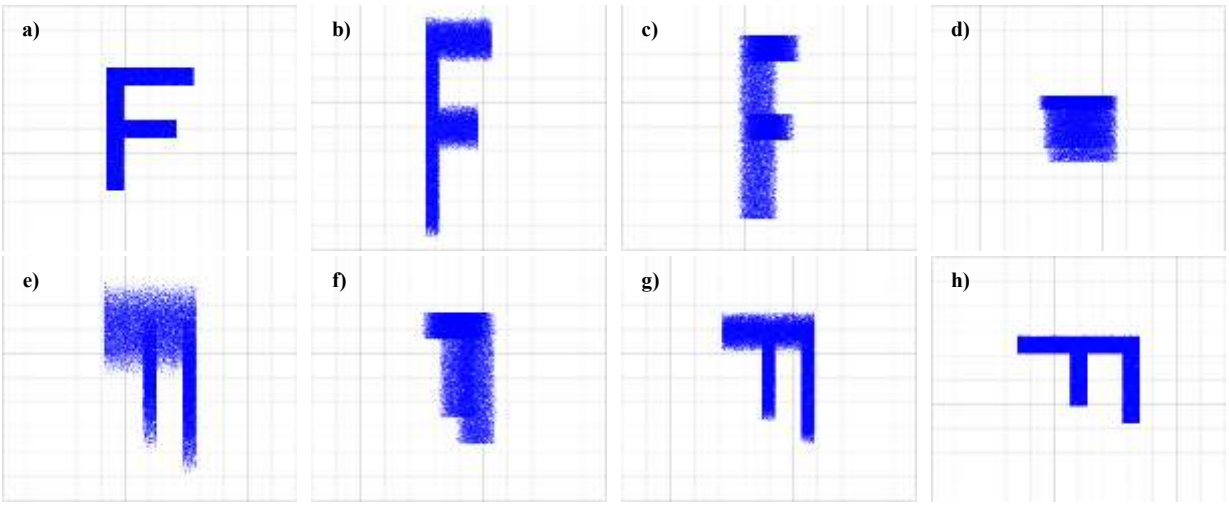


Figure 4.6: The ray-traced separation of orthogonal image planes throughout the system. a) Initial object b) 1st IIP_x plane c) 1st SLM plane d) 1st IIP_y plane e) 2nd IIP_x plane f) 2nd SLM plane g) 2nd IIP_y plane h) final image plane

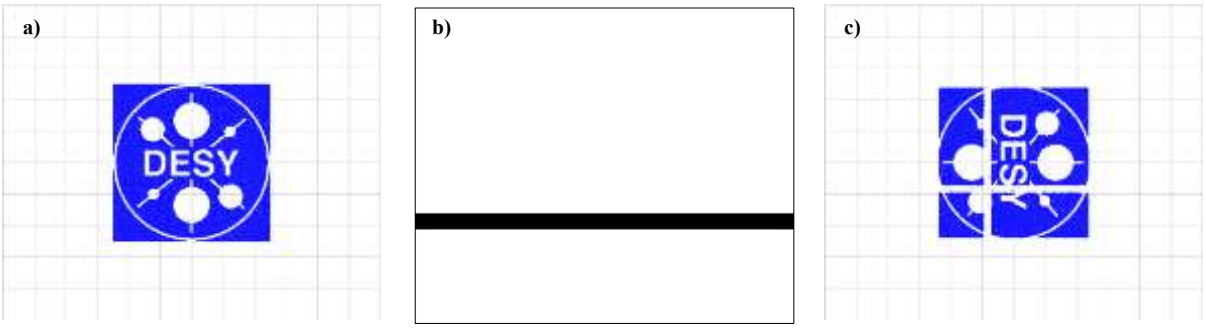


Figure 4.7: Validation of image transfer with a binary transmission mask 'slide' at the SLM surfaces. a) input image b) binary transmission mask c) output image

As can be seen from a ray tracing simulation (Figure 4.7) the spatial information is successfully transferred and the orthagonal symmetry of the SLM mask is evident.

4.1.2 Matlab numerical simulations

MATLAB, an abbreviation of matrix laboratory, is a script-based numerical computing environment specializing in multi-dimensional matrices [81]. This makes it particularly useful for volumetric numerical simulations.

The first undertaking in mathematical modelling of the system was calculation of the required masks and subsequent laser pulse properties. This is easier to conceptualize by first considering the complex spectral solution to the full volumetric distributions in an imaginary three-dimensional shaper with active voxels, and then determining the solution for the realistic planar device.

To do this the electric field of the input pulse was taken as a chirped, Gaussian laser pulse of truncated at R_c; an approximation to the illumination of an aperture with an oversized Gaussian pulse [82]:

$$\varepsilon_{input}(x,y,t) = e[x,y] \cdot e^{-\frac{t^2}{4\beta\gamma}} e^{-i\omega_0 t} e^{-at^2}, \tag{4.1}$$

where:

$$\beta = \frac{{\Delta t_{in}}^2}{8\ln(2)}, \tag{4.2}$$

$$\gamma = 1 + \frac{{\varphi_2}^2}{4\beta^2}, \tag{4.3}$$

$$a = \frac{\varphi_2}{8\beta^2\gamma}, \tag{4.4}$$

and the transverse radial components are the superposition of an nth-order, super-Gaussian and Gaussian distributions:

$$e[x,y] = e^{-\left|\sqrt[n]{\ln 2}\sqrt{\left[\frac{x}{R_c}\right]^2+\left[\frac{y}{R_c}\right]^2}\right|^n} e^{-\frac{(x+y)^2}{2\sigma^2}}. \tag{4.5}$$

Δt_{in} and φ_2 are respectively the FWHM of the input pulse and spectral chirp the latter of which can be determined from (2.49). A chirped pulse introduces a spectral-temporal correlation.

Similarly, the electric field of the goal pulse was defined as a chirped ellipsoidal pulse with an axially proportional nth-order, super-Gaussian distribution, with R_e and τ being the transverse radius and longitudinal radius, respectively:

$$\varepsilon_{goal}(x,y,t) = e[x,y,t] \cdot e^{-i\omega_0 t} e^{-at^2}, \tag{4.6}$$

where

$$e[x,y,t] = e^{-\left|\sqrt[n]{\ln 2}\sqrt{\left[\frac{x}{R_e}\right]^2+\left[\frac{y}{R_e}\right]^2+\left[\frac{2t}{\tau}\right]^2}\right|^n}. \tag{4.7}$$

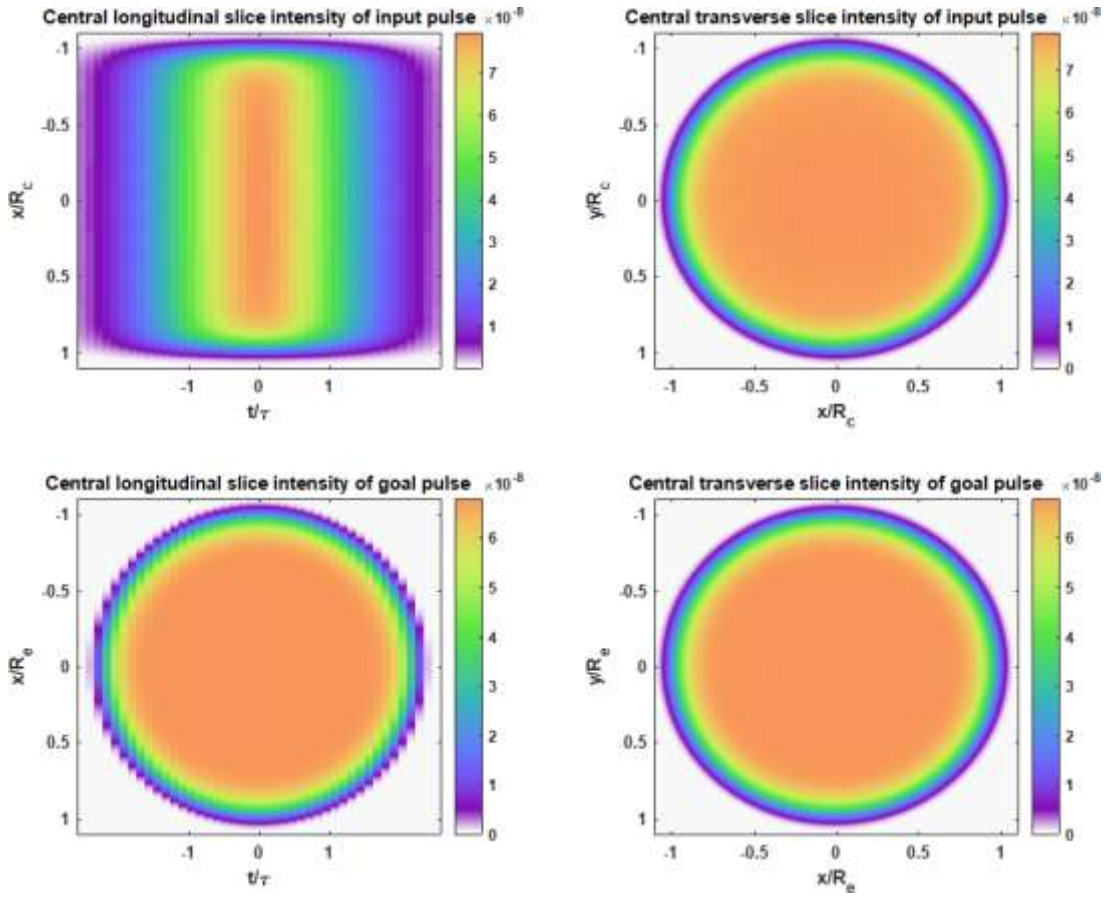


Figure 4.8: Transverse and longitudinal slices of the input and goal pulses.

It is immediately apparent from the longitudinal and transverse slices (Figure 4.8) that there should be a 'best-fit' for carving the longitudinal component of the ellipsoid from the Gaussian temporal envelope of the input pulse. The initial complex volumetric spectral mask $\tilde{M}_{3D}$ (Figure 4.9) with complex frequency ϑ required to generate the goal pulse can then be computed by taking the Fourier transformation across the temporal dimension and dividing one by the other:

$$\widetilde{M}_{3D}(x, y, \vartheta) = \frac{\hat{f}(\varepsilon_{goal})}{\hat{f}(\varepsilon_{input})}. \tag{4.8}$$

The solution is somewhat intuitive. The mask attempts to simultaneously carve out an ellipsoid and homogenize the temporal intensity variance. The former can be seen by the overall elliptical envelope of the mask and the latter can be seen by the higher attenuation in the center of the amplitude mask than the tails.

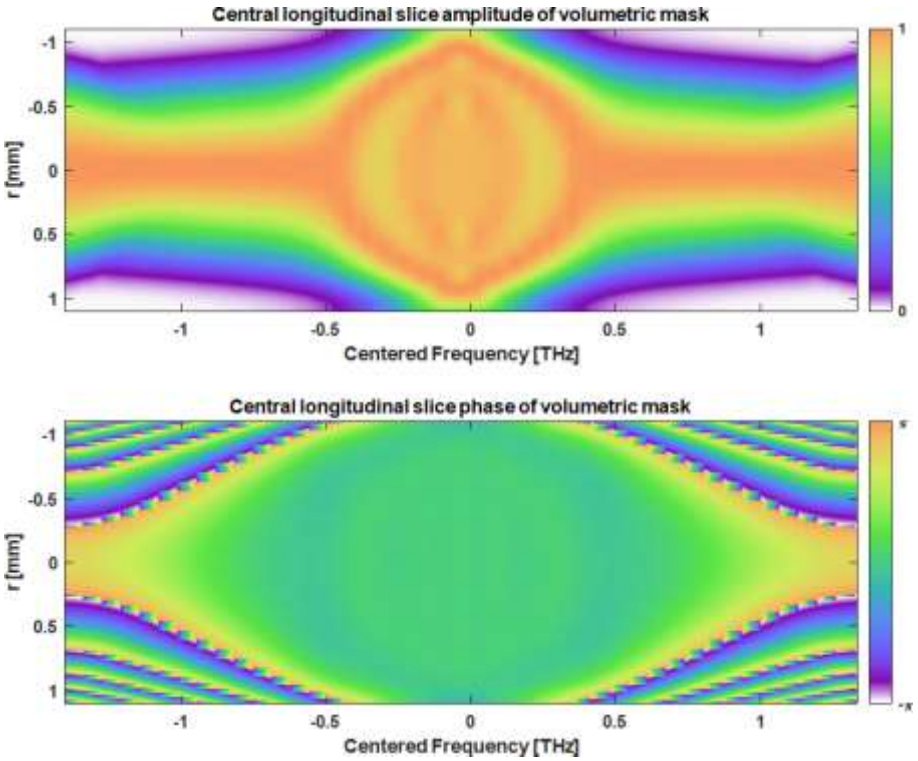


Figure 4.9: Longitudinal amplitude (above) and phase (below) slices of the normalized volumetric mask $\widetilde{M}_{3D}$ for a chirped input pulse and correspondingly chirped goal pulse.

Of course, this is a volumetric solution which cannot be applied in reality. SLMs are planar devices with a geometrically limited bandwidth that modulate phase or amplitude, therefore a pair of SLMs is required to apply both parts of any complex solution. Furthermore, a second pair is required to apply any solution in the orthogonal transverse direction.

The solution must therefore be recalculated for the planar devices, the SLMs, which perform the action in the X-λ, and Y-λ planar projections (Figure 4.10).

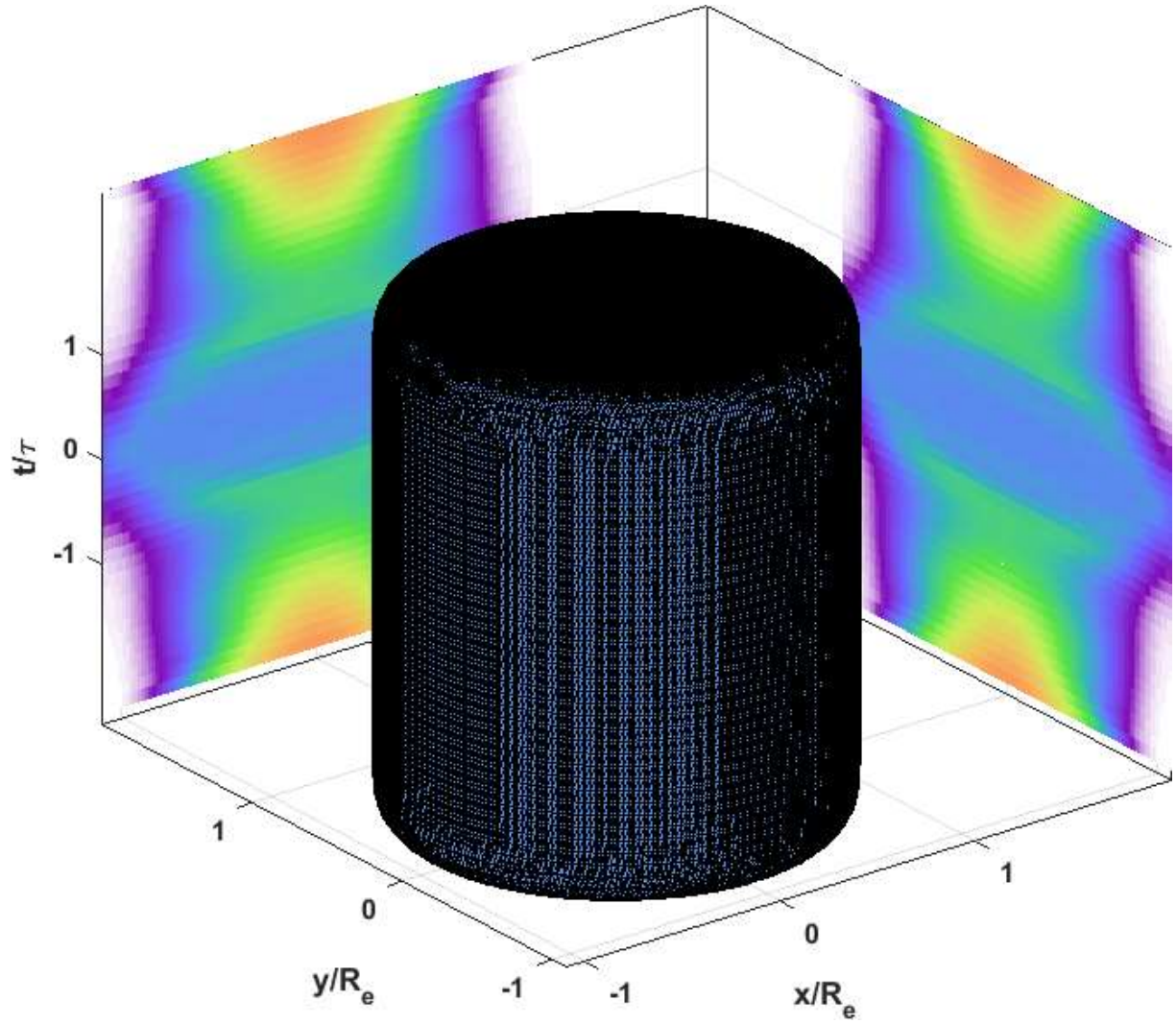


Figure 4.10: Attenuation masks projected transversely across the pulse (phase masks not shown).

As the distributions are rotationally symmetric any longitudinal slice solution around the Z axis is valid, but owing to the repeating shaping scheme required to access both transverse directions it is applied across both orthogonal transverse volume projections and must be rescaled to produce the correct results:

$$\widetilde{M}_{2D} = \frac{\widetilde{M}_{3D}(r,\vartheta)}{\sqrt{\widetilde{M}_{3D}(0,\vartheta)}}, \tag{4.9}$$

where $\widetilde{M}_{3D}(r,\vartheta)$ is the full volumetric mask, and $\sqrt{\widetilde{M}_{3D}(0,\vartheta)}$ is the rescaling factor along the longitudinal axis. Each transverse component is rescaled by the root of the peak intensity located at the center (Figure 4.11).

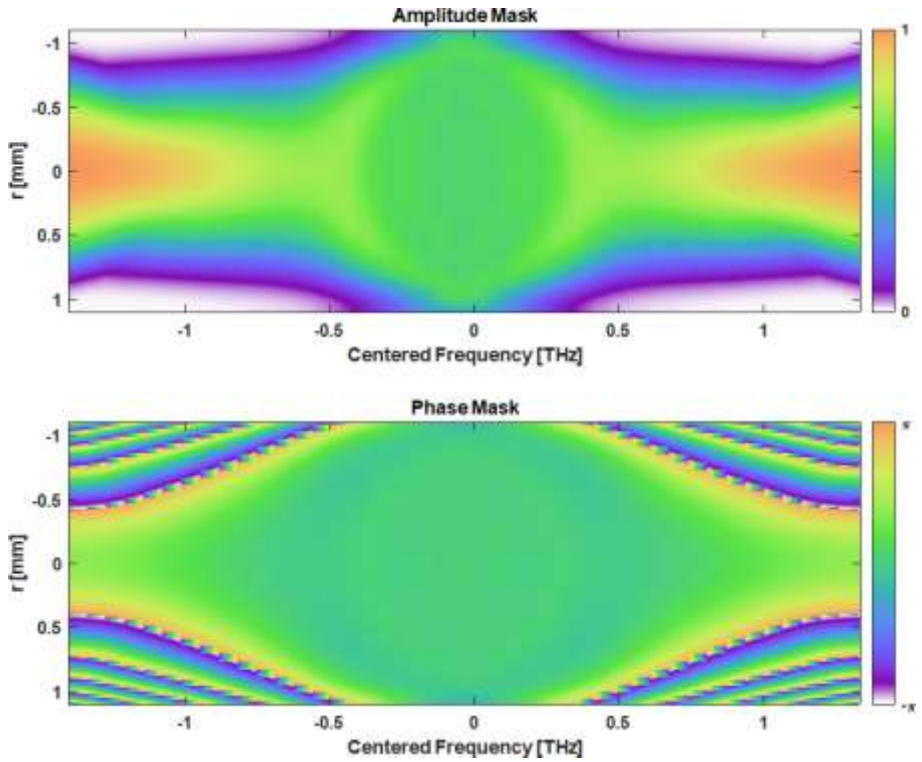


Figure 4.11: Normalized amplitude (above) and phase (below) masks for a homogenous cylindrical input pulse.

Both orthogonal longitudinal (x-λ, y-λ) planes impinging normally to the same planar mask will experience the scaled normalization mask as the mask (or the beam) is effectively rotated π/2 around the Z axis:

$$\hat{f}(\varepsilon_{ouput}) = \hat{f}(\varepsilon_{input})\widetilde{M}_{2D}. \tag{4.10}$$

The inverse Fourier transform then returns the modified electric field of the output pulse and it can then be evaluated as intensity I is proportional to the absolute value of the complex electric field:

$$I = \left|\hat{f}^{-1}\{\hat{f}(\varepsilon_{ouput})\}\right|^2. \tag{4.11}$$

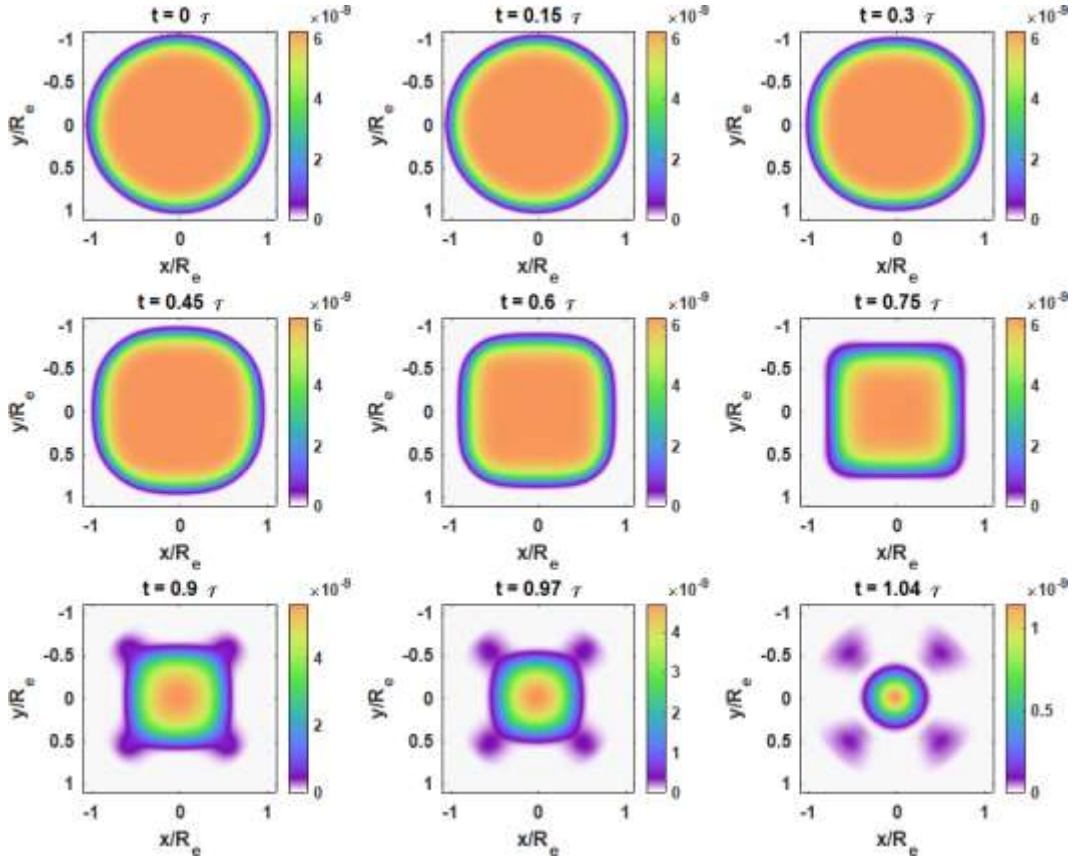


Figure 4.12: Transverse slices of the resulting produced pulse.

It is evident from the transversal slices (Figure 4.12) and volumetric plots (Figure 4.13) that the orthogonal nature of the shaping schemes imparts quadrilateral symmetry.

Furthermore, given the 2π phase range limitation of the commercially available SLMs, and the additional complication of utilizing two SLMs in parallel, it is also worthwhile to consider the result of amplitude-only masking. It is simple to reapply the generated amplitude masks, omitting the phase mask, back onto the initial pulse and evaluate the results.

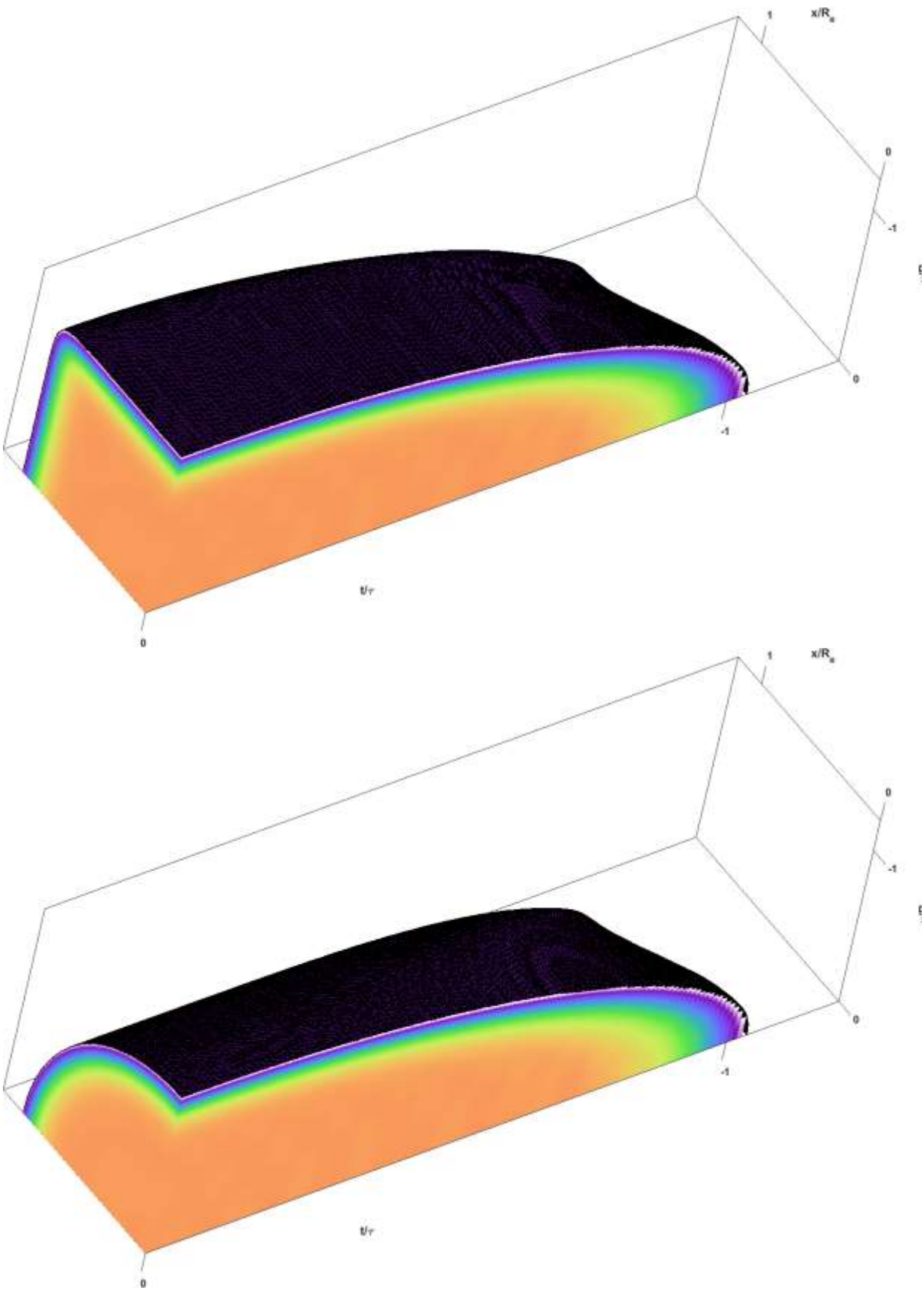


Figure 4.13: Volumetric plots of an a) un-cropped, and b) aperture-cropped quasi-ellipsoidal pulse.

It can be seen (Figure 4.14 & Figure 4.15) that the pulses generated with only planar amplitude masks contain peak-to-peak ripple along both transverse and temporal axes of 3.92% and 8.85%, respectively.

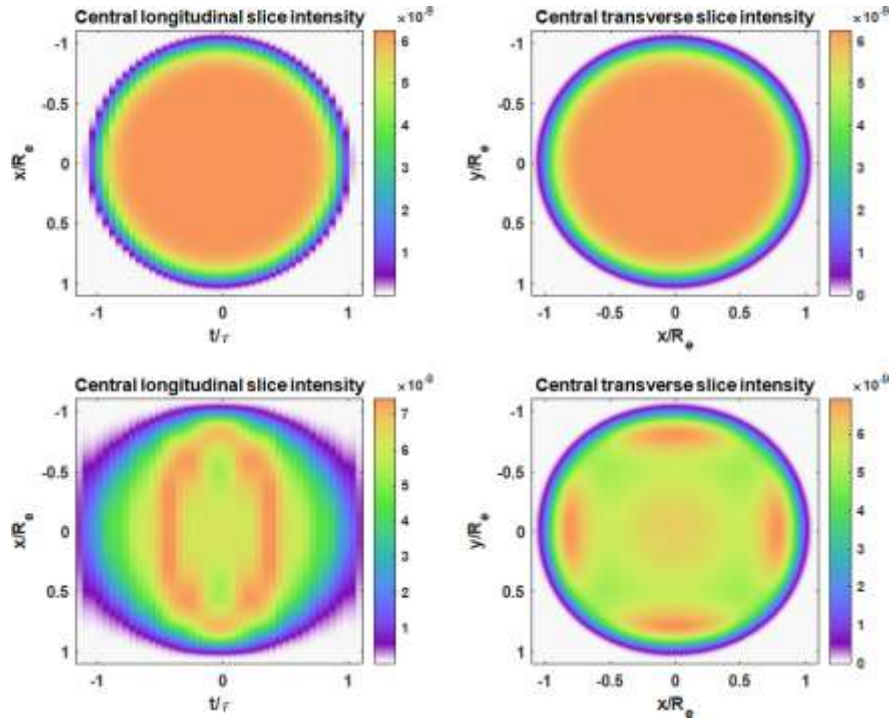


Figure 4.14: Transverse and longitudinal planar cuts of the intensity for the generated pulse with (upper plots) and without phase masking (lower plots).

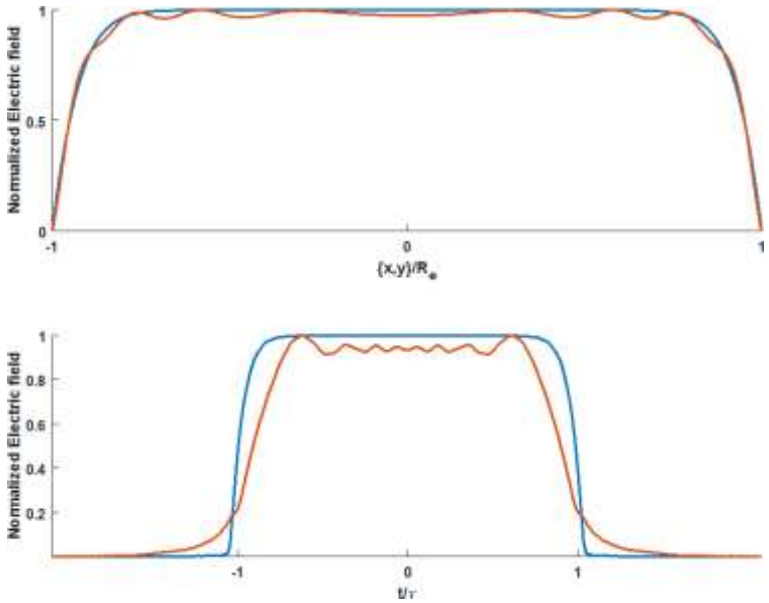


Figure 4.15: Comparative plots of the normalized intensity along the radial (top) and temporal axis (bottom) for generated ellipsoids with (blue) and without (red) phase masks. Transversal peak-to-peak ripple: 3.92%, and longitudinal peak-to-peak ripple: 8.85%.

Given that the full, complex volumetric spectral mask can be computed for any arbitrary input pulse and goal pulse it becomes trivial to numerically compute the efficiency for either imaginary volumetric masking or the realistic two-planar masking scheme.

4.1.3 Efficiency

An initial estimate of the efficiency of the pulse shaping scheme can be obtained by considering the planar geometries. For a Gaussian input beam with geometric rotational symmetry about the propagation axis and a Gaussian temporal envelope the maximum cutting efficiency can be found for various topologies.

The intensity, or energy "density", at a point is given by the standard normalized Gaussian distribution:

$$I(u) = \frac{1}{\sigma_u \sqrt{2\pi}} e^{-\frac{u^2}{2\sigma u^2}}, \tag{4.12}$$

where u = {r,t}, and r and t are the radial and temporal components.

Consider the normalized multi-dimensional Gaussian surface (Figure 4.16):

$$I(r,t) = \frac{1}{\sigma_r \sigma_t 2\pi} e^{-\frac{r^2}{2\sigma r^2}} e^{-\frac{t^2}{2\sigma t^2}}. \tag{4.13}$$

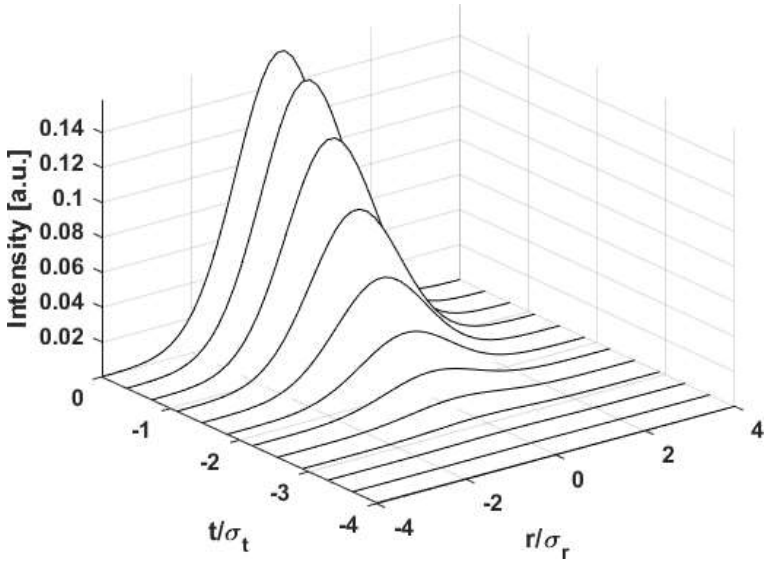


Figure 4.16: A time-varying Gaussian pulse with fixed geometric radius.

This corresponds to a series of transverse Gaussian "slices" with rotational symmetry whose intensity varies longitudinally (temporally) w.r.t a Gaussian envelope, with the intensity at any point is given by $I(r,t)$.

It can be easily seen that by comparing the transverse intensities, or instantaneous fluence, at t=0 and t = σ_t (Figure 4.17) that in order to have an equal transversal flattop intensity at both locations *with* equal radius that the intensity at σ_t is the minimum. The intensity at t=0 must be reduced to match, which is mirrored in the surface plots by the equal height of the inscribed flat-tops. By extending the same attenuation process for all temporal locations inbetween, mirroring it for -σ_t, and discarding the rest of the distribution, a cylindrical laser pulse is produced. It is then obvious that the upper limit of the homogenous intensity of a cylindrical pulse is limited by the ratio of radius and length.

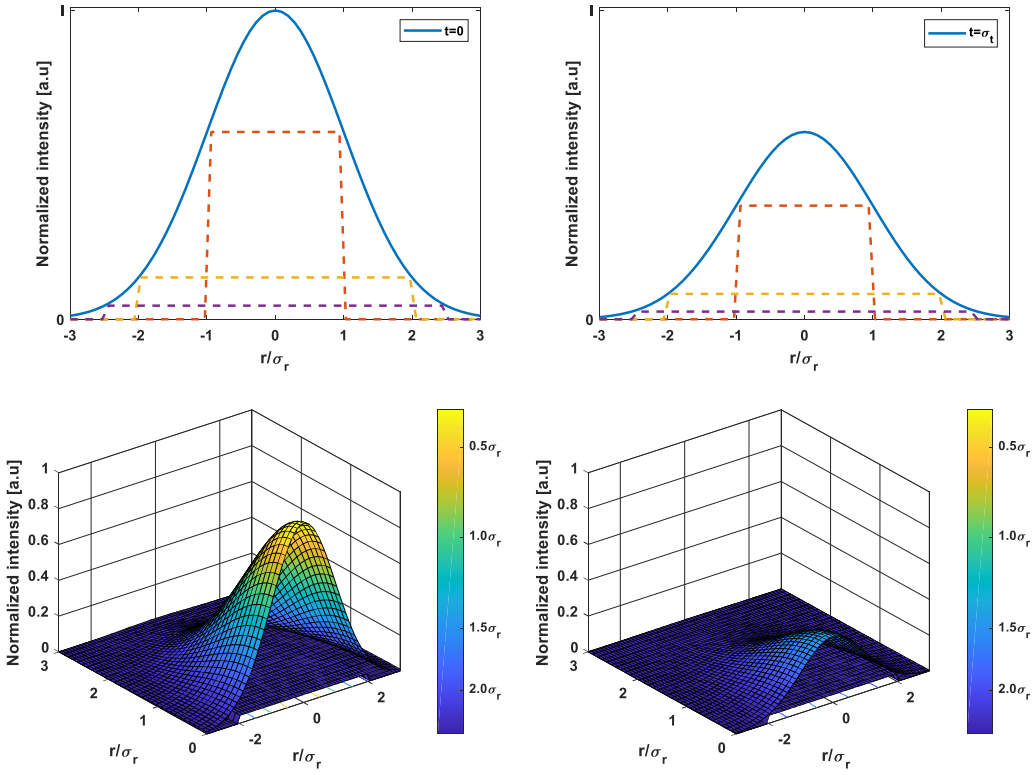


Figure 4.17: Radial cross sections and surface plots at t_0 (left) and σ_t (right) of a flattop transverse profile inscribed within a rotationally symmetric Gaussian pulse of normalized intensity.

This is represented by a series of flattops of equal height inscribed within the normalized multi-dimensional surface. It is also clear that there should be an ideal solution that maximizes the efficiency by the volume ($V = I \cdot r \cdot t$) contained within the series of flattops.

This is easily visualized (Figure 4.18) and can be shown that by cleaving the surface parallel to the base plane an ellipse is formed:

$$I(r,t) = e^{-\frac{r^2}{2\sigma r^2}} e^{-\frac{t^2}{2\sigma t^2}}, \tag{4.14}$$

substituting $a = \sqrt{2}\sigma_r$ and b= $\sqrt{2}\sigma_t$ then:

$$\frac{r^2}{a^2} + \frac{t^2}{b^2} = -\ln(I), \tag{4.15}$$

which is the general form of an ellipse.

By defining the major/minor axes as being along the coordinate system (t=0, r=0) the dimensions of the ellipse are given:

$$a(I) = \sqrt{-2{\sigma_r}^2 \ln(I)}\,, b(I) = \sqrt{-2{\sigma_t}^2 \ln(I)}. \tag{4.16}$$

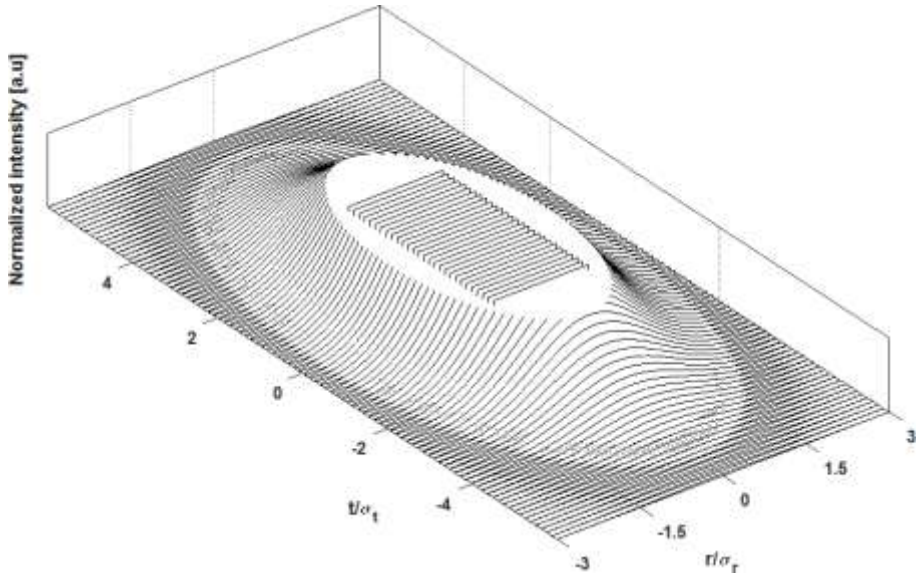


Figure 4.18: A cleaved Gaussian surface with a geometric flattop fit.

The optimal solution (see appendix D) to inscribe a rectangular volume within the Gaussian surface is found:

$$V(I, r, t) = e^{-1}\sigma_r\sigma_t. \tag{4.17}$$

The solution can now be extended to a cylindrical pulse in real volumetric space. This volumetric energy contained can be calculated from:

$$E_{cylinder}(r, t) = \pi r^2 e^{-\frac{r^2}{2\sigma r^2}} \cdot te^{-\frac{t^2}{2\sigma t^2}}. \tag{4.18}$$

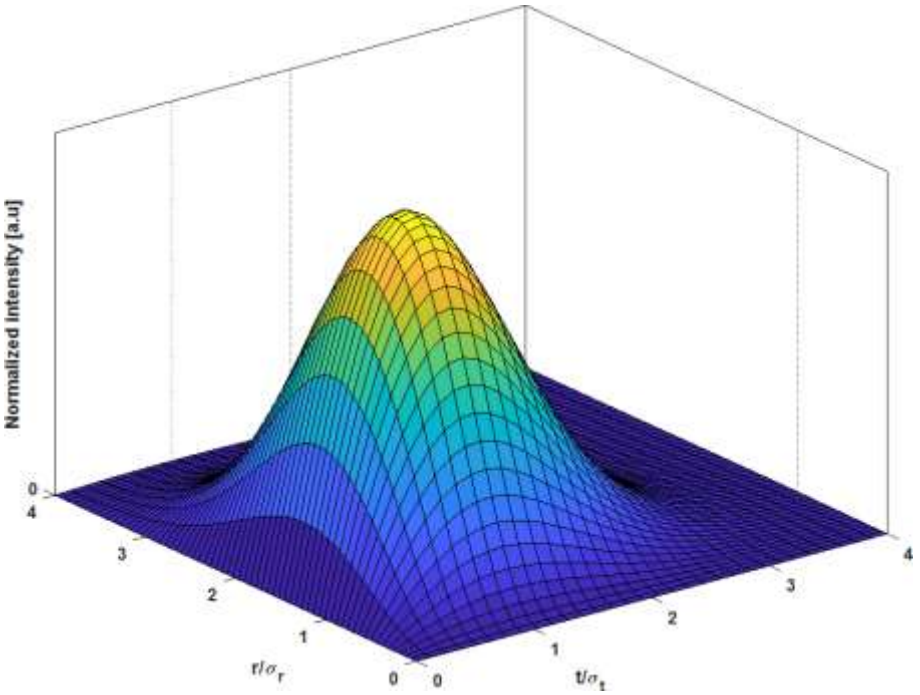


Figure 4.19: Normalized intensity surface for a cylindrical cut of varying length and radius for $\sigma_t = 2\sigma_r$.

The peak efficiency (Figure 4.19) is obtained by solving the simultaneous partial differential equations of the surface:

$$\frac{dE}{dr} = 0,\ \frac{dE}{dt} = 0. \tag{4.19}$$

Whose solutions are confirmed to be:

$$r = \sqrt{2}\sigma_r,\ t = \sigma_t. \tag{4.20}$$

$$E_{cylinder}\left(\sqrt{2}\sigma_r, \sigma_t\right) = 4\pi {\sigma_r}^2 \sigma_t e^{-\frac{3}{2}}. \tag{4.21}$$

The total efficiency can then be compared to the full volumetric input Gaussian integral:

$$E_{Gauss}(r,t) = {\sigma_r}^2 \sigma_t \sqrt{2\pi}^3, \tag{4.22}$$

which results in the peak efficiency obtainable for a cylindrical pulse *with* full volumetric shaping would be 17.8%.

This base concept can be further extended as an ellipsoid with transverse rotational symmetry, called a spheroid, can be considered as a series of flattops of constant intensity but with a temporally varying radius (Figure 4.20).

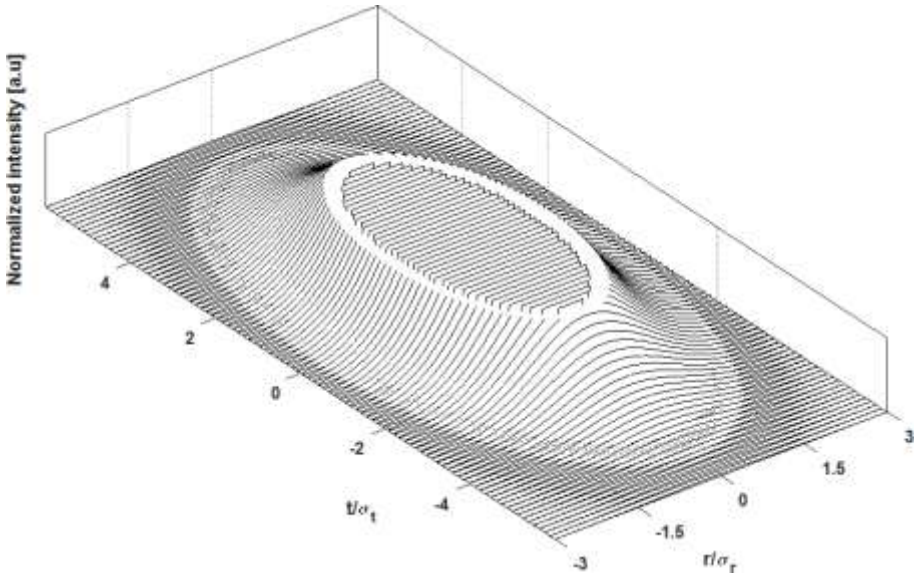


Figure 4.20: A cleaved Gaussian surface with a geometric elliptic fit.

It is immediately apparent that the cutting efficiency should be higher owing to the higher filling rate. The axes of the ellipse for an arbitrary intensity are already known and so the energy contained within the spheroid is simply:

$$E(I) = VI = \frac{4}{3}\pi a^2 bI. \tag{4.23}$$

It is then trivial to find the criteria for when this is maximized by insertion of the ellipse axes (4.16) and solving for dE/dI=0, which returns the criteria:

$$I = e^{-3/2}, \tag{4.24}$$

and the maximized energy contained within the pulse:

$$E(e^{-\frac{3}{2}}) = 4\pi\sqrt{3}{\sigma_r}^2 \sigma_t e^{-3/2}, \tag{4.25}$$

can then be compared to the Gaussian integral again and the efficiency calculated (Figure 4.21).

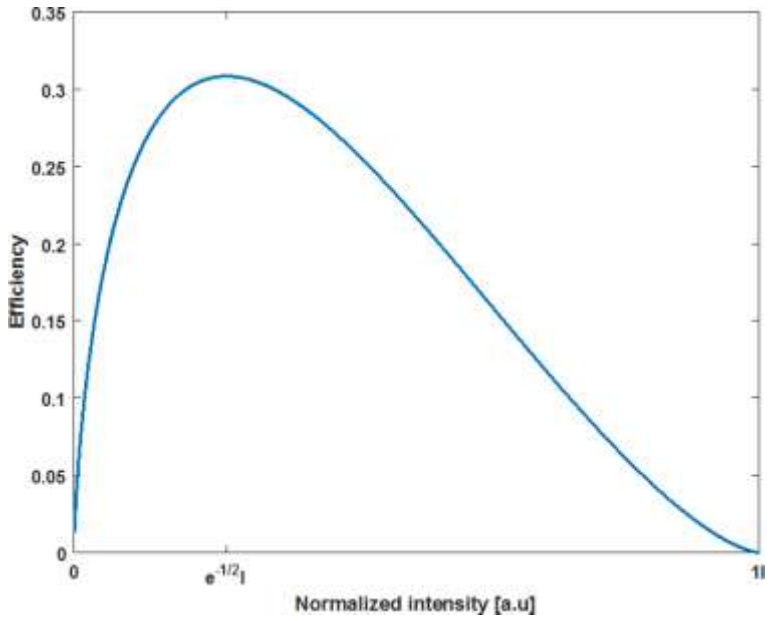


Figure 4.21: Efficiency curve for cutting a spheroid from a Gaussian pulse.

The maximum efficiency is found to be 30.8%. With a little work these solutions should be extendable to the asymmetric transverse case, but they only calculate the cutting efficiency in the ideal case of total volumetric control and should be taken as an estimate when working with projected masks. But they can be used as a starting point for numerical simulations with planar devices.

With these factors an estimate of the energy available for the non-linear conversion process is known and the expected pulse energy in the harmonics can also be determined.

4.1.4 Non-linear conversion

On the basis of non-linear optical theory preliminary simulations of non-linear conversion of the fundamental 1030 nm to its 515 nm and 257 nm harmonics were previously carried out by colleagues at Nizhny Novgorod [83] with their self-developed Matlab code.

In comparison, $Chi_2$3D [84] is a commercialized code for the propagation and modelling or ultrashort pulses in non-linear media. The former code was found to be in good agreement with $Chi_2$3D but with the advantage of significantly reduced computational overheads. This permits fast analysis of any arbitrary laser pulse. For example, the effect of crystal length, and angular chirp can be quickly determined (Figure 4.22).

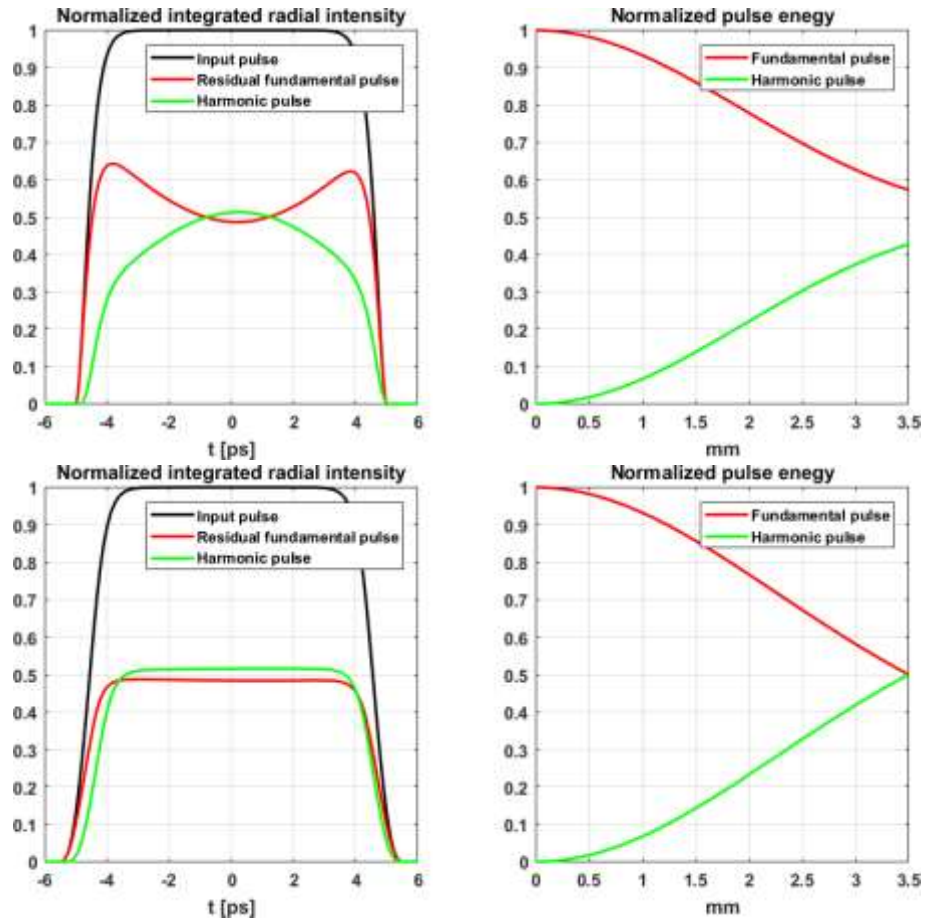


Figure 4.22: Longitudinal intensity (left) and efficiency curves (right) for harmonic conversion of a chirped, 1030 nm cylindrical pulse to its 515 nm harmonic in LBO with (bottom) and without (top) angular chirp matching..

Here, the impact of phase mismatch along the length of the chirped pulse can be seen and its overall influence on total efficiency. In the first plot, as only the central frequency (which corresponds to the center of the pulse), is properly phase matched, it can be seen the conversion efficiency varies along the length of the pulse and results in inconsistent conversion. In the second plot, in addition to deforming the pulse shape it also results in a reduced overall conversion efficiency as the pulse propagates through the crystal.

Conversely, the bottom plots contain an angularly-chirped pulse which conserves correct phase matching along the length of the pulse. It can be seen in the third plot that it maintains an almost constant conversion across the pulse duration. It therefore maintains the pulse shape and achieves ~10% more overall conversion efficiency as a result.

Furthermore, taking longitudal slices of the pulses (Figure 4.23) the phase front tilt induced by the angular chirp can be seen in the vertical y-t plane, along with the minor transversal walkoff of the harmonic pulse in the same plane. It can be seen again how angular chirp makes the longitudinal intensity more uniform by increasing conversion in the head and tail of the harmonic.

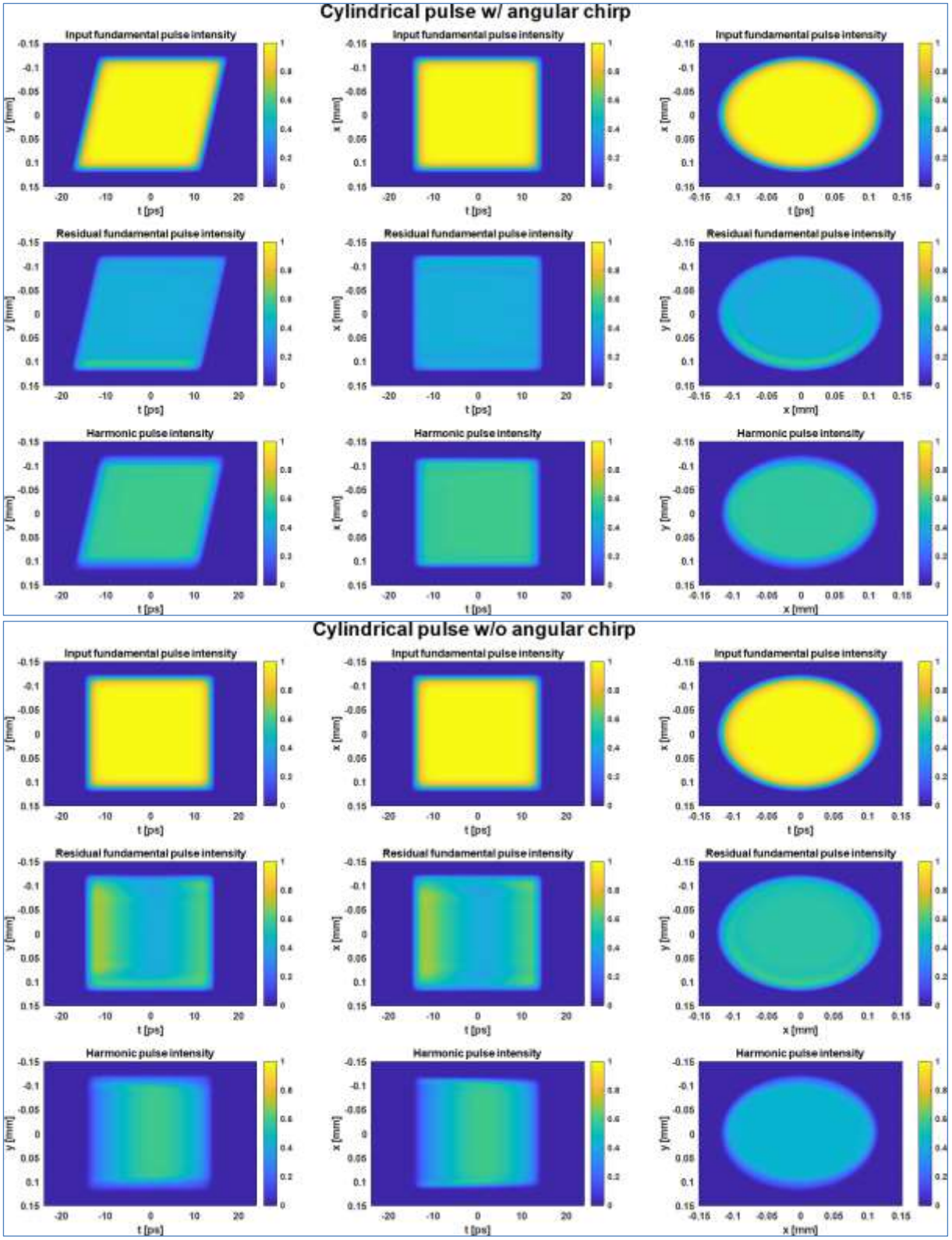


Figure 4.23: Longitudinal cross-sections (left, and middle) and normalized projections (right) for a 20 μJ, 30 ps, 1030 nm chirped cylindrical pulse (top), and its residual (middle) and harmonic (bottom) after conversion by 3.5 mm of LBO.

Applying the code to the uncropped quasi-ellipsoidal pulse (Figure 4.13) much the same results can be found for the same pulse energy and angular chirp (Figure 4.24). For the given parameters the efficiency is actually slightly higher (Figure 4.25) owing to the smaller volume, and therefore slightly higher intensity, of the quasi-ellipsoid.

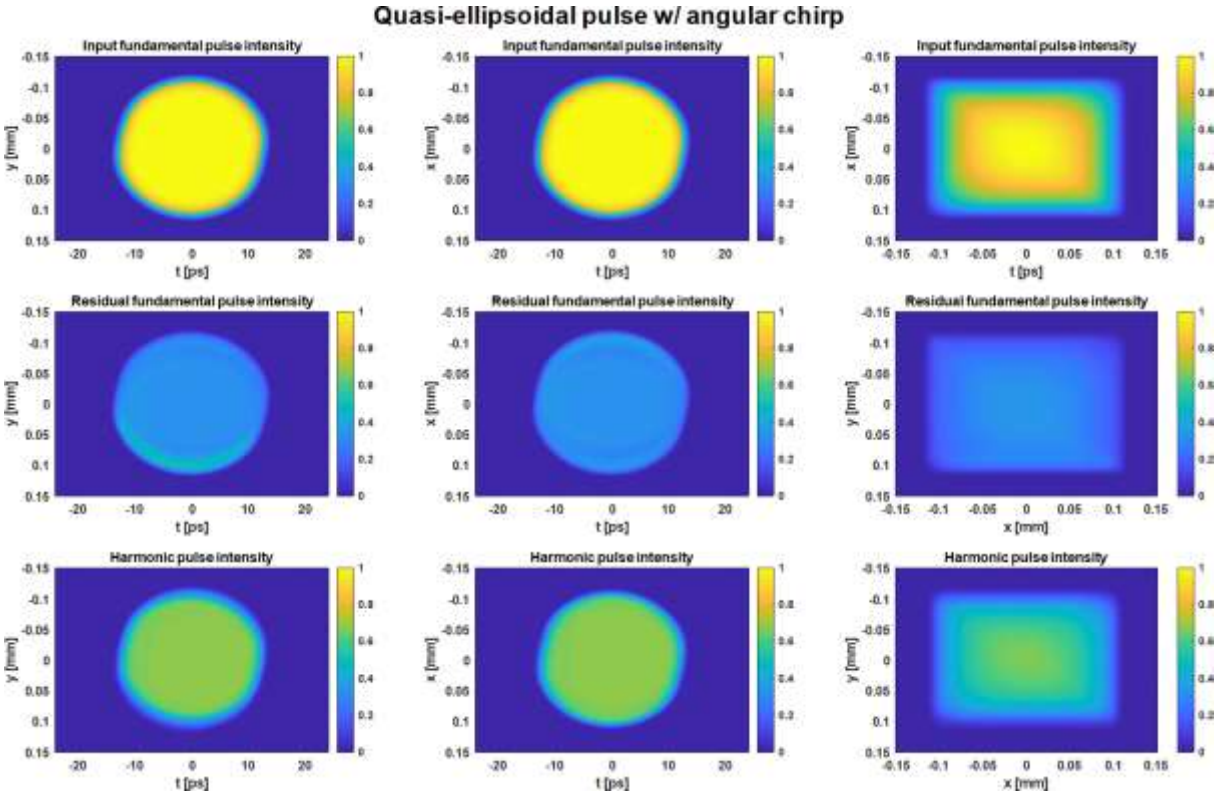


Figure 4.24: Longitudinal cross-sections (left, and middle) and normalized projections (right) for a 20 μJ, 30 ps, 1030 nm chirped quasi-ellipsoidal pulse (top), and its residual (middle) and harmonic (bottom) after conversion by 3.5 mm of LBO.

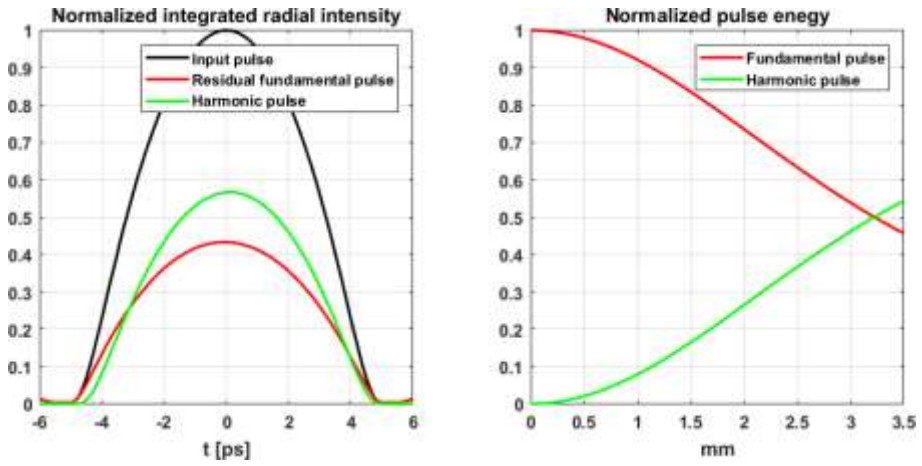


Figure 4.25: Longitudinal intensity (left) and efficiency curves (right) for harmonic conversion of a chirped quasi-ellipsoidal pulse in LBO.

4.1.5 Laser transport beamline

As stated previously in Sec. 2.7 the entire laser pulse shaping scheme rests on a foundation of telescopes that meet the imaging criteria. This concept follows on to the laser transport beamline to the accelerator tunnel and the photocathode.

After conversion of the shaped pulse it is necessary to transport it to the photocathode. The beam axis of the gun lies approximately 5.3 m underground of the laser table optical axis with a further ~6.8 m optical path in the accelerator tunnel itself.

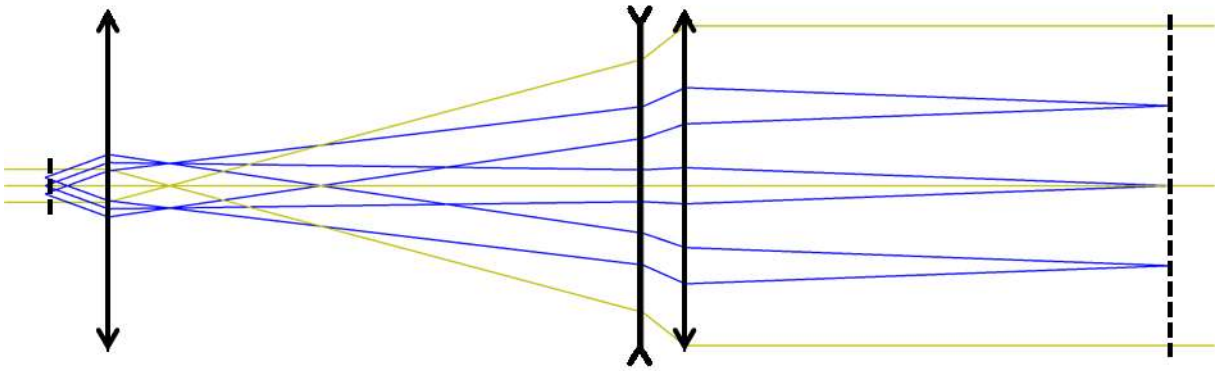


Figure 4.26: Generalized Galilean telescope utilized in the MBI transport beamline

The existing beamline [68] utilized to transport the MBI photocathode laser to the photoinjector is a 10x magnification three-element Galilean telescope (Figure 4.26) that images an intermediate image plane from the conversion crystals of the MBI laser to the BSA in the tunnel through a vertical shaft and projects a collimated laser beam onto the BSA.

In reality it consists of an on-table ⌀25.4 mm lens and two ⌀50.8 mm lenses in the shaft forming a ~14 m long imaging beamline (Figure 4.27) between the conversion crystals and the BSA.

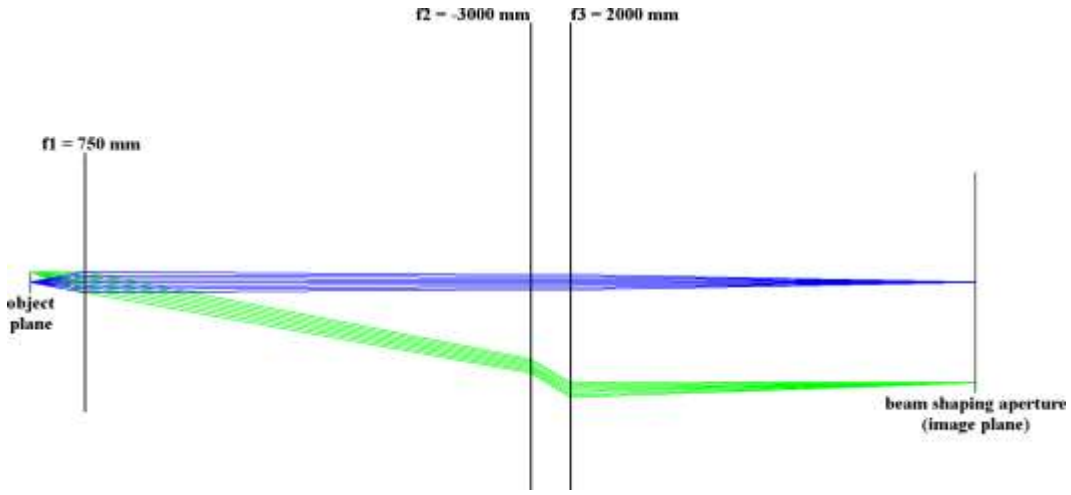


Figure 4.27: A rescaled (y/z = 150) OpticStudio simulation of the MBI beamline with a vertical field point 1 mm from the optical axis

In the accelerator tunnel the plane of the BSA was relayed onto the cathode 1:1 with a 6.88 m 4f Keplerian telescope but with each f1500 convex lens element decomposed into

⌀76.2 mm f±750 lens pairs (Figure 4.28). This was done as no optical elements could be situated in the last 4 m before the photocathode Furthermore, it is possible to observe the transverse distributions at the BSA and photocathode planes by inserting mirrors to produce an optically equivalent planes on two separate UV sensitive JAI cameras [85], entitled "vBSA" and "VC2", respectively.

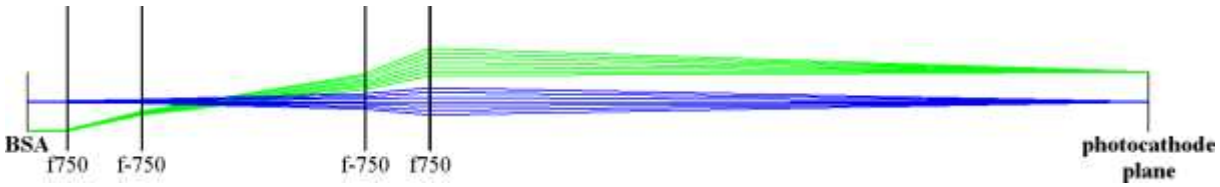


Figure 4.28: A vertically cropped and rescaled (y/z = 150) OpticStudio simulation of the tunnel relay beamline between the BSA and the photocathode plane with a vertical field point 0.6 mm from the optical axis

As this was the transport beamline for the primary MBI photocathode laser none of the relative in-line components for that system could be modified. This meant that the leeway in the design of the transport telescope for the ELLA system was heavily confined by the parameters of 10x imaging telescope already in place. Essentially, the only modifiable parameters were the focal length of the first on-table lens and pathlength between the object plane and the second f-3000 lens. However, the latter was confined to a minimum distance of >4.3 m in order to safely clear any walkways within the laser hutch. These parameters in turn dictate the object distance.

The final solution placed an on-table f2000 lens as the first lens on the ELLA optical table 10.16 m from the second lens of the laser transport beamline. This resulted in an object plane distance of 2.2 m, a magnification of 4x, and a total path length of almost 19 m.

In order to correctly match the beamsize into the transport beamline an on-table variable three-lens Keplerian telescope was utilized to couple in the image plane on the BBO crystal to the object plane of the transport beamline.

It can be useful to consider the transport beamline and the variable in-coupling telescope as 4f Kepelerian telescopes with one of the convex lenses decomposed into two lenses which can then be treated as a lens of variable focal length. For example, in Figure 4.29 the intermediary plane can be seen to shift to either side of the middle lens. Of course, with this design care must be taken not to place the middle lens at the focus of the collimated laser beam.

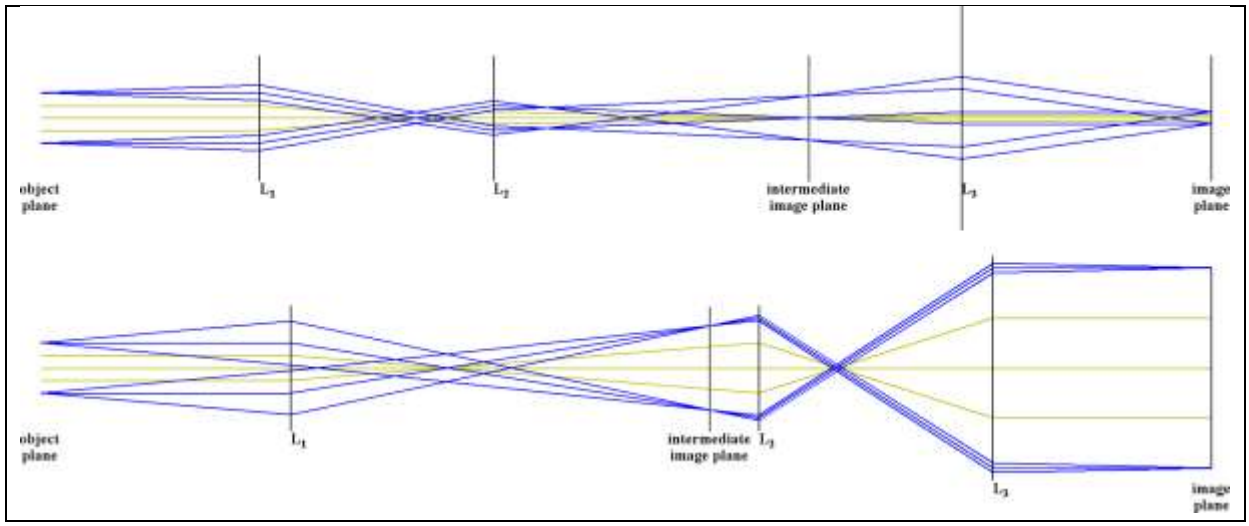


Figure 4.29: Relocation of an intermediate image plane on either side of the center lens in an example three-lens variable telescope at 4x demagnification (top) and 2x magnification (bottom).

The in-coupling was a f125:f50:f125 telescope with a possible magnification range of 0.5x-4x. By utilizing ABCD ray transfer matrices a set of simultaneous equations can be determined, and by fixing parameters and boundary conditions (total length, object distance, focal lengths, etc.) the solutions for a variable telescope can be calculated (Table 4.1). In this case the first lens was fixed and the locations and total length was permitted to vary within the limits of the optical table.

Table 4.1: Table of the in-coupling telescope magnifications and dimensions.

Image magnification	Object distance [mm]	f_1:f_2 distance [mm]	f_2:f_3 distance [mm]	Image distance [mm]	Total length [mm]
1/4	175	187.5	375	200	937.5
1/2	200	200	275	262.5	937.5
1	200	225	225	362.5	1013
2	200	275	200	450	1125
3	200	325	191.7	387.5	1104
4	200	375	187.5	175	937.5

In summary, the entire beamline from the image plane on the final BBO conversion crystal to the cathode plane can be considered as a chain of three imaging telescopes. The on-table, in-coupling telescope for matching the beamsize into the transport telescope, the modified transport beamline telescope that brings the image plane to the plane of the BSA, and the final telescope that images the BSA onto the photocathode.

4.2 ELECTRON BEAM DYNAMICS SIMULATIONS

ASTRA (A Space Charge Tracking Algorithm) is a DESY code available free of charge for non-commercial use [86]. It is a code used to track a bunch of “macro”-particles through the accelerator and their behaviour throughout as they experience various external fields and their

own internal space charge forces. This is done by Lorentz transformation of the grid into the rest frame, solving Poisson's equation, and transforming back into the laboratory frame. This can be done for either a cylindrical grid or fully Cartesian [87].

In particular for photoinjectors, it is highly desirable to evaluate the influence of space-charge forces near the cathode plane prior to full acceleration as this influences the balance of available charge and emittance, i.e. for the optimization of beam brightness.

In ASTRA, the fundamental PITZ setup is defined, for a given laser distribution, by the on-axial fields of the gun, booster, and solenoids (Figure 4.30). Additional magnetic and active elements can be included for more elaborate setups. The RF gradients are typically fixed to their nominal values of 60 MV/m at the cathode plane and 17.1 MV/m in the booster, and the phases are chosen as such to maximize the mean momentum gain of the bunch in both cavities.

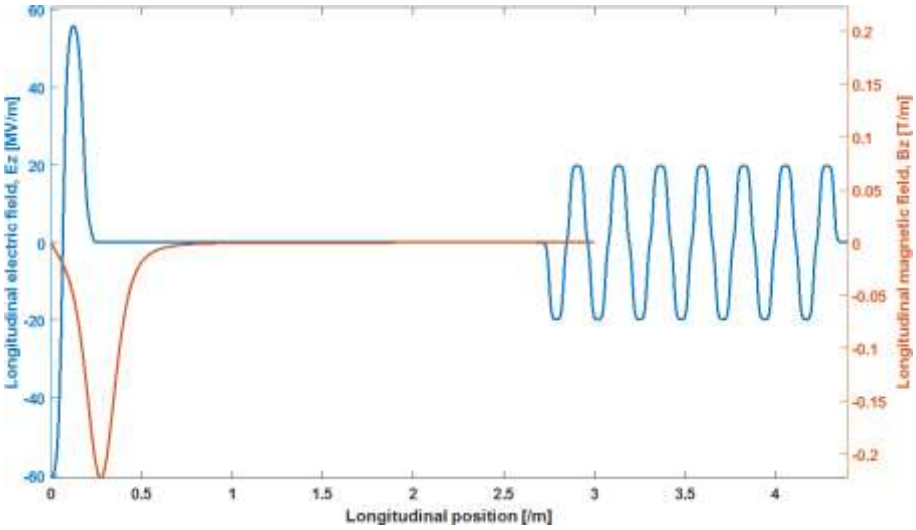


Figure 4.30: Typical longitudinal field components of the gun and booster (blue) and the main solenoid (red) used in ASTRA simulations.

The evolution of the bunch parameters is then tracked from the cathode to the desired z-position along the accelerator. Very often this is done to evaluate a single changing parameter, such as booster position, gradient, solenoid current, RF phase, bunch charge, laser distribution, etc. and its influence on the beam properties and to compare with experiment.

The bunch distributions under concern are the nominal ones typically available under experiment and real-world application and therefore it makes sense to consider them in simulation. The typical laser input distributions available are transversal quasi-flattops, produced by cropping the center of an oversized transverse Gaussian laser distribution by a variable aperture, with either a Gaussian temporal envelope of ~12 ps FWHM or a flattop super-Gaussian temporal profile of ~22 ps FWHM, and of course the ellipsoidal pulse (Figure 4.31) which is still under study with a comparable RMS pulse length and diameter.

These particle distributions are emitted at the photocathode plane and started correspondingly WRT to time of each macroparticle while calculating space charge forces and including image/mirror charge at the cathode plane.

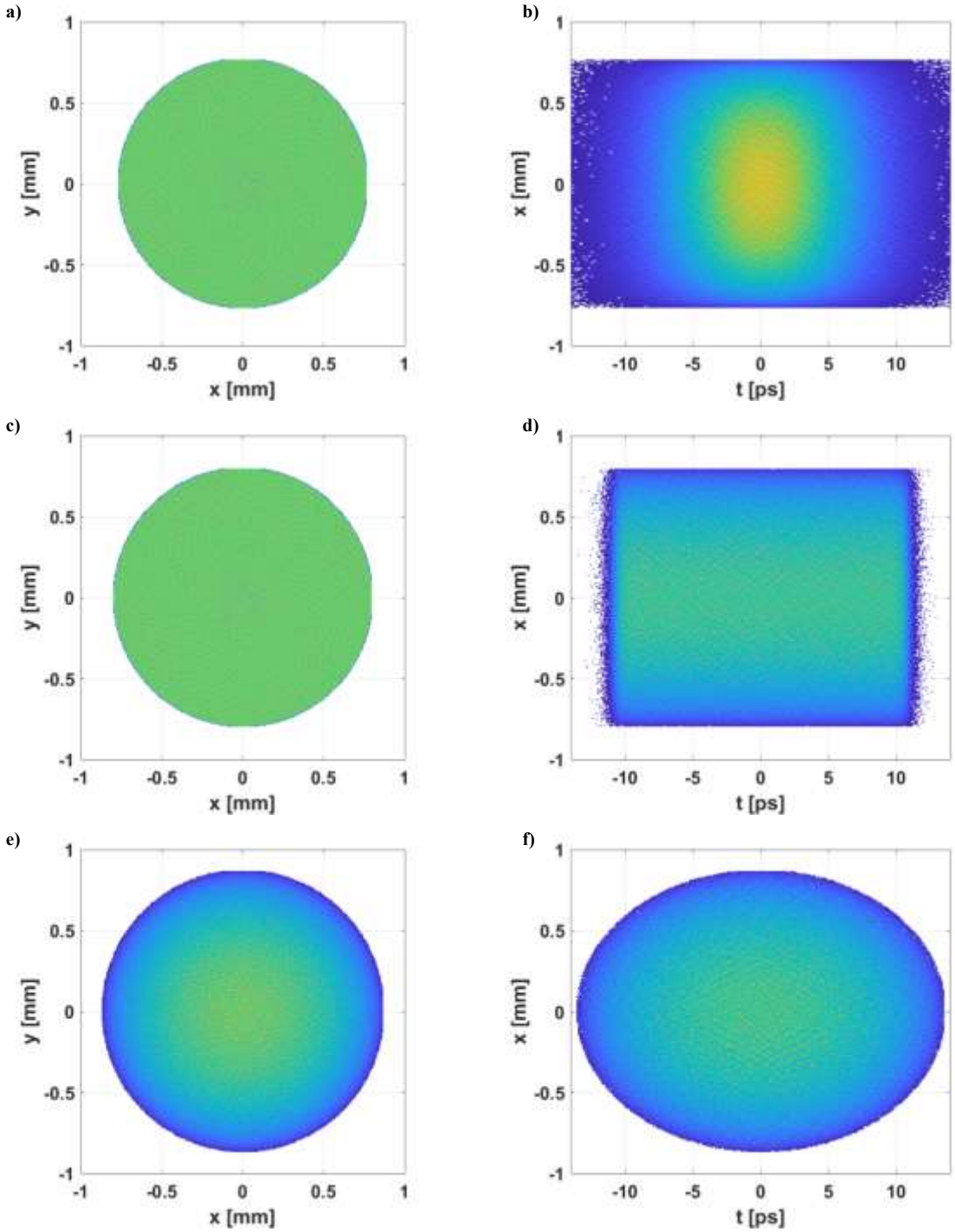


Figure 4.31: Transverse (left) and longitudinal (right) projections of the optimized ASTRA input particle distributions (Table 4.2), Gaussian (top), cylindrical (middle), and ellipsoidal (bottom).

4.2.1 Multi-charge bunches

A number of ASTRA simulations were performed [88] on various bunch charges in the PITZ injector setup to evaluate the performance of different laser pulse shapes and the subsequent bunches that they produce. In the course of this work these studies were repeated for the current PITZ setup and comparable results were found.

The parameters of the accelerating gradients in the machine (E_{cath}, φ_{cath}, E_{CDS}, φ_{CDS}) were initially fixed for all simulations for the various bunch charges to produce the same

momentum in the bunch. A multi-variate optimization was performed by "tuning" the main solenoid field, and varying the photocathode laser pulse dimensions (τ_{rms}, XY_{rms}) to produce electron bunches of the same RMS bunch length with minimized projected emittance at the position of the EMSY1 station 5.74 m downstream of the cathode plane (Figure 4.32).

It can be seen that the homogenous ellipsoidal input distribution offers a significant reduction in projected emittance in comparison to the traditional Gaussian temporal shape, and still an improvement when compared to the flat-top temporal envelope.

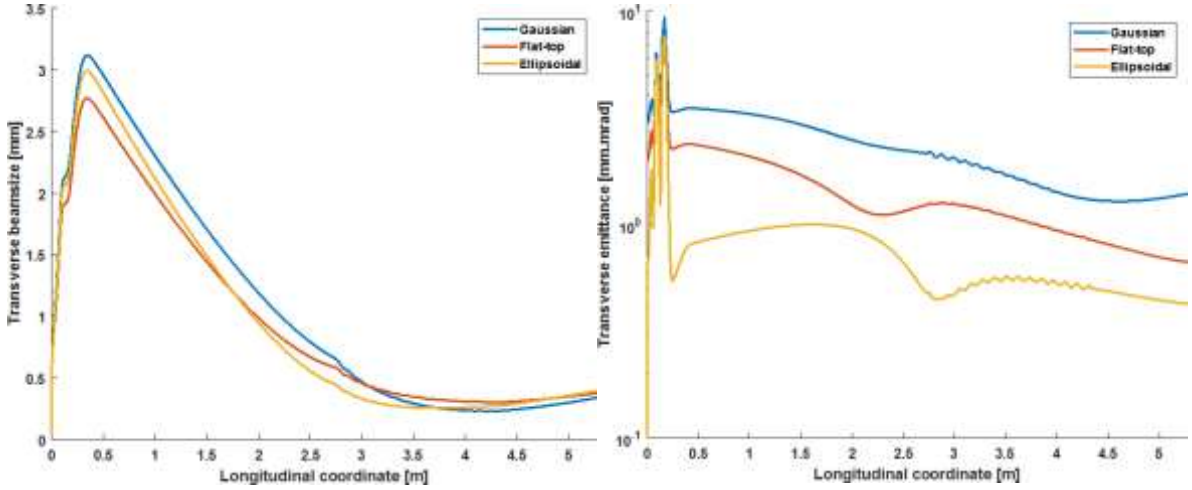


Figure 4.32: Beamsize (left) and projected emittance (right) of a 1 nC bunch along the photoinjector for various laser pulse shapes.

Similarly, an improvement in longitudinal emittance can also be seen, but where a significant difference can be seen is in the slice emittance (Figure 4.33). Unsurprisingly, the Gaussian temporal envelope results in a large central slice emittance due to the temporally varying charge density. Furthermore, the edge effect of non-linear space charge forces at the head and tail of the cylindrical bunch can be seen as respective emittance spikes at those locations. Only the smooth, linear space charge forces of the ellipsoidal bunch result in a smooth, minimized slice emittance along the entire bunch.

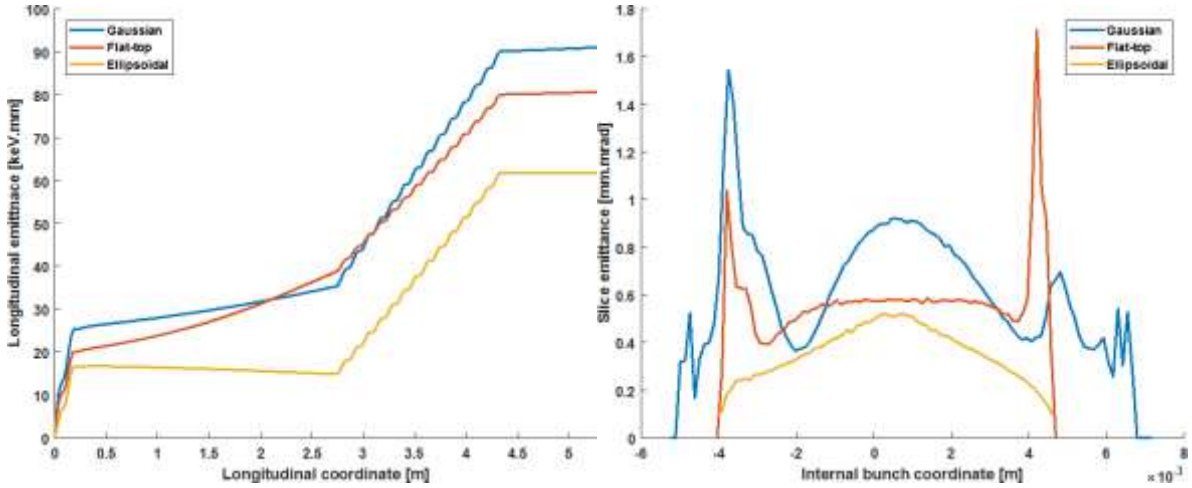


Figure 4.33: Longitudinal emittance (left) along the beamline, and slice emittance (right) along the electron bunch at EMSY1.

Table 4.2: Results of preliminary ASTRA simulations on shaped laser pulses.

Photocathode laser	Pulse shape→	cylindrical		ellipsoid
	Temporal profile→	Gaussian	Flattop	
	RMS pulse length	5.4 ps	6.272 ps	6.1 ps
	Transverse	Homogeneous radial		
	Optimized transverse size (RMS)	0.385 mm	0.401 mm	0.39 mm
RF gun	Electric field at the cathode (max)	60.58 MV/m (fixed)		
	Phase (w.r.t. MMMG)	0° (fixed)		
	Optimized solenoid peak field	-0.2275 T	-0.2279 T	-0.2297 T
Booster	Electric field (max)	19.76 MV/m (fixed)		
	Phase (w.r.t. MMMG)	0° (fixed)		
Electron beam (EMSY1, z=5.74)	Bunch charge	1.0 nC (fixed)		
	Beam mean momentum	23.96 MeV/c		
	Projected normalized emittance	1.08 mm·mrad	0.64 mm·mrad	0.42 mm·mrad
	Average slice emittance	0.78 mm·mrad	0.57 mm·mrad	0.39 mm·mrad
	Bunch length (RMS)	2.163 mm (fixed)		
	Peak current	35.4 A	39.5 A	37.8 A
	Longitudinal emittance	34 mm keV	22 mm keV	12.5 mm keV

Further studies were undertaken on the optimized beam parameters (Table 4.2) to determine the sensitivity of the bunch qualities to machine jitter and booster cavity location [88]. The projected emittance was taken as a figure of merit against variations in solenoid peak field, gun phase, laser spotsize, and beam momentum (Figure 4.34). It was found that for the correct booster location that the ellipsoidal bunch was typically less sensitive except for gun phase. The results prompted shifting of the booster cavity by 30 cm (3.0 m→2.7 m) and further simulations investigated the effect of bunch charge (Figure 4.35) with the optimized parameters.

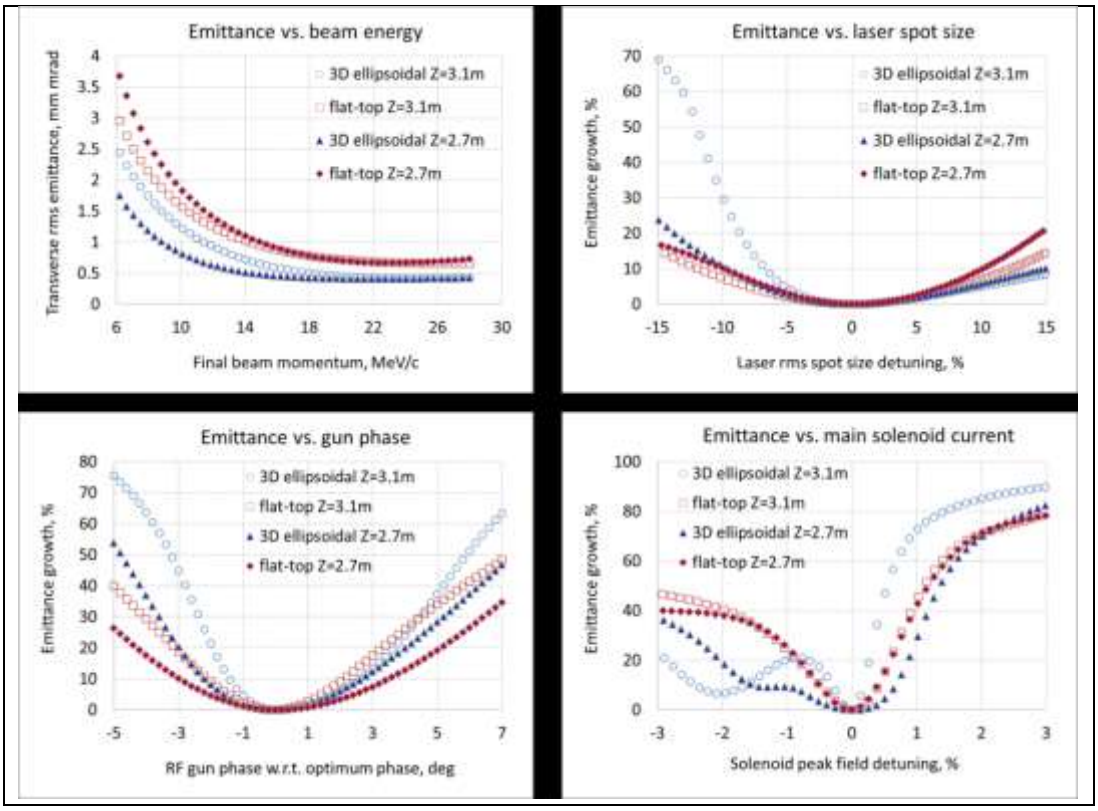


Figure 4.34: Emittance as a function of beam momentum, emittance growth as a function of deviation in the optimized parameters of laser spotsize, gun phase, and solenoid peak field for two booster cavity locations for ellipsoidal and cylindrical bunches [88].

This new booster position was then evaluated for optimized injector parameters yielding the lowest projected emittance for various bunch charges. As expected, the performance of the ellipsoidal bunch is superior due to the linearization of space charge forces.

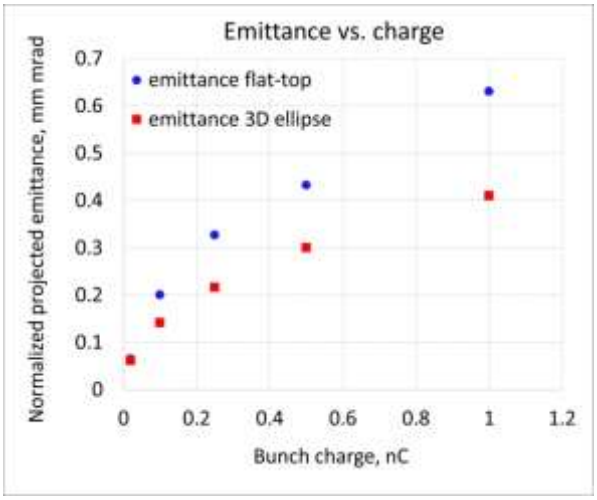


Figure 4.35: Transverse electron beam emittance for various bunch charges and laser pulse shapes. [89]

Finally, further studies were undertaken [27] to evaluate the emittance for different charges and to ascertain how susceptible beam quality was to possible edge deformation arising during the laser pulse shaping and conversion processes.

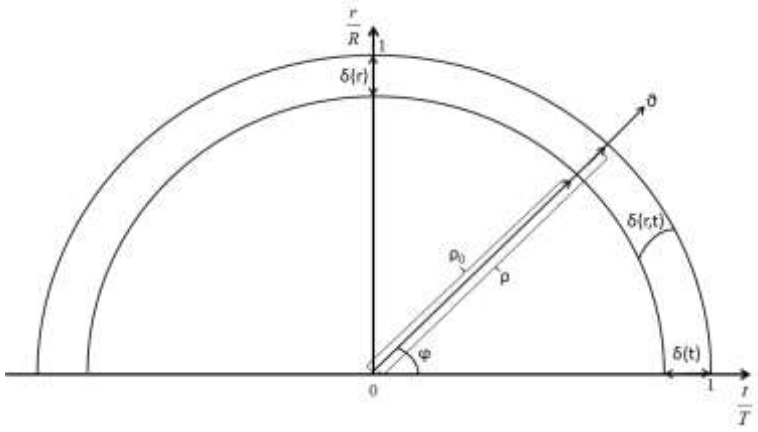


Figure 4.36: A radial cross-section of a spheroid with edge imperfections regions.

Here ρ_0 and ρ are the respective perfect and imperfect spheroid distributions with $\delta(r)$ and $\delta(t)$ being the radial and temporal border sharpness parameters (Figure 4.36), defined as:

$$\rho(r,t) = \sqrt{\left(\frac{r}{R}\right)^2 + \left(\frac{t}{T}\right)^2}, 0 \le r \le R, 0 \le t \le T, \tag{4.26}$$

$$\rho_0(r,t) = \sqrt{\frac{\left(\frac{r}{R}\right)^2}{(1-\delta_r)^2} + \frac{\left(\frac{t}{T}\right)^2}{(1-\delta_t)^2}}, 0 \le r \le R, 0 \le t \le T, \tag{4.27}$$

$$\delta(r,t) = 1 - {}^{\rho}/_{\rho_0}. \tag{4.28}$$

The final bunch charge distribution modelled in ASTRA (Figure 4.37) is then:

$$q = q_0 \begin{cases} \frac{1}{2} - \frac{1}{2}\sin\left[\pi\left(\frac{\vartheta-1}{\delta(r,t)} + \frac{1}{2}\right)\right], 1-\delta(r,t) \le \vartheta \le 1 \\ 1, \vartheta < 1-\delta(r,t) \end{cases}, \tag{4.29}$$

where q_0 is the initial bunch charge.

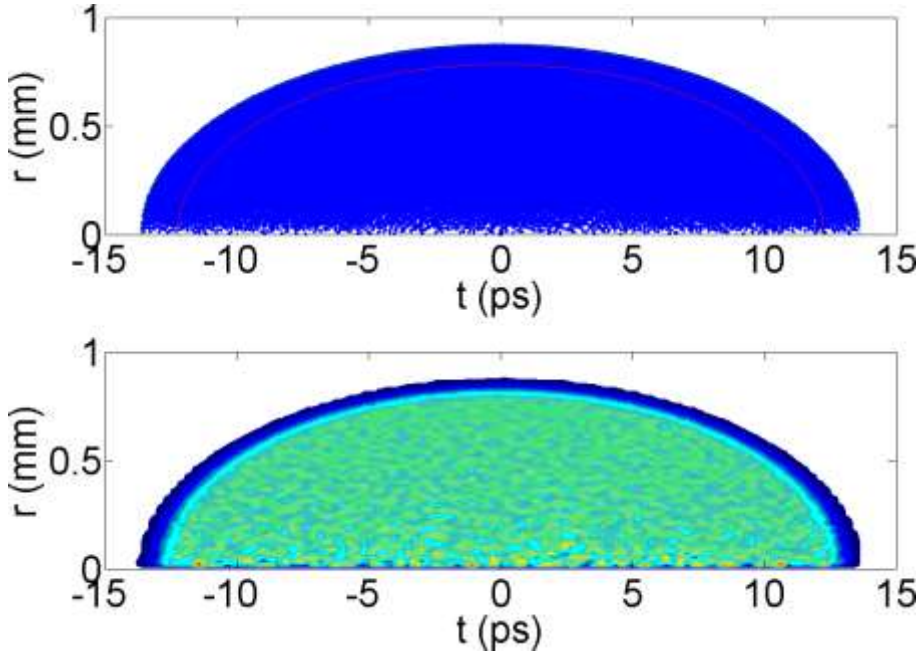


Figure 4.37: Border sharpness modelling in ASTRA w/ $\delta=0$ (top) and $\delta\neq0$ (bottom) [27].

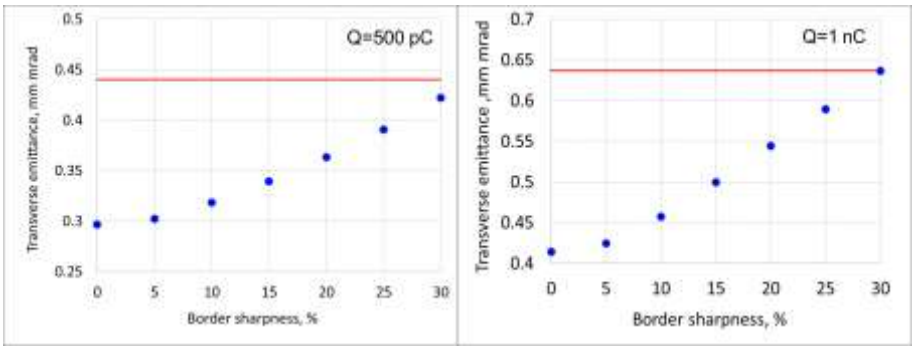


Figure 4.38: Projected emittance as a function of border sharpness for $\delta_t=\delta_r=\delta$ for 0.5 nC (left) and 1 nC (right) bunch charges [27].

It was found that the bunches of up to 1 nC (Figure 4.38) can suffer up to 30% border smearing concurrently in both the radial and temporal dimensions and still match cylindrical pulses in terms of emittance.

Furthermore, it was found that emittance growth was more sensitive to overall radial sharpness than temporal sharpness (Figure 4.39). It should kept in mind that radial sharpness affects the two transverse axes as opposed to the singular temporal axis and a degree of one-dimensional lateral smearing can be expected due to birefringent walk-off in the harmonic conversion process. The magnitude of such walk-off is compounded by the unique material properties and thickness of each crystal required as the walk-off direction is conserved and requires finding a balance between conversion efficiency and shape preservation.

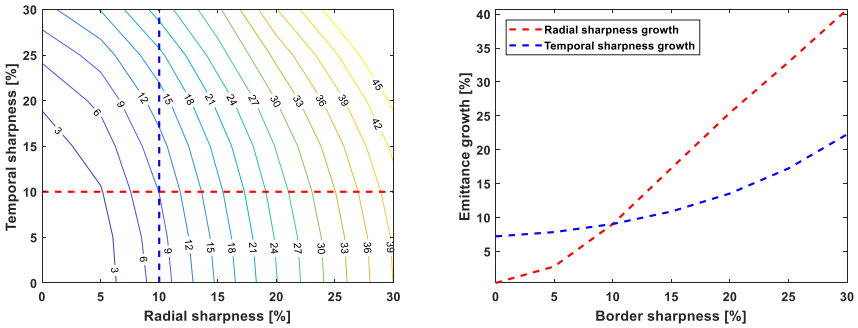


Figure 4.39 Emittance growth as a function of border sharpness parameters (left), and cross-sections of the emittance growth map for fixed sharpness (right).

4.2.2 Simulations of startup experiments at PITZ

In experiment significant pulse shortening (24 ps → 12 ps) originating from spectral distortions was experienced (Figure 5.25) which limited the equivalent electron bunch length and the maximum possible extractable charge. These combined effects effectively halved the laser pulse duration to <12 ps and limited the amount of charge that could be generated to ~0.5 nC.

Although the primary advantage of an ellipsoid is linearization of the space charge forces and therefore the primary benefit is for high charge bunches in the nC range, it was still expected from previous simulations to see improvements at 0.5 nC (Figure 4.35). However, those previous simulations were done for comparable nominal pulse lengths of ~20 ps.

Therefore it was instructive to repeat the ASTRA optimizations for various pulse shapes at 0.5 nC and shorter pulse lengths of 9.5 ps for experimental comparison. [90]

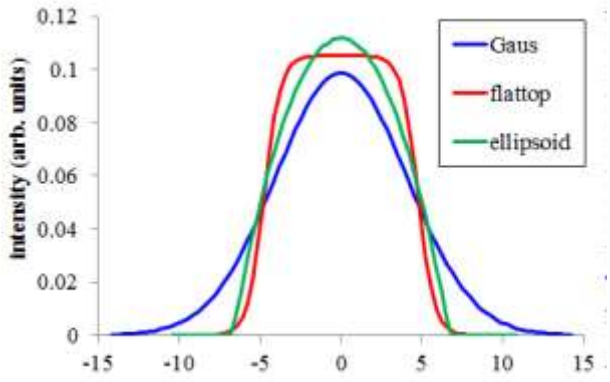


Figure 4.40: Laser pulse envelopes of equivalent FWHM duration (9.5 ps) [90].

Three pulse shapes were considered, two pulses with radially homogenous transverse distributions and either a flat-top or Gaussian temporal envelope as well as an ellipsoidal, all three cases had equivalent FWHM durations of 9.5 ps (Figure 4.40).

These distributions were tracked from the cathode plane, through the booster to the position of projected emittance measurement, EMSY1, and a scan of the main solenoid current, the gun phase, and the laser spotsize on the cathode was done to find the minimum projected emittance (Figure 4.41).

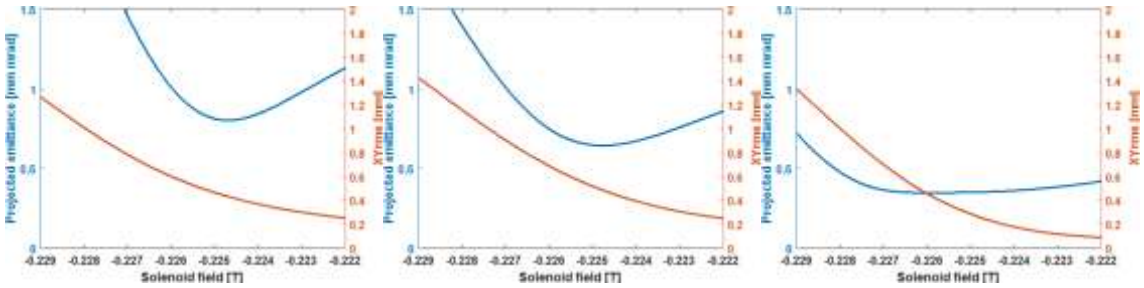


Figure 4.41: Example scans of the main solenoid for transverse emittance and beam spotsize at EMSY1 for Gaussian (a), flat-top (b). and ellipsoidal distributions (c).

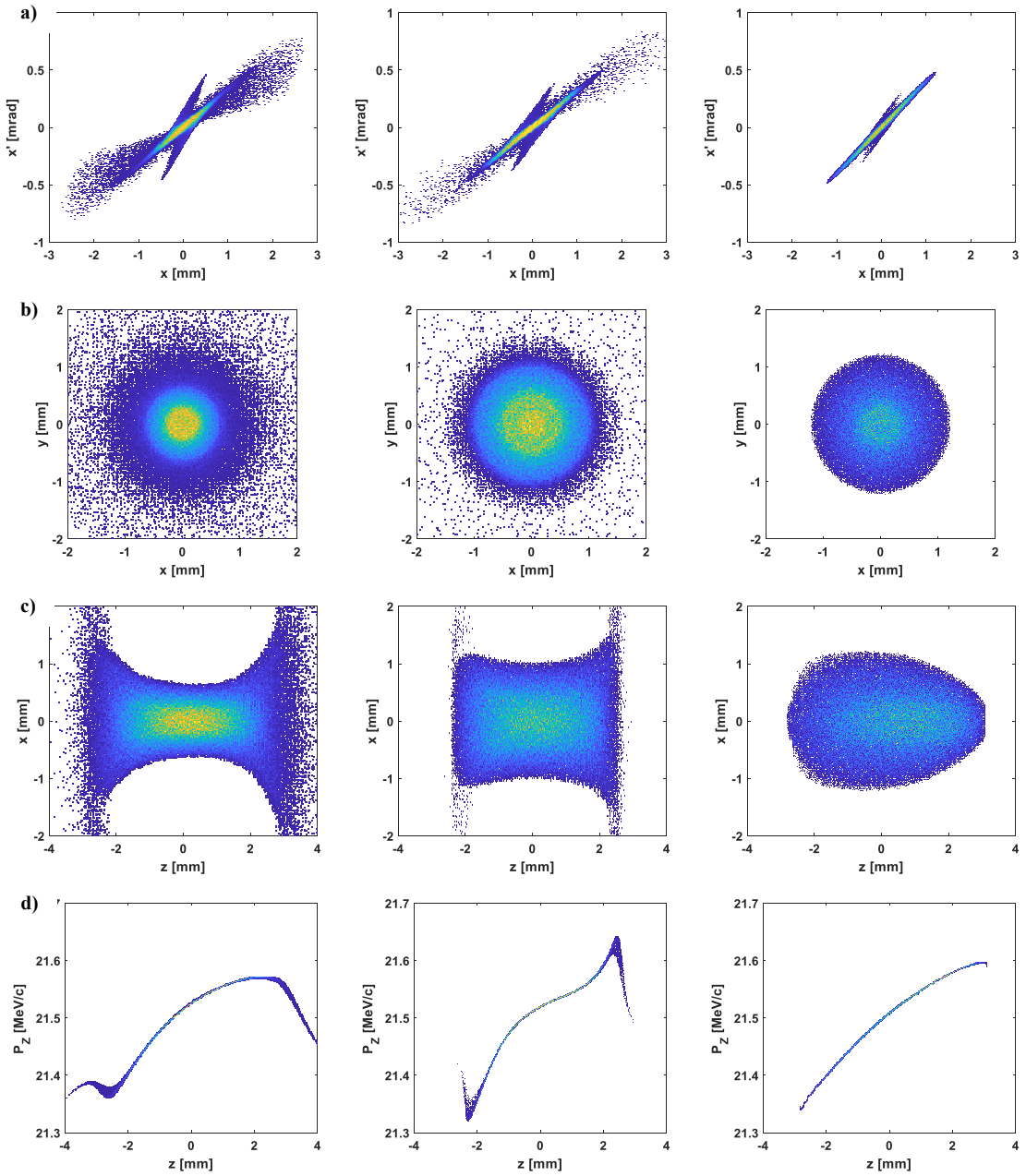


Figure 4.42: a) Transverse phase space, b) transverse distribution, c) sideview, d) and longitudinal phase spaces for the three distributions. (left – Gaussian, middle – Flattop, right – Ellipsoidal, mainly based on [90])

The improved qualities of the ellipsoidal pulse can be seen from the above plots (Figure 4.42) and the table (Table 4.3). A significant reduction in beam halo can be seen in both the longitudinal and transverse phase spaces, as well as in the longitudinal projection. This has benefits for the reduction of background radiation in long beamlines due to halo loss.

Furthermore, the transverse and longitudinal projections have maintained much of their shape in relation to the input distribution (Figure 4.31). Finally, in the longitudinal phases spaces, much like the slice emittance in the previous 1 nC case, the effects of the long tails of the Gaussian temporal envelope, the effect of non-linear space charge forces at the tails ends of the cylindrical pulse, in comparison to the significantly reduced modulations of the ellipsoidal distribution can call be seen.

Table 4.3: Table of numerically optimized machine and laser parameters for 0.5 nC bunch charge.

Photocathode laser	Pulse shape→	cylindrical		ellipsoidal
	Temporal profile→	Gaussian	Flattop	
	length (FWHM)	9.5 ps (fixed)		
	Transverse	Homogeneous radial		
	Optimized transverse size (RMS)	0.385 mm	0.423 mm	0.353 mm
RF gun	Electric field at the cathode (max)	60 MV/m (fixed)		
	Optimized phase (w.r.t. MMMG)	-1.2°	-4.2°	-2.8°
	Optimized solenoid peak field	-0.2247 T	-0.2248 T	-0.2260 T
Booster	Electric field (max)	17.1 MV/m (fixed)		
	Phase (w.r.t. MMMG)	0° (fixed)		
Electron beam (EMSY1, z=5.277m)	Bunch charge	0.5 nC (fixed)		
	Beam mean momentum	21.0 MeV/c		
	Projected normalized emittance	0.80 mm·mrad	0.64 mm·mrad	0.35 mm·mrad
	Average slice emittance	0.49 mm·mrad	0.57 mm·mrad	0.33 mm·mrad
	Bunch length (RMS)	1.44 mm	1.20 mm	1.34 mm
	Peak current	35.4 A	39.5 A	37.8 A
	Longitudinal emittance	34 mm keV	22 mm keV	12.5 mm keV

Numerically, the emittances between the cylindrical and ellipsoidal pulses almost halve under ideal conditions, despite the lower bunch charge of 0.5 nC as the shorter pulse length partially counteracts the reduced bunch charge.

However, in practice BSA cropping was necessary owing to the excessively large transverse beamsize on the photocathode (Figure 5.32) which originated from design restrictions due to "piggybacking" of the MBI laser transport beamline. Therefore, further ASTRA simulations were undertaken to evaluate the electron beam properties of a "truncated" ellipsoid (Figure 4.43).

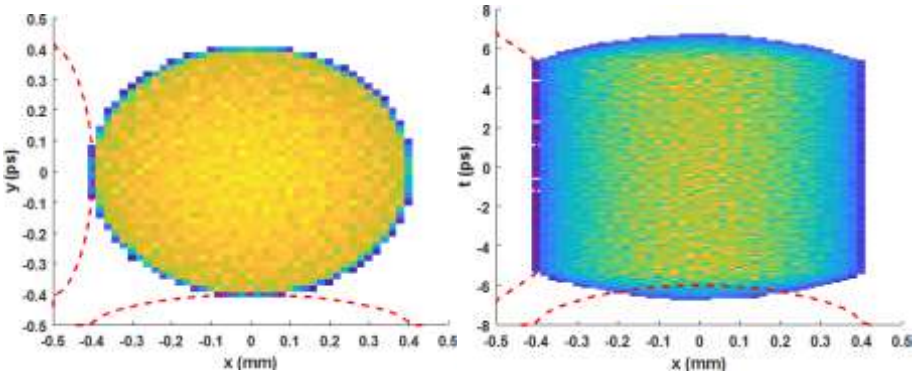


Figure 4.43: Transverse (left) and longitudinal (right) projections of a truncated ellipsoidal distribution and current profile (red).

The results (Table 4.4) of the truncated ellipsoid are not too dissimilar to that of the ideal ellipsoid with only slight distortions in projected emittance, a slight increase in beam beam halo, and deformation and modulation in the longitudinal projection and phase space (Figure 4.44) owing to its approximation to a cylindrical bunch.

Table 4.4: Table of numerically optimized machine and laser parameters for 0.5 nC bunch charge.

Photocathode laser	Pulse shape	ellipsoidal	truncated ellipsoidal
	length (FWHM)	9.5 ps	
	Transverse size (RMS)	0.353 mm	0.405 mm
RF gun	Electric field at the cathode (max)	60 MV/m	
	Phase (w.r.t. MMMG)	-2.8°	-3.15°
	Solenoid peak field	-0.2261 T	-0.2251
Booster	Electric field (max)	17.1 MV/m	
	Phase (w.r.t. MMMG)	0°	
Electron beam (z=5.277m)	Bunch charge	0.5 nC	
	Beam mean momentum	21.0 MeV/c	
	Projected normalized emittance	0.35 mm·mrad	0.45 mm mrad
	Average slice emittance	0.33 mm mrad	0.41 mm mrad
	Bunch length (RMS)	1.34 mm	1.32 mm
	Peak current	37.8 A	35.4 A
	Longitudinal emittance	12.5 mm keV	25.9 mm keV

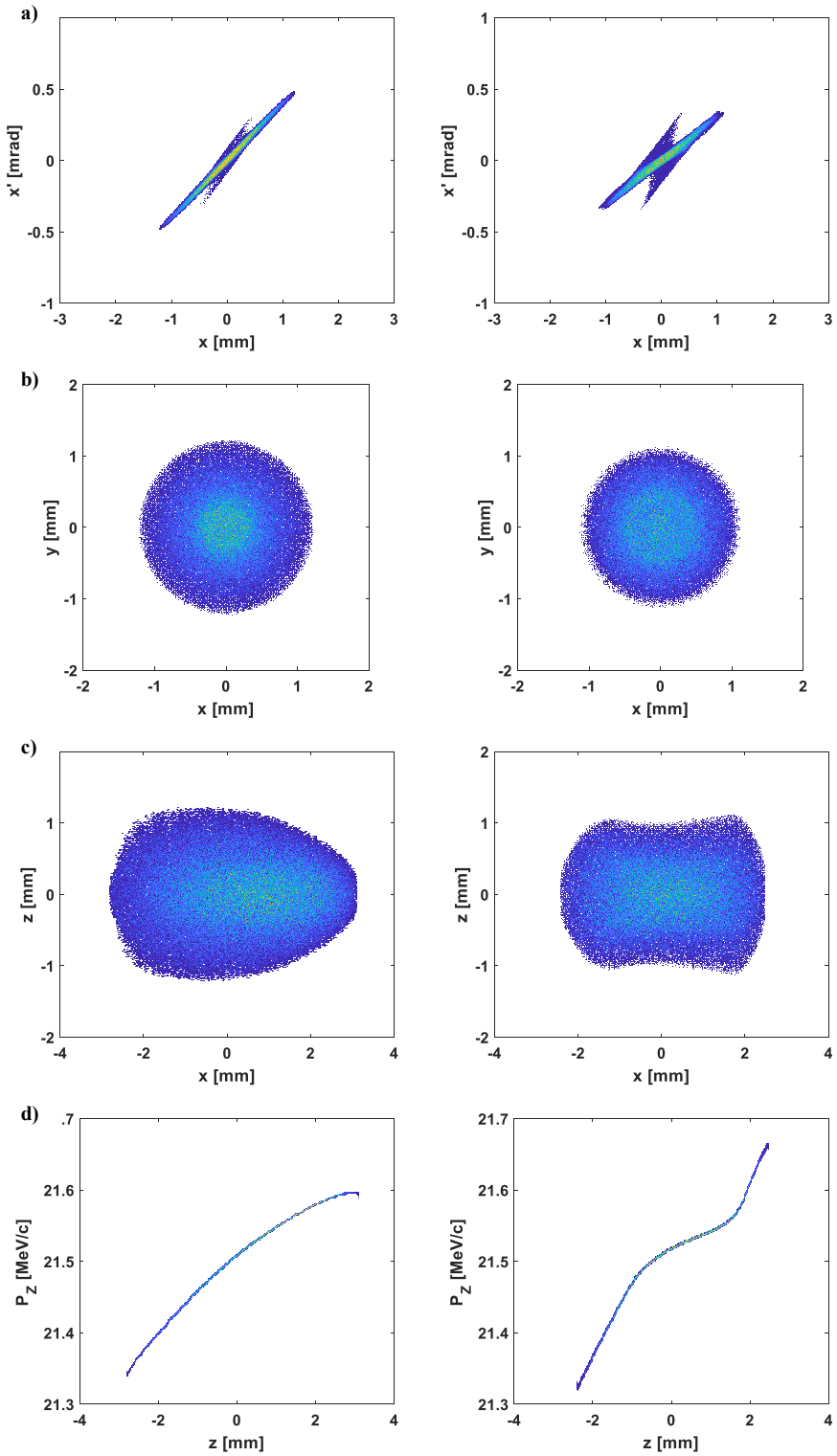


Figure 4.44: Comparative plots of transverse phase space (a), transverse distribution (b), sideview (c), and longitudinal phase spaces (d) for ellipsoidal (left) and truncated ellipsoidal (right) bunches.

From these simulations it can be seen that the truncated ellipsoid still has better properties than that of a Gaussian or cylindrical pulse. The longitudinal emittance is on par with that of the cylindrical pulse while still demonstrating superior projected and slice emittance.

In conclusion, from the various simulations a greater understanding of the motivation of laser pulse shaping and the impact of those pulses on electron bunch parameters can be obtained.

By unfolding the optical layout in ray tracing simulations it is possible to deconstruct and demonstrate the unintuitive reciprocal design: how it forms, and asymmetrically manipulates images in offset planes and eventually compensates and recombines those planes to produce three dimensional shaping.

Ray tracing further confirms the validity of the laser beam transport beamline parameters and proper transport to the photocathode can be evaluated.

Further mathematical modelling in Matlab provides insight into the shaping process and expected efficiencies for chirped pulses. It produces an estimation of the expected amplitude/phase masks, the edge deformation and squaring arising out of the quadratic nature of the shaping scheme, and the possible repercussions of neglecting the phase mask.

Furthermore, it allows calculation of cutting efficiency of an ellipsoid from a 3D Gaussian pulse under the ideal case.

Finally, simulations of shaped electron bunches in the photoinjector demonstrate the superior bunch qualities of the ellipsoidal distribution at various charges. This is particularly true for the minimization of projected, longitudinal, and sliced emittances, as well as a reduced sensitivity to photoinjector parameter jitter.

Chapter 5 The Ellipsoidal Laser (ELLA) system

The laser system utilized in this work was conceived, designed, developed, realized, and installed at PITZ, by the Institute of Applied Physics (IAP, Nizhny Nnovgorod) in collaboration with PITZ and the Joint Institute for Nuclear Research (Dubna).

The Ellipsoidal Laser system, henceforth referred to as "ELLA" in this work, was a Er-doped fiber-based laser system with dual channel synchronized outputs producing ~1 µJ, 1030 nm laser pulses generated as 300 µs pulse trains at a rate of 10 Hz. The primary channel was amplified in a multi-pass thin-disc Yb:KGW amplifier and shaped in the transverse-temporal domain by an innovative dual-pass shaper utilizing Spatial Light Modulators (SLMs) based upon a 4f-line (Sec. 4.1.1) which is a zero-dispersion stretcher/compressor. These shaped pulses were then converted into the ultraviolet pulses required for electron beam generation through frequency conversion in non-linear crystals before being transported to the cathode of the RF photoinjector.

5.1 GENERALIZED SCHEME

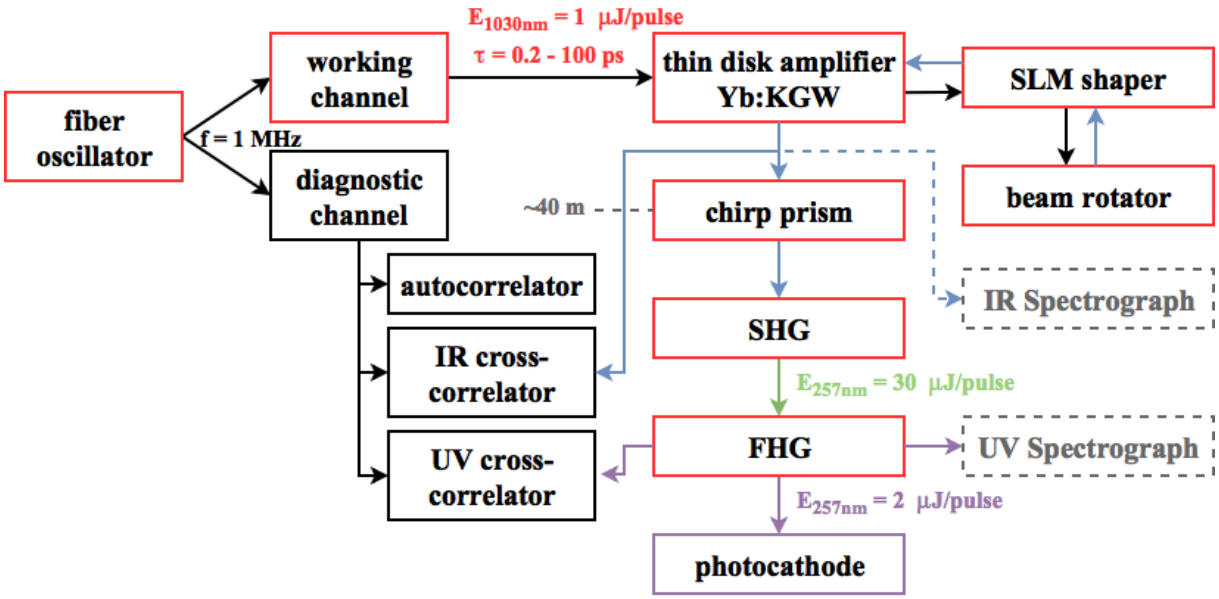


Figure 5.1: A simplified operational block diagram of the ELLA system.

The generalized scheme (Figure 5.1) shows the operations of the ELLA system. The fiber-based oscillator pulses are split into two pre-amplified channels to maintain synchronicity. The primary channel referred to as the 'working channel', produces chirped 1 µJ pulses on the order of a few ps and are prescribed for pulse shaping. The secondary channel, referred to as the 'diagnostic channel', similarly produces transform limited 1 µJ pulses on the order of ~0.3 ps. These pulses are prescribed for the time-resolved diagnostic self-characterization of the working channel in the cross-correlators.

The working channel was sent through a multi-pass thin-disc Yb:KGW amplifier and passed onto the shaping unit. The shaping unit consisted of a Spatial Light Modulator (SLM) configured as an amplitude mask in the Fourier plane of a zero-dispersion grating stretcher/compressor, in which an arbitrary mask can be applied to the spatio-temporal domain of the laser pulse.

The pulse is then rotated 90° about its propagation axis in the beam rotator and passed back through the scheme to reapply the mask in the second transverse plane orthogonal to the first pass. This results in the beam passing back through the amplifier and again being amplified in the thin disc amplifier in order to recover losses sustained in the shaping process. The pulse was then coupled out of the scheme and a small fraction of the pulse energy is split off for the IR cross-correlator, while the rest proceeds into the harmonic conversion section for non-linear frequency conversion to the UV in the LBO and BBO crystals. Here the pulse could be destructively sampled in the UV cross-correlator or finally transported down the tunnel and the photocathode for photoelectron production.

5.2 ACTUAL LAYOUT

The output of the working channel from the oscillator-preamplifier was projected onto a pinhole and utilized Faraday rotators and birefringent wedges (Figure 5.13) to couple in (and out) the beam into the amplifier-shaper sections. On the first pass this truncated Gaussian distribution is relay imaged from the input pinhole with a 4f telescope onto the first crystal of the multi-pass thin-disc amplifier which is also a 4f relay imaging system simply folded and skewed in the tangential/sigiatial plane wherein it is relayed for up to 10 passes between the two Yb:KGW amplifier crystals.

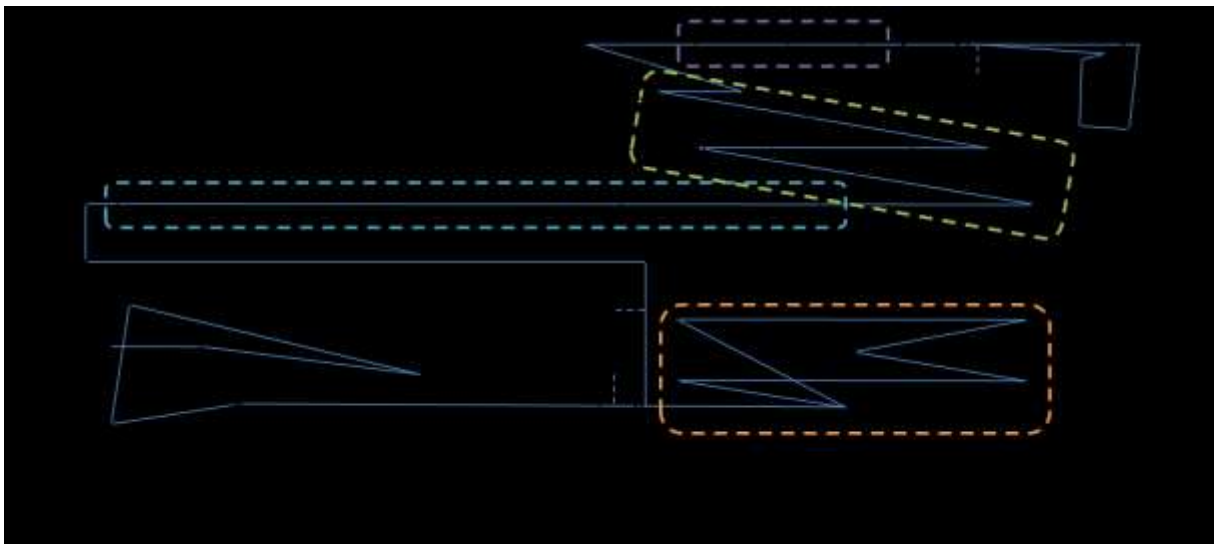


Figure 5.2: Actual reciprocal layout (not to scale) of the ellipsoidal laser system with amplifier stage (orange), up-telescope (blue), shaping section (green), down-telescope (purple). PH – pinhole, FR – Faraday rotator, BW – birefringent wedge, SLM – Spatial Light Modulator, Pol. BS – polarizing beamsplitter, Cx – Camera X.

A three-element, ~4.3 m, ~3.5x magnifying telescope then relays the amplified pulse image through the grating and onto the first SLM, thus bringing the beam diameter up to ~7mm of the 12 mm SLM chip height. The 4f-line in the shaping section itself contained uniaxial relay imaging of the x-axis between the grating thanks to the cylindrical lenses, and another 4f telescope relay images the plane of the first SLM chip onto the plane of second SLM chip. In conjunction with a half-wave plate the SLMs acted as independent amplitude and phase masks.

The second telescope reverses the operation of the first telescope by imaging the plane of

the second SLM chip and de-magnifying the diameter to pass it through the second Faraday rotator and generating an image plane on the midpoint of the rotator tower (Figure 5.12).

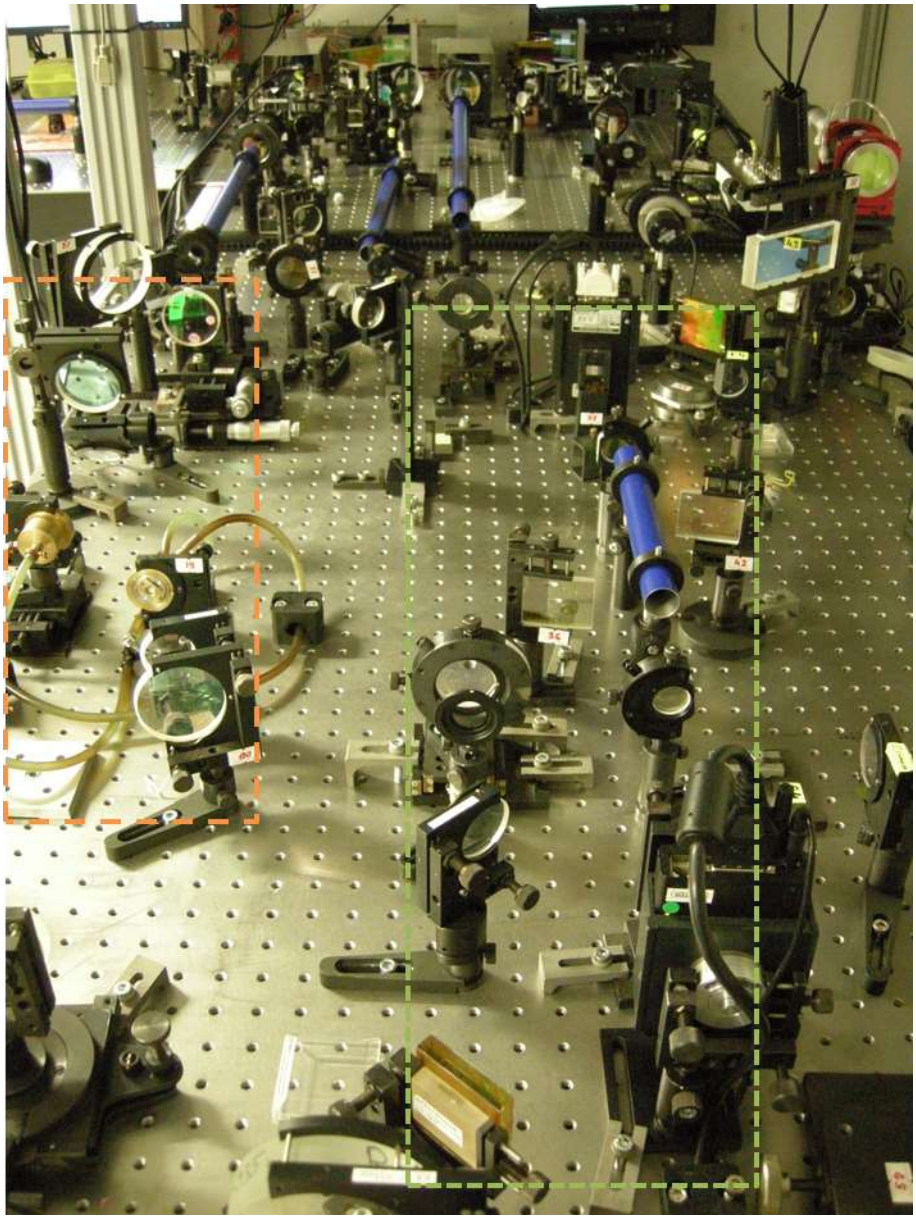


Figure 5.3: A photograph of the actual system with the SLM 4f-line (green) and the multi-pass amplifier stage (orange).

In the rotator tower the image plane is simply rotated 90° transversely and fed back into the system in the opposite direction effectively reversing the order of operations for the orthogonal plane until it is finally picked out at the pinhole by a birefringent calcite wedge for harmonic conversion.

5.3 THE ER-YB OSCILLATOR-PREAMPLIFIER

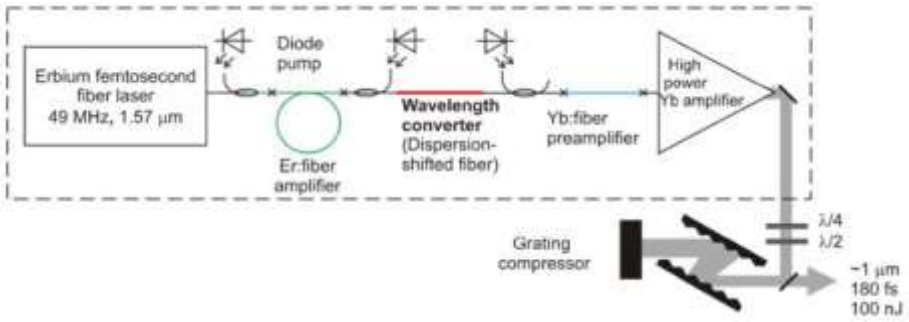


Figure 5.4: Basic schematic of the Er-based fiber oscillator [91].

The Er-based fiber oscillator (Figure 5.4) produces pulses at a fundamental frequency of 54 MHz (re-tuned from 49 MHz). These pulses are amplified in an Er-fiber amplifier and converted to about 1030 nm in the dispersion-shifted fiber (DSF). The pulses are amplified in a Yb-based fiber before linearization and rotation of the polarization with wave-plates and recompression in the grating.

The low energy output of this oscillator is then down-counted to 1 MHz by an acousto-optic modulator (AOM). Using the basic principle of Chirped Pulse Amplification the 1 MHz train is stretched (chirped) in a Single Mode Fiber (SMF), split into two channels, and parallel AOMs are used to shorten both train channels from continuous to 300 μs trains every 100ms. These short pulse trains are amplified in the final, separate fiber-amplifiers to ~1 μJ/pulse and propagated in free space to grating compressors. In these free-space grating compressors they are re-compressed to a few ps and to their transform limit of ~0.3 ps, respectively. The still-chirped pulses form the main "working channel" and the transform limited pulses for the "diagnostic channel.

Two control mechanisms were incorporated into the construction to maintain the fundamental oscillator frequency, and the temporal delay between the two channels. For the former, a thermoelectric Peltier cell was used to coarsely tune the oscillator frequency by a few kHz and a piezoelectric actuator was used to fine tune the frequency by a few Hz. For the latter, a section of fiber in the diagnostic channel is coiled around a piezoelectric washer which expands under a potential difference therefore precisely stretching the fiber and causing an increase in the optical path length up to 22.5 ps (4.5 mm) [92]. This coil also helps offset the difference in optical path length that would occur due to the long path of the working channel through the optical systems.

5.4 THE YB:KGW THIN-DISC MULTIPASS AMPLIFIER

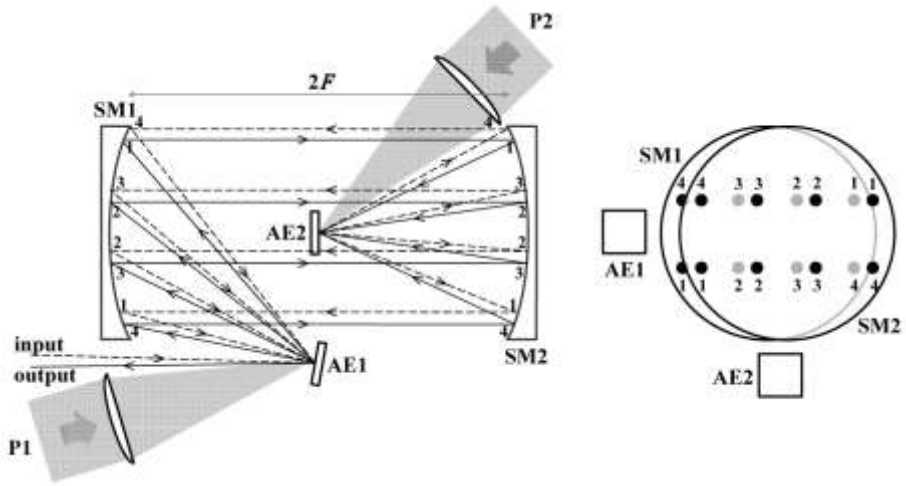


Figure 5.5: The top view of the optical scheme of the Yb:KGW amplifier (left) and the side view showing relative lateral displacement (right) [93]. SM – spherical mirrors of focus F, AE – active element, P – pump channel

Owing to the high pulse energies required in the design specification for photoelectron production (1 µJ UV, 10 µJ IR) and given in the inherent losses in the shaping process it is obvious that further amplification of the 1 µJ IR oscillator-preamplifier pulses is required. To that end a thin-disc multi-pass Yb:KGW amplifier was also constructed. It utilizes a fixed geometry and Yb-doped KGW crystals mounted in a skew 4f configuration (Figure 5.5). These crystals have dielectric coatings with a dual-wavelength (1030 nm/938 nm) antireflective coating on the incident size and a high-reflective coating on the rear. Furthermore, there are secured in water-cooled mounts to facilitate rear-side temperature stabilization.

The crystals are pumped with by a ~935 nm, 2 kW CW multimode diode laser from Laserline (LDM 2000) pulsed in a short duty-cycle mode. Typical operating parameters were 50% power setpoint for 450 µs at 10 Hz. This permitted amplification of the ~1 µJ pulses produced by the oscillator of up to ~20 µJ (Figure 5.6).

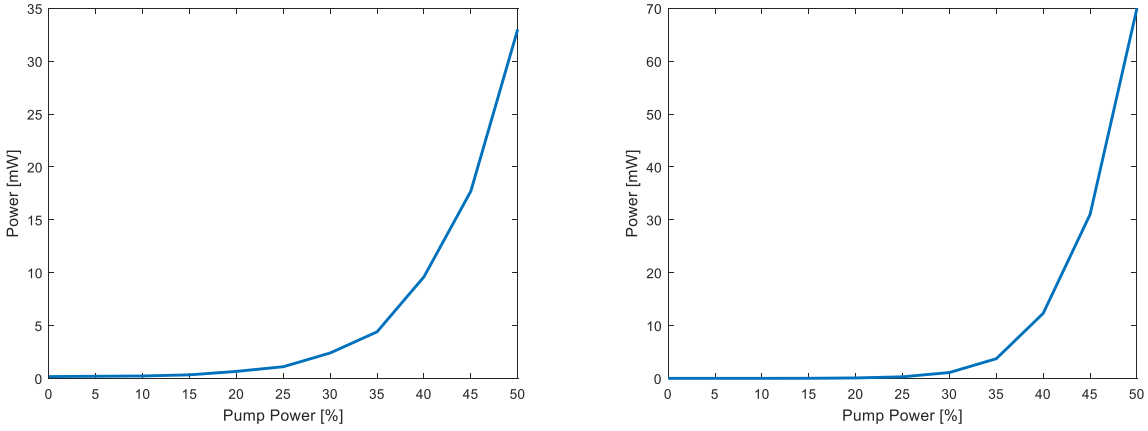


Figure 5.6: The output power after thin-disc amplifier (left), and output power after two passes through the amplifier (measured at C5, see: Figure 5.2) with a full transmissive shaper (right).

The pump laser itself shows a minor wavelength-temperature dependence specified as 0.1 nm.K^{-1}. Therefore, for a given pump level the laser wavelength may be optimized to maximize absorption [94] (Figure 5.7b) in the crystals and reduce temperature related energy jitter.

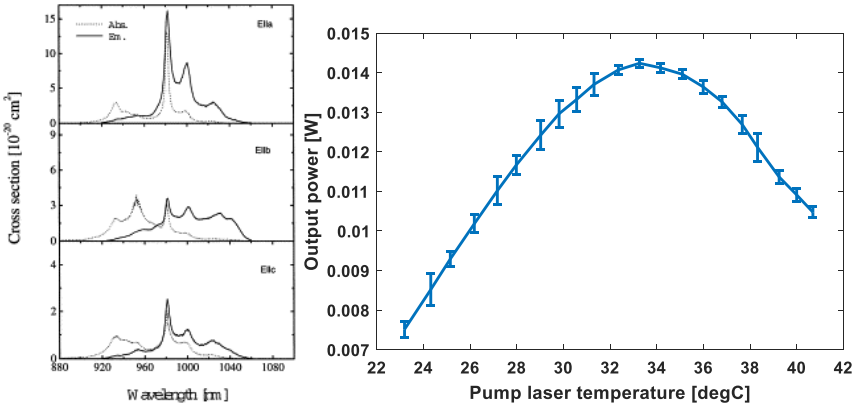


Figure 5.7:a) Emission and absorption spectra for Yb:KGW [95], b) Amplifier optical power as a function of pump diode temperature.

One of the significant characteristic disadvantages of the multi-pass thin-disc amplifier is distortion, narrowing, and shifting of the spectrum about the 1030 nm line; which exacerbates the already distorted oscillator pulse spectrum (Figure 5.8). This is an issue as the spectrally-dependent chirped pulse shaping is contingent upon a preferably smooth, broad spectrum.

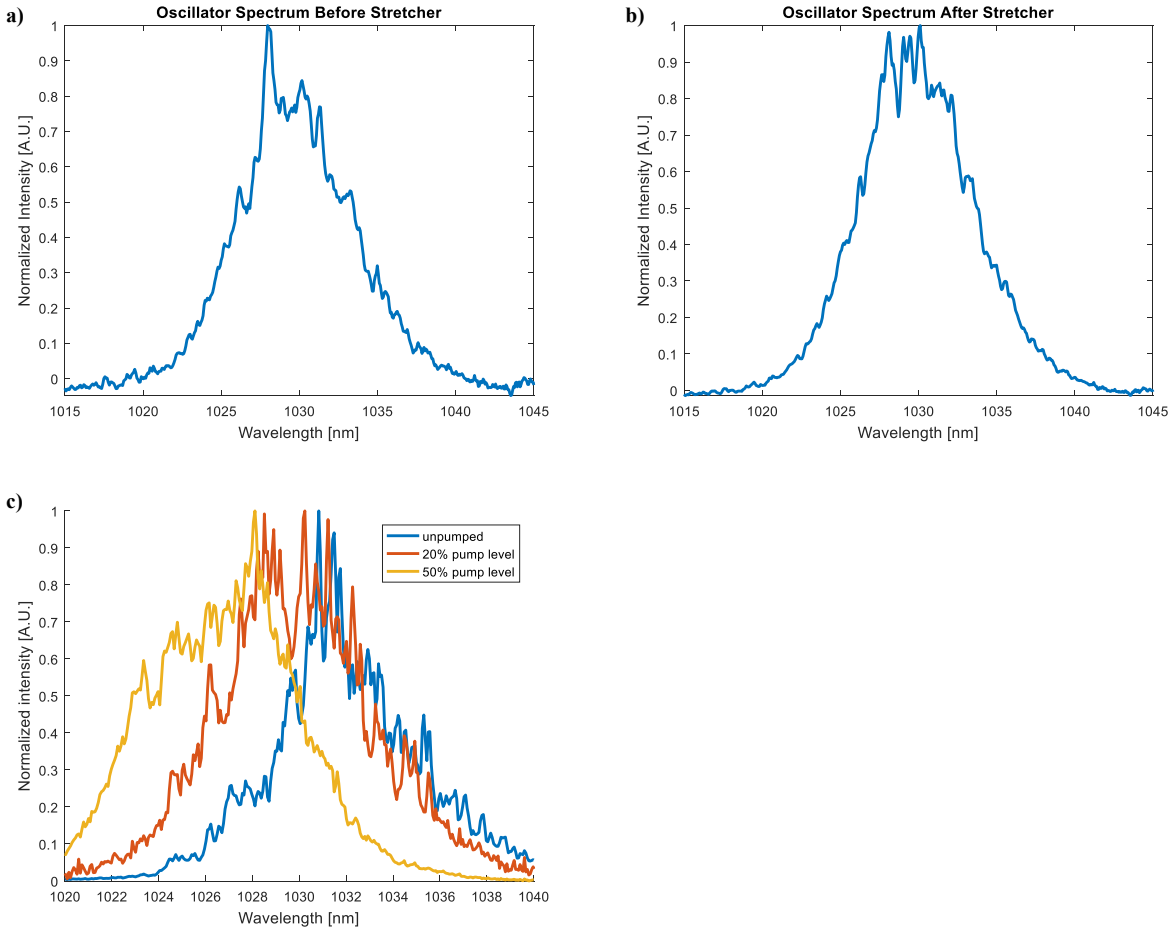


Figure 5.8: A high-resolution spectrum of the oscillator-preamplifier output. b) Spectrum of the oscillator-pre-amplifier after stretching. c) Laser spectra after amplification and one pass through the SLM pulse shaper.

5.5 THE SHAPING SCHEME

The shaping scheme is based on an approximation of the simulations outlined earlier. The radially uniform transverse distribution was approximated in practice by projection of the chirped, collimated Gaussian output of the oscillator-preamplifier's working channel onto a 2 mm aperture to generate a modulated flat-top transverse profile (Figure 5.9). This spatially modulated beam is then relayed onto the first crystal of the thin-disc amplifier

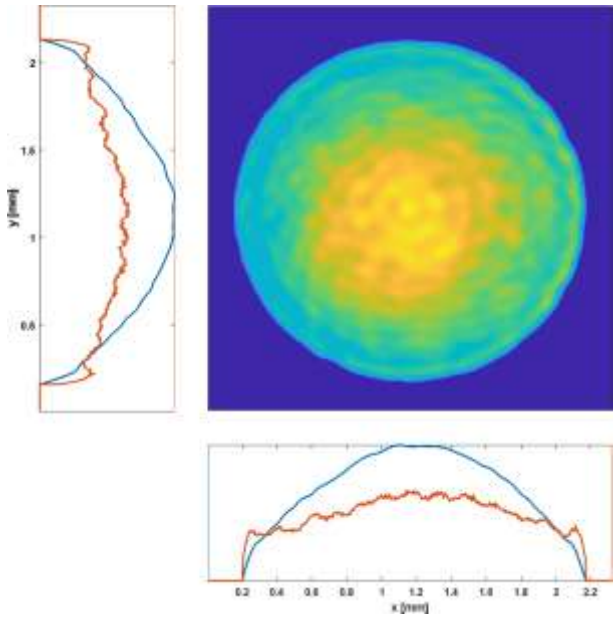


Figure 5.9: A truncated Gaussian flattop profile generated by aperture clipping of an expanded Gaussian laser beam with axial cross-sections (red) and projections (blue).

The original prototype pulse shaper scheme, based upon the theoretical description, utilizes a combination zero-dispersion stretcher/compressor with an internal 4f scheme to duplicate the Fourier plane on two reflective, phase-retarding Holoeye Pluto SLMs [51]. One of which was transformed into an amplitude mask by inclusion of a λ/2 plate at the SLM and a polarizer after the recombination grating.

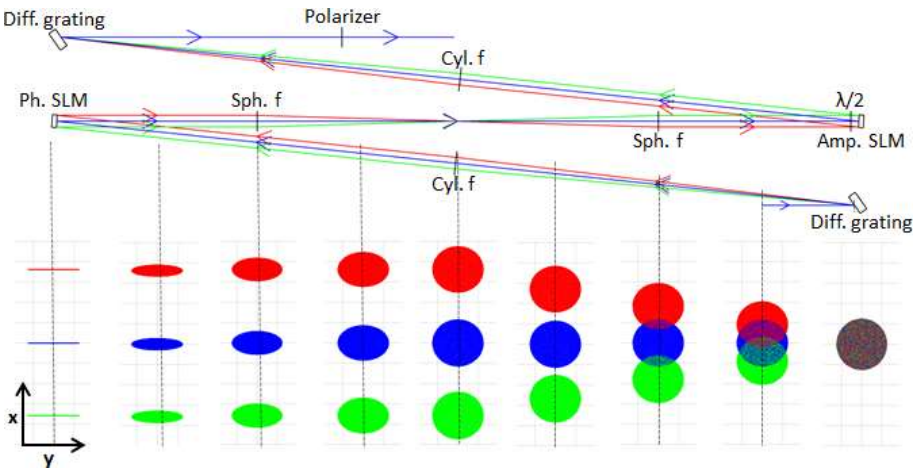


Figure 5.10: Practical realization of the zero-dispersion grating stretcher/compressor scheme used in the SLM shaping unit (top) with transversal cross-sections along the first diffractive arm (bottom).

The cylindrical lenses placed at an f-distance between the SLMs and gratings produce a line focus of the diffracted spectral components of the input beam into vertical columns on the SLM chip (Figure 5.10, lower), and spherical lenses in a 4f configuration simply relay the Fourier planes between the SLMs. The operation was then reversed with another cylindrical lens and grating and a polarizer used to apply the amplitude mask.

In practicality, the original SLM-pair setup was decommissioned due to the asynchronicity of the Holoeye SLMs. These SLMs use pulse-width modulation to control the phase at a 60 Hz clock rate determined by the driving computer's vsync clock which meant they could not by synchronized to the base 10 Hz bunch train repetition rate of the PITZ accelerator. They were replaced by a single Hamamatsu SLM acting as an amplitude mask which operates in a standing mode and a mirror at the second SLM location. It was found in practical experience, and theory (see: Figure 4.15), that the phase mask was not crucial.

Naturally, the SLM should be calibrated for the phase-amplitude correlation of the amplitude mask, and this can then be used for spectro-temporal and transversal calibration. This was done by scanning the full phase range of the corresponding SLM and integrating the sum-of-pixels on the subsequent camera (see: Figure 5.2, C4). As can be seen, the SLM follows the expected sinusoidal response (Figure 5.11a) and was easily linearized across the 2π phase range to a normal scale (Figure 5.11c).

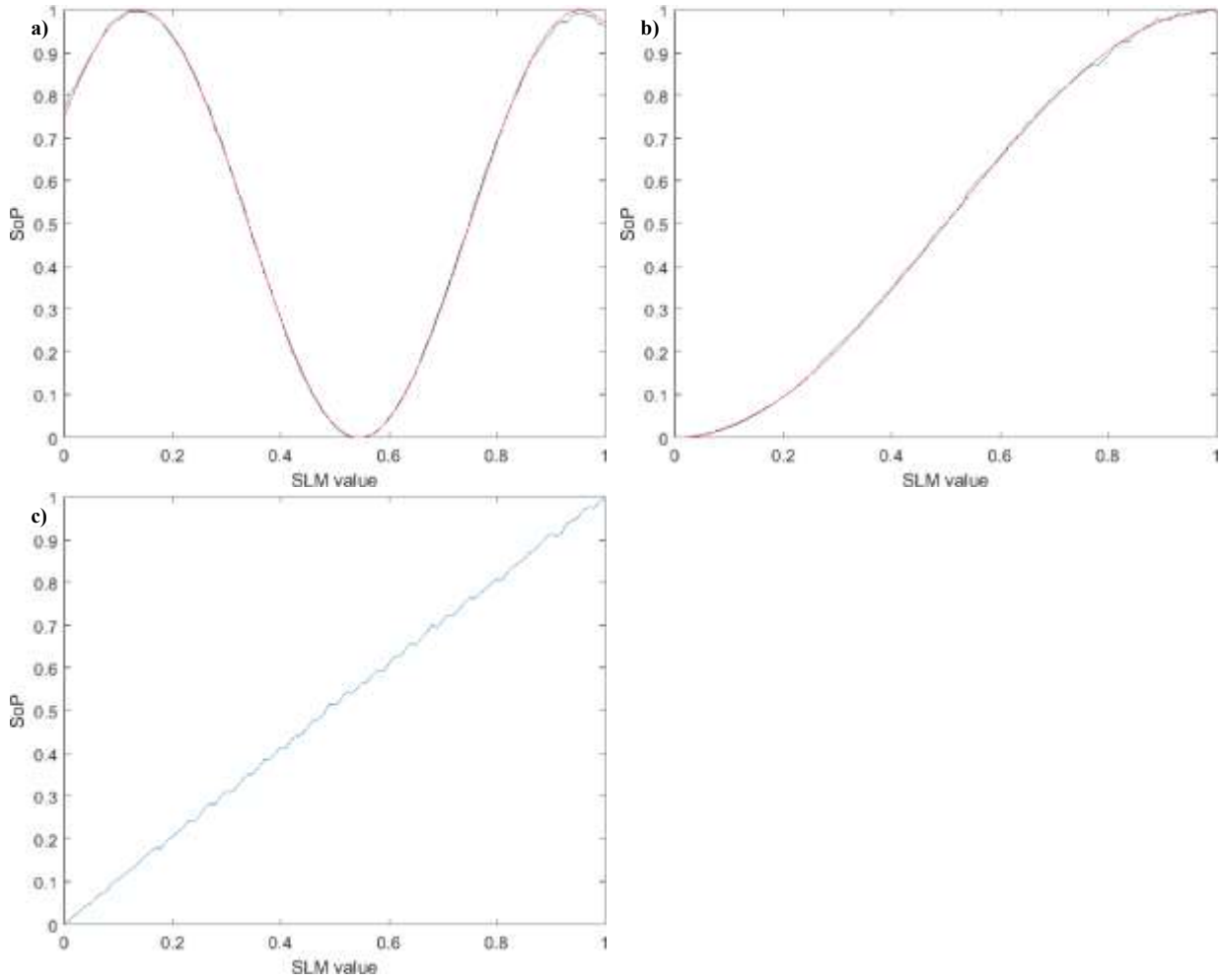


Figure 5.11: a) The normalized integrated sum-of-pixels at C4 (Figure 5.2) for a full range scan of the SLM. b) Renormalized scan range from 0.535 to 0.98 c) Linearized transmission response

Naturally, as the scheme only shapes in a single transverse direction, the operation must be repeated for the other transverse direction by rotating the beam 90° about its propagation axis. In order to do this the beam is coupled into a 4-element transaxial reflective tower (Figure

5.12).

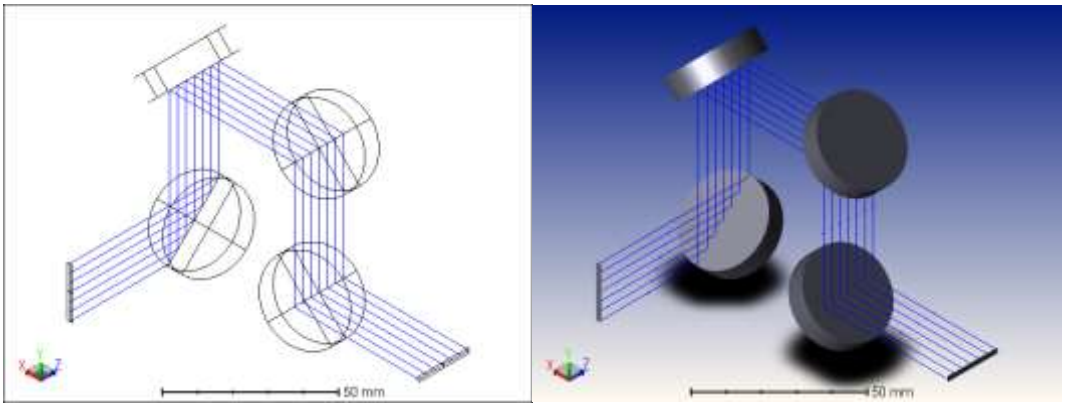


Figure 5.12: Basic reflective scheme of polarization-maintaining, beam rotating “tower”.

The tower rotates the image while maintaining the polarization of the incoming beam with it. This latter property can be used to couple the beam back through the shaping system to reapply the mask in the orthogonal direction by exploiting this characteristic with a birefringent Calcite ($CaCO_3$) wedge paired with a faraday rotator and a half-wave retarder plate (Figure 5.13).

A birefringent wedge is a simple optical element that can be used to angularly separate orthogonal polarizations or combine them when the operation is geometrically reversed. When used in sequence with a Faraday rotator and a half-wave retarder it produces a non-reciprocal optical system than can be used to rotate the polarization in one direction and to maintain polarization in the reverse direction.

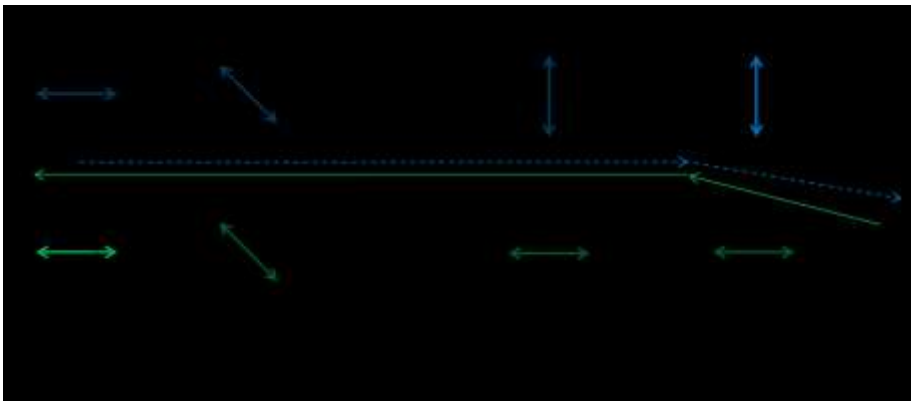


Figure 5.13: Orthagonal polariziaton in/out coupling scheme used in conjunction with the beam rotating tower.

5.6 INFRARED DIAGNOSTICS

A number of diagnostic tools where implemented to monitor and characterize the laser system. Naturally, photodiodes were placed throughout the scheme to monitor bunch train properties and beam position. One primary example is the Thorlabs DET10A [96] installed behind the second resonator mirror of the multi-pass thin-disc amplifier. It was used to monitor leakage of the bunch train after a single pass through both crystals, and to observe rough alignment of the system.

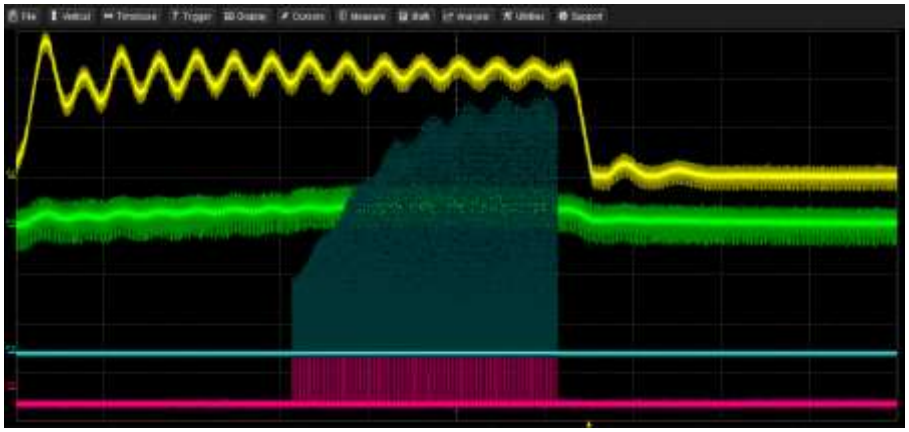


Figure 5.14: Photodiode diagnostics. The CW pump laser leakage (yellow), multi-pass amplifier leakage (green), the amplified pulse train prior to harmonic conversion (blue), and the oscillator output (pink).

The diodes provided simple feedback and monitoring of the system. Of note is the imprinting of the CW pump laser ripple (Figure 5.14) onto the amplified pulse train, which was subsequently seen on the electron bunch train later (Figure 6.3). This arose due to "ringing" of the CW pump laser as it switched.

5.7 SELF-CHARACTERIZATION

A number of techniques were available and developed for self-characterization of the system without the use of a reference. This was done both temporally, and spectrally, as part of the calibration and alignment process.

Knowing the dimensions of the input beam it becomes a trivial procedure to perform the transversal calibration of the mask. By simply applying a binary row mask (Figure 5.15b) and measuring the resultant transversal cropping on the 1.8 mm diameter input the calibration factor can be determined.

It can also be seen from Figure 5.15d that the beam rotating tower was partially misaligned, and that there was degradation of the imaging back through the system.

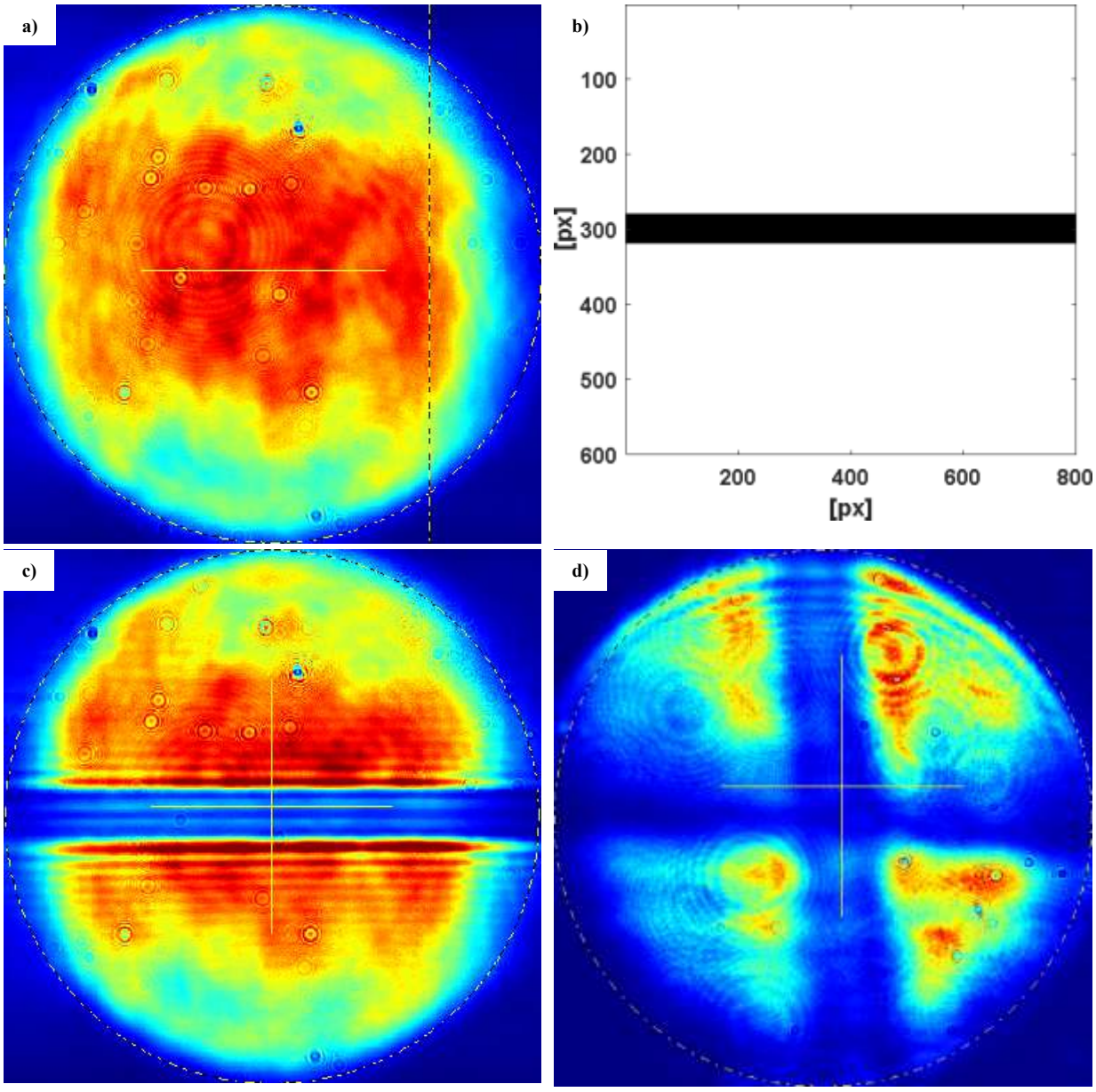


Figure 5.15: a) The transverse laser profile after the first pass through the pulse shaper (w/o amplifcation). b) The centered, 40 px high SLM amplitude mask. c) The resulting transverse profile on C4 (see: Figure 5.2). d) The same mask viewed on C5 (see: Figure 5.2).

If a high-resolution spectrometer is unavailable one obvious way to obtain a high resolution laser spectrum is to exploit the wavelength-dependent SLM amplitude mask for self-characterization. Each column of the SLM chip represents a discrete spectral slice, therefore a simple column scan in conjunction with a photodetector after the shaping unit can be used to reconstruct the laser spectrum.

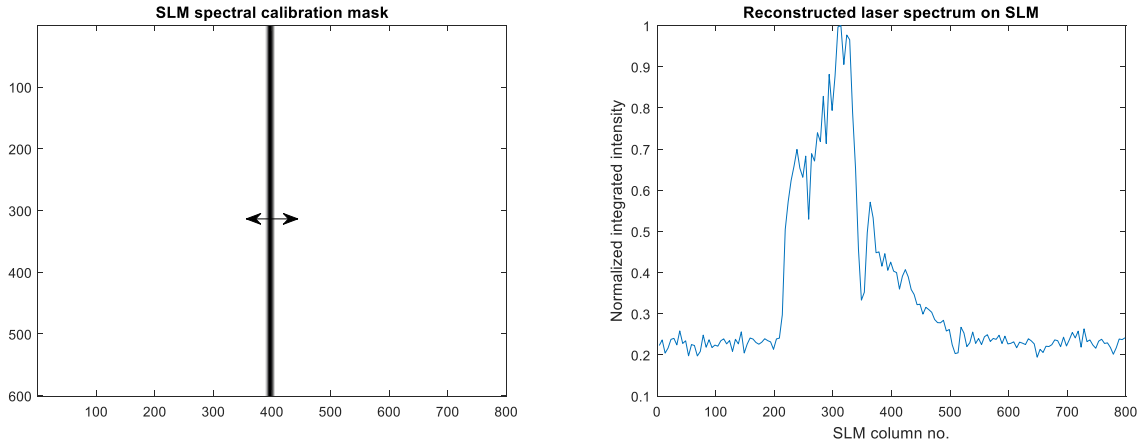


Figure 5.16: Scanned inverted binary calibration mask (left), and reconstructed amplified laser spectrum on SLM at position C4 (right) (Figure 5.2).

In practice this was done by integrating an area of interest on C4 (see: Figure 5.16) on a per 10 px column basis and reconstructing the spectrum. This can then be cross-calibrated with the cross-correlator to determine the calibration factor, or preferably used as confirmation against a high-resolution spectrometer.

A Newport Long Scan Autocorrelator [97] was constructed and used to confirm the duration of the transform-limited diagnostic pulse from the diagnostic channel of the laser system (Figure 5.17). The device uses a standard motorized stepped delay stage to construct the pulse envelope.

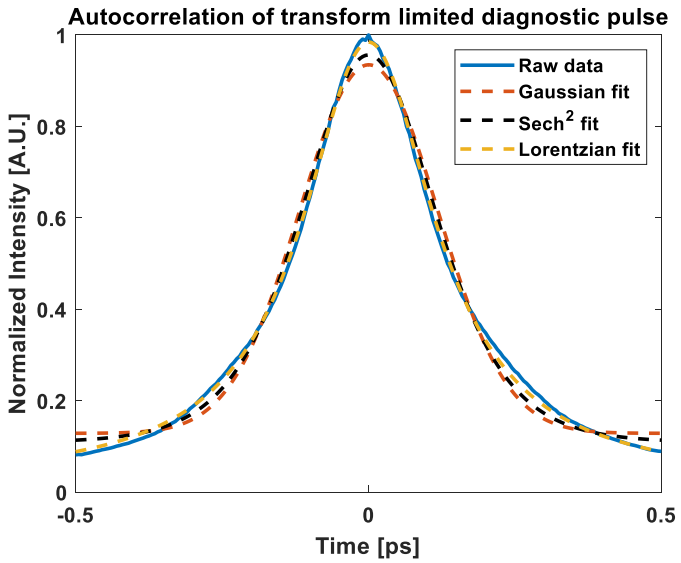


Figure 5.17: Autocorrelation measurement of the transform limited laser pulse of the second channel.

It can be seen that by fitting a selection of distributions (Gaussian, $Sech^2$, and Lorentzian) from among some of the standard assumed envelopes used in autocorrelation that the Lorentzian fit is the best. It returns a FWHM pulse duration of 281.4 fs.

5.8 SPECTRAL DIAGNOSTICS

Spectral analysis of the system is of course crucial owing to the significant amount of dependencies of the laser performance on the spectrum. Pulse duration, shaping, frequency conversion, and amplification are all vital qualities that depend on the laser spectra.

5.8.1 Spectrometer

A broadband Ocean Optics HR2000+ [98] visible spectrometer with a range of 200 nm-1100 nm and a resolution of 0.9 nm was initially used for characterization of the system (Figure 5.18).

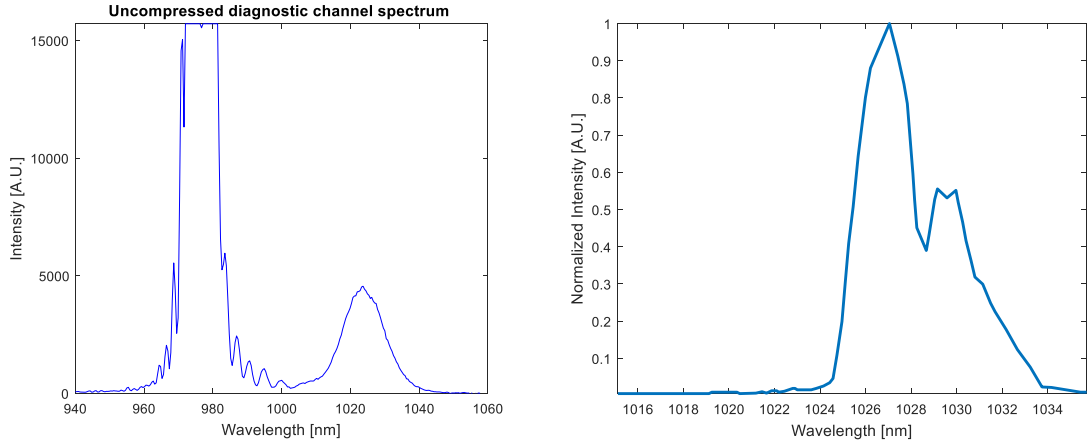


Figure 5.18: a) The spectrum of the chirped diagnostic channel prior to recompression with visible peaks in the from the 970 nm pump light and the amplified pulse at 1028 nm. b) Spectrum of the unshaped, amplified laser pulse prior to harmonic conversion (Figure 5.2 C5).

As can be seen, the low-resolution spectrum (Figure 5.18b) roughly resembles that of the reconstructed spectrum obtained by self-characterization (Figure 5.16b).

5.8.2 Spectrograph

Two reflective, folded Czerny-turner spectrographs (Sec. 2.9.3) were designed in the course of this work, one for IR and one for UV. Components were ordered and the IR spectrograph was constructed with f = 203.2 spherical mirrors, a 1200 l.mm^{-1} grating, and a AVT Proscillica GC1350 CCD camera [66]. This resulted in a system with a wavelength range of ~20 nm over the 6.4 mm camera chip. The resolution was determined by the slit size which was itself switchable between 10 µm, 25 µm, and 50 µm, therefore giving possible resolutions of 0.04 nm.px^{-1}, 0.1 nm.px^{-1}, and 0.2 nm.px^{-1}, respectively. The spectrograph sampled an intermediate image plane along the cross-correlator sampling path equivalent to that of C5 (see: Figure 5.2). By recording spectrograms of the pulse the inferred full intensity distribution can be reconstructed.

It can be seen for the unshaped, amplified pulse that by interpolating and mapping voxels of equivalent value that a (slightly deformed) ellipsoidal surface is formed (Figure 5.19) as expected. It was determined earlier (sec. 4.1.3) that an ellipsoidal envelope is formed in any Gaussian volumetric distribution by points of equal intensity (Figure 4.20). Although deformation of the spectrum can also be observed in the total integral along the spectrum the

fine detail cannot be seen due to a combination of factors. Slit roughness and bandwidth of the optical system limit the resolution of each spectrogram which can be exacerbated by spectral "walking" of each spectrogram as the slit scans and is an inherent aspect of the technique. This results in sheering in the raw data that must be corrected in post-processing and analysis.

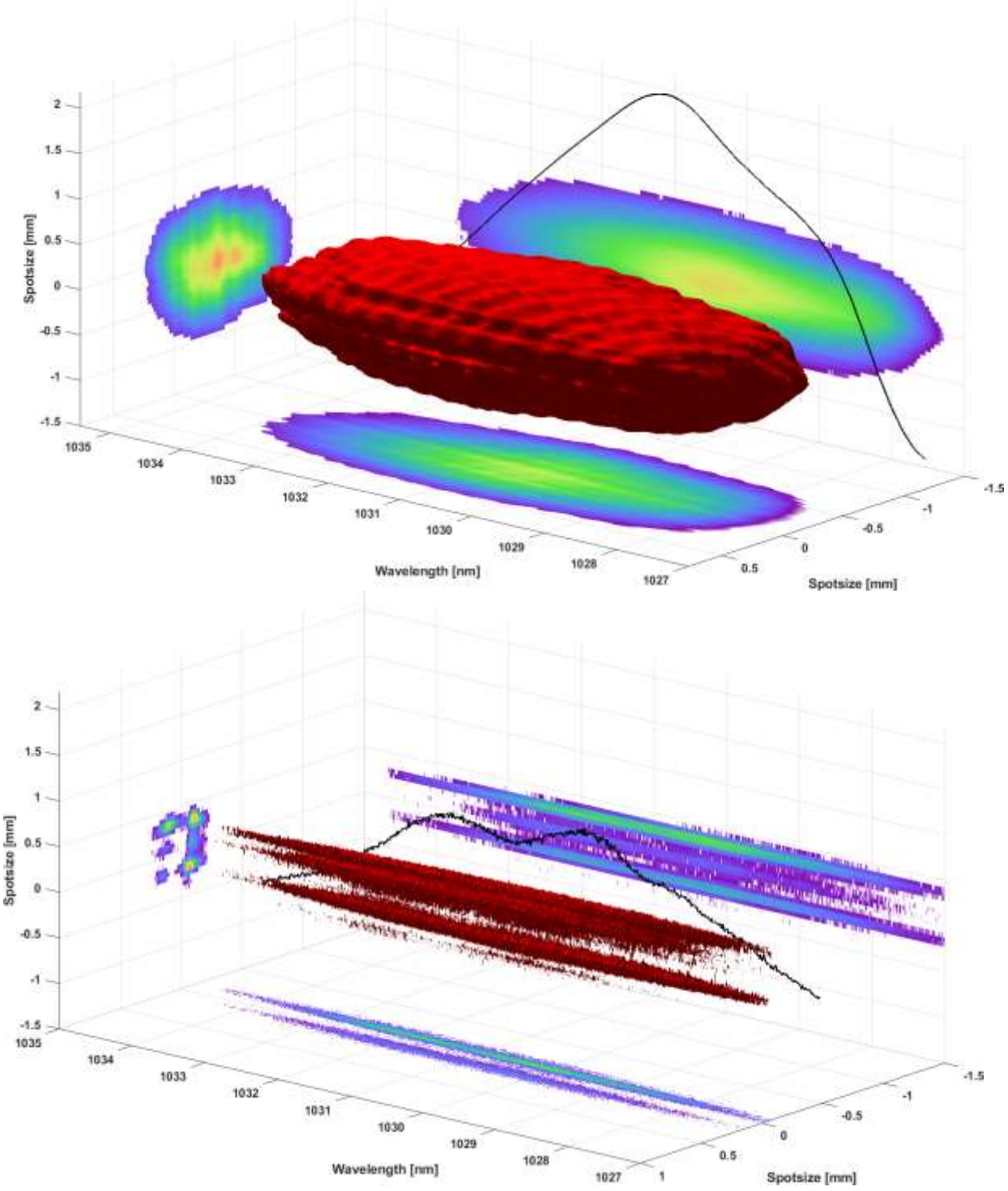


Figure 5.19: Volumetric distribution of amplified ELLA laser reconstructed from IR spectrograms w/ (top) and w/o (bottom) spectral band calibration mask prior to harmonic conversion. Integral projections of the total volume are shown on the back planes as well as total integral along the spectral axis (black line).

5.9 TEMPORAL CHARACTERIZATION

While the spectrograph is a very useful diagnostic tool for volumetric reconstruction of the pulse distribution its primary limitation is that it conveys only spectral information about the laser pulse and any temporal information must be inferred and so it must be cross-calibrated with causal instruments.

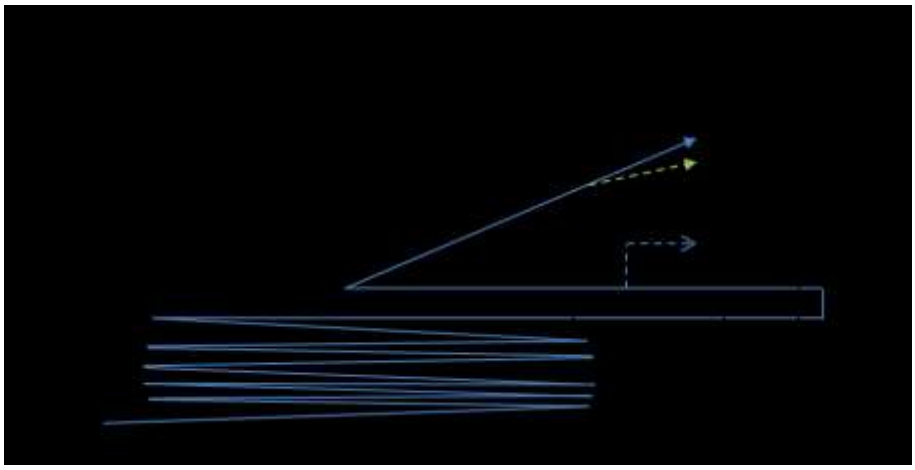


Figure 5.20: Layout of infrared cross-correlator.

The infrared cross-correlator [92] (Figure 5.20) utilized a pair of 4f telescopes to compress and pickoff a sample of the shaped beam. In this case f222:f100, and f784:f100 pairs are used to reduce the beamsize down by a factor of ~17.4 from 2 mm to ~100 μm,. This was coupled with a 4f f54:f170 magnifying telescope in the diagnostic channel intended to balance cross-correlation signal intensity and to approximate a uniform transverse diagnostic beam distribution (Figure 5.21).

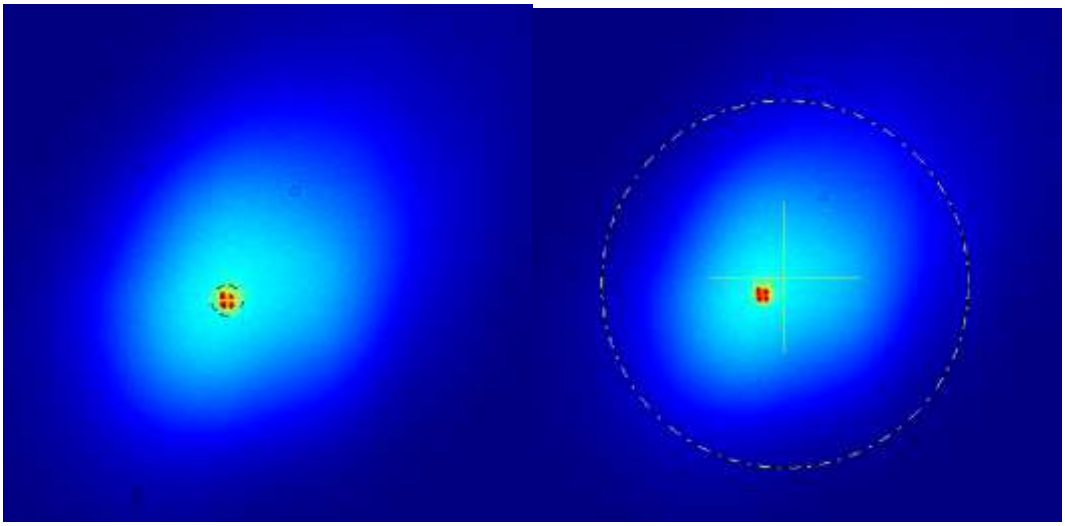


Figure 5.21: The working channel with a horizontal calibration band (circled) overlaid with the magnified diagnostic cross-correlation channel at the image plane of the crystal (left), and the magnified diagnostic channel encircled (right).

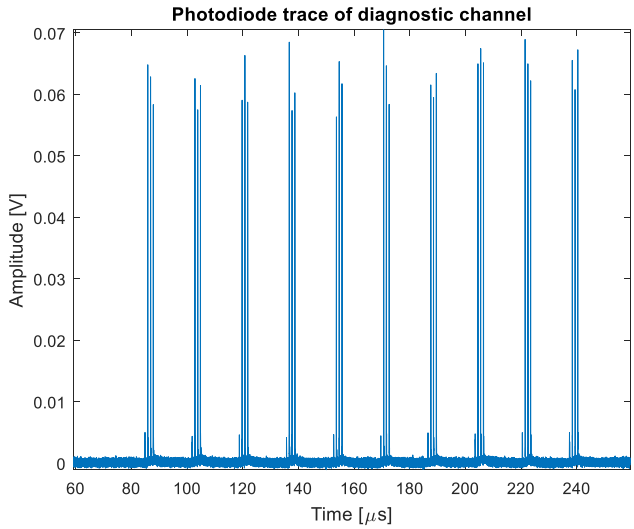


Figure 5.22: The temporal structure of the diagnostic channel as recorded by photodiode.

Unfortunately, the cross-correlator suffered from a number of weaknesses. The original fast scanning cross-correlator design [92] acquired a low number of temporal sample points, typically 8-10 as the temporal structure of the diagnostic pulse train consists of ten individual µs triplets separated by 17 µs (Figure 5.22). This structure arises from gating of the AOM (CW → bunch train operation) in the diagnostic channel prior to the pre-amplifier to prevent damage to the amplifier. As a simplification the delay of each triplet relative to the primary pulse train can be considered as static. This scheme permitted live characterization of the pulse envelope via photodiode but at the cost of resolution with only ten data points per envelope (Figure 5.23).

Given the low resolution it becomes difficult to produce distributions with good confidence. It can be seen by slowly varying the optical path difference in the cross-correlator that the temporal envelope suffers from significant distortions. Furthermore, multiple diffractive orders of the primary beam can be seen at the crystal plane (Figure 5.23). This is very clearly an artefact of the SLM discretization as the applied binary calibration band mask (Figure 5.15b&d) can be seen. These low-intensity diffractions transversely overlap with working channel signal and the whole diagnostic pulse potentially reducing the SNR on the detectors.

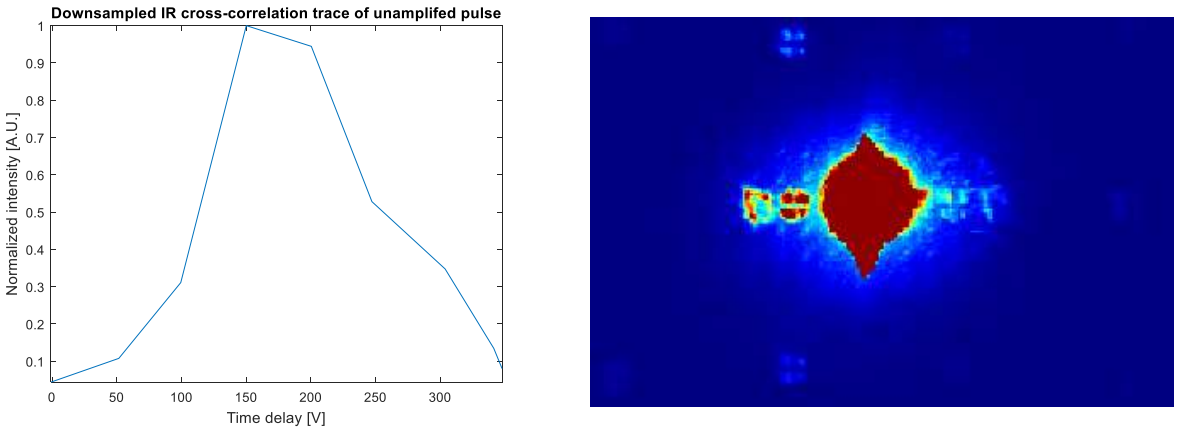


Figure 5.23: A downsampled cross-correlation trace (left), and visible diffractive orders of the working channel at the cross-correlation crystal plane (right).

The design [92] utilized a polarization-maintaining, single-mode fiber coiled around a piezoelectric washer as a fiber delay line. A high voltage ramp was applied over the duration of the 300 us pulse train to induce a linear increase of the fiber length resulting in a linearly increasing effective delay for the ten sets of triplets along the pulse train.

However, in comparison it can be seen (Figure 5.24) that by manually stepping an external delay stage in 0.05 mm increments, or by slowly increasing the high voltage applied to the fiber delay line in 2.5 V steps, that a much different story is presented and that a higher resolution was required for accurate pulse shaping.

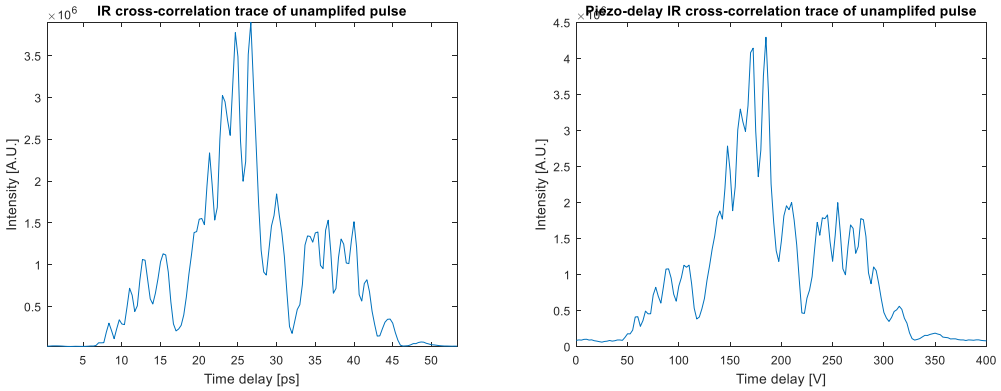


Figure 5.24: a) IR cross-correlation envelope of the unamplified pulse from a linear stage manually stepped in 0.05 mm (⅓ ps relatively) increments. b) similar IR cross-correlation envelope for the piezoelectric delay fiber from 0 V to 400 V in 2.5 V steps.

With this high resolution cross-correlator the temporal envelope of the amplified pulse was found to be in good agreement with its spectrum (Figure 5.25). By extension, it also followed that the spectral distortion from the amplifier (Figure 5.8) distorted both the temporal envelope and the transverse profile simultaneously (Figure 5.26).

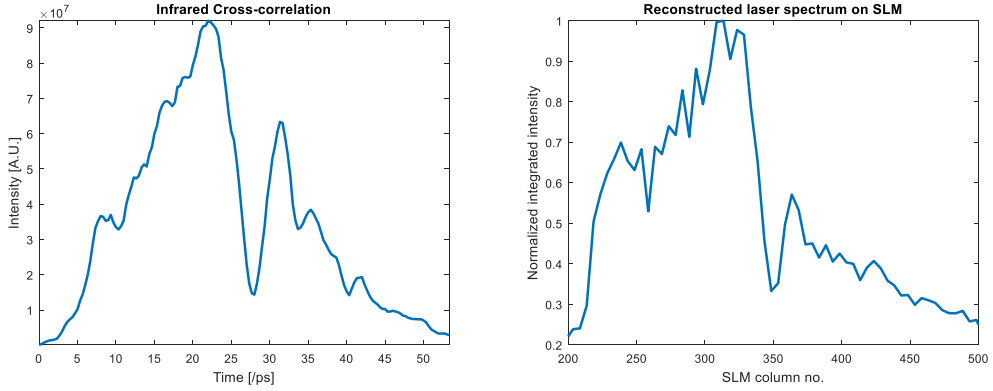


Figure 5.25: a) Unshaped amplified IR cross-correlation trace. b) Comparative reconstructed spectrum at C4 (see: Figure 5.2).

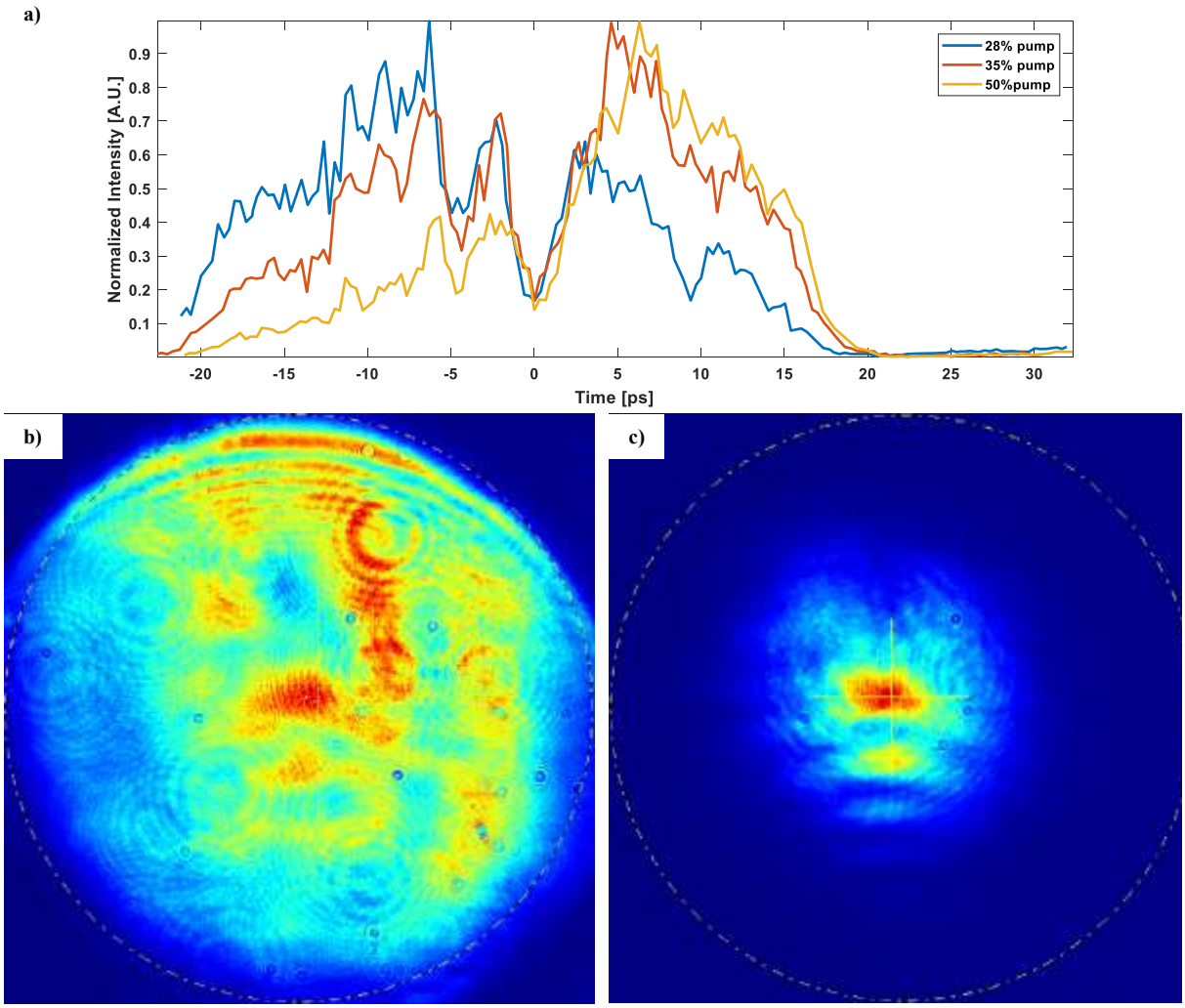


Figure 5.26: a) Spectral distortion and shifting measured at C5. b) Unamplified flattop transverse distribution at C5, and (c) amplified transverse distribution with Gaussian narrowing (Ø=1 mm →σ_r=0.25 mm).

5.10 HARMONIC CONVERSION

The conversion section consists of three 4f Keplerian telescopes in series with a spectrally dispersive element, in this case a prism, located after the first telescope (Figure 5.27). The first Keplerian telescope pair before the 2nd harmonic LBO crystal, a f222:f563 pair and a f337:f21 pair, can be considered in parallel as two optical systems.

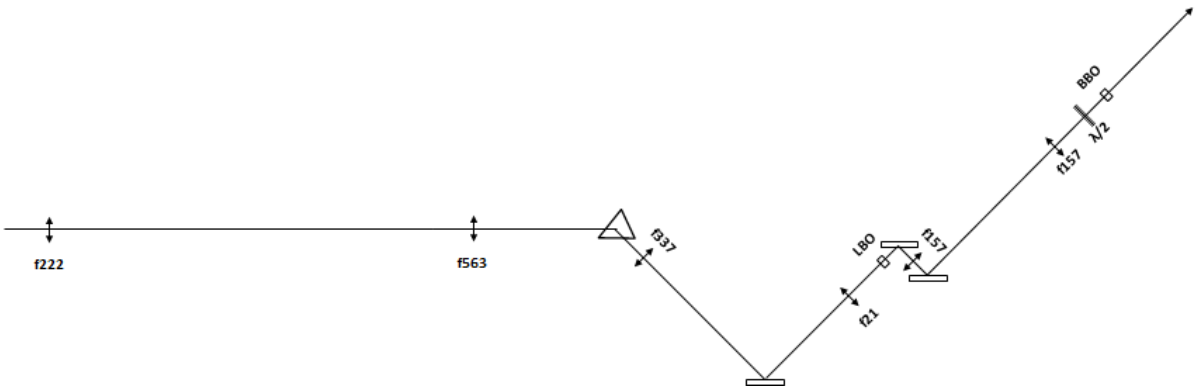


Figure 5.27: The layout of the conversion section.

In one case as a double Keplerian pair with a variable separation that act overall to reduce the collimated beamsize on the crystal with the latter pair adjusting the angular dispersion introduced by the intervening prism as required for full bandwidth conversion in the non-linear conversion (Sec. 4.1.4).

Simultaneously, the double lens pairs can be regarded as an imaging three-element telescope with the centre lens decomposed into two separate lenses permitting a variable magnification and an intermediate image plane at the first surface of the prism (Figure 5.28). A boundary condition to this is that the internal distance of the separate lens pairs must remain the sum of the respective focal lengths to maintain collimation.

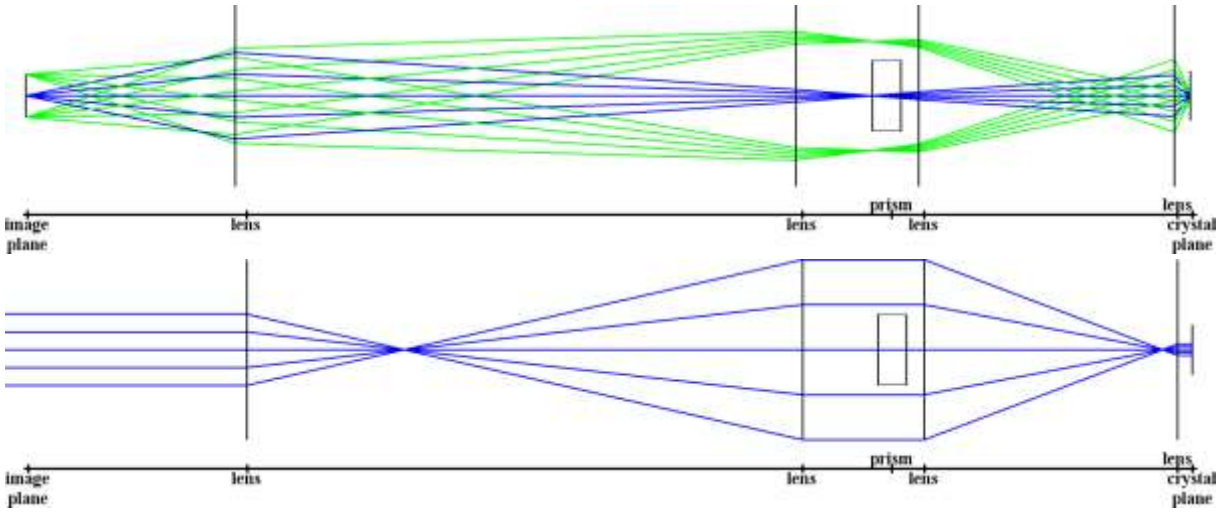


Figure 5.28: Relation of image planes and the collimated laser relative to the input BSA and LBO crystal plane.

The final f157.75: f157.75 Keplerian telescope after the 1st harmonic conversion crystal simply relays the generated harmonic pulse through two laser-line mirrors to the final BBO conversion crystal as the required angular chirp for both LBO and BBO is similar.

Ultimately the size of the input image plane is limited by the ⌀2 mm aperture placed there. The system resulted in a maximum image size of ~0.3 mm on the LBO crystal with an angular magnification of the prism dispersion of ~16.

Which, for the given prism made of TF12, with a 60° apex angle, incident angle of ~60°, and material dispersion of 0.03×10^{-3} nm^{-1}, resulted in the angular chirp of 0.004 deg/nm from the prism being magnified to the required 0.066 deg/nm.

As stated previously, non-linear conversion is a transversely distortive process owing to intensity-dependent non-linearities, and spatial walkoff, the latter of which is exacerbated by crystal length. In practice, 4 mm LBO and 2 mm BBO crystals were used to obtain sufficient UV pulse energy. This was unfortunately a compromise between UV pulse energy (and subsequent losses at the BSA) and shape preservation (Figure 5.29).

By varying the width of the binary calibration line mask a "star" profile was obtained at the reference image plane (see: Figure 5.2, C5) which was then compared to the generated 2nd harmonic from the LBO crystal located at the image plane at the BBO crystal. This profile was in turn compared to the generated 4th harmonic from the BBO crystal located at the intermediate image plane on the table which coincided with the image plane of the UV cross-correlator.

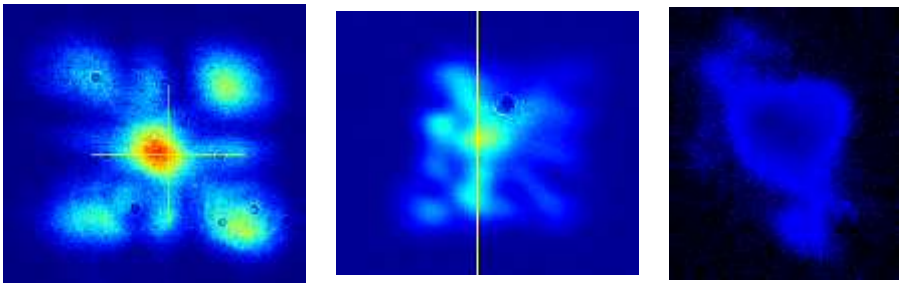


Figure 5.29: Transverse profile of horizontal line mask prior to conversion (left), converted to green (middle), and in the UV (right).

It can be seen that although there is a very weak conservation of the transverse shape during conversion to the 2nd harmonic the final result bears only a very weak resemblance to the fundamental profile. Since harmonic conversion is a non-linear process some of the deterioration can be attributed the inhomogenous profile as the differing intensities would be expected to produce further variable harmonics. Furthermore, this was exacerbated by birefringent walkoff of the harmonics in the crystals.

While walkoff is arguably negligible through 4 mm of LBO as it has only a 32 µm walkoff of the harmonic for a ~300 µm input beam this is not the case for BBO. Walkoff in BBO is an order of magnitude worse (Table 2.2) which results in 170 µm of walkoff for the relayed, ~300 µm LBO harmonic.

5.11 LASER BEAM TRANSPORT

On the laser table a final three-element variable (1x-4x) Keplerian telescope (sec. 4.1.5) was used to match the beamsize of the image plane on the BBO crystal to the object planes of either the transport beamline or the UV cross-correlator.

Unfortunately there was a coupling issue with the transport beamline in that it was originally designed as a magnifying telescope for projection of the original MBI laser onto the

BSA in the tunnel for the generation of flattop transverse distributions. This conflicts with the design requirements of the ELLA system which prefer direct imaging of the beam onto the photocathode.

From design, and in the practical realization, it can be seen that the expected image size on the final BBO harmonic conversion crystal should be ~0.3 mm, and with the existing MBI transport telescope producing a magnification of ~4x it immediately becomes apparent that to produce a nominal 1.2 mm diameter beam at the BSA plane that a 1:1 relay of the in-coupling telescope would be ideal.

However, in practice it was found that any magnification of <4x of the final on-table Keplerian telescope resulted in a highly divergent beam that was heavily cropped by the 1st ⌀50.8 mm f2000 lens in the transport telescope which resulted in no discernible transmission of light in the tunnel.

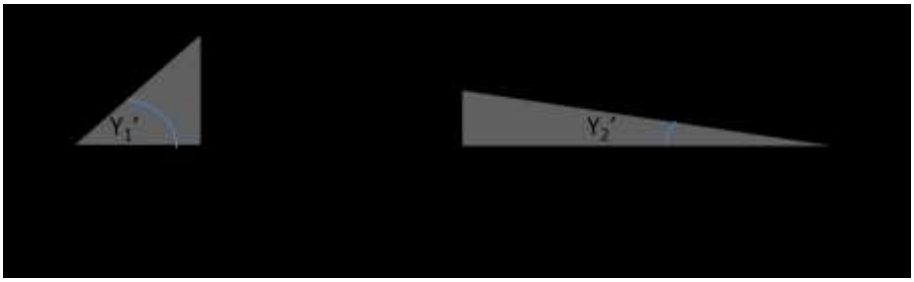


Figure 5.30: Principle of optical invariance for an arbitrary optical system.

The cause was poor coupling of the Optical Invariant. Optical invariant (Figure 5.30) is the product of the image size and ray angle and is constant for any arbitrary, unconfined optical system:

$$y_1 \cdot y_1{}' = y_2 \cdot y_2{}'. \tag{5.1}$$

It is insightful to consider the input invariance of the transport telescope:

$$y \cdot y' = 150\ \mu m \cdot 11.5 mrad = \ 1.73\ mm \cdot mrad, \tag{5.2}$$

where the acceptance angle y' is limited by the diameter of the lens and its distance from the image plane which are fixed quantities. However, the image size is limited by the lens diameter and is determined by the preceding variable telescope.

Looking at the variable telescope's invariance for the same image size:

$$y \cdot y' = 150\ \mu m \cdot 63.6\ mrad = \ 9.54\ mm \cdot mrad, \tag{5.3}$$

it is found that there is a large discrepancy in the acceptance angle of the transport telescope against the output angle of the variable telescope which leads to unacceptably large losses.

This was rectified by matching the acceptance angles and therefore increasing the image size entering the transport telescope. This is easily visualized in the phase space (Figure 5.31) where the overlapping areas of the transport beamline and in-coupling telescope determines the effectiveness of the optical transmission.

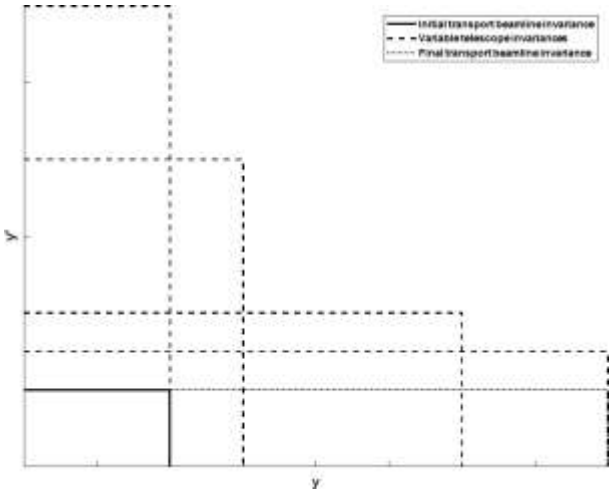


Figure 5.31: Phase space plots of the optical invariance of the in-coupling telescope and transport beamline.

As such, the only possible way to get sufficient light on the photocathode was to increase the spotsize and utilize the variable Beam Shaping Aperture (BSA) in the tunnel to crop the transverse distribution and create a “truncated” beam (Figure 5.32).

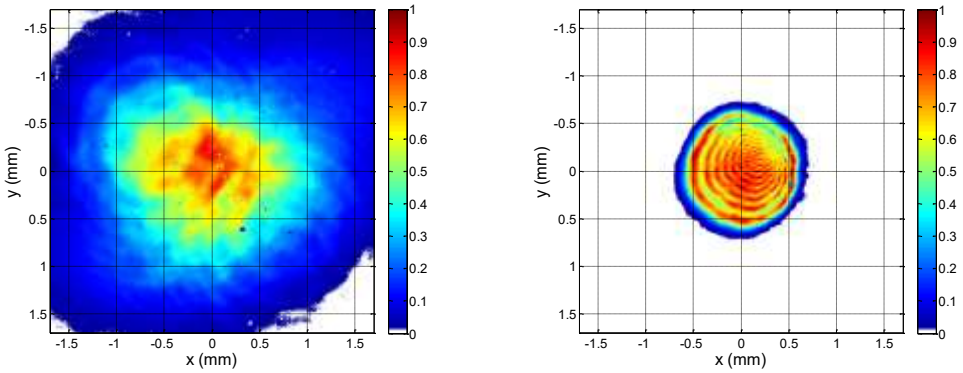


Figure 5.32: Transverse laser profile at a virtual cathode plane without (left) and with the beam shaping aperture (right).

5.12 SYNCHRONIZATION

Unfortunately, the original, high-resolution Holoeye SLMs were found to be unsuitable for photoelectron operation owing to their continuous, asynchronous refresh rate at 60 Hz and the pair was exchanged for a single Hamamatsu phase-modulating SLM acting as an amplitude mask.

Furthermore, the reliability of the oscillator synchronization was found to depend heavily on the environmental humidity (Figure 5.33), and the synchronous resolution was limited to the ps scale. This was as a result of eigenmodes in the piezoelectric regulator and a poor SNR on the feedback photodiode.

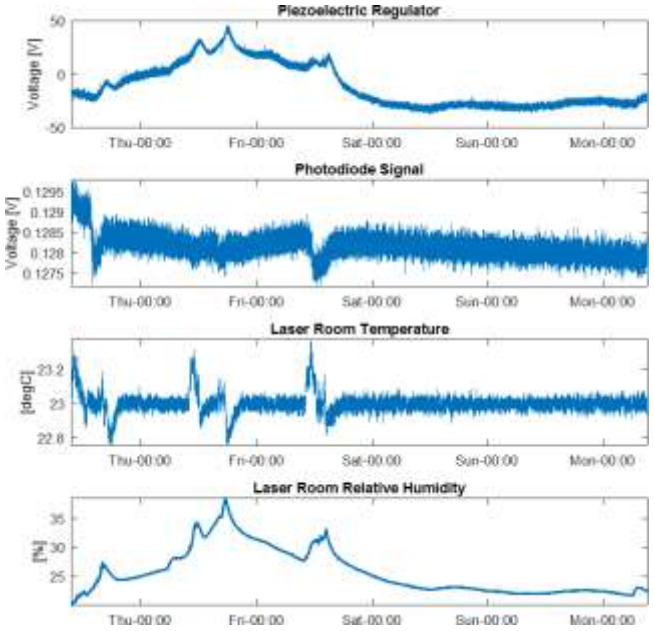


Figure 5.33: Environmental and feedback data of the µTCA synchronization of the ELLA oscillator with the master oscillator.

Owing to the very stable thermal environment of the laser hutch the only environmental factor influencing the fundamental frequency of the laser oscillator was the humidity. However unforeseen flaws in the choice of the frequency regulation piezo limited the scale of synchronization with the RF to the ps scale.

In conclusion, the conceptualization and design of the laser system contains a number of resourceful solutions and approaches. The reciprocal design solves a number of issues; it compensates the nature of the highly-lossy pulse shaping scheme, provides shaping in both transverse axes, compensates for the axial separation induced by the cylindrical lenses in the 4f-line, and coupled with Faraday rotators exploits the inherently necessary polarization control in order to do so.

The inclusion of angular chirp for spectral phase-matching compensation of the harmonic conversion process inside a double 4f telescope also allows for fine tuning of the magnitude of the chirp and the spotsize on the crystals.

Furthermore, the ramping of the piezoelectric fiber delay within the duration of the macropulse train permitted “live” pulse shaping feedback from both photodiodes and a fast-shifting CCD camera, albeit at a low resolution.

However, a number of practical flaws were discovered in the implementation. The long pathlengths, multiple up-down magnifying telescopes, and poorly constructed optomechanics all added to long-term stability troubles. Furthermore, the original Holoeye SLMs were incompatible with the accelerator’s timing scheme, and only a fraction of the active area was utilized.

The thin-disc, multi-pass amplifier exacerbated the already poor spectral quality of the oscillator output and the large amount of optics (and optical surfaces) compounded misalignments and imperfections while simultaneous narrowing the transverse profile.

It was similarly determined that the low sample rate of the temporal diagnostics was

insufficient as it clearly overlooked the temporal oscillations within the pulse envelope.

Piggybacking of the ellipsoidal laser beam into the pre-existing laser transport beamline (of opposite design requirements) further complicated matters ultimately leading to the need of cropping of the transverse profile with the BSA and side-lining of the spectrograph. Although IR and UV spectrographs were was conceived and designed; only the IR spectrograph was constructed, and commissioned during this work. The cross-correlators took precedent owing to the decision to transversely crop the laser beam.

Finally, the resolution of the synchronization was fundamentally limited to the ps scale as the SNR for the higher order harmonics of the oscillator was too low.

Overall, many issues were discovered, and corrected as much as practically feasible but ultimately many had to be endured as systematic flaws of the implementation. Many of these flaws became part of the focus for the redesign in Chapter 7.

Chapter 6 Electron beam results

Ultimately the qualities of the electron bunch are the litmus test for any photocathode laser pulse shaping endeavour. It is the culmination of many scientific and engineering difficulties, often with conflicting solutions. It unities the frontend laser system, with the pulse shaping scheme, the harmonic conversion section, the transport beamline, and finally photoemission and acceleration.

6.1 COMISSIONING

As stated, owing to laser beam transport issues arising from 'piggy-backing' onto the primary MBI laser transport beamline the transverse diameter on the cathode was unavoidably increased. Beam quality was further exacerbated by the one-dimensional walk-off in the thick 4 mm BBO crystal required to reach sufficiently high non-linear conversion.

Owing to these limiting factors it was decided to make measurements by cropping, or truncating, the transverse profile with the BSA (Figure 6.1) and to reduce the charge to 500 pC. The results are compared with the nominal MBI laser with a 12 ps Gaussian temporal envelope as a reference because falt-top shaping of the MBI laser was not available at the time of the experiment since the OSS-system (Figure 3.3) was broken.

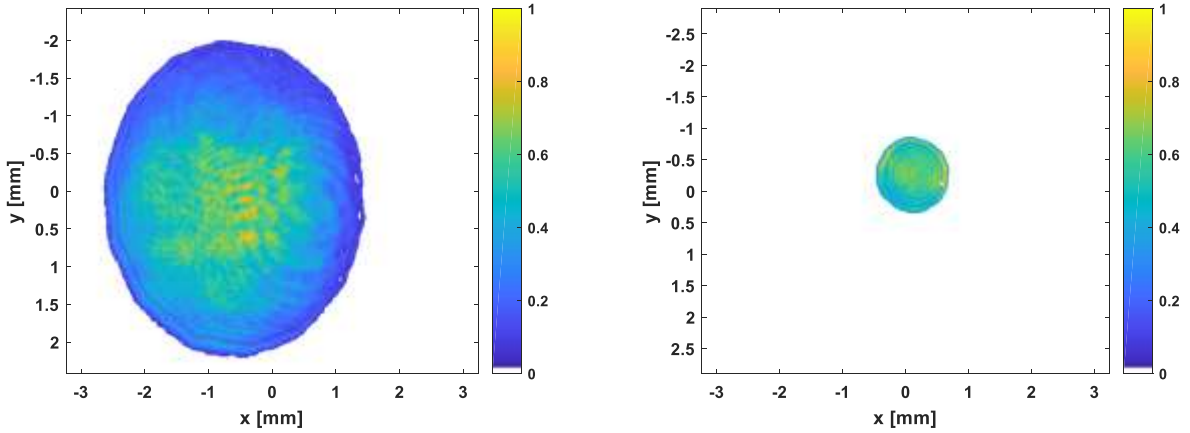


Figure 6.1: ELLA laser on VC2 with a 4 mm BSA and 3 pulses at 9% transmission (left). Truncated ELLA laser beam on VC2 with with a 1.2 mm BSA and 3 pulses at 9% transmission (σ_{XY} =0.29 mm) (right).

The gun phase ranges of both lasers initially differed (Figure 6.2) due to minor optical path offsets after µs timing correction, and any minor change or correction of the optical path length of ELLA on the order of 0.5 mm would result in a 1° phase shift. This was eventually overcome with a firmware update of the µTCA synchronization hardware that enabled phase-shifting of the ELLA laser timing to bring its gun RF phase in-line with that of the MBI laser system.

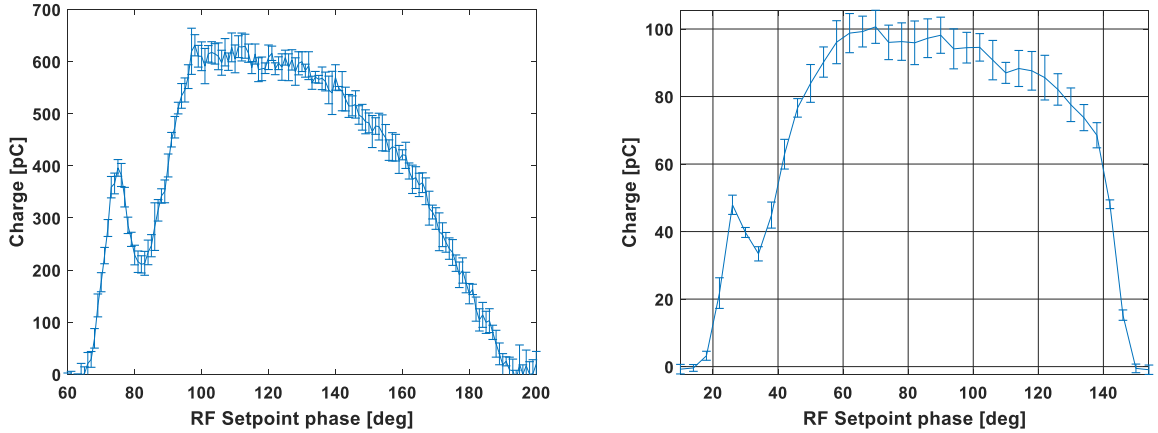


Figure 6.2: A comparison of initial measurement of bunch charge measured at 1.38 m downstream of the cathode as a function of RF gun phase setpoint for the MBI (left) and ELLA (right) laser systems.

The beam properties were checked by standard measurement procedures; the laser beam diameter was measured on VC2, and the laser transmission was adjusted to obtain the correct charge measurement on the Faraday cup 1.38 m downstream of the cathode plane. Of note is that for long bunch trains of the ELLA system the long oscillation period of the CW pump laser (Figure 5.14) for the thin-disc amplifier could be seen imprinted on the bunch charge (Figure 6.3). This could potentially impact the precision of multi-bunch measurements, such as low-charge emittance measurements, or the tails of emittance solenoid scans where defocussing requires a longer pulse train to achieve a reasonable beamlet intensity. It shows how even the simplest aspects of the laser system impact electron beam operation.

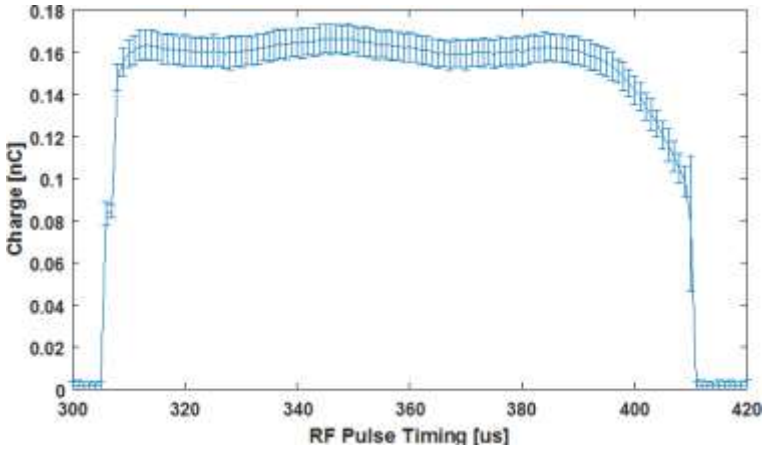


Figure 6.3: Bunch charge oscillations arising from ELLA's CW pump laser.

The electron beam momentum was measured in both the low (Figure 6.4) and high energy sections to determine the maximum mean momentum gain (MMMG) phase for gun and booster and the corresponding beam energies. The pulse duration as a function of charge was checked with the TDS (Figure 6.5). As expected, the bunch length is shorter for the larger laser spot sizes on the cathode due to the lower space charge density and correspondingly lower longitudinal

space charge forces, but the absolute bunch length values were found to be significantly shorter than expected, but it was decided to make projected emittance measurements to compare between the two laser systems.

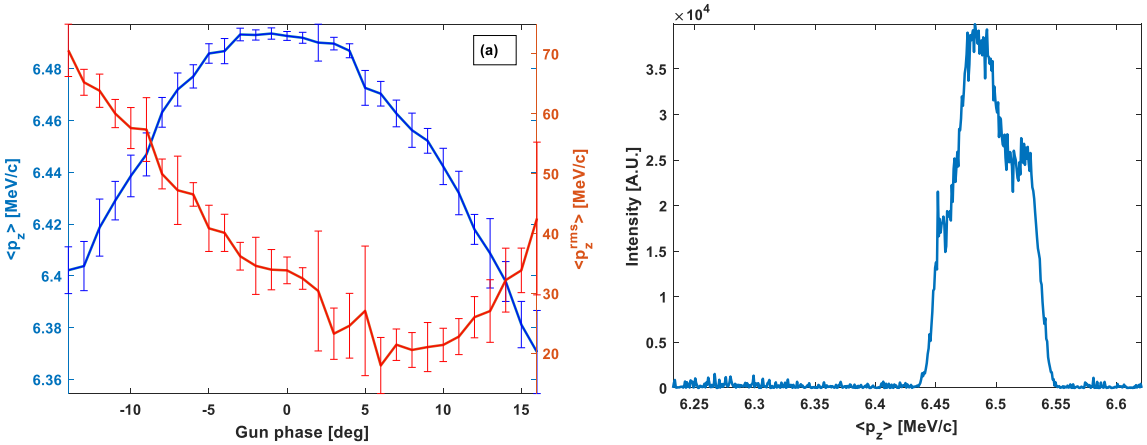


Figure 6.4: Measurements taken downstream of the gun of momentum and momentum spread as a function of gun RF phase (left), and the momentum spectrum at the gun RF phase of the maximum mean momentum gain (right) of the unshaped, 500 pC ELLA laser.

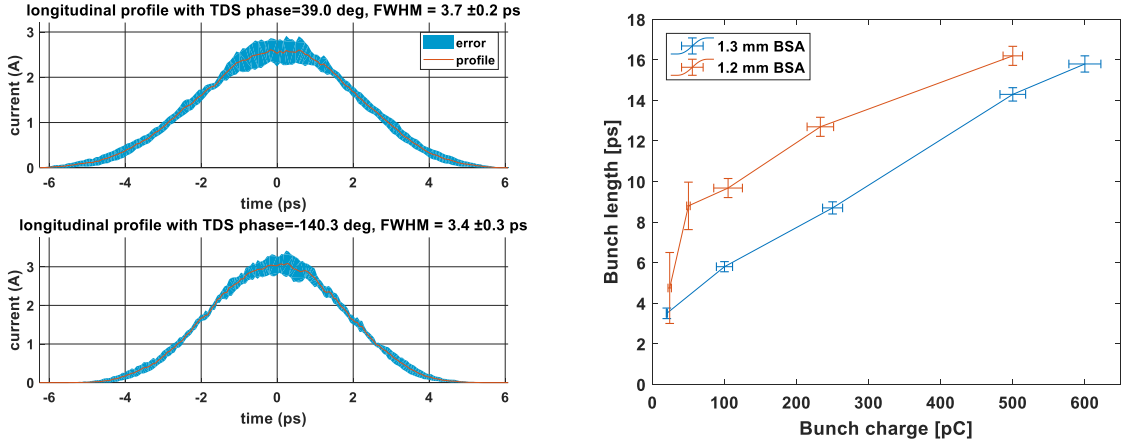


Figure 6.5: Temporal projections of a streaked 25 pC bunch (left) and measured FWHM bunch length as a function of charge and aperture (right) of the ELLA laser.

For the comparative emittance measurements a standard scan of projected emittance versus main solenoid current and in both transverse planes was taken for 500 pC pulses with a 1.2 mm transverse cropping. This was done for the <12 ps FWHM ELLA laser pulse without spectral shaping, the “long” 12 ps FWHM MBI laser pulse, and the shorter 2 ps FWHM MBI laser pulse. The latter two pulse lengths were achieved by inclusion of a Lyot filter in the MBI laser system suppressing bandwidth and removal of the filter, respectively.

As can be seen from the measurements of projected emittance as a function of main solenoid current (Figure 6.6), both laser systems present comparable minimized projected emittances of

1.26 and 1.04 mm mrad for bunches of comparable charge and diameter.

Unfortunately, at this time the cross-correlators of both laser systems were not operational. The pulse length of the MBI laser was assumed to have a “long” Gaussian temporal envelope of ~12 ps FWHM based on previous measurements for the same laser setup, and this was corroborated with the electron bunch length measurement with the TDS to be 15.4 ps. The ELLA laser was later measured to have a comparable electron bunch length of ~16 ps, however low-charge TDS measurements (Figure 6.5) show the ELLA laser pulse length to be ~4 ps.

These two measurements stand in contrast to the more “pancake” like pulse with a BSA of 1.6 mm and a 2 ps Gaussian temporal enevelope. It has a higher projected emittance of 1.46 mm mrad.

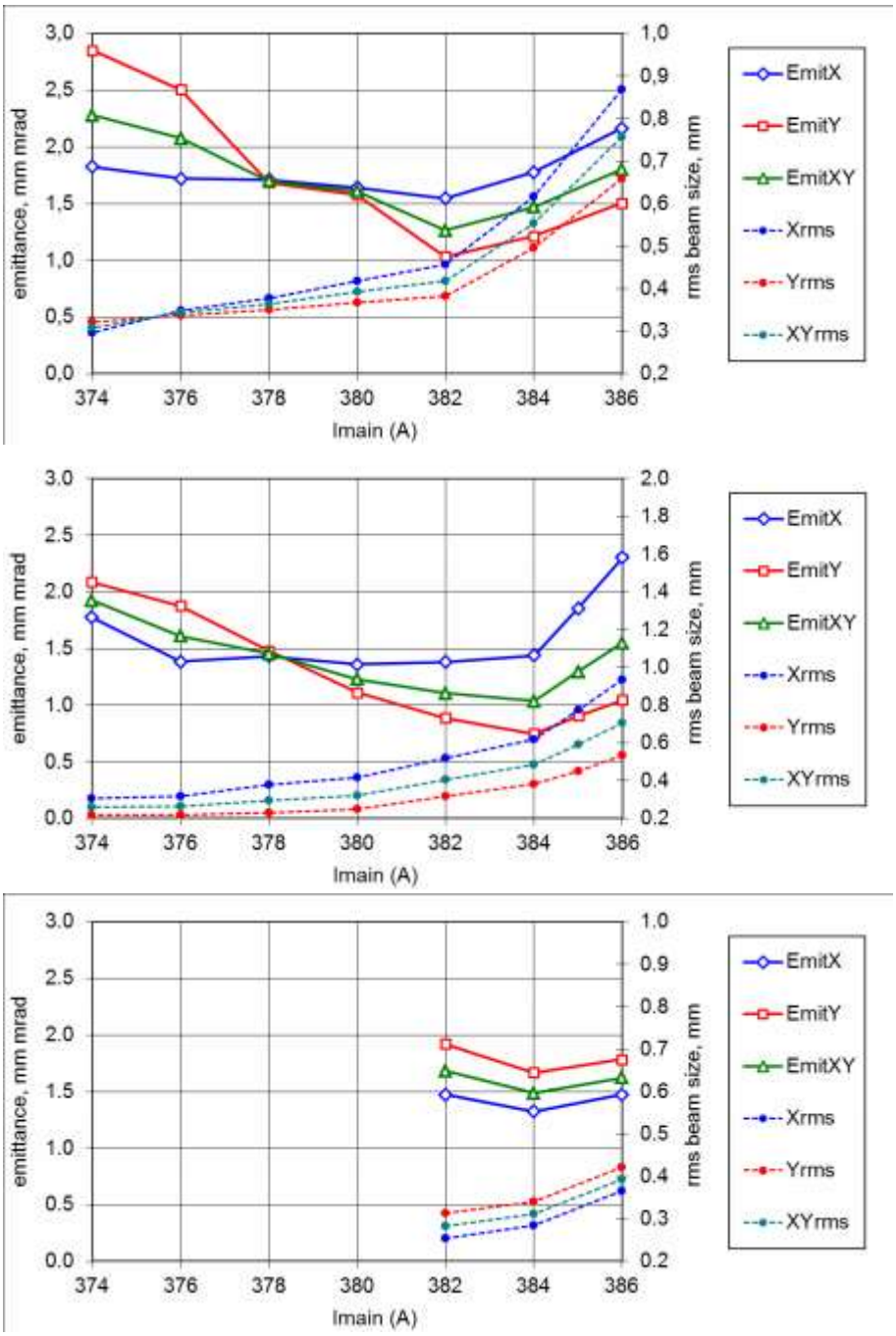


Figure 6.6: Projected emittance versus main solenoid for 500 pC bunches. Unshaped, <12 ps, 1.2 mm BSA ELLA laser (top), 1.2 mm BSA, "long" 12 ps Gaussian MBI laser pulse (middle) and 1.6 mm BSA, "short" 2 ps Gaussian MBI laser pulse (bottom).

6.2 ELECTRON BEAM SHAPING

There were a number of complications impeding an extensive experimental electron beam measurement program. The short pulse length previously measured was confirmed with the rebuilt IR cross-correlator which demonstrated spectral distortion and a FWHM of the primary spectral peak of 6 ps. This necessitated elongation of the grating compressor on the table to bring

the pulse length up to 16 ps but at a small cost of spectral width and intensity.

The increase was confirmed by electron bunch length measurement (Figure 6.7). The same rough structure of the laser pulse also roughly correlated to the structure of the bunch. It was also clear that the left-hand peak should be supressed (Figure 6.8) and that any mask applied must have a spectral boundary condition.

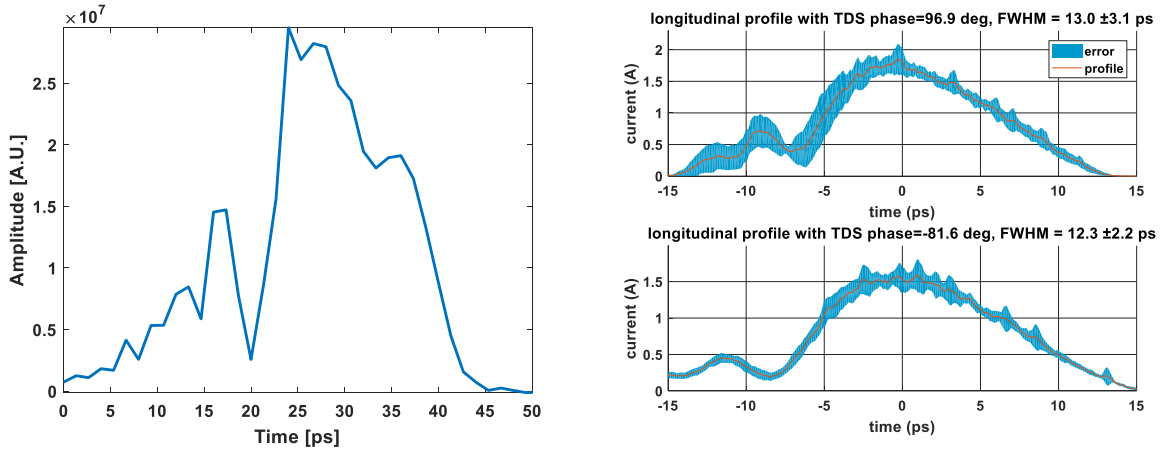


Figure 6.7: An IR cross-correlation of the laser pulse with a ~16 ps FWHM of the main peak (left). A low-charge (100 pC) electron bunch length measurement with a shorter FWHM of the main bunch of ~13 ps (right).

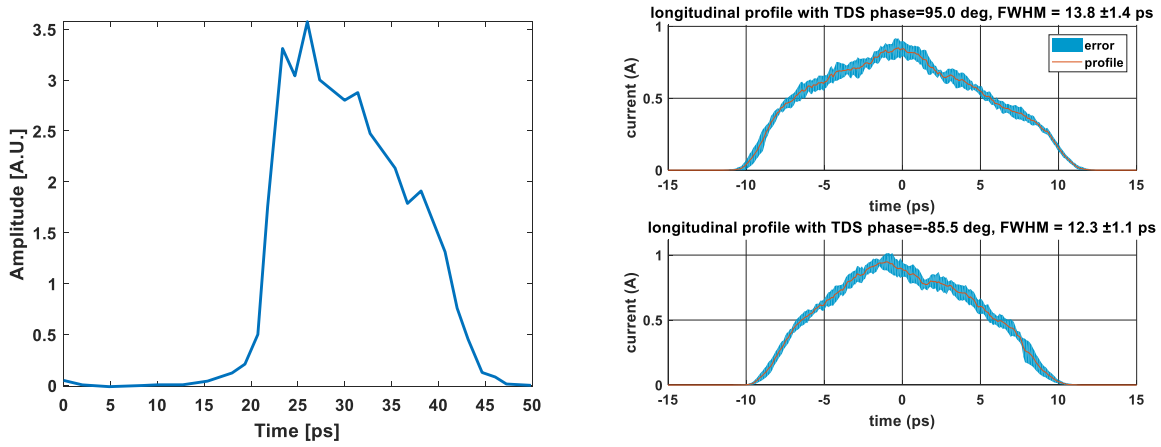


Figure 6.8: Removal of side peak with spectral masking (left). Electron bunch result (right)

The spectrum was experimentally adjusted to produce a parabolic IR cross-correlation to match the ellipsoidal line integral and the asymmetry of the electron beam was compensated for by using the gun quads to symmetrize the spot at the emittance measurement screen, high1.scr4, 8.41 m downstream of the cathode plane. The standard projected emittance procedure was then followed. The bunch charge, stability and the charge as a function of gun RF phase were measured (Figure 6.9). Also the momentum and momentum spread after the gun and the booster were measured and the cavity phases set to their respective MMMG phases (Figure 6.10).

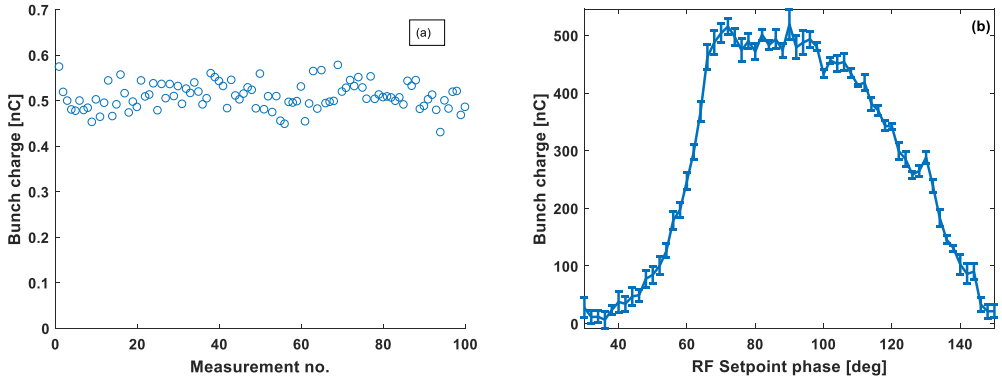


Figure 6.9: a) Measured charge statistics and b) charge as a function of gun phase.

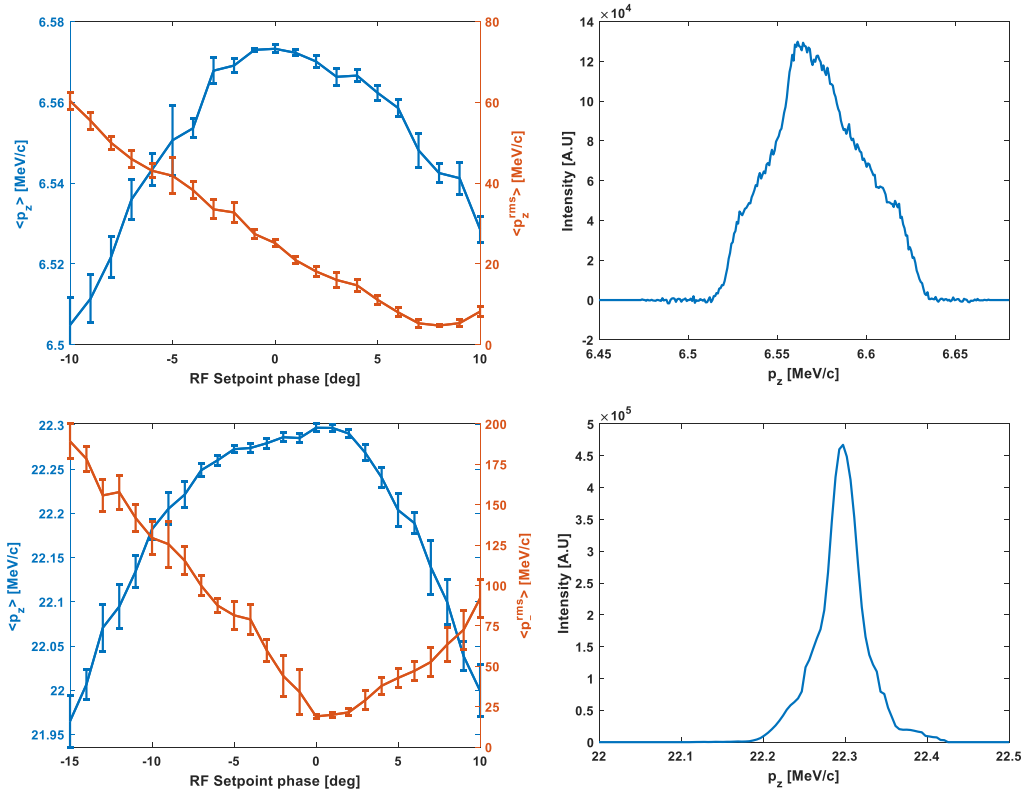


Figure 6.10: Gun (above) and booster (below) momentum as a function of respective RF phases (left) and the momentum spectra (right).

An improvement in projected emittance was found (Figure 6.11) as the minimum emittance of the solenoid scan was reduced by 0.20 mm mrad from the unshaped, shorter case to $\sqrt{\varepsilon_{n,x}\varepsilon_{n,y}} = 1.06\ mm\ mrad$ [90]. Although the minimum emittance achieved is only comparable with the 12 ps FWHM MBI Gaussian laser pulse, which was itself an assumed quantity, it demonstrates that spatio-spectral laser pulse shaping works and can improve laser systems with poor laser beam quality. Poor phase stability is already known from simulation to degrade emittance measurements [99] and the limited synchronization was another restricting factor in these measurements.

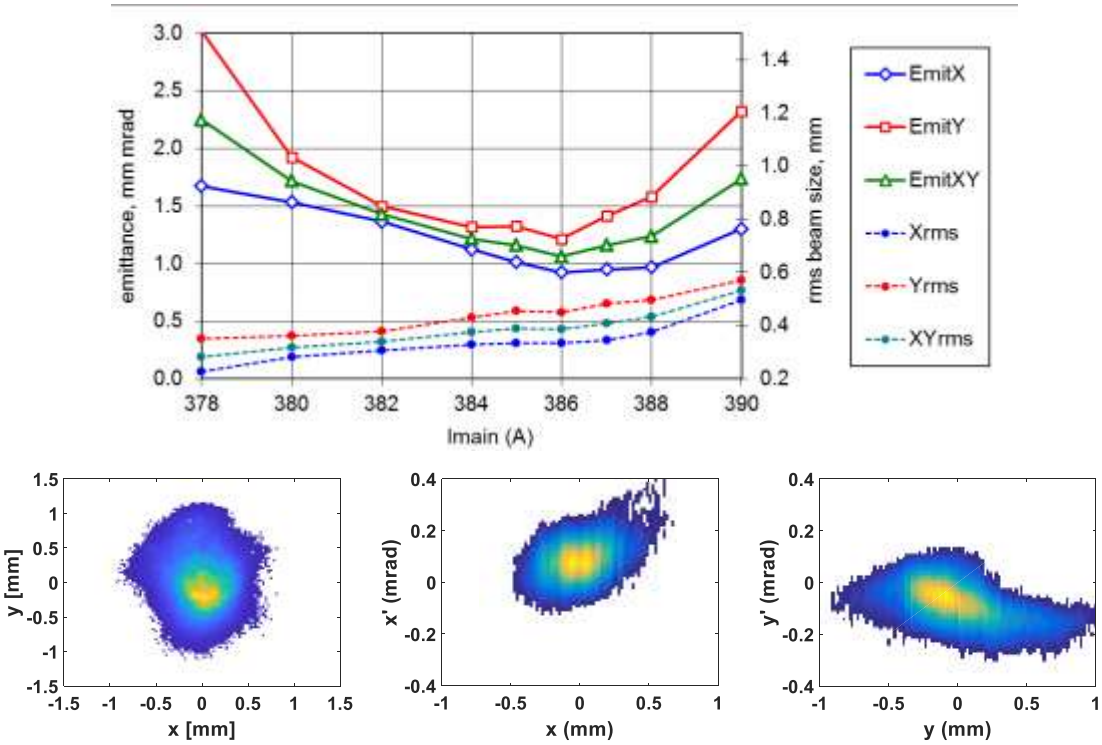


Figure 6.11:(upper) Projected emittance as a function of main solenoid current (min ε_{xy} = 1.06 mm mrad), and beamsize and phase space plots for the optimized main solenoid current (lower row).

The electron bunch was also streaked with the TDS onto PST.scr1 to evaluate its temporal structure (Figure 6.12). With the TDS off the beam was focussed to a horizontal line with the two preceding quadrupole magnets (Q9, Q10) and up to three pulses were streaked with the TDS on.

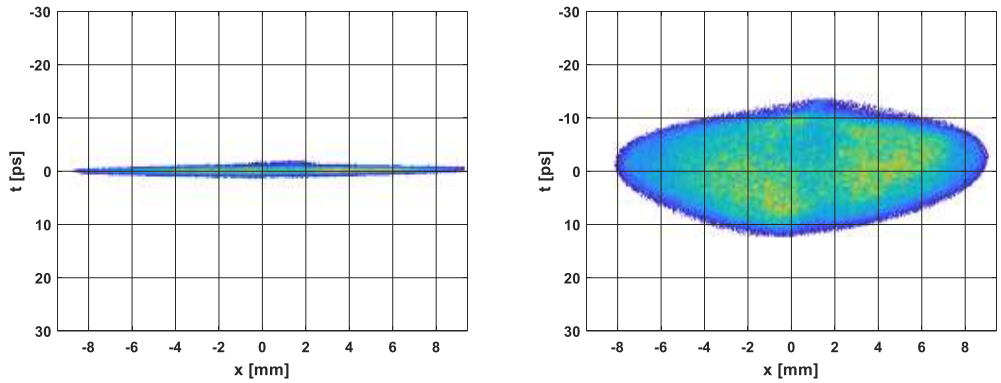


Figure 6.12: Unstreaked and streaked shaped bunch images.

The bunch current, the projection of the streaked bunch onto the temporal axis, shows the expected parabola-like line integral. Another indication that the bunch was quasi-ellipsoidal.

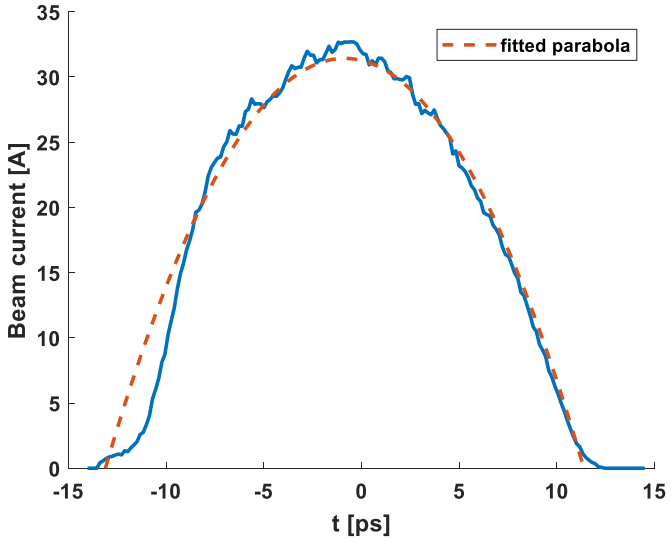


Figure 6.13: Integrated beam current from TDS projection and parabolic fit.

Soon after bringing the laser system into synchronized photoinjector operation issues with the cathode spring and cathode exchange system in the gun, Gun 4.6 [100], occurred. This effectively halted any further possible electron beam measurements and the original ELLA laser system was soon decommissioned thereafter

In conclusion, a novel, spatio-spectral pulse shaping photocathode laser was commissioned and brought into limited operation within a photoinjector facility environment. UV pulses were generated, synchronized, and delivered to the photocathode and used to produce photoelectrons. These electron bunches were characterized and found to be comparable with nominal photoinjector parameters.

Active, live electron bunch shaping was demonstrated with the time resolved electron bunch shape measurement with the TDS cavity and confirmed with cross-correlation measurements in the laser system. An improvement in emittance was measured. Due to the failure of the gun cathode spring further corroborative and potentially improved, electron beam measurements could not be undertaken. This, coupled with the general stability issues and limited synchronization meant that only a preliminary improvement in emittance could be measured on par with that of the nominal, Gaussian MBI photocathode laser.

But many lessons have been learned to be implemented in a next generation of ELLA system which should allow more robust and further improved 3D laser pulse shaping capabilities.

Chapter 7 Redesign

A simplified redesign of the original scheme was undertaken to rectify a number of conceptual limitations encountered and identified with the original system:

- Poor pointing & opto-mechanic stability
- Poor spectral/temporal quality (Figure 5.18b)
- Amplifier transverse distortion (Figure 5.26)
- Underutilization of SLM chip area
- Beam transport

Stability issues

The original system suffered from poor stability with slow pointing drift of both the oscillator output and subsequent opto-mechanics. This necessitated daily re-alignment of the system for on-table experiments, with continuous monitoring, and drift-induced realignment, during shift operation and time-consuming electron beam measurements. For a user facility such as FLASH or the European XFEL this would be unacceptable.

Poor beam quality

The spectral quality, and by extension the temporal envelope, was modulated coming from the oscillator itself [92]. This was further exacerbated by spectral shifting in the multi-pass amplifier. The transverse distribution of the pulse was also non-uniformly amplified resulting in beam narrowing and inhomogeneity.

SLM Chip area

The illumintaed area on the SLM chip was approximately 300 px * 200 px of the available 600 px * 800 px, utilizing only roughly 12.5% of the active area. This arose due to the choice of focal elements in the shaping section, the in-coupling magnifying telescope, and spectral narrowing in the amplifier. It simultaneously raised concerns on instantaneous high-fluence damage thresholds (LIDT), thermal loading, and low-resolution control of the laser beam.

Furthermore the non-modular design made it difficult to contain stray optical radiation and to retrofit parasitic monitoring devices after the design and installation phases, and the reciprocal aspect made it problematic to isolate issues within the optical chain. This also made it difficult to protect the optics from dust, particularly the non-vertical surfaces in the compressors and beam rotator, as the sections could not be isolated within their own separate enclosure and protected from coincidental contamination.

Based on these practical experiences a number of design goals were set:

- Linearization & simplification of the optical scheme
- A robust and stable layout
- To minimize optical distortion and losses
- Expand pulse shaping capability

A conservative energy budget (Table 7.1) was considered to ascertain the power requirements for any replacement laser system.

Table 7.1: The estimated pulse energy budget for any ellipsoidal pulse shaping photocathode laser at PITZ.

Required charge	1 nC	
Required UV pulse energy at cathode	~100 nJ	(~5% QE)
Margin of error (2x)	~200 nJ	
Transport losses (5x)	~1 uJ	
4th harmonic conversion (515 nm->257 nm)	~10 uJ	(~10% eff.)
2nd harmonic conversion (1030 nm->515 nm)	~20 uJ	(~50% eff.)
Pulse shaping losses	~60 uJ	(~30% eff.)
Margin of error (+40 uJ)	~100uJ	

Fortunately, owing to contemporary advances in high power, ultrashort solid state laser systems a number of commercial systems are available on the market which can meet this budget. A 20 W, 1 MHz, ultrafast Pharos laser [101] was selected for its flexibility, stability, and variable pulse energy of up to 200 µJ (at proportionally reduced repetition rates). It was also foreseen as an auxiliary laser system to substitute for the primary MBI photocathode laser when necessary at its maximum repetition rate and lower pulse energy of 20 µJ.

It was ordered in late 2016 and delivered in Spring 2017.

7.1 PHAROS LASER

The Pharos laser (Table 7.2) is a solid-state oscillator-amplifier laser developed by industry for scientific and industrial applications and is utilized by collaboration partners such as MBI [102] and DESY's FS-LA [103] [104]. Its primary advantages, in a scientific capacity, are pulse energy scalability, incorporated rough/fine oscillator frequency regulation for RF synchronization, an internal stretcher-compressor, and an optional 300 mW tap of the transform-limited oscillator pulses for cross-correlation experiments.

Conveniently, the 72 MHz oscillator pulses simplify any cross-correlation scheme as synchronous pulses need not be utilized. Given the difference in repetition rates (72 MHz ↔ 1 MHz) between the two pulses any combination of pulses within the train can be utilized as the next oscillator pulse is only 14 ps (4 m) away. However, this does come at a comparative cost of pulse energy as the oscillator pulses are only ~4 nJ/pulse.

Table 7.2: Measured Pharos parameters from the factory test certificate [105].

Beam quality, M^2	20 W, 1 MHz	$M^2_x = 1.08$ $M^2_y = 1.12$
	20 W, 100 kHz	$M^2_x = 1.09$ $M^2_y = 1.15$
Waist width, $FW1e^{-2}$	20 W, 1 MHz	$d_x = 4.14$ mm $d_y = 4.07$ mm
	20 W, 100 kHz	$d_x = 4.09$ mm $d_y = 4.15$ mm
Astigmatism	20 W, 1 MHz	<0.04
	20 W, 100 kHz	<0.03
Ellipticity	20 W, 1 MHz	$d_{minor}/d_{major} > 0.94$
	20 W, 100 kHz	$d_{minor}/d_{major} > 0.92$
Pulse width	20 W, 1 MHz	245 fs
	20 W, 100 kHz	237 fs
Spectral width	20 W, 1 MHz	5.9 nm
	20 W, 100 kHz	7.5 nm
Polarization	20 W, 1 MHz	Horizontal >2000:1

Furthermore, an optional harmonics module was also installed as a backup of an unshaped UV source for direct photoelectron generation. This was preliminarily tested under accelerator conditions to produce charge and evaluate the frequency synchronization.

The Pharos is a diode-pumped laser with Yb:KGW (ytterbium doped potassium gadolinium tungstate) as its active media. It utilizes a compact, chirped-pulse amplification scheme with a regenerative amplifier and variable compressor (Figure 7.1) to deliver pulses of up to 200 µJ and ps length pulses.

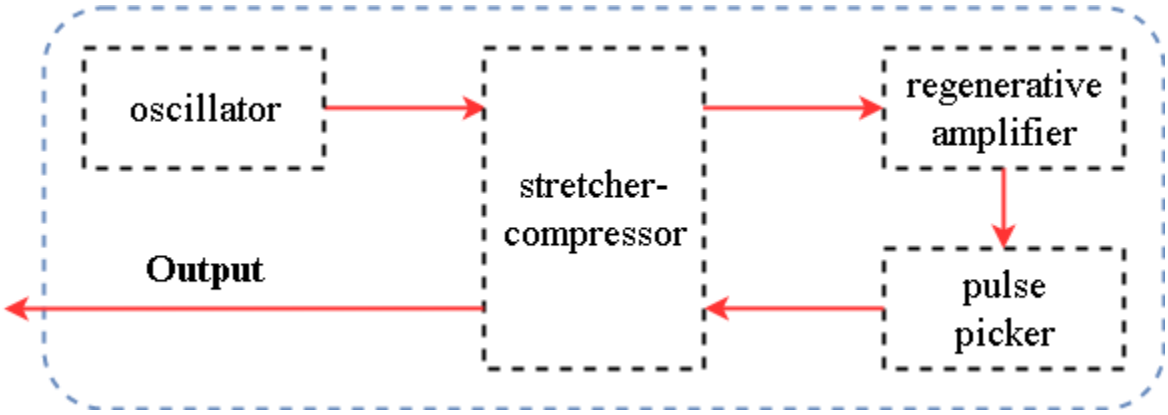


Figure 7.1: Schematic overview of the Pharos amplification chain.

As the pulse energy of the Pharos is inversely proportional to fractional regenerative amplifier frequency down to 100 kHz (Figure 7.2) the ceiling of any energy budget can be varied to accommodate different loss mechanisms. Of course, this has consequence on the effective SNR of any multi-bunch electron beam experiment.

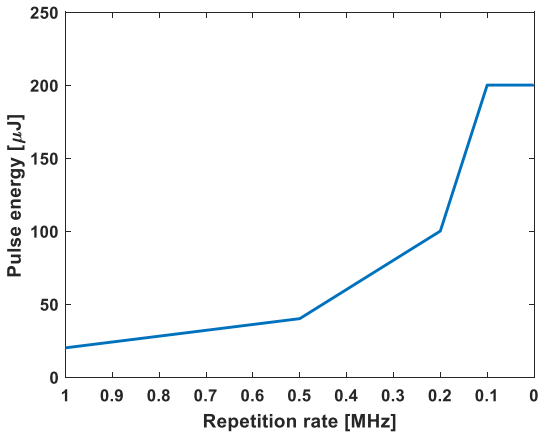


Figure 7.2: Pulse energy scaling for the full repetition rate range.

This combined oscillator-amplifier can seed any new shaping scheme with high energy laser pulses thereby circumnavigating the pre-/post-shaping pulse amplification in the original design. By extension this also reduces the effective optical path length, the number of optical surface interactions, and non-uniform pulse amplification; already meeting a number of design goals.

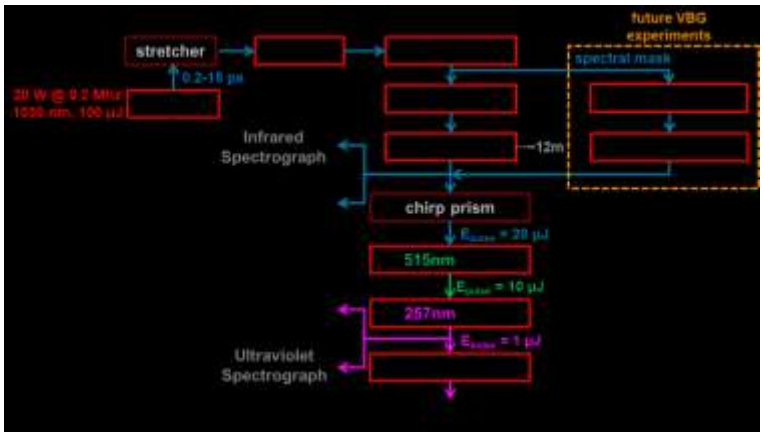


Figure 7.3: Simplified block diagram of the new optical scheme.

The new scheme (Figure 7.3) was heavily inspired by the old scheme but drastically simplified. The internal stretcher-compressor chirps the pulse to the order of ps and a beam expander increases the transverse diameter to maximize the vertical height on the SLM. The reciprocal shaping unit has been decomposed into two separate, serial stages with independent control.

In the bridging section a dove prism is used as an axial beam rotator instead of the rotating

tower to avoid tangentially tilted optical surfaces, and every stage is interconnected with optical path delays for image plane matching. The shaped pulse is again expected to be characterized by the standard temporal and spectro-spatial diagnostics such as IR/UV cross-correlators and spectrographs, while implementing phase matching of the harmonic conversion with angular chirp from either a prism or grating.

Furthermore, preparations were included to accommodate future spatio-spectral pulse shaping experiments utilizing profiled Volume Bragg Gratings (VBGs) [26]. Profiled VBGs can be imagined as a fixed set of wavelength specific mirrors in series with a radial diameter variation following an elliptical envelope. When illuminated with a chirped laser pulse with a flat-top spectrum a radial symmetric ellipsoid is reflected back. This has the significant advantage of radial symmetry but comes at the cost of a fixed shape.

An insertable mirror is therefore foreseen in the collimated section after the 1st SLM unit to provision for pre-spectral shaping to produce the flat-top spectrum as the transverse profile shall be defined and homogenized by a second independent transverse SLM plane.

The pulse energy on the cathode is finally defined by a waveplate-polarizer pair which act as a Laser Transmission (LT) controller. This is intended to minimize potential instabilities arising from the alternative method of simply varying the pulse energy coming from the Pharos backend.

7.2 ZEMAX STUDIES

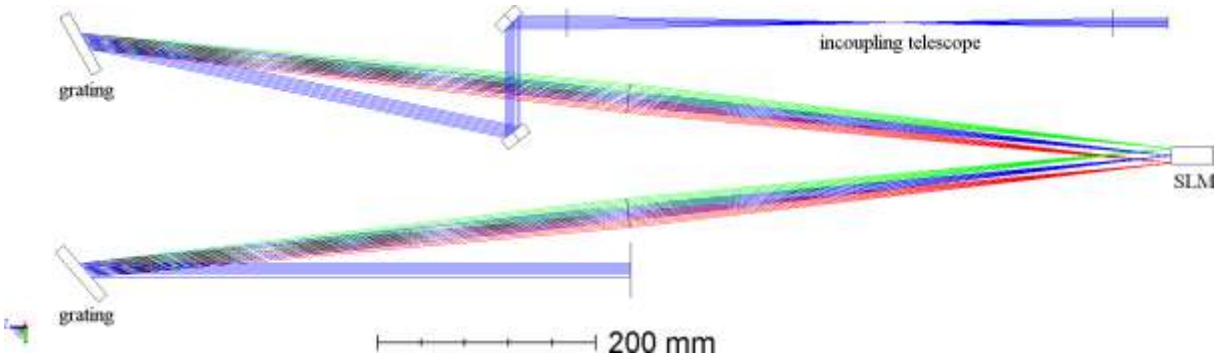


Figure 7.4: A single redesigned spatio-temporal shaper with a magnified collimated broadband input.

The first design consideration was to maximize utilization of the SLM chip area in order to utilize a high mask resolution and avoid Laser Induced Damage Thresholds (LIDT) arising due to high fluence. Therefore the optical components had to be chosen to maximize the vertical component of the transverse profile on the chip, which has been horizontally compressed for each spectral component, and to determine the correct dispersion of the spectral components horizontally across the chip (Figure 7.4).

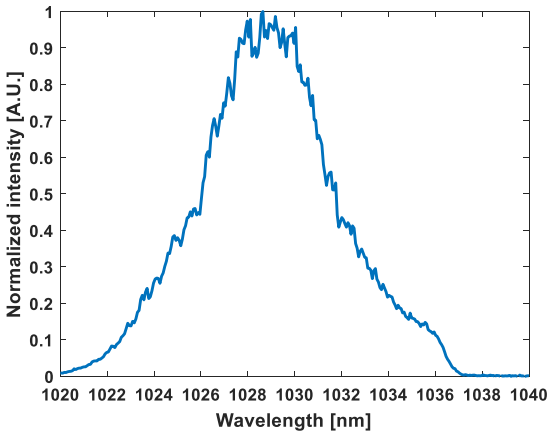


Figure 7.5: Measured Pharos output spectrum at 1 MHz repetition rate and 14.4 W, FWHM = 5.7 nm.

As the 4σ transverse size of the Pharos output beam is ~4mm an input 4f Keplerian telescope is used with a f100:f150 in a 1.5X beam expander configuration to enlarge the transverse size of the laser to the 6 mm half-height of the chip. Furthermore, as the FWHM spectral range is up to ~7nm (Table 7.2) a 1200 l.mm^{-1} diffraction grating blazed to the -1st order and f500 cylindrical lens were chosen to provide ~20 nm spectral range across the 16 mm width of the SLM chip.

The second spatio-spectral shaper is simply the inverted mirror of the first unit with a Dove prism in one of the collimated sections of a 4f bridge to provide axial rotation.

The operation of the pulse shapers follows the same decomposed principles outlined in the Zemax simulations (Sec. 4.1.1) but with the aperture removed and treated as an imaginary construct. This also permits the input 4f to be treated as a simple 4f expander and the image distance at its exit can be neglected. Therefore, the relative position of the lenses and the choice of focal lengths of the lenses is simply one of convenience as the spatial information will be *created* at the first SLM.

Finally, after validation of the axial system the dimensions can be used to put together a real, folded sequential system that is optically equivalent to the real layout (Figure 7.6). This includes spectral boundaries, lenses, polarizers, waveplates, estimations of opto-mechanical boundaries, and a geometrically correct beam rotator, a Dove prism in the bridge. The Dove prism is modeled as a non-sequential trapezoidal BK7 wedge.

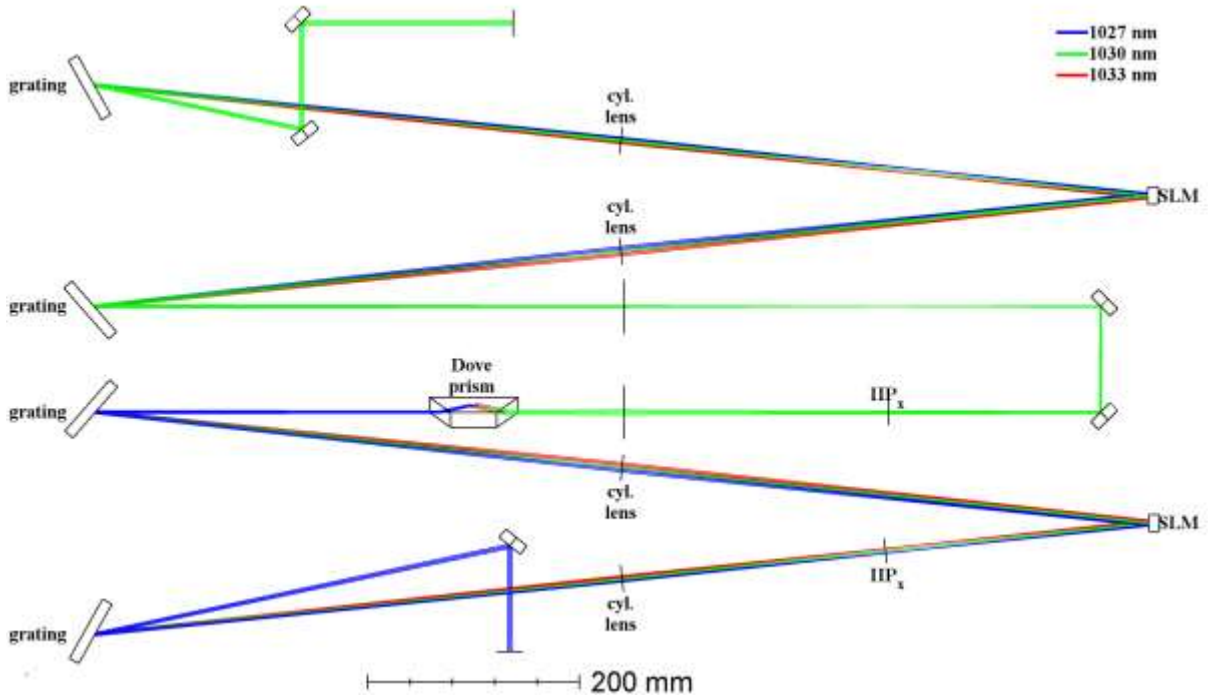


Figure 7.6: Coupled λ-X, λ-Y shapers with a Dove prism as an axial rotation element.

The y-component of the spatial information of the beam is *created* at the first SLM, the beam is rotated, and then the x-component of the spatial information of the beam is created at the second SLM. The combined spatio-spectral modulation can then be picked up by an imaging telescope and brought to the harmonic section. However, in this case the telescope must have an object distance long enough to image the final SLM plane.

7.3 ELLA2 CONSTRUCTION AND OUTLOOK

Under the new initiative, the project was furnished with a completely new set of ultra-stable optomechanics, optics, optical breadboards and more (Figure 7.7) [59]. Provisions were made for parasitic and destructive diagnostic measurements, a beam drift-compensator system, signal digitization, and integration into the PITZ control system.

The opto-mechanics chosen were of the Thorlabs Polaris family of low deformation [105] [106], thermally matched optomechanics; a series of Ø25 mm posts, board clamps, lens and mirror mounts all of which meet to specify an angular deviation of < 1 μrad after a 12.5 ℃ cycling.

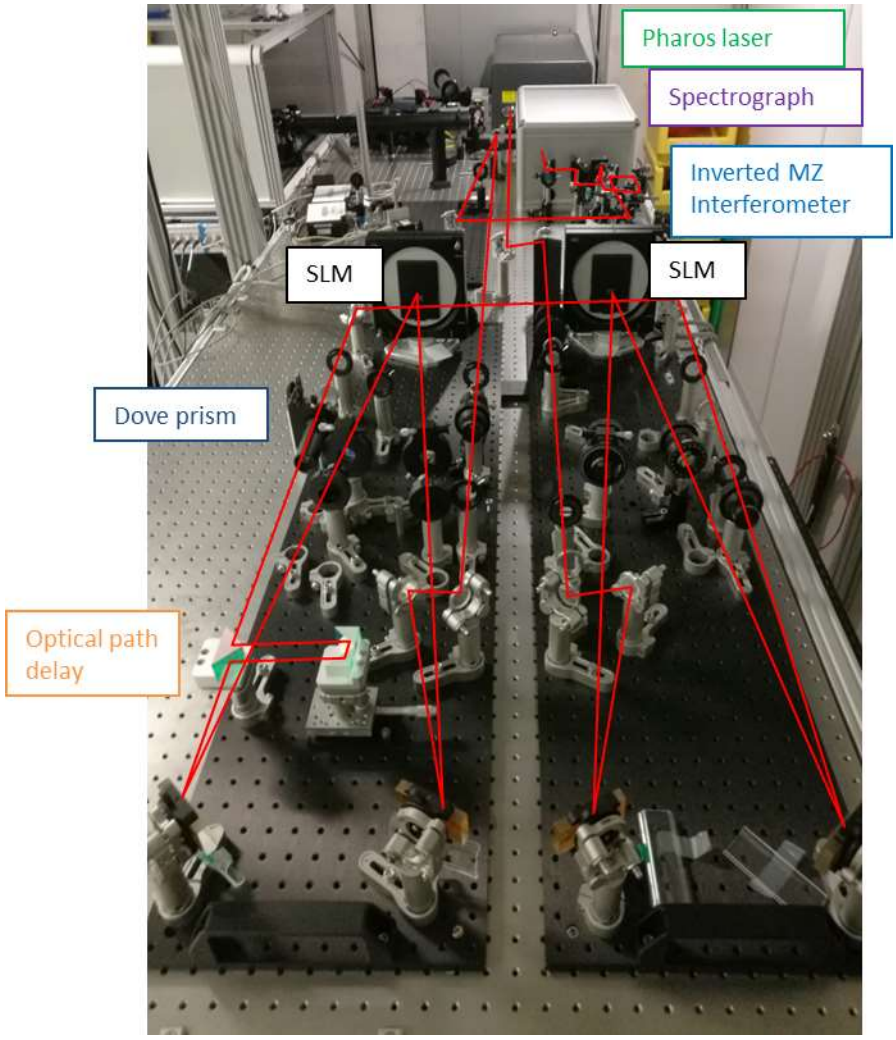


Figure 7.7: ELLA2 on-table construction with independent SLM (λ-X, λ-Y) IR shaper boards and basic spectral diagnostics.

The drastically simplified optical scheme has already shown a marked improvement in long-term stability, shape preservation (Figure 7.8) and spectral quality.

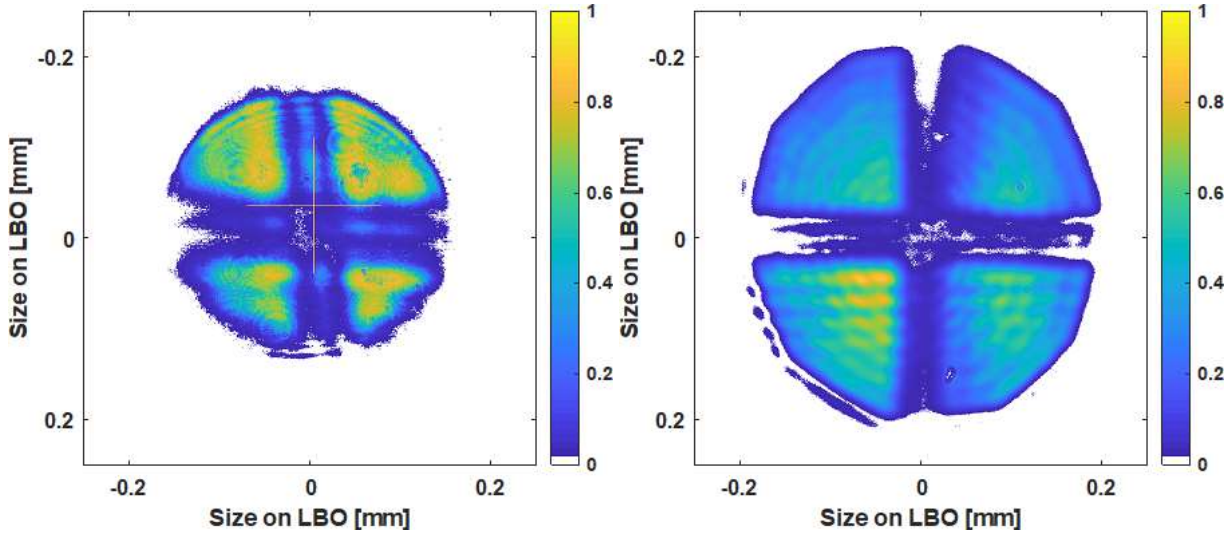


Figure 7.8: The original ELLA transverse distribution at the plane of the LBO crystal (left) and the new ELLA2 transverse distribution at its equivalent LBO crystal plane (right).

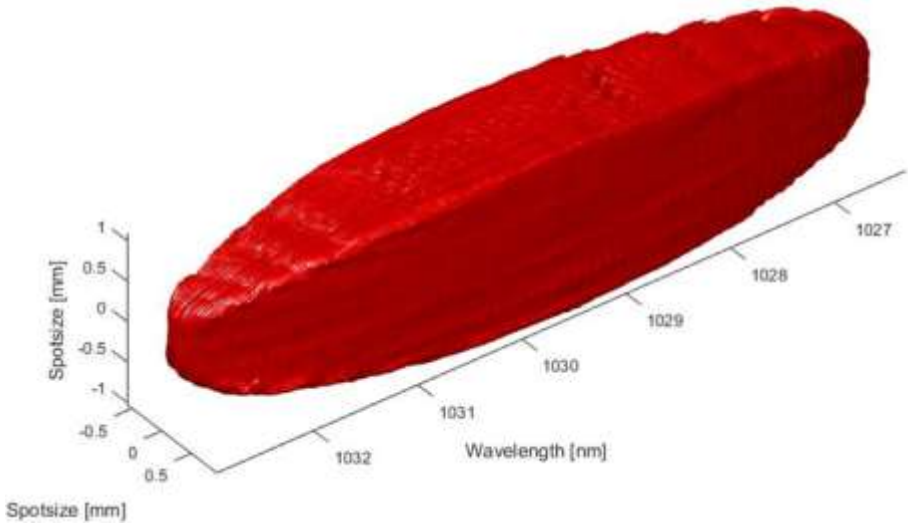


Figure 7.9: Spectrographical reconstruction of an uncropped (quasi-)ellipsoidal IR pulse produced by ELLA2.

In conclusion, under provision of a new, high-power laser system the pulse shaping system was easily remodeled to minimize the amount of required optics, and their subsequent optomechanics, and to accommodate the full active area of two independent SLMs for a broadband, ultra-short source.

The new Pharos laser has already proved itself an optically reliable, clean platform on which to build a dependable, stable laser pulse shaping system for long-term operation in a photoinjector. The smooth spectral output and variable pulse energy provide ample margin in which to produce shaped IR pulses, and the simplified pulse shaping scheme and high quality optomechanics have demonstrated the long term stability required for exhaustive measurement campaigns and improved the quality of the produced pulses.

Quasi-ellipsoidal pulses have already been successfully produced in the infrared (Figure 7.9)

and characterized via spectrographic analysis with the new ELLA2 system and is expected to be corroborated by cross-correlation in the future.

With further improvements of the µTCA synchronization and completion of the conversion section and UV diagnostics the redesigned laser system is expected to be able to provide definitive quasi-ellipsoidal laser pulses for measurement in the photoinjector and adaptive, reliable pulse shaping for any forthcoming experiments.

Chapter 8 Summary

The relevance and benefits of shaped charged particle distributions in photoinjectors have been realized and known for years but their realization has only been truly accessible with the advances of laser and materials engineering in the last few decades.

The drive towards shaped bunches has been primarily limited by the high energy demands of UV photocathodes and the subsequent challenge of providing laser pulses with sufficient excess energy to sacrifice during the laser pulse shaping process while meeting operational requirements on phase and energy stability, duty cycle, pulse length, etc.

Being trivial to implement, transverse masking with apertures quickly found success and application in photoinjectors worldwide which soon led to encouraging simulations and a desire for cylindrical pulses.

Cylindrical pulses themselves only found solid ground in the last decade demonstrating unequalled low-emittance beams at PITZ. With this success a collaboration was formed with the Institute of Applied Physics (Nizhny Novgorod) together with PITZ and the Joint Institute of Nuclear Research (Dubna) to push even further to the theoretical minimum with the development of a laser system capable of producing (quasi-) ellipsoidal laser pulses (ELLA).

This theoretical minimum of ellipsoidal bunches is evident from the combination of basic electrostatics and electron beam dynamics where it can be seen how the linearized space charge forces reduce deformation of the phase space and the emittance during emission and how the forces are reduced for relativistic bunches.

However, the complications of practical realization of the laser pulses required to produce said bunches (by first order approximation) are then seen in optical theory where the difficulties and engineering trade-offs reveal themselves.

A shaped pulse laser system capable of accessing both the transverse and longitudinal dimensions must strike a balance between available bandwidth, pulse shaper dimensions, cross-correlator resolution, and non-linear frequency conversion all under the constraints of pulse energy and shape preservation.

Such a novel laser system can be ideally situated at PITZ, as a “little sister” to facilities such as FLASH and the European XFEL PITZ is an ideal candidate to test and evaluate new prototype photoinjector technologies and their possible application to bigger, high-demand user-facilities where such experimentation would be costly or operationally prohibitive. With its broad suite of available electron beam diagnostics, flexible machine parameters, and dedicated runtime PITZ is situated in a unique position and prototyping new laser pulse shaping technologies fits snugly within the framework of the facility.

Simulations are an indispensable tool where practicality and insight overlap and the ramifications and the physics of the systematic complications can be explored. Decomposition of the pulse shaping scheme utilized into its reciprocal and transverse components simplifies the

complexities of the multidimensional concept. Clarification is obtained of both the conservation of the imaging condition, despite the non-axial components, through the system and the mechanism by which the scheme accesses the transverse components of a spectrally dispersed laser pulse.

Mathematical modelling of the fundamental electric fields of the laser pulse permits prediction of the amplitude-phase masks required at the shaping plane in a reciprocal SLM pulse shaper, and also estimates of efficiency in the pulse shaping process.

Furthermore, available physics codes have shown the effectiveness of solutions to the problems of efficiency and shape conservation on non-linear conversion of broadband, spatio-spectrally shaped pulses with spectral chirping. Albeit, with some reservations on one-dimensional, transverse shape conservation due to walkoff in BBO which can only be concretely determined in experiment.

Electron beam dynamics codes confirmed the applicability and improved performance of ellipsoidal bunches in the PITZ accelerator and were a major motivation behind the development of the project. Regardless of situation, simulation has shown that for high-charge bunches an ellipsoidal bunch is almost always superior in terms of bunch quality than any other distribution. This was borne out in simulation for the abnormal case experienced in reality, where lower charge and shorter pulse length still demonstrated an improvement compared to the nominal cylindrical pulse as any approximation to a true ellipsoidal bunch relaxes space-charge forces.

Description, characterization, and experience with the prototype ELLA laser system revealed a combination of clever design solutions to engineering challenges which were often limited by practical realization.

A single, fibre-based laser oscillator was used to provide two separate, synchronous, broadband laser pulses for both spectral shaping and for high-resolution temporal cross-correlatoion. This basis enabled the exploitation of the fiber as its own delay line by stretching it with a piezoelectric driven over the pulse train duration.

The reciprocal design capitalized on the inherent polarization property of the scheme to accomplish quadratic spatio-spectral pulse shaping in a (relatively) compact form while minimizing the number of active elements and providing access to both the amplitude and phase of the Fourier components.

These technical feats resulted in a sophisticated setup which placed high demands on the qualities of the system with the even more stringent requirements of the photinjector facility environment stressing the system further.

During the commissioning and operational phases it was revealed that stability issues were underestimated and that a number of fundamental requirements had been overlooked during the initial conceptual design phase. For a spatio-spectral laser pulse shaping scheme the spectral quality of the system as a whole was very poor, and the reciprocal design and multi-pass, thin-disc amplifier further exacerbated the issue. Ultimately, the combination of all these issues restricted the amount of development and electron beam measurements that system was capable

of.

The electron beam measurements, in corroboration with laser beam diagnostics, showed active laser-driven electron bunch shaping and beam parameters comparable with nominal PITZ operation. Successful oscillator synchronization was achieved albeit at a restricted resolution, with 500 pC bunch charge, 12 ps FWHM pulses and typical beam energies of 22 MeV.

Comparable emittance measurements were made between the standard MBI photocathode laser and the prototype ELLA photocathode laser, however due to an oversight in the design of the transport telescope, only a comparison between a cropped ellipsoid and the “long” 12 ps Gaussian laser pulse of the MBI laser could be carried out.

The number, and quality, of electron beam measurements was cut short by the failure of the cathode spring in Gun 4.2 and limited by the poor phase stability which is known to had a detrimental effect on emittance measurements. Nevertheless, it was possible to show basic properties and advantages of the 3D pulse shaping capabilities.

A great many lessons were learned from the experiences with the prototype and used to drive a redesign of the concept. This concept was centered around a single oscillator-amplifier backend, two independent, dichroic spectro-spatial SLM pulse shapers, with stability as a core design tenets as to provide a flexible, reliable photocathode laser for future electron beam experiments.

The redesign, currently under construction, has already demonstrated superior spectral quality, image quality, IR pulse shaping capabilities, and stability all within a single platform. It is expected to be completed with on-table UV pulse shaping experiments, fs-scale oscillator synchronization, and full integration into the control systems by the end of 2019, with routine operation by shift operators in 2020.

Appendix

A. Auxiliary tables

Below is given the relative values for the homogenous cylindrical volume of full-length L, and radial length r, and the half-length L and radial r for the ellipsoidal distribution, along with the rms value of the relative projections. It can be seen that for equivalent rms values the ellipsoidal distribution has a slightly larger volume and therefore, for distribution of equal charge, a slightly lower charge density on the order of ~7.5%.

Table A.1: Distribution relations.

Distribution	**L [ps]**	**L [mm]**	**σ_L [ps]**	**σ_L [mm]**	**r [mm]**	**σ_r [mm]**	**Vol. [mm^3]**
Cylindrical	20	6	5.774	1.732	0.6	0.3	6.786
Ellipsoidal	12.91	3.873	5.774	1.732	0.6708	0.3	7.300
Ellipsoidal	10	3	4.472	1.342	0.6	0.2683	4.524

Table A.2: Longitudinal coordinates of important beamline components in this work.

Object	**Location, [m]**
Bucking	-0.104
Cathode plane	0.000
Main solenoid (center)	0.276
LEDA entrance	0.963
CDS booster entrance	2.675
High1.scr1	5.277
High1.scr3	7.125
HEDA1 entrance	7.370
High1.scr4	8.410
High1.scr5	8.920
TDS entrance	10.642
PST.scr1	12.278

B. Gaussian relation

Laser beams are typically characterized as a transversely fundamentally Gaussian distribution (Figure B.1) which is given by the formula:

$$y(r,\sigma) = \frac{1}{\sqrt{2\pi\sigma^2}} e^{-\frac{r^2}{2\sigma^2}}. \tag{B.1}$$

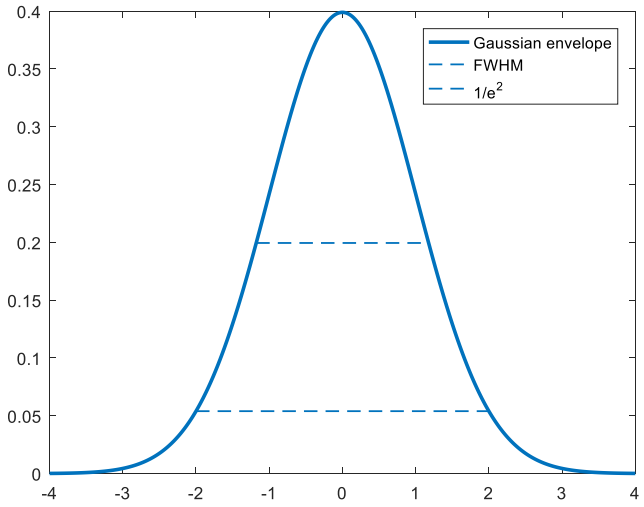


Figure B.1: A normalized Gaussian distribution with the Full Width Half Maximum (FWHM) and e^{-2} lines.

Typically, lasers are measured or specified as either Full Width Half Maximum or FW1e^{-2}. While both can be used to calculate the parameters of the original distribution, the former is measure of convenience while the latter has more statistical significance.

Table B.3: Gaussian measures and their statistical properties.

Measure	Amplitude	Width	Statistical Significance
FW1e^{-2}	$e^{-2} = 0.135$	4σ	95%
FW1e^{-1}	$e^{-1} = 0.367$	$2\sqrt{2\sigma^2}$	84%
FWHM	0.5	$2\sqrt{2\ln(2)}\sigma$	76%
FW1σ	$e^{-1/2} = 0.606$	2σ	68%

Table B.4: Time-bandwidth products for various relations.

Relation	TBP value
$\Delta t\Delta\omega$	$4\ln(2)$
$\Delta t\Delta f$	$4\ln(2)/2\pi$
$\Delta t\Delta\lambda c/\lambda^2$	$4\ln(2)/2\pi$

C. Flattop fit of a Gaussian envelope

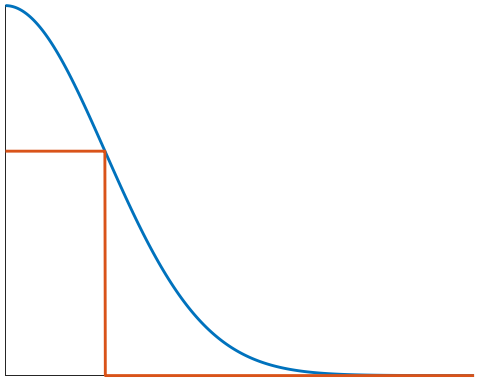


Figure C.2: A flattop inscribed within a Gaussian envelope.

For a flattop centred at the origin inscribed within a Gaussian envelope (Figure C.2) the generalized form is:

$$y(x) = e^{-x^2/2\sigma^2}. \tag{C.2}$$

The area contained within the rectangle is simply:

$$A(x) = xy = xe^{-x^2/2\sigma^2}. \tag{C.3}$$

Therefore, the maxima of the area can be found by solving the differential:

$$\frac{dA}{dx} = y\left(1 - {2x^2}/{2\sigma^2}\right) = e^{-x^2/2\sigma^2}\left(1 - {2x^2}/{2\sigma^2}\right). \tag{C.4}$$

Solving for dA/dx = 0 the maxima is found at:

$$x = \sigma. \tag{C.5}$$

Therefore a flattop with maximized area inscribed within a Gaussian envelope is given by:

$$y(\sigma) = e^{-\sigma^2/2\sigma^2} = e^{-1/2}, \tag{C.6}$$

$$A(x) = \sigma e^{-1/2}. \tag{C.7}$$

D. Rectangular fit of elliptical envelope

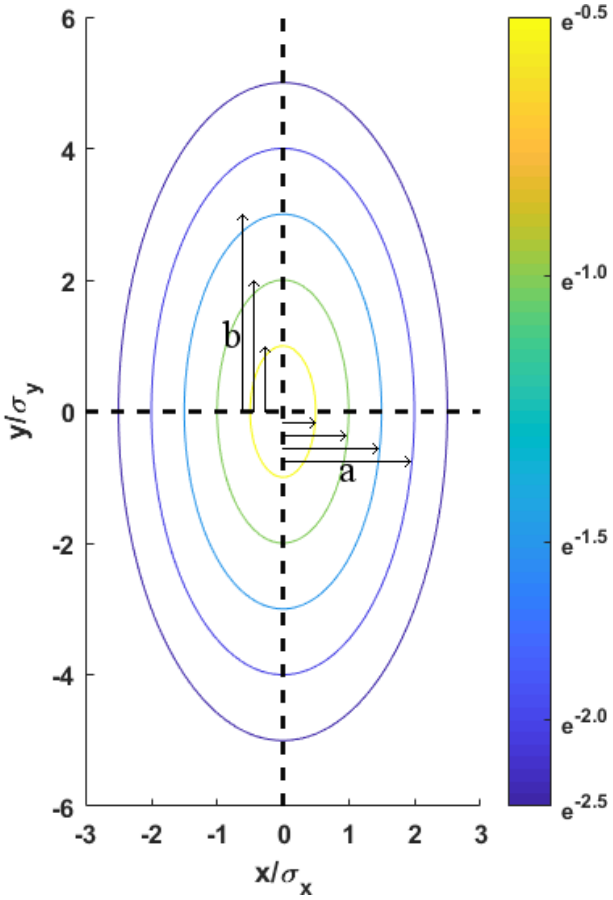


Figure D.3: Ellipses formed on a Gaussian surface at various heights.

For any Gaussian surface (Figure D.3) the height z at a point is given by:

$$z(x,\mathrm{y}) = e^{-\frac{x^2}{2\sigma x^2}} e^{-\frac{y^2}{2\sigma y^2}}. \tag{D.8}$$

It can be seen by substitutions $a = \sqrt{2}\sigma_x$ and b= $\sqrt{2}\sigma_y$ then that for any arbitrary height z an ellipse is formed:

$$\frac{x^2}{a^2} + \frac{y^2}{b^2} = -\ln(z). \tag{D.9}$$

There should also be a best fit for a rectangular area inscribed within the ellipse (Figure D.4).

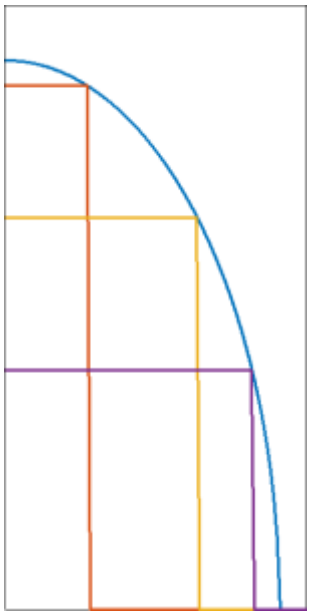


Figure D.4: A series of rectangles inscribed within an elliptical envelope.

The generalized form of an ellipse is given by:

$$y(x) = \frac{b}{a}\sqrt{a^2 - x^2}, \tag{D.10}$$

and so the area of a rectangle inscribed under the curve is:

$$A(x) = xy = x\frac{b}{a}\sqrt{a^2 - x^2}. \tag{D.11}$$

However, in this case the horizontal a, and vertical b, axes of the ellipse are tied to the dimensions of the Gaussian surface and the principle axes:

$$z(x,0) = e^{-\frac{x^2}{2\sigma_x{}^2}}, z(0,\mathrm{y}) = e^{-\frac{y^2}{2\sigma_y{}^2}}, \tag{D.12}$$

$$a(z) = \sqrt{-2\sigma_x{}^2 \ln(z)}, b(z) = \sqrt{-2\sigma_y{}^2 \ln(z)}. \tag{D.13}$$

From this the eccentricity e, where b/a is the aspect ratio, of an ellipse formed at any height z of the Gaussian surface is constant:

$$e = \sqrt{1 - \left(\frac{b}{a}\right)^2}, \tag{D.14}$$

$$\frac{b}{a} = \frac{\sqrt{-2\sigma_y{}^2 \ln(z)}}{\sqrt{-2\sigma_x{}^2 \ln(z)}} = \frac{\sigma_y}{\sigma_x}. \tag{D.15}$$

Thus, any solution for the maximized area inscribed within the ellipse should be valid for any height. Solving the differential equation to find the maxima returns:

$$\frac{dA}{dx} = 0 \rightarrow x = \pm\frac{\sqrt{2}a}{2}, \tag{D.16}$$

and therefore the area is maximized at:

$$A\left(\pm\frac{\sqrt{2}a}{2}\right) = \pm\frac{1}{2}ab. \tag{D.17}$$

This solution can then be utilized to determine the rectangular volume under the area as it scales with height z:

$$V = zA = \pm z\frac{1}{2}ab, \tag{D.18}$$

which yields:

$$V = \pm z\frac{1}{2}\sqrt{-2{\sigma_x}^2\ln(z)}\sqrt{-2{\sigma_y}^2\ln(z)}, \tag{D.19}$$

$$V = \pm z\ln(z)\,\sigma_x\sigma_y. \tag{D.20}$$

Solving the differential equation to find the maxima again:

$$\frac{dV}{dz} = 0, \rightarrow z = e^{-1}, \tag{D.21}$$

and the largest possible volume inscribable within a Gaussian surface reduces to:

$$V = e^{-1}\sigma_x\sigma_y. \tag{D.22}$$

E. Circular fit of a Gaussian envelope

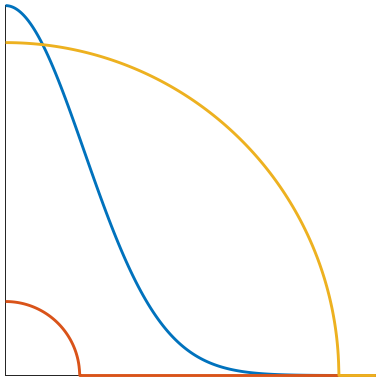


Figure E.5: Circles of varying radii centered within a Gaussian envelope.

For a circle centred at the origin inscribed within a Gaussian envelope (Figure E.5) of the generalized form:

$$r^2 = x^2 + y^2, \tag{E.23}$$

it can be seen that by running the radius of the circle along the envelope that there is a point where the radius is minimized while also touching the envelope only at a single point.

Therefore the radius of a circle ran along the envelope is given by:

$$r^2 = x^2 + e^{-x^2/\sigma^2}, \tag{E.24}$$

and the minimum is found by the derivative:

$$\frac{d(r^2)}{dx} = 2x - 2\frac{x}{\sigma^2}e^{-x^2/\sigma^2}. \tag{E.25}$$

Solving for dr/dx = 0 and the radius is found when:

$$x = \sigma\sqrt{\ln\left(\frac{1}{\sigma^2}\right)}. \tag{E.26}$$

Therefore the radius, and therefore the maximized area, for a circle inscribed within a Gaussian envelope is:

$$r^2 = \sigma^2 \ln\left(\frac{1}{\sigma^2}\right) + \sigma^2. \tag{E.27}$$

F. Elliptical fit of a Gaussian envelope

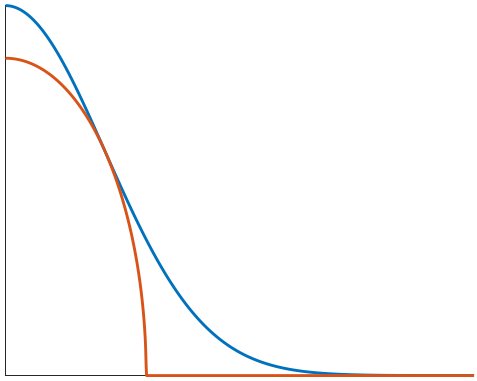


Figure F.6: An ellipse inscribed within a Gaussian envelope.

An ellipse centred at the origin is given by the general form:

$$y(x) = \frac{b}{a}\sqrt{a^2 - x^2}. \tag{F.28}$$

To inscribe it within a Gaussian envelope the curve must touch the envelope at a single point (Figure F.6). This point must lie on the envelope and the slope of both geometries must be equal at that location. Therefore the radii and slopes must be equal:

$$r^2 = x^2 + y^2, \tag{F.29}$$

$$x^2 + \left[e^{-x^2/2\sigma^2}\right]^2 = x^2 + \left[\frac{b}{a}\sqrt{a^2 - x^2}\right]^2, \tag{F.30}$$

$$\frac{d}{dx}e^{-x^2/2\sigma^2} = \frac{d}{dx}\frac{b}{a}\sqrt{a^2 - x^2}. \tag{F.31}$$

Solving the set of simultaneous equations to find the major and minor axes a and b returns:

$$a(x) = \sqrt{\sigma^2 + x^2}, \tag{F.32}$$

$$b(x) = \frac{e^{-x^2/2\sigma^2}\sqrt{\sigma^2 + x^2}}{\sigma}. \tag{F.33}$$

Since the area of an ellipse is simply:

$$A(x) = \pi ab, \tag{F.34}$$

the maxima of the area is given by solving for dA/dx = 0, which is found when:

$$x = \sigma. \tag{F.35}$$

Therefore, the area of an ellipse inscribed within a Gaussian envelope is maximized when:

$$a(\sigma) = \sqrt{2}\sigma, \tag{F.36}$$

$$b(\sigma) = \sqrt{2}e^{-1/2}. \tag{F.37}$$

Bibliography

[1] E. D. Courant, M. S. Livingston and H. S. Snyder, "The strong-focusing synchroton—A new high energy accelerator," *Physical Review,* vol. 88, p. 1190, 1952.

[2] H. Motz, W. Thon and R. N. Whitehurst, "Experiments on Radiation by Fast Electron Beams," *Journal of Applied Physics,* vol. 24, pp. 826-833, 1953.

[3] J. S. Fraser, R. L. Sheffield and E. R. Gray, "High-brightness photoemitter development for electron accelerator injectors," *AIP Conference Proceedings,* vol. 130, pp. 598-601, 1985.

[4] M. Altarelli, R. Brinkmann, M. Chergui, W. Decking, B. Dobson, S. Düsterer, G. Grübel, W. Graeff, H. Graafsma, J. Hajdu and others, Eds., XFEL: The European X-Ray Free-Electron Laser. Technical design report, 2006.

[5] I. Robinson, G. Gruebel and S. Mochrie, "Focus on X-ray beams with high coherence," *New Journal of Physics,* vol. 12, p. 035002, 2010.

[6] P. Schmüser, M. Dohlus and J. Rossbach, Ultraviolet and Soft X-Ray Free-Electron Lasers: Introduction to Physical Principles, Experimental Results, Technological Challenges, Springer Berlin Heidelberg, 2008.

[7] K.-J. Kim, "An analysis of self-amplified spontaneous emission," *Nuclear Instruments and Methods in Physics Research Section A: Accelerators, Spectrometers, Detectors and Associated Equipment,* vol. 250, pp. 396-403, 1986.

[8] J. Early, J. Barton, G. Busch, R. Wenzel and D. Remelius, "The Los Alamos FEL photoinjector drive laser," *Nuclear Instruments and Methods in Physics Research Section A: Accelerators, Spectrometers, Detectors and Associated Equipment,* vol. 318, pp. 381-388, 1992.

[9] J. Bähr, K. Abrahamyan, G. Asova, G. Dimitrov, H. Grabosch, J. H. Han, H. Henschel, S. Khodyachykh, M. Krasilnikov, S. Liu and others, "Upgrades of the Laser Beam-line at PITZ," in *Proceedings of the Free Electron Laser Conference*, 2005.

[10] I. Will and G. Klemz, "Generation of flat-top picosecond pulses by coherent pulse stacking in a multicrystal birefringent filter," *Opt. Express,* vol. 16, pp. 14922-14937, 9 2008.

[11] C. Froehly, B. Colombeau and M. Vampouille, "II Shaping and Analysis of Picosecond Light Pulses," vol. 20, E. Wolf, Ed., Elsevier, 1983, pp. 63-153.

[12] X. M. Tong and C. D. Lin, "Empirical formula for static field ionization rates of atoms and molecules by lasers in the barrier-suppression regime," *Journal of Physics B: Atomic, Molecular and Optical Physics,* vol. 38, p. 2593, 2005.

[13] A. Laskin, "Achromatic refractive beam shaping optics for broad spectrum laser applications," in *Laser Beam Shaping X*, 2009.

[14] G. Vashchenko and others, "Emittance Measurements of the Electron Beam at PITZ for the Commissioning Phase of the European X-FEL," in *Proceedings, 37th International Free Electron Laser Conference (FEL 2015): Daejeon, Korea, August 23-28, 2015*, 2015.

[15] M. Krasilnikov, F. Stephan, G. Asova, H.-J. Grabosch, M. Groß, L. Hakobyan, I. Isaev, Y. Ivanisenko, L. Jachmann, M. Khojoyan, G. Klemz, W. Köhler, M. Mahgoub, D. Malyutin, M. Nozdrin, A. Oppelt, M. Otevrel, B. Petrosyan, S. Rimjaem, A. Shapovalov, G. Vashchenko, S. Weidinger, R. Wenndorff, K. Flöttmann, M. Hoffmann, S. Lederer, H. Schlarb, S. Schreiber, I. Templin, I. Will, V. Paramonov and D. Richter, "Experimentally minimized beam emittance from an L-band photoinjector," *Phys. Rev. ST Accel. Beams,* vol. 15, no. 10, p. 100701, 10 2012.

[16] M. Bakr, M. Khojoyan, M. Krasilnikov, F. Stephan and G. Vashchenko, "Beam Dynamics Simulation for the Upgraded PITZ Photo Injector Applying Various Photocathode Laser Pulses," in *Proceedings, 37th International Free Electron Laser Conference (FEL 2015): Daejeon, Korea, August 23-28, 2015*, 2015.

[17] I. M. Kapchinskij and V. V. Vladimirskij, "Limitations Of Proton Beam Current In A Strong Focusing Linear Accelerator Associated With The Beam Space Charge," pp. 274-287, 1959.

[18] C. Limborg-Deprey and P. R. Bolton, "Optimum electron distributions for space charge dominated beams in photoinjectors," *Nuclear Instruments and Methods in Physics Research Section A: Accelerators, Spectrometers, Detectors and Associated Equipment,* vol. 557, pp. 106-116, 2006.

[19] C. C. Lin, L. Mestel and F. H. Shu, "The gravitational collapse of a uniform spheroid," in *Selected Papers of CC Lin with Commentary: Vol. 1: Fluid Mechanics Vol. 2: Astrophysics*, World Scientific, 1987, pp. 571-586.

[20] L. Serafini, "The short bunch blow-out regime in RF photoinjectors," in *AIP Conference Proceedings*, 1997.

[21] B. O'Shea, J. B. Rosenzweig, G. Asova, J. Bähr, M. Hänel, Y. Ivanisenko, M. Khojoyan, M. Krasilnikov, L. Staykov, F. Stephan and J. Rönsch-Schulenburg, "Measurement of self-shaped ellipsoidal bunches from a photoinjector with postacceleration," *Phys. Rev. ST Accel. Beams,* vol. 14, no. 1, p. 012801, 1 2011.

[22] Y. Li, S. Chemerisov and J. Lewellen, "Laser pulse shaping for generating uniform three-dimensional ellipsoidal electron beams," *Phys. Rev. ST Accel. Beams,* vol. 12, no. 2, p. 020702, 2 2009.

[23] H. Tomizawa, H. Dewa, T. Taniuchi, A. Mizuno, T. Asaka, K. Yanagida, S. Suzuki, T. Kobayashi, H. Hanaki and F. Matsui, "Adaptive shaping system for both spatial and temporal profiles of a highly stabilized UV laser light source for a photocathode RF gun," *Nuclear Instruments and Methods in Physics Research Section A: Accelerators, Spectrometers, Detectors and Associated Equipment,* vol. 557, pp. 117-123, 2006.

[24] M. B. Danailov and I. P. Christov, "Time-space Shaping of Light Pulses by Fourier Optical Processing," *Journal of Modern Optics,* vol. 36, pp. 725-731, 1989.

[25] A. M. Weiner, "Femtosecond pulse shaping using spatial light modulators," *Review of Scientific Instruments,* vol. 71, pp. 1929-1960, 2000.

[26] S. Y. Mironov, A. K. Poteomkin, E. I. Gacheva, A. V. Andrianov, V. V. Zelenogorskii, R. Vasiliev, V. Smirnov, M. Krasilnikov, F. Stephan and E. A. Khazanov, "Generation of 3D ellipsoidal laser beams by means of a profiled volume chirped Bragg grating," *Laser Physics Letters,* vol. 13, p. 055003, 2016.

[27] M. Khojoyan, M. Krasilnikov, F. Stephan, G. Vashchenko and others, "Beam dynamics optimization for the high brightness PITZ photo injector using 3D ellipsoidal cathode laser pulses," in *TUPSO36, Proceedings of the 35th International Free Electron Laser Conference, Manhattan, USA*, 2013.

[28] T. H. Maiman, "Stimulated Optical Radiation in Ruby," *Nature,* vol. 187, pp. 493-494, 1960.

[29] B. Holst, "„Undulator-prinzip“, translation by James Good, Attribution-ShareAlike 3.0 Unported (CC BY-SA 3.0)," [Online]. Available: https://commons.wikimedia.org/wiki/File:Undulator-prinzip.svg.

[30] J. Rosenzweig, L. Serafini and G. A. Travish, The Physics and Applications of High Brightness Electron Beams: Proceedings of the ICFA Workshop, Chia Laguna, Sardinia, 1-6 July 2002, World Scientific, 2003.

[31] R. A. Powell, W. E. Spicer, G. B. Fisher and P. Gregory, "Photoemission studies of cesium telluride," *Physical review B,* vol. 8, p. 3987, 1973.

[32] D. Sertore, P. Michelato, L. Monaco, S. Schreiber and A. Bonucci, "Review of the Production Process of TTF and PITZ Photocathodes," in *Proceedings of the 2005 Particle Accelerator Conference*, 2005.

[33] A. Aryshev, M. Shevelev, Y. Honda, N. Terunuma and J. Urakawa, "Femtosecond response time measurements of a Cs2Te photocathode," *Applied Physics Letters,* vol. 111, p. 033508, 2017.

[34] F. Gerigk, "Cavity types," in *Proceedings, CAS - CERN Accelerator School: RF for Accelerators, Ebeltoft, Denmark, 8 - 17 Jun 2010*, 2011.

[35] D. A. Edwards and M. J. Syphers, An introduction to the physics of high energy accelerators, John Wiley & Sons, 2008.

[36] K.-J. Kim, "Rf and space-charge effects in laser-driven rf electron guns," *Nuclear Instruments and Methods in Physics Research Section A: Accelerators, Spectrometers, Detectors and Associated Equipment,* vol. 275, pp. 201-218, 1989.

[37] E. J. Jaeschke, S. Khan, J. R. Schneider, J. Hastings and others, Synchrotron light sources and free-electron lasers, Springer Reference,, 2016.

[38] K. Flottmann, "Estimation of the thermal emittance of electrons emitted by cesium telluride photocathodes," in *19th International Conference on Free Electron Lasers Beijing, China, August 18-21, 1997*, 1997.

[39] E. Branlard, "On the implementation of a 3D space charge algorithm to understand and further study the physics of linear accelerators," Fermilab-Supaero technical report, 2009.

[40] O. D. Kellogg, Foundations of potential theory, vol. 31, Springer Science & Business Media, 2012.

[41] M. Ferrario, M. Migliorati and L. Palumbo, "Space charge effects," *arXiv preprint arXiv:1601.05214,* 2016.

[42] B. Colombeau, M. Vampouille and C. Froehly, "Shaping of short laser pulses by passive optical Fourier techniques," *Optics Communications,* vol. 19, pp. 201-204, 1976.

[43] A. M. Weiner, S. Oudin, D. E. Leaird and D. H. Reitze, "Shaping of femtosecond pulses using phase-only filters designed by simulated annealing," *J. Opt. Soc. Am. A,* vol. 10, pp. 1112-1120, 5 1993.

[44] M. M. Wefers and K. A. Nelson, "Programmable phase and amplitude femtosecond pulse shaping," *Optics Letters,* vol. 18, pp. 2032-2034, 1993.

[45] M. M. Wefers and K. A. Nelson, "Analysis of programmable ultrashort waveform generation using liquid-crystal spatial light modulators," *J. Opt. Soc. Am. B,* vol. 12, pp. 1343-1362, 7 1995.

[46] CambridgeBayWeather, "„Twinkle Twinkle Little Star“, (Public Domain)," [Online]. Available: https://commons.wikimedia.org/wiki/File:Twinkle_Twinkle_Little_Star_plain.ogg.

[47] A. Webster, *Useful Mathematical Formulas for Transform Limited Pulses,* Dover publications, 1964.

[48] R. W. Boyd, Nonlinear Optics, Third Edition, 3rd ed., Orlando, FL: Academic Press, Inc., 2008.

[49] Aesopus, "„LCOS-eng“, Simplified Schematic by James Good, (CC BY-SA 3.0)," [Online]. Available: https://commons.wikimedia.org/wiki/File:LCOS-eng.png.

[50] G. Lazarev, A. Hermerschmidt, S. Krüger and S. Osten, "LCOS Spatial Light Modulators: Trends and Applications," in *Optical Imaging and Metrology*, Wiley-Blackwell, 2012, pp. 1-29.

[51] "Holoeye Plotu Specifcation Sheet," [Online]. Available: https://www.elliotscientific.com/pdf/Pluto-Instructions_409.pdf.

[52] "Hamamatsu X10468 Specifcation Sheet," [Online]. Available: https://www.hamamatsu.com/resources/pdf/ssd/x10468_series_etc_kacc1172e.pdf.

[53] E. Collett, Field Guide to Polarization, Society of Photo Optical, 2005.

[54] J. Goodman, "Introduction to Fourier optics," 2008.

[55] V. G. Dmitriev, G. G. Gurzadyan and D. N. Nikogosyan, Handbook of nonlinear optical crystals, vol. 64, Springer, 2013.

[56] M. Bass, C. DeCusatis, J. Enoch, V. Lakshminarayanan, G. Li, C. Macdonald, V. Mahajan and E. Van Stryland, Handbook of optics, Volume II: Design, fabrication and testing, sources and detectors, radiometry and photometry, McGraw-Hill, Inc., 2009.

[57] A. Smith, "Select Non-Linear Optics (SNLO)," [Online]. Available: http://www.as-photonics.com/snlo.

[58] J. P. Torres, M. Hendrych and A. Valencia, "Angular dispersion: an enabling tool in nonlinear and quantum optics," *Advances in Optics and Photonics,* vol. 2, pp. 319-369, 2010.

[59] C. Koschitzki, "Progress in photo cathode laser pulse shaping towards ultimate low-emittance beams - Experimental progress in infrared shaping & Progress of conversion section design by Christian Koschitzki," in *Hamburg Alliance New Beams and Accelerators, Hamburg (Germany)*, 2018.

[60] S. Linden, J. Kuhl and H. Giessen, "Amplitude and phase characterization of weak blue ultrashort pulses by downconversion," *Optics letters,* vol. 24, pp. 569-571, 1999.

[61] M. Czerny and A. F. Turner, "Über den Astigmatismus bei Spiegelspektrometern," *Zeitschrift für Physik,* vol. 61, pp. 792-797, 01 11 1930.

[62] R. Trebino, K. W. DeLong, D. N. Fittinghoff, J. N. Sweetser, M. A. Krumbügel, B. A. Richman and D. J. Kane, "Measuring ultrashort laser pulses in the time-frequency domain using frequency-resolved optical gating," *Review of Scientific Instruments,* vol. 68, pp. 3277-3295, 1997.

[63] A. S. Radunsky, E. M. K. Williams, I. A. Walmsley, P. Wasylczyk, W. Wasilewski, A. B. U'Ren and M. E. Anderson, "Simplified spectral phase interferometry for direct electric-field reconstruction by using a thick nonlinear crystal," *Opt. Lett.,* vol. 31, pp. 1008-1010, 4 2006.

[64] J. A. Armstrong, "Measurement of picosecond laser pulse widths," *Applied Physics Letters,* vol. 10, pp. 16-18, 1967.

[65] A. Scheeline, "How to design a spectrometer," *Applied spectroscopy,* vol. 71, pp. 2237-2252, 2017.

[66] "AVT Prosilica GC Data sheet 1350," [Online]. Available: https://www.alliedvision.com/en/products/cameras/detail/Prosilica%20GC/1350/action/pdf.html.

[67] V. V. Paramonov, N. I. Brusova, A. I. Kvasha, A. A. Menshov, O. D. Pronin, A. Donat, M. Krasilnikov, A. Oppelt and F. Stephan, "Design parameters of the normal conducting booster cavity for the PITZ-2 test stand," in *Proc. Linac*, 2004.

[68] M. Hänel, "Experimental investigations on the influence of the photocathode laser pulse parameters om the electron bunch quality in an RF Photoelectron source," Ph.D. dissertation, 2010.

[69] I. Isaev, "Stability and Performance Studies of the PITZ Photoelectron Gun," Verlag Deutsches Elektronen-Synchrotron, Hamburg, 2018.

[70] G. Vashchenko, "Transverse phase space studies with the new CDS booster cavity at PITZ," 2013.

[71] M. Reiser, Theory and design of charged particle beams, John Wiley & Sons, 2008.

[72] M. Krasilnikov, I. Isaev, G. Amatuni, G. Asova, P. Boonpornprasert, Y. Chen, J. Good, B. Grigoryan, M. Gross, H. Huck and others, "Electron beam asymmetry compensation with gun quadrupoles at PITZ," in *38th Int. Free Electron Laser Conf.(FEL'17), Santa Fe, NM, USA, August 20-25, 2017*, 2018.

[73] S. Khodyachykh, J. Bähr, M. Krasilnikov, A. Oppelt, L. Staykov, F. Stephan, T. Garvey, D. Lipk and J. Rönsch, "Design of multipurpose dispersive section at PITZ," in *28th International Electron Laser Conference (FEL 06)*, 2006.

[74] V. Paramonov and others, "The PITZ CDS Booster Cavity RF Tuning and Start of Conditioning," in *Proceedings, 25th International Linear Accelerator Conference, LINAC2010: Tsukuba, Japan, September 12-17, 2010*, 2011.

[75] L. Serafini and J. B. Rosenzweig, "Envelope analysis of intense relativistic quasilaminar beams in rf photoinjectors: mA theory of emittance compensation," *Physical Review E,* vol. 55, p. 7565, 1997.

[76] F. Stephan, C. H. Boulware, M. Krasilnikov, J. Bähr, G. Asova, A. Donat, U. Gensch, H. J. Grabosch, M. Hänel, L. Hakobyan and others, "Detailed characterization of electron sources yielding first demonstration of European X-ray Free-Electron Laser beam quality," *Physical Review Special Topics-Accelerators and Beams,* vol. 13, p. 020704, 2010.

[77] L. Staykov, J. Bähr, H. J. Grabosch, S. Khodyachykh, S. Korepanov and M. Krasilnikov, "Commissioning of a New Emittance Measurement System at PITZ," in *Proceedings of the Free Electron Laser Conference*, 2006.

[78] V. Miltchev, "Investigations on the transverse phase space at a photo injector for minimized emittance," Ph.D. dissertation, 2006.

[79] S. Rimjaem, F. Stephan, M. Krasilnikov, W. Ackermann, G. Asova, J. Bähr, E. Gjonaj, H. J. Grabosch, L. Hakobyan, M. Hänel and others, "Optimizations of transverse projected emittance at the photo-injector test facility at DESY, location Zeuthen," *Nuclear Instruments and Methods in Physics Research Section A: Accelerators, Spectrometers, Detectors and Associated Equipment,* vol. 671, pp. 62-75, 2012.

[80] "Zemax OpticStudio," [Online]. Available: https://www.zemax.com/.

[81] "Mathworks," [Online]. Available: http://www.mathworks.com.

[82] M. Wollenhaupt, A. Assion and T. Baumert, "Femtosecond laser pulses: linear properties, manipulation, generation and measurement," *Springer Handbook of Lasers and Optics,* pp. 937-983, 2007.

[83] S. Mironov, E. Gacheva, A. K. Potemkin, E. A. Khazanov, M. Krasilnikov and F. Stephan, "Generation of the Second and Fourth Harmonics with Retaining the Three-Dimensional Quasi-Ellipsoidal Distribution of the Laser Pulse Intensity for a Photoinjector," *Radiophysics and quantum electronics,* vol. 61, pp. 456-466, 2018.

[84] *Chi23D Homepagew.*

[85] "JAI RM-1405 Datasheet," [Online]. Available: https://www.jai.com/uploads/documents/Discontinued-Products/English-Manuals-Datasheets/TM-Series/Datasheet_TM-TMC-1405GE.pdf.

[86] "A Space Charge Tracking Algorithm (ASTRA)," [Online]. Available: http://www.desy.de/ mpyflo/A Space Charge Tracking Algorithm.

[87] G. Pöplau, U. Rienen and K. Flöttmann, "New 3D space charge routines in the tracking code Astra," in *Proceedings of ICAP*, 2006.

[88] M. Khojoyan, M. Krasilnikov and F. Stephan, "Studies on the Application of the 3D Ellipsoidal Cathode Laser Pulses at PITZ," in *Proceedings, 5th International Particle Accelerator Conference (IPAC 2014): Dresden, Germany, June 15-20, 2014*, 2014.

[89] K. M. S. F. Khojoyan and G. Vashchenko, "Optimization of the PITZ photo injector towards the best achievable beam quality," *Proc. FEL2014, Basel, Switzerland,* 2014.

[90] S. Y. Mironov, A. V. Andrianov, E. I. Gacheva, V. V. Zelenogorskii, A. K. Potemkin, E. A. Khazanov, P. Boonpornprasert, M. Gross, J. Good, I. Isaev and others, "Spatio-temporal shaping of photocathode laser

pulses for linear electron accelerators," *Physics-Uspekhi,* vol. 60, p. 1039, 2017.

[91] A. Andrianov, E. Anashkina, S. Muravyev and A. Kim, "All-fiber design of hybrid Er-doped laser/Yb-doped amplifier system for high-power ultrashort pulse generation," *Optics letters,* vol. 35, pp. 3805-3807, 2010.

[92] V. V. Zelenogorskii, A. V. Andrianov, E. I. Gacheva, G. V. Gelikonov, M. Krasilnikov, M. A. Mart'yanov, S. Y. Mironov, A. K. Potemkin, E. M. Syresin, F. Stephan and others, "Scanning cross-correlator for monitoring uniform 3D ellipsoidal laser beams," *Quantum Electronics,* vol. 44, p. 76, 2014.

[93] E. I. Gacheva, V. V. Zelenogorskii, A. V. Andrianov, M. Krasilnikov, M. A. Martyanov, S. Y. Mironov, A. K. Potemkin, E. M. Syresin, F. Stephan and E. A. Khazanov, "Disk Yb: KGW amplifier of profiled pulses of laser driver for electron photoinjector," *Optics express,* vol. 23, pp. 9627-9639, 2015.

[94] S. Biswal, S. P. O'Connor and S. R. Bowman, "Thermo-optical parameters measured in ytterbium-doped potassium gadolinium tungstate," *Applied optics,* vol. 44, pp. 3093-3097, 2005.

[95] A. A. Lagatsky, N. V. Kuleshov and V. P. Mikhailov, "Diode-pumped CW lasing of Yb:KYW and Yb:KGW," *Optics Communications,* vol. 165, pp. 71-75, 1999.

[96] "Thorlabs DET10A datasheet," [Online]. Available: https://www.thorlabs.com/catalogpages/Obsolete/2018/DET10AM.pdf.

[97] "Newport Long Scan Autocorrelator specsheet," [Online]. Available: http://assets.newport.com/pdfs/e6235.pdf .

[98] "Ocean Optics HR2000+ Data Sheet," [Online]. Available: https://oceanoptics.com/wp-content/uploads/OEM-Data-Sheet-HR2000plus.pdf.

[99] S. Rimjaem, J. W. Bähr, H.-J. Grabosch, M. Hänel, Y. Ivanisenko, G. Klemz, M. Krasilnikov, M. Mahgoub, M. Otevrel, B. Petrosyan and others, "Generating low transverse emittance beams for linac based light sources at PITZ," 2010.

[100] Oppelt and others, *Report on Gun4.6 run at PITZ in 2016-2017,* 2018.

[101] L. GmbH, "LDM series," [Online]. Available: https://www.laserline.com/en-int/ldmseries/.

[102] J. Tümmler, R. Jung, H. Stiel, P. V. Nickles and W. Sandner, "High-repetition-rate chirped-pulse-amplification thin-disk laser system with joule-level pulse energy," *Optics letters,* vol. 34, pp. 1378-1380, 2009.

[103] B. Marchetti, R. Aßmann, S. Baark, F. Burkart, U. Dorda, K. Flöttmann, I. Hartl, J. Hauser, J. Herrmann, M. Hüning and others, "Status of the ARES RF Gun at SINBAD: From its Characterization and Installation towards Commissioning," in *9th Int. Particle Accelerator Conf.(IPAC'18), Vancouver, BC, Canada, April 29-May 4, 2018*, 2018.

[104] D. Göries, B. Dicke, P. Roedig, N. Stübe, J. Meyer, A. Galler, W. Gawelda, A. Britz, P. Geßler, H. Sotoudi Namin and others, "Time-resolved pump and probe x-ray absorption fine structure spectroscopy at beamline P11 at PETRA III," *Review of Scientific Instruments,* vol. 87, p. 053116, 2016.

[105] D. Echeverri, N. Jovanovic, J.-R. Delorme, G. Ruane, J. Fucik, J. K. Wallace and D. Mawet, "Optimizing optics and opto-mechanical mounting to minimize static aberrations in high-contrast instruments," in *Adaptive Optics Systems VI*, 2018.

[106] B. D'alessio, A. Cable and B. Jacobus, *Monolithic optical mounting element,* Google Patents, 2016.

Eidesstattliche Versicherung / Declaration on oath

Hiermit erkläre ich an Eides statt, dass ich die vorliegende Dissertationsschrift selbst verfasst und keine anderen als die angegebenen Quellen und Hilfsmittel benutzt habe.

I hereby declare upon oath that I have written the present dissertation independently and have not used further resources and aids than those stated.

Zeuthen, 20.12.2019

Ort, Datum

Unterschrift